DYNAMIC STUDY OF PIEZO DRIVEN ARM IN HDD

LEE CHONG WEE

NATIONAL UNIVERSITY OF SINGAPORE

2015

DYNAMIC STUDY OF PIEZO DRIVEN ARM IN HDD

LEE CHONG WEE

A THESIS SUBMITTED
FOR THE DEGREE OF DOCTOR OF PHILOSOPHY

DEPARTMENT OF MECHANICAL ENGINEERING
NATIONAL UNIVERSITY OF SINGAPORE
2015

DECLARATION

I hereby declare that the thesis is my original work and it has been written by me in its entirety. I have duly acknowledged all the sources of information which have been used in the thesis.

This thesis has also not been submitted for any degree in any university previously.

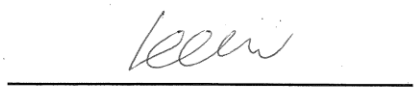

LEE CHONG WEE

21 JANUARY 2015

ABSTRACT

Thanks to the rapid improvements in the development of better piezoelectric materials, more precise fabrication capabilities as well as power electronics circuitry, Ultrasonic Motors (USMs) are beginning to find more applications in many engineering applications. One such potential application is in the area of Hard Disk Drives (HDD) as a precision actuation device for actuator arm placement and seeking of data tracks on disk. However, the actual implementation of such an actuation technology faces serious impediments as preliminary studies reveals several major issues that concerns its vibration robustness, speed-torque sufficiency as well as acoustical noise issues.

Preliminary experimental data on a prototype HDD piezo actuator arm has indicated several issues with their dynamical performances. First, experimental transfer function measurement of the prototype shows a significant response occurring at around hundreds of hertz. This low frequency rippling will result in severe interference when doing track positioning. Second, the ultrasonic excitation frequency (120 kHz) content was found to have been transmitted to the HDD slider. This should not surprise as the slider resonant frequencies are also in the range of hundreds of kilohertz. Again, this means degradation in read/write performance as there is an additional unwanted vibration component. Third, the torque and hence seeking speed of the piezo arm is slower and less powerful than a traditional Voice Coil Motor (VCM) actuator arm. This will further translates to a slower data transfer rate and also degrade the control speed and bandwidth.

Most studies available in the literature do not concern themselves with the detailed study of the dynamical motion of the rotor. The lack of literature concerning the above issues stems from the fact that rotor vibrations are not the main concern in the design of USM. Insofar as

rotor vibrations are studied, it is because they can affect the overall motor performance in terms of the speed-torque characteristics that the study is undertaken. Rotor vibrations are not studied explicitly for its own sake as overall motor performance still takes precedence. The second reason is that rotor vibrations are inconsequential for most applications and therefore do not enter into the radar of researchers. For precision positioning stages, the operation of the USM is often perform statically or quasi-statically, this means that rotor vibrations, if present, are allowed to damp out naturally. On the other hand, if the USM is functioning as a motor, the vibrations of the rotor would be insignificant compared to the dynamically moving rotor. However, the situation is very different when we are considering the application of USM to drive the actuator of a HDD. Now, not only is motor performance important, the vibrations of the rotor also take center stage. This is because the vibration of the rotor is synonymous with the vibrations of the actuator arm. To ensure superior read/write performance, it is necessary to keep the vibrations of the actuator arm and hence the USM rotor to the bare minimum.

The objective of this thesis is to develop an analytical model of a Travelling Wave Rotary Ultrasonic Motor (TRUM) capable of capturing the rigid body dynamics of rotor motion as it interacts with the stator vibrations. The goal of the study is to allow designers to study the vibrations experienced by the rotor during TRUM operation. Due to the highly non-linear nature of operation of a TRUM, a purely finite element based approach to capture its dynamical behavior would be highly impractical as the very fine mesh and time step requirements would make the computational effort humungous. The analytical based modeling approach is coupled with numerical finite element method in the study. FEA is employed in the initial extraction of natural frequencies and mode shapes vibration data for complex geometries while the analytical model takes care of the dynamical computation. An energy approach using a modified Hamilton's Principle for electromechanical system is

employed in the formulation. Rayleigh-Ritz assumed modes are used in the description of the vibration modes. Non-linear interfacial forcing terms which arises during physical contact between rotor and stator surfaces has also been accounted for and included into the model. A contact search algorithm was also implemented in order to track and update system parameters in line with the time evolving states of contact between the rotor and stator surfaces. Given the system inputs, general motor performance measures such as its speed-torque characteristics, power consumption, efficiency as well as rotor vibration profile can be obtained through the model. To obtain experimental results, a prototype TRUM based actuator arm was fabricated. Simulation and experimental results were corroborated to verify the effectiveness of the analytical model.

An analytical simulation platform using results computed with numerical finite element method for the study of the dynamical behavior of a TRUM was developed. The approach presented here has provided us with valuable insights into the mechanics and dynamical behavior of TRUM. The analytical foundation which included the description of rotor dynamics of TRUM established here enables the possibility of better design for improved vibration isolation and speed performance when TRUM is used as a HDD actuator. It also represents a general framework whereby further modeling of other kinds of USM design is possible as well as serves as a useful design tool which can be used to optimize motor parameters before the actual fabrication or prototyping. With such a tool, it will contribute to improved quality of TRUM while at the same time reduce product development cycle time and cost.

ACKNOWLEDGEMENTS

I would like to express my deepest gratitude to both my supervisors, Associate Professor S.P Lim from the Mechanical Engineering Department, National University of Singapore and Dr Lin Wuzhong, my colleague at Data Storage Institute, A-Star Singapore, who is now with the Singapore University of Technology and Design. I am deeply appreciative for their friendship and guidance during my study. Their encouragement and patience with me is most outstanding and I am very grateful to be under their care for these few years.

I would like to thank my colleagues over at Data Storage Institute who have helped me a lot during the course of my study. They are excellent friends and colleagues and I greatly treasure our relationships. I would like to make special mention of a few of my colleagues such as Dr Gao Feng, Dr Liu Meng Jun, Dr Lai Fu Kun, Dr Ong Eng Teo and Ibrahim See Boon Long, and I wish to express my thanks to them.

I would like to express my thanks to the collaborator of this project, Pinanotec and Broadway who has helped in the provision of the design and in the fabrication support for the TRUM actuator.

Finally, I wish to express my heartfelt gratitude to my family for their love and support with which they have given me. I would not have moved this far without them. They are a constant source of joy and solace for me. I dedicate this thesis to them.

Table of Contents

LIST OF FIGURES

LIST OF TABLES

CHAPTER 1 -- INTRODUCTION

1.1 Objectives of Thesis

The motivation underlying the thesis is to study the dynamic behavior of a piezo driven actuator arm in a Hard Disk Drive (HDD) with an intention of replacing the existing VCM. There are several advantages that a piezoelectric based construction offers over the traditional Voice Coil Motor (VCM) technology. These includes the potential cost savings as expensive rare earth magnets are avoided, reduced size of the HDD as space are free up from the VCM, reduced assembly effort as there is no need to assemble the VCM, reduced electrical cross talk as there can be separation between the signal and actuation traces as well as reduced heat generation and power consumption. These are very attractive offerings for the highly cost conscious HDD makers around the world. However, there are several performance indicators which the piezo driven arm must meet in order for it to replace the basic functionality of the VCM. The main technical specifications include the seeking time required, the control bandwidth and track following precision achievable. There are also other technical specifications that does not directly relate to the read/write performance. This includes the actuator acoustical noise characteristics, the particle contamination effects of the wear as well as the shock and robustness performance. In particular, the vibration robustness of the piezo driven arm is found to be lacking as it is plague with unwanted vibrations during the seeking process. The objective of this thesis then is to develop a hybrid analytical – numerical platform dynamic model that is capable of capturing and explaining the presence of parasitic vibrations experienced by the actuator arm. The model developed can also provide us with a framework which serves as a useful and efficient parametric design tool.

1.2 Shortcomings of PZT Actuation

Preliminary experimental data on a prototype HDD piezo actuator arm has indicated several issues with their dynamical performances. First, experimental transfer function measurement of the prototype shows a significant response occurring at around 520Hz (Figure 1). This low frequency rippling will result in severe interference when doing track positioning. Second, the ultrasonic excitation frequency (120 kHz) content was found to have been transmitted to the HDD slider (Figure 1.2). This should not surprise as the slider resonant frequencies are also in the range of hundreds of kilohertz. Again, this means degradation in read/write performance as there is an additional unwanted vibration component. Third, the torque and hence seeking speed of the piezo arm is smaller than a VCM arm (Figure 1.3). This will translates to a slower data transfer rate and also control speed. Lastly, the acoustic noise of the piezo arm is much more pronounced (Figure 1.4). This is unacceptable as many HDD are intended for use in consumer electronics and the noise criteria is of utmost importance.

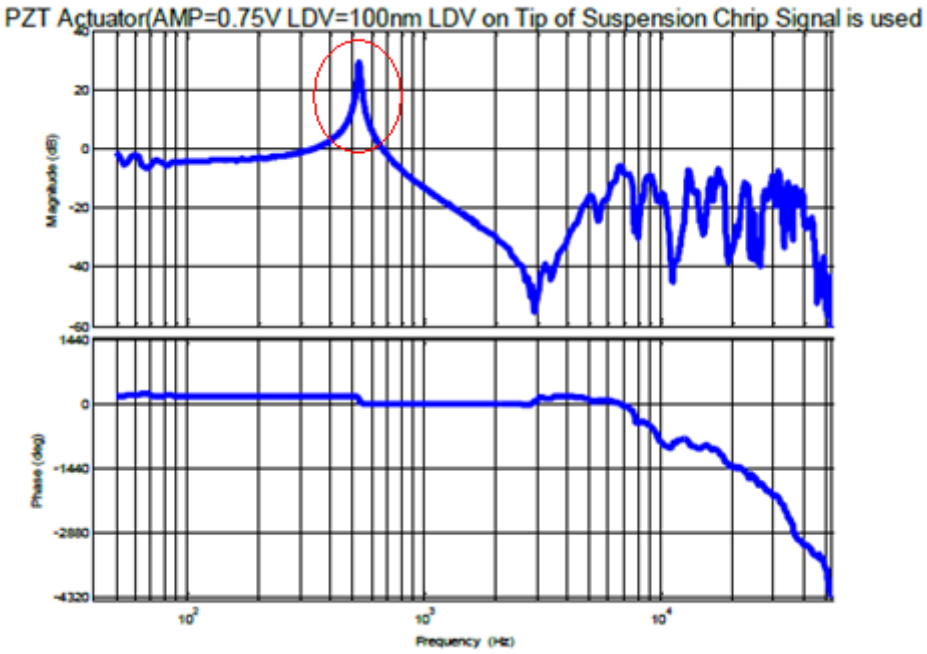

Figure 1.1: Frequency response function of PZT motor with high resonance mode of ripple frequency at around 500Hz clearly visible.

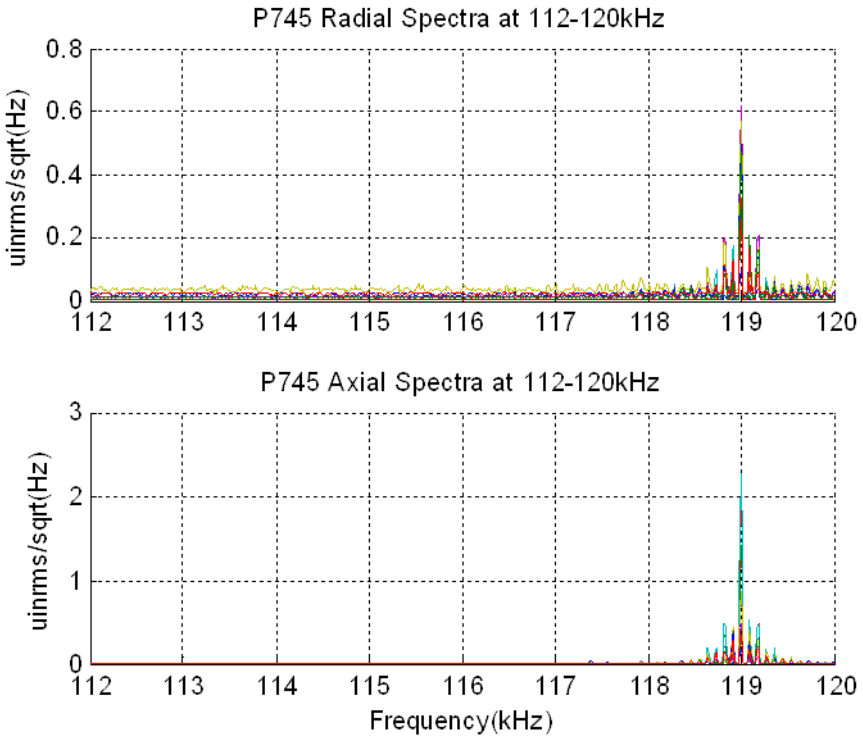

Figure 1.2: Frequency Spectrum of vibrations at arm tip showing present of ultrasonic excitation components at 119kHz.

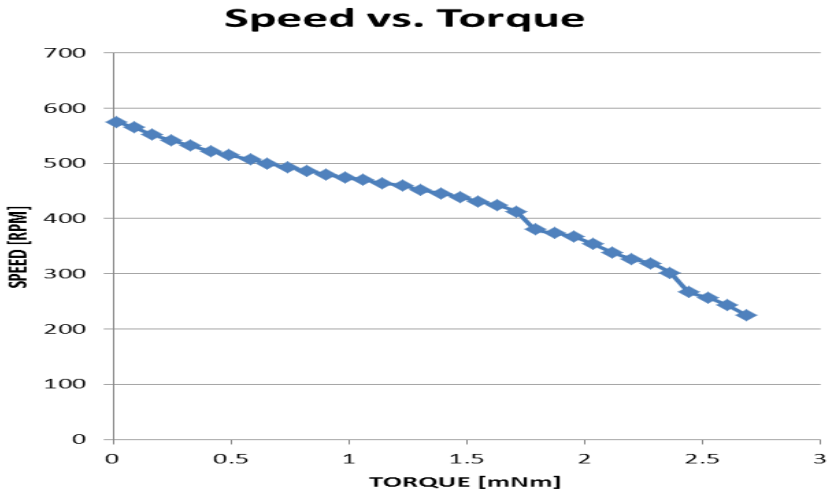

Figure 1.3: Torque-Speed Curve of PZT motor. Inadequate when compared with VCM motor reference values of 900rpm at 4Nmm.

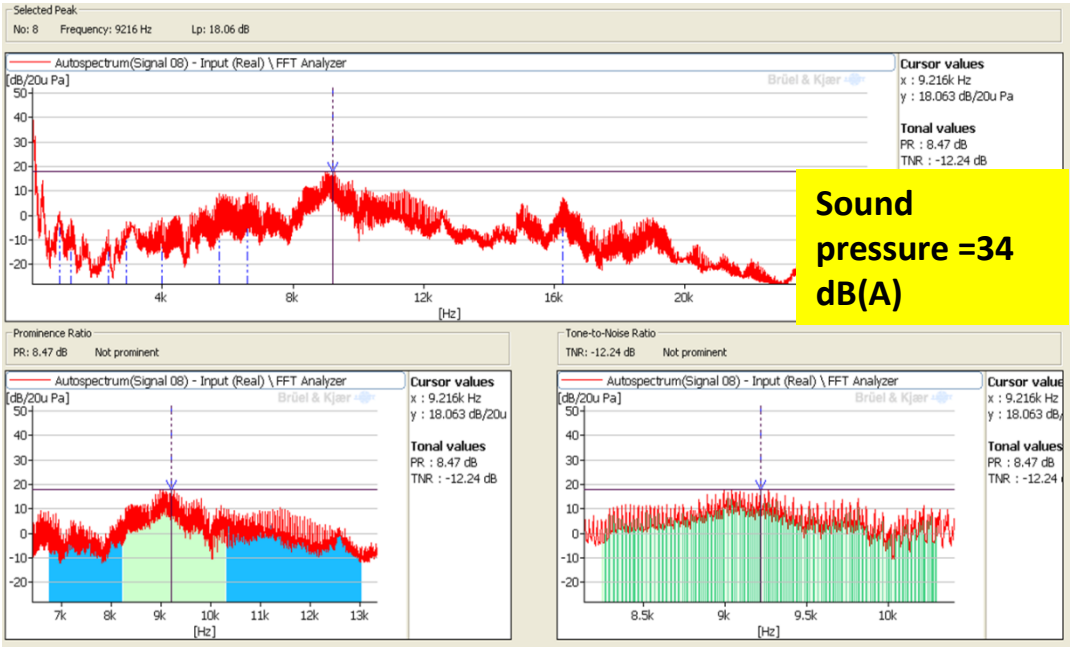

Figure 1.4: Acoustic spectra of PZT motor showing sound pressure and sound tones.

Sound pressure of 34dB (A) is high when reference to Hitachi 7mm 2.5 inch drive of 23dB (A). Obvious sound tones are also present.

In an attempt to address the problems highlighted above, several modifications have been introduced to the prototype motor. These changes include modifying the design of the pre-loading spring, re-balancing the actuator arm mass and changing the profiling of the stator notch. Harmonic simulation of the piezo motor has indicated that the onset of the rippling frequency at 520 Hz occurs whenever there is an unbonded condition between one of the stator teeth to the rotor. The 520 Hz mode is associated with the rigid body motion of the actuator arm "held" loosely by the rotor. This looseness has also result in significant transmission of the ultrasonic excitation frequency towards the slider. The problem is further amplified by the inherent unbalance in the actuator design. One way to alleviate this problem is to ensure that the contact between the rotor surface and stator teeth is uniform and stable. Special shaped springs that exert the pre-loading have been designed to achieve this. On the other hand, the springs must also have sufficient isolation and damping to prevent ultrasonic vibrations transmission to the slider. Experimental data with the improved spring designs are

encouraging but for HDD purposes there is still some way from the desired specifications. To improve the torque and seeking speed, the stator teeth have been modified such that it becomes more compliant. The profiling of the teeth shape has also been design such that the angular contact to the rotor is optimized for better compatibility. Despite these design changes, the seeking speed of the piezo actuator still falls short compared to a conventional VCM actuator. The squealing issue of the piezo actuator has not been addressed at the moment.

1.3 Outlines of this thesis

Chapter 2 presents a brief literature survey of the research areas involving Ultrasonic Motors (USMs). Different modelling approaches to understand and predict behavior of USMs have been developed over the years. These methods range from equivalent circuit method which employs experimental data sets, to pure analytical modelling techniques and to the construction of elaborate numerical finite element models. The contact interface between the stator and rotor of a USM has also been an intense area of research interest; this is primarily due to its importance in influencing the overall mechanics of the operation of USMs. Researchers have tried to improve the analytical model of USMs by developing a more realistic but complex contact interface model. Others, through experimental techniques, have tried to characterized and better understand the complex processes at work. There is also another branch of researchers who searches for better frictional materials for usage in actual USMs. The workings of a USMs involves many non-linear processes at work, therefore, extensive experimentation and characterization are usually carried out to map out behaviors of actual prototypes and products. To account for the many non-linear characteristics of USMs, in depth control strategies and optimization studies have also been a hot topic of research to improve the overall performance of USMs. Following this, the basic principle of

operation of a Travelling Wave Ultrasonic Motor (TRUM) is explained and illustrated in Chapter 3. In Chapter 4, numerical finite element results from both modal and harmonic analysis of a TRUM will be presented. The simulation results are corroborated with experimental data which indicated the presence of low frequency rippling vibrations as well as unwanted transmission of high frequency ultrasonic vibrations. Several pre-loading spring designs are studied which shows that they are important factors that can influence the level of parasitic vibrations experienced. In order to better study the transient dynamics of the TRUM and rotor vibrational characteristics, the governing equation of motions for the entire TRUM system are developed in Chapter 5. A Rayleigh – Ritz energy approach is adopted in the formulation which also includes the interfacial forces and frictional effects. Unique in the present modelling framework is the introduction of all six degree of freedom for the rotor subsystem. This is to allow for the onset of tilting vibrations of the rotor to be modelled for and be captured physically. Chapter 6 shows the simulation results for the analytical model developed in the previous chapter. The numerical results are compared with experimental data and gross agreements in the TRUM behavior have been observed. In Chapter 7, a study of the TRUM speed torque behavior is carried out by varying parameters such as the axial pre-loading, the tooth height as well as the tooth width. It is found that optimum behavior of the TRUM in terms of speed, torque ratings and efficiency and power involves trade-off which needs to be balanced in view of operating requirements. Finally, in Chapter 8, the conclusions from the thesis are summarized and a brief discussion of possible future works which can be undertaken are presented.

CHAPTER 2 – LITERATURE SURVEY

2.1 Introduction

Motors actuated by means of mechanical vibrations have a long history and are generically termed vibromotors by Ragulskis et al. [1]. An Ultrasonic Motor (USM), which utilizes vibrations in the ultrasonic range, is but only a subclass of such motors. However, research interest in this particular area has flourished ever since the introduction by Sashida [2] of the travelling wave rotary ultrasonic motor (TRUM). Solid state motors based on ultrasonic vibrations of piezoelectric ceramics offers several unique advantages over traditional electromagnetic based motors. First, they have very high torque to mass ratio which translates to the possibility in compactness of design. Thus, high torque at low rotational speed is possible and speed reducing gears are also not necessary. These features allow them to be able to be utilized in specialized applications such as micro-actuators and robotic arms. Second, there exist a natural holding torque due to the frictional contact between the rotor and stator. This inherent braking mechanism is advantageous for fast slow down response and avoids backlash problems. Third, because of the compactness and usage of high frequency vibrations, quick response time can also be achieved. Fourth, they allow very accurate sub-nano meter positioning of actuators. This is made possible as gross motor motion is realized through the summation of microscopic displacements of the high frequency vibrations. Lastly, there is no danger of electromagnetic interference effects which traditional motors face as USM operates by means of mechanical vibrations.

However, there are also limitations inherent in ultrasonic motors as stated by Ueha et al. [26]. Speed of such motors are often much slower than VCM actuation, this is due to the fact that in order to generate gross mechanical actuation, the displacements of many micro-deformations are required to be summated. This places an upper bound on how fast such

motor can run. Another serious deficiency with them arises from the wear and tear associated with the physical frictional contact between the stator and rotor, Sashida and Kenjo [5]. This will reduce the lifespan of such structures, restricting it usefulness to the low cycle applications, also, it will cause contamination by the worn off particles. Piezoelectric materials are also highly susceptible to temperature influences, their piezoelectric properties will start to degrade when their Curie temperatures are approached. Moreover, their material behavior characteristics are often non-linear, exhibiting hysteresis. This means that a control strategy is often required to compensate for these anomalies of the ultrasonic motor.

There are several modes of operation of solid state motors. There are those that rely on the ultrasonic resonant mode and those that rely on other physical mechanisms such as the inchworm motors or peristaltic motors. Within ultrasonic resonant modes based solid state motors, it can be further subdivided into those that operate by standing waves and those that operate by travelling waves. The focus of this report will be on piezoelectric rotary ultrasonic travelling wave motor. A comprehensive survey of the various operating principle of ultrasonic piezomotors can be found in Spanner [3].

2.2 Modelling approaches

In view of the above limitations which USM, there have since been intensive research on many different fronts to overcome these challenges. They cover many different aspects, from the study of the fundamental vibration characteristics of the stator, to the contact modelling, to the control algorithms and finally to the prototyping, characterization and optimization of USM.

One of the earlier methods in the mathematical modelling of USM was performed by means of the Equivalent Circuit Method (ECM) Ikeda [4]. In this formulation, USM

electromechanical behavior is represented in terms of electrical circuit components. The measured admittance values of the actual motor are taken to be characteristics analogy of the motor mechanical counterpart. The same approach was also adopted by Sashida and Kenjo [5] and Nogarede and Piecourt [6]. The advantage of ECM is that it allows one to take into account of practical non-linearity of real USM by subsuming it into a few electrical parameters. However, there are still many challenges in the application of this method. This is due to the complexities of the contact process involved and the high temperature dependence of the stator and piezoelectric materials. The physics of these processes is rather involved and it is still not clear at the moment how they can be incorporated into the ECM model for more accurate simulation.

The first complete analytical model of a TRUM was presented by Hagood et al. [7]. The model took into account of both the interactions between the vibrating stator and the rotating rotor as well as the contact interface between the two components. The equation of motions was derived by applying the variational on the modified Hamilton's Principle which included the piezoelectric coupling effects. Several drawbacks with the model include its assumption of a pure slip law for the contact interface and perfect rigidity of the rotor with only a single degree of freedom in the axial and radial direction. Experimental studies by Sattel [8] have shown that rotor flexibility factors strongly into the flatness of the USM torque-speed characteristics, overall operability and reliability. Further studies by Lu et al. [9] and Le Letty et al. [10] combined finite element modelling with a contact algorithm to simulate the motor performance. Finite element method is used to obtain the stator mode shapes and eigenfrequencies. While the dynamic contact process between the stator and rotor is modelled separately using specific algorithm. This approach was adopted in order to avoid the huge computational effort if a pure FEM model is employed.

In recent years, the analytical model developed by researchers has become more elaborate as they try to take into more physics that were neglected in previous studies. Duan et al. [12] simulated the converse piezoelectric effects using thermal analogy to model the contact behaviour, Yao et al. [13] developed analytical solution of the non-linear vibration of the travelling wave ultrasonic motor by incorporating the effects of shearing deformation, rotary inertia and damping effects of the piezoelectric ceramic. Boumous et al. [14] studies the transient response of a travelling wave USM by including the shearing deformation experienced by the friction material layer. Zhao [15] in his recent book even included the 3-dimensional motion of the stator tip in the contact interaction. It was found that motion in the other axis can account for the apparent degradation in predicted speed and efficiency of the USM.

2.3 Contact interface

The contact interface between the stator and rotor is one of the most crucial aspects governing USM performances. Wallashek [11] gave a comprehensive review of the contact process in USM. The author remarked that a rigorous solution for the dynamic contact problem was still not available yet. Many experiments have been conducted to better understand the contact mechanics of USM. Endo and Sasaki [16] studied the effects of the hardness of the contact layer on USM operation. They pointed out that material hardness could change the motor behavior drastically. Other researchers have also discovered that the tribological characteristics of contacting surfaces are frequency dependent. This has direct implications for USM since they are normally operated at very high frequencies. Rehbein and Wallaschek [16] observed experimentally that the coefficient of friction measured at low frequency is much lower than measured at high frequencies (>20kHz). They attributed the difference to the presence of micro impacts between colliding asperities when surfaces

interact at high frequencies. In a separate study, Maeno et al. [18] stated that hydrodynamic bearing effects could also be at play in USM contact process. This observation were drawn based on differences between measured friction coefficients and calculated values obtained through curve fitting of measured speed-torque curve. This view was supported by another study by Kamano et al. [19] .They reported the much severe wear process in sliding friction when compared to that of a USM. They believed that lubrication was afforded by the fluid dynamic effect of air between the stator and rotor gap.

Analytical methods to model the contact mechanics of USM have also been actively studied. Zharii [20] used half space method to derive analytical expressions for the relative velocities as well as normal stresses between the surfaces. A similar approach was also adopted by Le Moal and Minotti [21]. Cao and Wallaschek [22] studied the case whereby the contact layer is directly bonded onto the rotor while Hagedorn et al. [23] model consist of a rigid rotor with a layer of viscoelastic contact layer. Their studies have shown that the inclusion of the rotor feedback does not significantly change the stator motion in the resonance region. Sattel and Hagedorn [24] analyzed the contact zone in further detail by segmenting a single contact zone into several stick – slip regimes. Flynn [25] and Wallaschek [11] proposed several contact model that ranges from simple line, linear spring contact simplifications to more complex area, Herzian contact.

The materials of the contact layer in USM have also been the topic of intense research. Desirable mechanical and tribological properties of the friction material include a low friction coefficient, good self-lubrication, temperature and chemical stability and a low wear rate. Authors such as Rehbein and Wallaschek [17], Ueha and Tomikawa [26] and Fan et al. [27] formulated friction layers with different polymers blends and special composites and tested the material performance experimentally with actual USM. In Fan et al. [27], he studied the effects of the content of Potassium titanate whiskers (PTWs) on the properties of

Polytetrafluoroethylene (PTFE) friction materials. His experimental results suggest that an optimum performance can be achieved by incorporating 5% of PTWs. Higher concentrations of PTWs actually leads to a degradation of performance as it causes too much stress concentration in the material matrix.

2.4 Applications and modifications

Despite the many challenges in the modelling and performance prediction of USM highlighted above, there are still many commercial products utilizing USM. The prime example is the autofocus lens of camera. Many precision positioning stages such as those made by Physik Instrumente are also operated based on USM. In Schenker et al. [28], USM are also used as robotic manipulators and as robot wrist actuator in Schreiner [29] as well as in the active control sticks for airplanes, Maas [30]. Ever since the pioneering work by Flynn [25] in the construction of a USM based micro motor, attention has shifted towards miniaturization and applications which requires small size actuators found in MEMs devices. In recent years, there are many papers that discuss the applications of USM in a myriad of configurations and designs. Guo et al. [31] talks about a rotary ultrasonic motor that is driven by its inner circumferential surface instead of the traditional notched teeth located at the outer rim of the circular stator. Avirovik [32] developed an analytical model for a L-shaped piezoelectric motor. Yoon et al. [33] proposed a domed shaped piezoelectric actuator that can be used as a linear motor. On the other hand, Liu et al. [34] studied a U-shaped USM for linear positioning. In another extension of this paper, a variant of the previous motor through modification into square-shaped allows rotary positioning, Liu and Chen [35]. In Ting et al. [36], a 3 DOF spherical motor was developed using curved actuators. However, precise positioning in 3 axis proved to be very difficult due to the complex mutual interactions

between driving modes which causes the formation of disturbance waves. Sun et al. [37] have also constructed a linear motor which comprises of a circularly shaped cylinder and slider.

In most of the above studies, researchers creatively mixed and matched vibration modes with mechanical geometry to develop USM that operates differently. Even though their basic operating mechanisms remains the same, variations in their configuration stack up can open up new application areas. For example, in terms of driving mechanisms, by superimposing the flexural and longitudinal mode of a bar, the same elliptical driving motion can be realized. Also, by having a bolt clamped USM design, higher output power and efficiency can be achieved when compared with the bonded type USM. This is because through the pre-loading of the piezoelectric layer, a higher voltage can be applied without any danger of delaminating due to excess stress or fatigue related failure. USM designs that have employed these concepts include Kondo [38] and Zhai [39]. USM micro motors have also been developed in recent years. Yun et al. [40] developed a micro motor that measures only 240 um in diameter and is able to rotate three dimensionally. The author pointed out that the new motor can be employed as a guide wire of catheter devices in minimally invasive vascular surgeries. A tiny "Squiggle" motor has also been patented by Henderson [41]. The motor measures only 1.55 x 1.55mm and 6mm in length. It operates by means of the wobbling mode of the cylindrical stator. The motor can be used as a positive displacement microfluidic pumps as well as micro dispenser for drugs.

2.5 Experimentation and characterization

The different designs of USM described above will usually be submitted through a series of experiments to characterize and benchmark their performance. The basic characterization features include the motor speed-torque behavior, the average input and output power,

efficiency and finally their transient start stop properties. With proper feedback control and power electronics set up, the above parameters can be obtained without much difficulty. However, there are still many other aspects of USM behavior that is still not well understood and these phenomena have been documented by many researchers over the years. An example is the resonance behavior of the stator. Although the basic resonance characteristics of a simple stator is fairly well understood, upon introducing contact with the rotor, the resonance behavior of the stator was observed experimentally to be non-linear with a jump phenomenon in the resonance curve. This was reported in Ueha [26] and Maas [30]. Sattel and Schmidt [42] attributed this "softening" of the resonance curve to the non-linear stator rotor contact, whereby there is a decrease in the contact stiffness when approaching the stator resonance peak.

Some authors have also reported instability in motor operation, Ueha [26]. Furuya et al. [43] reported a sudden breakdown in the rotational speed if the excitation voltages fall below a certain value. This critical voltage is load dependent. In a similar study, Kamano [19] highlighted that the rotor will fail to operate if stator vibration amplitude falls below a certain value. USM instability is also reflected in the phenomenon of squealing whereby vibrations in the audible range are excited. Herzog [44] reported that the onset of squealing occurs when there is a degradation of friction layer material. Sattel and Hagedorn [45] measured the vibrations of the rotor and stator when the motor is under unstable operation; they found the presence of 2nd and 4th order sub harmonics of the excitation frequencies in the signal. Sattel [8] pointed out in his experimental study that for a given preload, squeal will occur only within a range of rotational speed. The optimum design and reliability of USM is also highly temperature dependent. This is due to the fact that temperatures can rise up to 100 degrees in a USM because of the frictional rubbing and also to the fact that the stator and rotor resonance characteristics varies with temperature because of material effects. Izuno [46]

remarked about the drift in motor characteristics when there is a temperature variation. Sattel and Hagedorn [47] observed a strong relation between the motor speed-torque characteristics and temperature. There are many other studies on the effects of temperature on USM operation. Ueha and Mori [48] measured the temperature of a bolt clamped Langevin transducer and tried to established the relation between the tip velocity amplitude and measured temperature. Hu et al. [49] studies the temperature distribution of piezoelectric components. Lu [50] analyzed the temperature field of a travelling wave rotary ultrasonic motor using FEM. The study indicated that the variation of the heat conductivity of the friction material has little effects on the minimum temperature experienced, but has a profound influence on the maximum temperature reached.

2.6 Control and optimization

In view of the many non-linearity and complexities of USM behavior encountered, most practical applications using USM are implemented concurrently with the appropriate control schemes to account for and compensate for these unmodelled physics. Another popular approach to obtain good motor performance is through optimization schemes whereby selected parameters which are deemed important are optimized based on a proposed model. Lin and Kuo [51] applied adaptive control system to control the position of a USM. Senjyu et al. [52] uses the same control principle to control for both speed and position. Izuno and Nakaota [53] apply fuzzy logic control to maintain motor speed despite large variation in torques and commanded speed. The main drawback of sophisticated controllers is that they are difficult to implement as they require many advanced hardware. A series of control schemes was presented by Schulte and Maas [54]. Cheng et al. [55] uses a back propagation neural network BPNN-PID based control scheme to achieve log stroke nano-positioning accuracy.

Many novel optimization schemes have also been proposed over the years to guide designers. Flynn [56] uses Design of Experiments (DOE) to optimize the performance of USM. A parametrical model of the stator was introduced by Pons et al. [57] to optimize stator performance. Bouchilloux and Uchino [58] uses genetic algorithm. Fernandez et al. [59]) also optimized the stator vibration amplitude with a factorial design approach. Li and Yang [60] used particle swarm optimization to optimize the working frequencies of their curvilinear ultrasonic motor. The main advantage of optimization is that it allows designers to converge upon an optimal design systematically and rapidly. However, the main drawback is that it does not shed insights into the underlying mechanism of USM behavior. The problem is worse when the optimization is not based on a series of actual experimental prototypes but only on a proposed analytical model. Any unmodelled physics which are deemed unimportant will never enter into the picture thereafter and can potentially invalidate the entire subsequent analysis.

2.7 Alternative aspects

In recent years, there are also growing interest on a special class of USM that does not involve physical contact between the stator and rotor. Non-contact USM operate on an entirely different principle from contact based USM. It operates by means of a phenomenon known as Near Field Acoustic Levitation (NFAL). In NFAL, acoustic radiation pressure impacting on the surface of the rotor caused an upward lift force that is able to levitate the entire rotor, Hashimoto and Ueha [61]. NFAL have the capacity to even lift up objects as heavy as 10 kg, allowing them to be able to be use as non-contact transportation devices. Hirom [62] studies the frequency characteristics of a non-contact USM couples with a error correction code. Yano [63] discuss the positioning potential of such motors. Hu et al. [64] in his studies discovered that there is a linear relationship between the motor revolution speed

and the stator vibration velocity. It is therefore possible to increase the speed of such USM either by utilizing the air gap resonance between the stator and rotor or increasing the mode number of the stator vibrations or narrowing the gap. He reported that for a 6mm diameter stator, a top rotational speed of 1000rpm can be achieved.

Another interesting development is the Amplified Piezoelectric Actuators (APA), Claeyssen [65]. The unique features of them are that they are capable of achieving large deformation of up to 8% and large strokes of up to 1000um. By pre-stressing the piezoelectric and mechanically amplifying the deformations, the actuations achieved can be applied for both static and dynamic conditions. The device was originally developed for space application, but because of its usefulness it has attracted large market interest and is slowly finding applications in cost effective industrial applications for micro positioning, structure shaping, active structure damping, vibration generation, fluid control and even as energy harvester. Kawai et al. [66] has also reported on novel constructions that promises as much as four times the power output from conventional designs.

2.8 Conclusions

There are several papers being reviewed in this chapter. They show that in order to better understand the physics of TRUM, research in TRUM must encompass over several interconnected fields, with each covering certain aspects of a fully functional motor. For our purposes, it can be seen from the literature survey that with regards the current state of the art, the analytical model available for TRUM is insufficient for our present endeavor. The existing analytical model of TRUM treats the rotor as having only the axial and rotating degree of freedom. This is usually adequate for most applications as TRUM either functions as a motor possessing large and gross motion or as a precision positioning stage which

behaves quasi-statically. Motions of the rotor in other dimensions can be safely ignored or safely damped out. However, if we are to adopt TRUM as an actuating device in a HDD, the picture changes drastically as now not only rotational motion matters. Motion and vibrations in the other axis becomes important as they can contribute to the degradation in the read write efficiency of the device. The purpose of this study is to introduce such degree of freedoms into the overall TRUM governing equation of motions with the view of capturing and understanding these parasitic vibrations and motions. The extension is not trivial, as many complications in the modelling efforts are introduced with the need to track time evolving contact regimes, account for the non-uniformity in the contact interfaces and resolve for the additional forces between the stator and rotor as well as modelling the dynamics of the free moving rotor.

CHAPTER 3 -- OPERATIONAL MECHANISMS OF TRUMS

3.1 Principle of Operating Mechanisms of USMs

The basic working mechanism underlying any Ultrasonic Motors (USMs) involves the conversion of high frequency (> 20kH) mechanical vibration energy of the stator to gross kinetic energy of the rotor via a frictional interface. Generally, USMs have been primarily classified into 2 broad groups according to their specific operating mechanics; either the standing wave type or the travelling wave type. Other categorization exists which are based on their geometrical construct and also on the type of motional actuation effected. In this thesis and for the discussion that follows, a Travelling Wave Rotary Ultrasonic Motor (TRUM) type of USM will be used for the subsequent study and for illustration purposes of its operational method. Practical devices that employs such an operating principle includes the many different USMs available from the market such those from Shinsei Corporation and Jiangsu TransUSM Corporation. The operating mechanism of TRUMs has also been elaborated upon by authors such as Zhao [15] and Ueha et al. [26]. This chapter will briefly present the underlying mechanics upon which a TRUM operates on.

Figure 3.1 below shows a generic diagram capturing the interaction between the vibrating stator and rotating rotor of a TRUM. The key feature underlying a travelling wave type USM is the generation of an elliptical trajectory for each and every vibrating stator surface points. In order to achieve this, a travelling wave vibrational mode must be established on the vibrating stator.

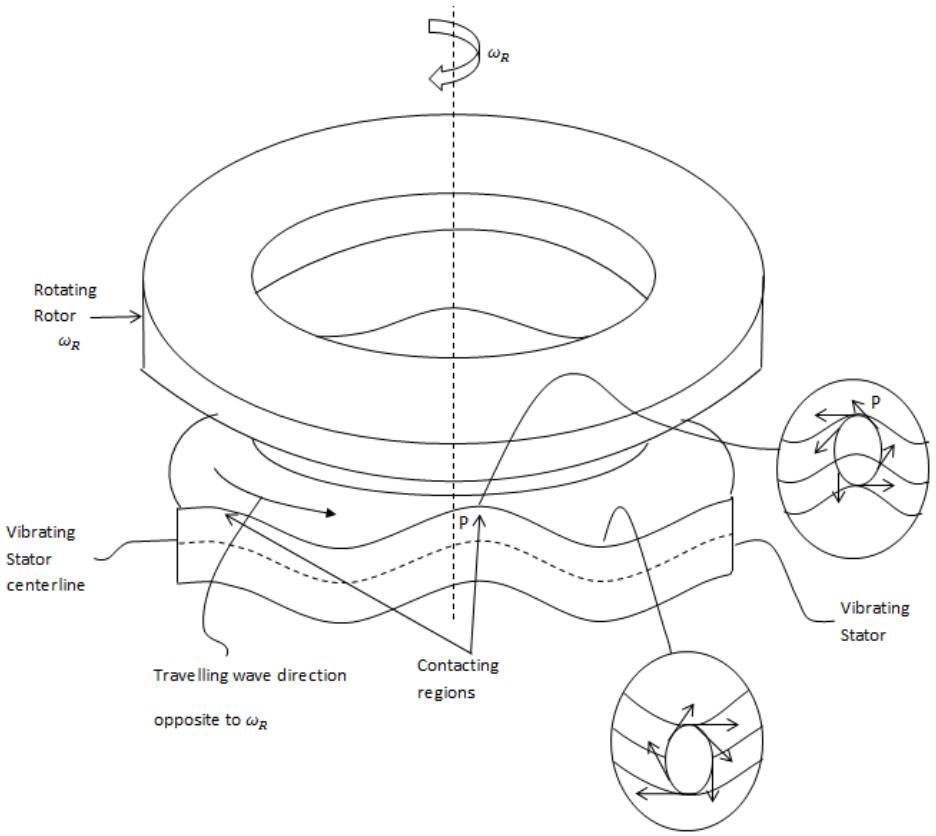

Figure 3.1: Generic schematic showing interactions between rotor and stator

For a circularly shaped plate or ring type TRUM as shown in Figure 3.1 above, a travelling wave can be generated on the stator by exciting simultaneously 2 degenerate eigenmodes sharing the same eigenfrequency. The superposition of the 2 orthogonal modes induces the formation of a travelling wave. Figure 3.2 below shows a typical operational mode shape of a ring type USM having 2 vibration bending mode with m=0 nodal circle and n=4 nodal diameter. There is a relative spatial shift between these 2 orthogonal modes of a quarter of a wavelength or a phase difference of $\pi/4$. As will be explained later, this phase offset is a necessary criterion for the formation of a travelling wave on the stator.

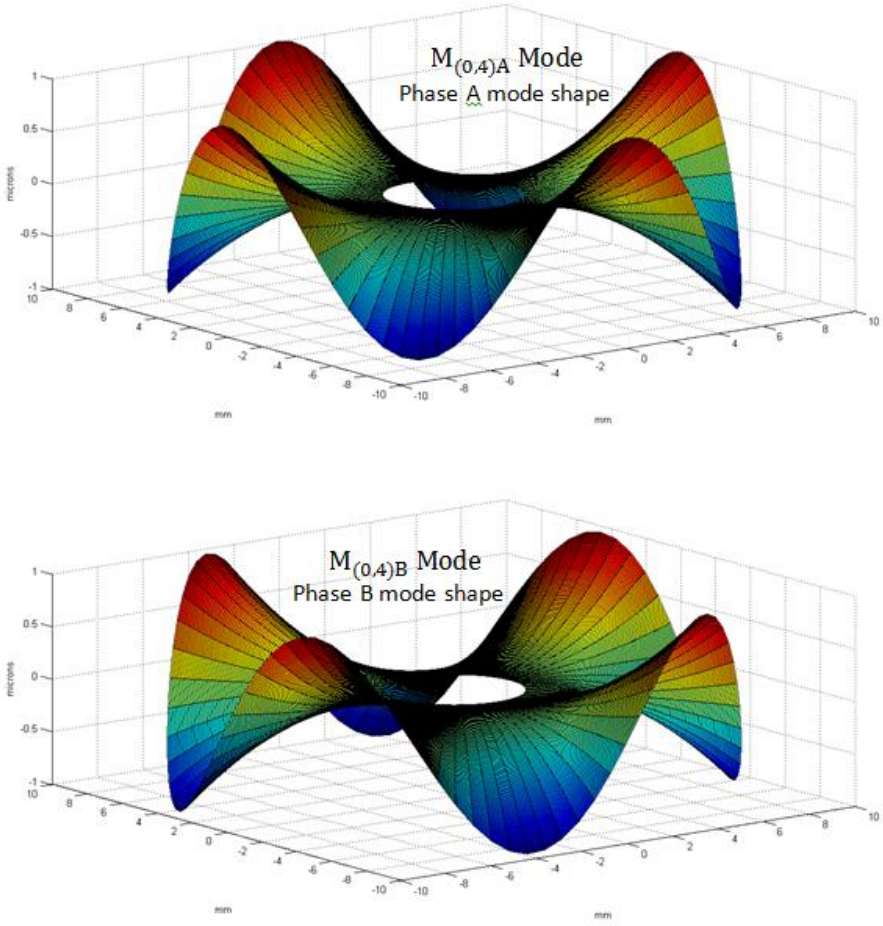

Figure 3.2: Orthogonal mode shapes of a circularly shaped stator

3.2 Mathematical Description of Motion Generation

Let w_s represents the out of plane deflection of the stator plate's mid plane, which is given by the superposition of the 2 orthogonal modal responses of the stator vibration $w_A(r, \theta, t)$ and $w_B(r, \theta, t)$,

$$w_s(r, \theta, t) = w_A(r, \theta, t) + w_B(r, \theta, t)$$

$$= \Phi_A(r, \theta)\xi_A(t) + \Phi_B(r, \theta)\xi_B(t) \quad (3.1)$$

Whereby $\Phi_A(r, \theta)$ and $\Phi_B(r, \theta)$ represent the assumed mode shapes of the vibration profile of the stator. They are time independent and are functions of only the radius r and angular coordinates θ. $\xi_A(t)$ and $\xi_B(t)$ are the modal coordinates of the respective vibration modes.

The assumed mode shapes Φ_A and Φ_B can be represented by a combination of two shape functions given by,

$$\Phi_A(r,\theta) = \mathcal{R}(r)\sin(n\theta) \tag{3.2}$$

$$\Phi_B(r,\theta) = \mathcal{R}(r)\cos(n\theta) \tag{3.2}$$

$\mathcal{R}(r)$, $\sin(n\theta)$ and $\cos(n\theta)$ describe the radial shape function and the circumferential shape functions of the eigenmodes respectively. The parameter n determines the number of nodal diameters of a given mode. The temporal character of the modes are given by the modal coordinates $\xi_A(t)$ and $\xi_B(t)$ which can be written as,

$$\xi_A(t) = \hat{w}_{S,A}\cos(\omega_n t) \tag{3.3}$$

$$\xi_B(t) = \hat{w}_{S,B}\cos(\omega_n t + \alpha) \tag{3.3}$$

$\hat{w}_{S,A}$ and $\hat{w}_{S,B}$ are the amplitudes of the modal responses w_A and w_B respectively. The two modal responses also possess a phase difference given by α , while ω_n is the eigenfrequency of the vibration mode. Inserting (3.2) and (3.3) into (3.1), we have the stator mid-plane lateral displacements given by,

$$\begin{aligned} w_s(r,\theta,t) = \frac{1}{2}\mathcal{R}(r)\{&\left(\hat{w}_{S,A} - \hat{w}_{S,B}\sin(\alpha)\right)\sin(n\theta + \omega_n t) \\ &+ \left(\hat{w}_{S,A} + \hat{w}_{S,B}\sin(\alpha)\right)\sin(n\theta - \omega_n t) \\ &+ 2\hat{w}_{S,B}\cos(\alpha)\cos(n\theta)\cos(\omega_n t)\} \end{aligned} \tag{3.4}$$

From equation (3.4) above, if the amplitudes of the two orthogonal modes are equal, $\hat{w}_{S,A} = \hat{w}_{S,B} = \hat{w}_S$ and the temporal phase difference $\alpha = \pi/2$. The equation reduces to a pure travelling wave equation,

$$w_s(r,\theta,t) = \hat{w}_{S,}\mathcal{R}(r)\sin(n\theta - \omega_n t) \quad (3.5)$$

Thus, from the above discussions, we can infer that three conditions must be met for the formation of a travelling wave on the stator. First, the two orthogonal modes must be spatially shifted relative from each other by a quarter of a wavelength $\lambda/4$. Second, they need to have a temporal phase difference of $\pi/2$. Third, they must share equal amplitudes. From (3.4), it can be deduced that if any of these conditions are not met completely, a standing wave component apart from the travelling wave component will be generated simultaneously on the vibrating stator. The presence of the standing wave serves to degrade the performance of USMs.

In order to achieve the abovementioned conditions for the formation of a travelling wave on the stator, the placement of piezoelectric patches onto the stator must be arranged in a certain pattern. Figure 3.3 below shows an example of how a rotary USM stator with n=8 nodal diameter can be excited to establish a travelling wave. There are two electrode patterns, A and B, which will each individually excite the 5^{th} bending mode on the stator, as each electrodes pair will span across a single wavelength. Their relative orientations have been displaced by a quarter of a wavelength from each other to produce the two orthogonal mode shapes. The excitation voltage applied on each piezoelectric patch has a relative phase lag of 90 degree to realize the temporal phase difference required.

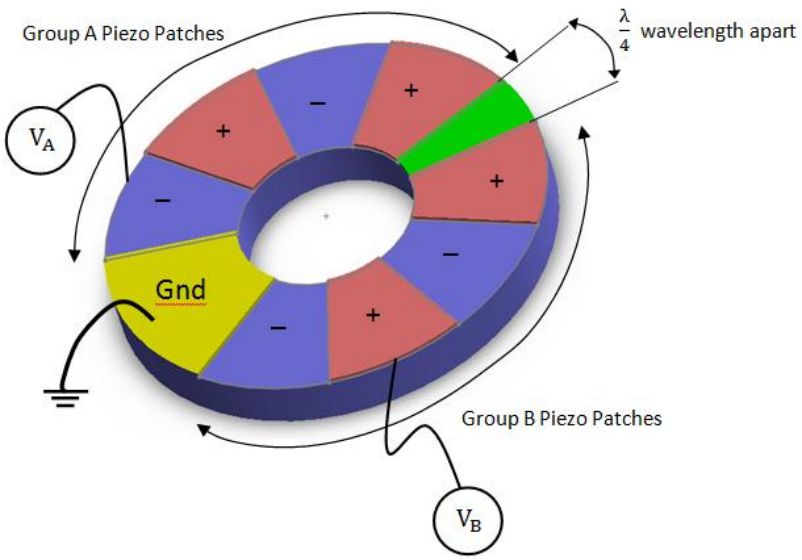

Figure 3.3: Piezoelectric electrodes pattern on stator

After a travelling wave has been established on the stator, we will need to examine the trajectories of surface points on the stator in order to appreciate how it can drive up the rotor. Figure 3.4 below shows a generic close up view of a stator undergoing a travelling wave bending vibration. On the neutral mid-plane of the stator, only vertical velocity components exist as stator points only moves along the X_3 axis even as the travelling wave traverses. However, for all other points which are lying off-center from the neutral plane, they will possesses both X_1 and X_2 velocity components which result in elliptic motion.

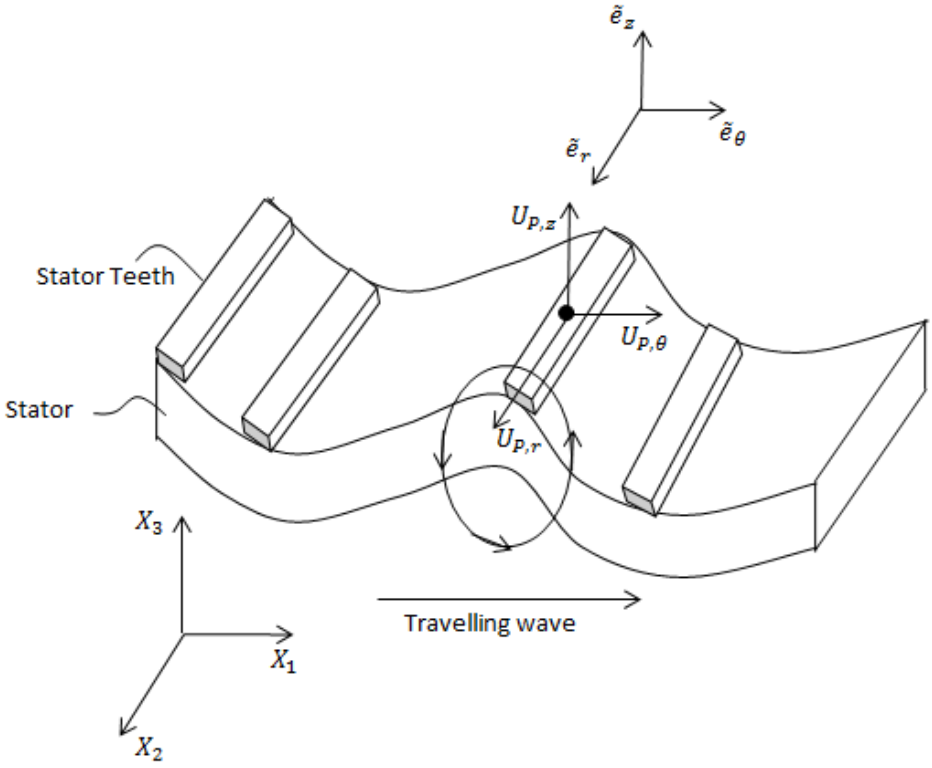

Figure 3.4: Velocity components of points on stator surfaces

Using Kirchhoff's Plate Theory, we can represent the displacement $\mathcal{U}_p$ and velocity $\dot{\mathcal{U}}_p$ of points on the stator mathematically in terms of the lateral displacements w_S and velocities $\dot{w}_S$ experienced by the neutral plane in cylindrical coordinates with,

$$\mathcal{U}_p(r,\theta,x_3,t) = \mathcal{U}_{p,r}\tilde{\mathbf{e}}_\mathbf{r} + \mathcal{U}_{p,\theta}\tilde{\mathbf{e}}_\boldsymbol{\theta} + \mathcal{U}_{p,z}\tilde{\mathbf{e}}_\mathbf{z}$$

$$= -\frac{h_s}{2}\frac{\partial w_S(r,\theta,t)}{\partial r}\tilde{\mathbf{e}}_\mathbf{r} - \frac{h_s}{2r}\frac{\partial w_S(r,\theta,t)}{\partial \theta}\tilde{\mathbf{e}}_\boldsymbol{\theta} + w_S(r,\theta,t)\tilde{\mathbf{e}}_\mathbf{z} \qquad (3.6)$$

h_s is the stator thickness while $\tilde{\mathbf{e}}_\mathbf{r}$, $\tilde{\mathbf{e}}_\boldsymbol{\theta}$ and $\tilde{\mathbf{e}}_\mathbf{z}$ are units vectors denoting the local cylindrical coordinate reference frame with coincides in orientation with the global X_1, X_2 and X_3 directions respectively. Substituting (3.5) into (3.6) above gives us an equation describing an elliptic motion. It can be observed from these equations that at each wave crest, we have $\cos(n\theta - \omega_n t) = 1$ which gives us $\dot{\mathcal{U}}_{p,\theta} = \left|\dot{\mathcal{U}}_{p,\theta}\right|_{max}$ while $\dot{\mathcal{U}}_{p,z} = \dot{\mathcal{U}}_{p,r} = 0$. This

means that at a wave crest, only circumferential velocity exist on the stator surface. At all other points however, both radial and lateral velocity components exist which serve as an energy dissipater and does not contribute to the driving of the rotor.

3.3 Frictional Contact between Rotor and Stator

When a rotor is pressed against the stator by means of an external pre-loading spring, physical contact between both surfaces begins the transformation of vibrational energy in the stator to rotational kinetic energy of the rotor. At the vertical extremes of the elliptical orbits, points on the stator surface will be moving in a purely circumferential direction while in physical contact with the rotor. Differences in relative velocity between the rotor and stator surface points will result in the stator pulling the rotor by means of frictional forces which drags the rotor into motion. Figure 3.5 below illustrates the frictional interface of such a system.

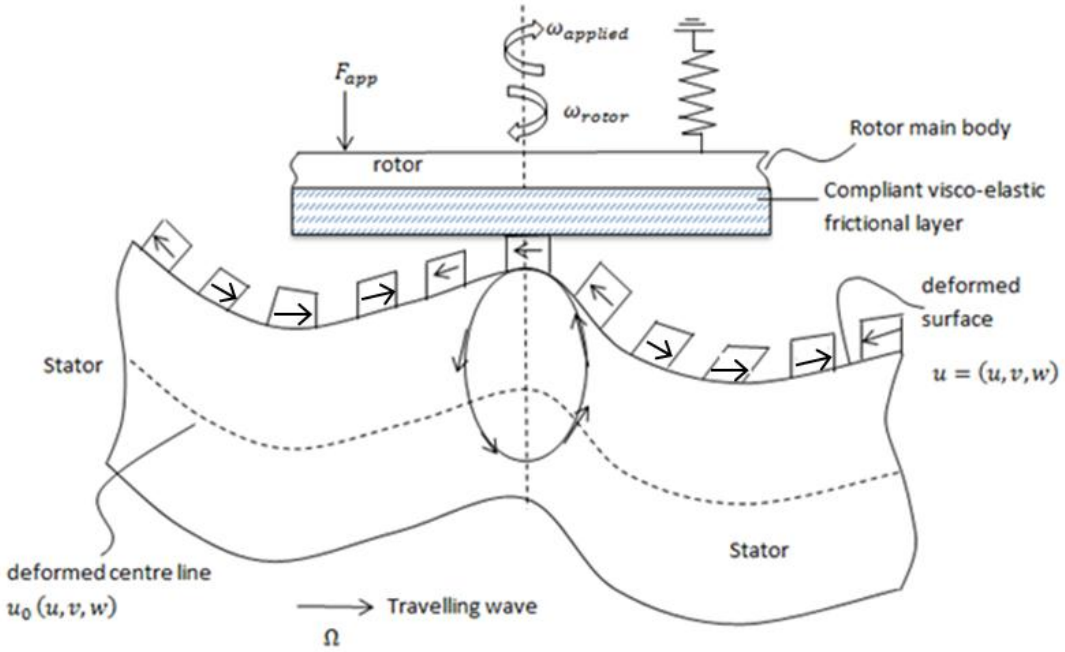

Figure 3.5: Frictional interface when rotor is being pressed down onto stator surface

The direction of the travelling wave generated on the stator and the direction of rotor motion induced are oppositely oriented. This is due to the elliptic orbits being directed inversely to that of the travelling wave. From the brief description above on how the stator interacts with the rotor, it is quite clear that the interface concerning the physical contact process between the stator and rotor is of much importance. It is the crucial feature which allows the conversion of the microscopic vibration energy of the stator deformations to the macroscopic kinetic energy manifested as gross motion of the rotor. Therefore, it plays an important role in the determination of overall USM performance in terms of torque-load characteristics, energy efficiency as well as transient behavior. The analysis of the behavior of USMs therefore requires studying how the interface forces between the stator and rotor will affect the modal amplitude and the dynamics of the overall system.

3.4 Conclusions

In this chapter the fundamental working mechanism underlying a typical TRUM is illustrated. Central to all TRUM requirements is the generation of a travelling wave mode which can be achieved by proper placement of electrodes patches as well as time shifted electrical excitation. It was shown that given the formation of a travelling wave, the points on the stator actually traverses in an elliptical fashion. The lateral velocities possess by these surface points is what drives up the rotor. Upon applying a pre-load onto the rotor, physical the onset of physical contact between the stator and rotor begins the energy transformation from stator vibrational energy to rotor kinetic energy. The conversion takes place across the interface via a frictional mechanism whereby differences in relative velocities drags the rotor into motion. High frequency microscopic vibration thus becomes low frequency gross kinetic motion.

CHAPTER 4 – Finite element Approach in the study of TRUM

4.1 FEM Approach taken to Study TRUM

Normally, real world implementation of ultrasonic motors involves complex geometries, this would at best reduce the accuracy of the "analytical" model developed, and at worst the entire model could be invalidated. The only approach available to study these motors is through computational finite element method. The advantage of this tool is that complex geometries and other non-linearity can be calculated; provided the boundary conditions are well understood and input parameters values are reasonably accurate.

However, simulating the behaviour of ultrasonic motor using the finite element method involves the introduction of contact elements into the picture. Contact problems are often highly nonlinear and require much computing resource. There are two significant difficulties when solving contact problems. The first is the fact that the exact contact region is often unknown prior to the analysis. How much contacting area, the degree of penetration as well as the time evolution of the contacting regions between two structures are examples of contact features which remains vague in the first analysis. The second challenge associated with contact problems is that involving frictional effects between surfaces. There is a whole plethora of theories available attempting to describe the frictional behaviour between contacting surfaces. Coupled to these, contact often introduces additional other effects such as thermal conductance, electric and magnetic fluxes. The central feature of an ultrasonic motor is to convert microscopic vibrations into macroscopic gross motion. The physical process governing this conversion is the contact between the vibrating stator teeth and the rotating rotor face. In order to have a reasonable prediction of the motor performance through the finite element method, we need to capture or model the actual contact behaviour with sufficient accuracy.

In view of the above difficulty, simple FEM modal and harmonic analysis of an ultrasonic motor can be directly simulated by assuming a bonded contact between the rotor and the stator. This allows us to easily yield the modes shapes, frequencies as well as the transfer function of the structure.

In chapter 5, the analytical model to study the dynamics of the TRUM actuator will be developed. In this chapter, the results using Finite Element Analysis (FEA) package ANSYS software shall be presented. The chapter begins first with the Computer Aided Design (CAD) model introduction of the prototype under study with the relevant material properties and data. Next, the constraints and excitation input conditions will be explained briefly. Modal and harmonic analysis dynamic simulation will be performed to extract the operating mode shapes. Relevant experimental data from frequency response measurement which shows the rippling problem will be highlighted. Finally, different harmonic analysis showing how rippling and ultrasonic vibrations varies with spring type will be performed.

4.2 HDD Actuator Prototype CAD and FEM Inputs.

Figure 4.1 below shows the CAD model of a typical TRUM type HDD actuator under study. There are many components and the actual prototype has very complex structure, but for this thesis we will be simplifying the analysis by representing the entire actuator arm as consisting of only 3 major components. The analytical model contains only the stator, rotor and the spring loading. For the FEM model, a coupled field Solid 98 element is used to describe the PZT material of the stator. This is a 10 node higher order tetrahedral element which is capable of accepting voltages as input conditions and structural strains as the output. For the remaining model, a three dimension 10 node structural Solid 187 tetrahedral element is used

to describe the normal engineering material. In total, there is around 200,000 elements and 150,000 nodes for the entire assembled model.

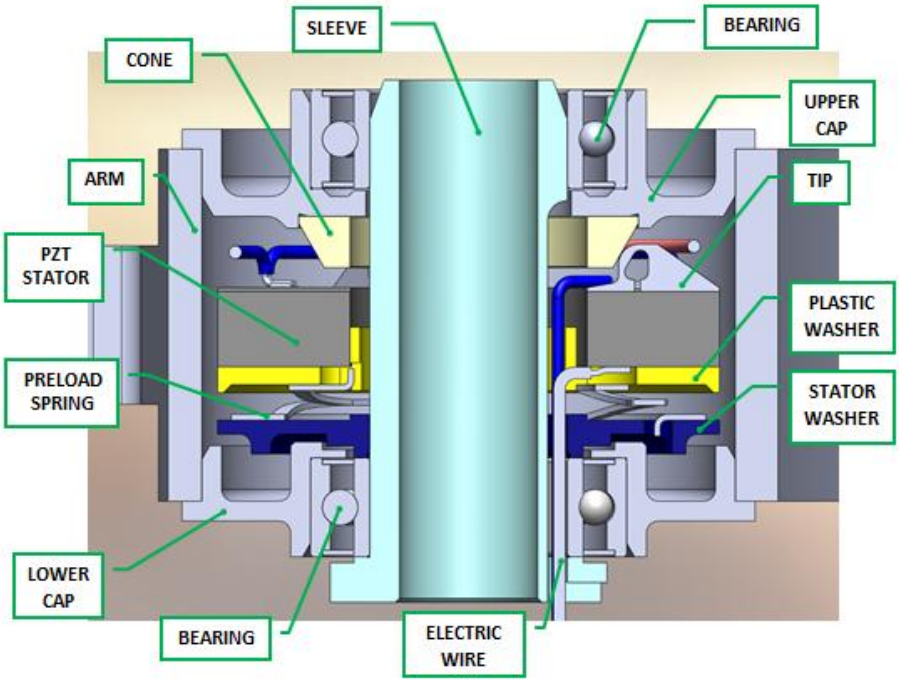

Figure 4.1: Cross sectional view of a sample prototype of a TRUM HDD Actuator

The relevant material data properties employed for the analysis is given by Table 4.1 below. The piezoelectric constitutive properties are also presented as follows in Table 4.2.

	PART	MATERIAL	MATERIAL DATA		
			DENSITY [kg/m^3]	ELASTICITY MODULE [GPa]	POISSON RATIO
1	Upper cap	Aluminum 6061	2700	69	0.33
2	Lower cap	Aluminum 6061	2700	69	0.33
3	Sleeve	Stainless steel 304	8000	193	0.29
4	Stator washer	Stainless steel 304	8000	193	0.29
5	Preload spring	Spring steel	7850	205	0.29
6	Plastic washer	PEEK	1300	3.6	0.39
7	Arm	Aluminum 6061	2700	69	0.33
8	Rotor cone	Alumina	3950	380	0.22
9	Tip	Alumina	3950	380	0.22
10	Bearing	Bearing steel 440C	7800	200	0.29

Table 4.1: Material data inputs for the FEM analysis

PZT material data [PI PIC-181]

PROPERTY	VALUE
Density	7800 [kg/m^3]
Poisson ratio	0.29
Stiffness matrix C_E [x1e+10 N/m^2]	15.2 8.91 8.54 0 0 0 15.2 8.54 0 0 0 13.1 0 0 0 2.83 0 0 2.83 0 3.16
Piezo coupling matrix dE [x1e-10 C/N]	0 0 0 0 4.75 0 0 0 0 4.75 0 0 −1.2 −1.2 2.65 0 0 0
Relative permittivity matrix εT	1500 0 0 0 1500 0 0 0 1200

Table 4.2: Piezoelectric material property

Next the modelling constraints applied for the modal analysis is shown below. For the rotor and stator interface, we are only limited to employ the “bonded” contact functionality for our analysis. A bonded contact types means that no slippage and separation are allowed at that interface. Other contact types except for the “unbonded” contact elements type will mean that the analysis is non-linear, making it unsuitable for a standard modal and harmonic analysis. Below, five important conditions are highlighted in the simulation as shown in Figure 4.2 to Figure 4.6. They involve the specifications for the boundary conditions, bearing spring model and the contact conditions.

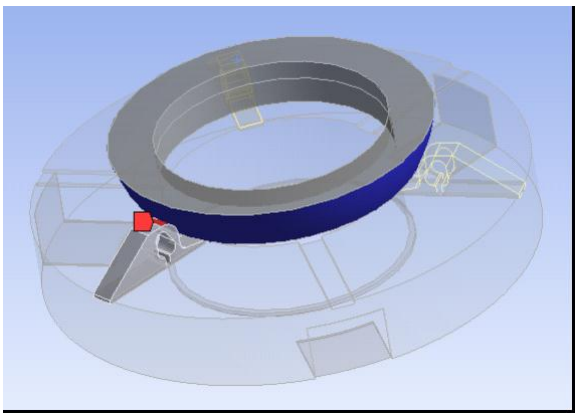

Figure 4.2: Stator tips and Rotor bonded condition

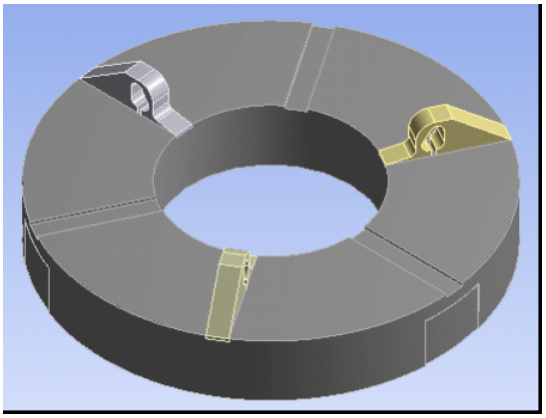

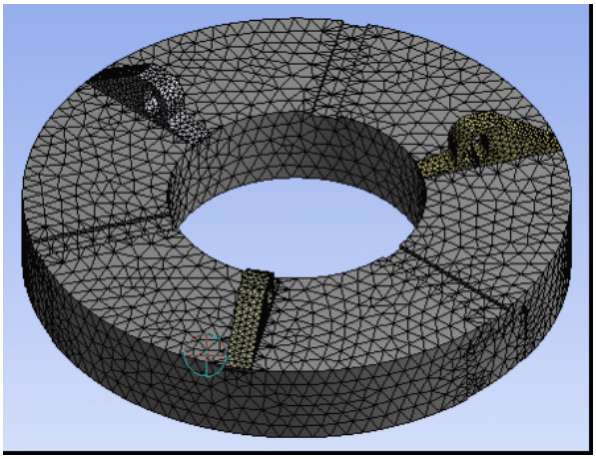

Figure 4.3: Teeth and rotor treated as a single body and bonded together (10-node tetrahedral)

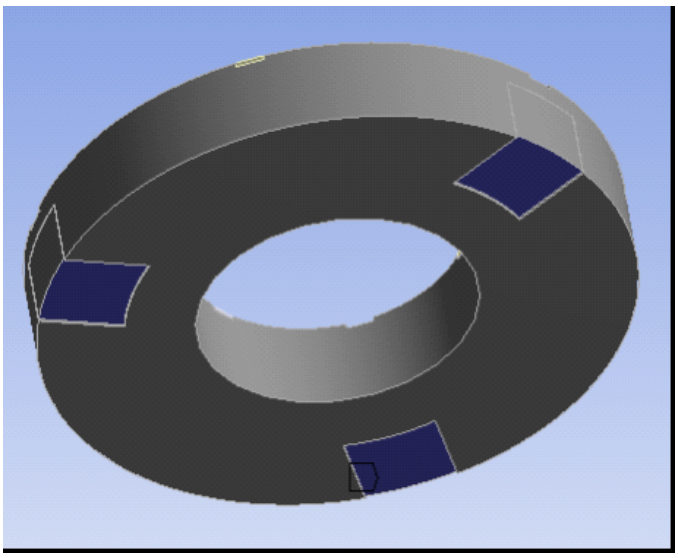

Figure 4.4: Stator fixed constraints attachment areas

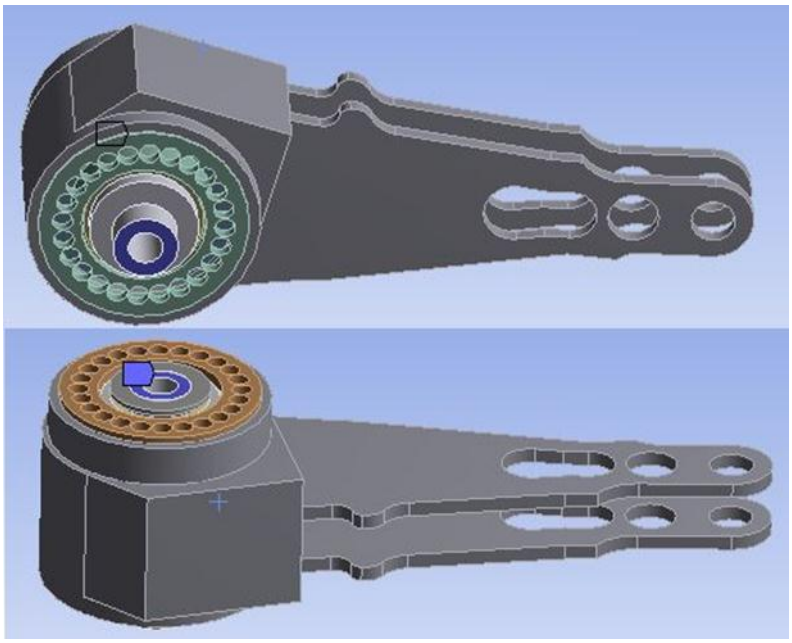

Figure 4.5: Top and bottom surface of shaft are supported by washers and given fixed support

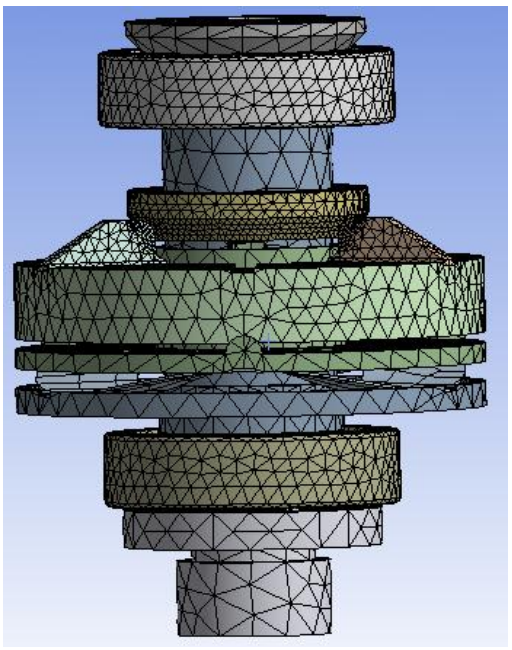

Figure 4.6: Inner and outer ball bearing simulated using 3D spring

The above few conditions have been highlighted because they govern the major dynamical behaviour of the simulation results. For example, the contact conditions between the stator teeth and rotor cone actually can influence the onset of rippling type modes. For the stator fixed constraints, it directly impacts on the accuracy of operating modes shapes and eigenfrequencies. Lastly, the shaft supports and ball bearing description are also important in lending the overall anchoring point for the rotation of the actuator. Whether a purely fixed support, constrain coupled equations or a 3D spring model to mimic ball bearings behaviour is a reasonable approximation to real world conditions is a challenge for all FEM analysts.

4.3 Modal and Harmonic Analysis

After the CAD model has been prepared, meshed, allocated with material data, boundary conditions applied and contact formulations completed. The next step is to proceed with the analysis. For a standard modal analysis, no excitation forces specification is needed. An external exciting force is needed to conduct a harmonic analysis though. For our purposes, in

which we are studying an electromechanical system, we will apply exciting voltage to the piezoceramics to induce strains deformation as the source of excitation. Figure 4.7 below shows where the sinusoidal voltages are applied in the FEM model. A 100V voltage is being applied on the segmented red area and segmented blue area. The phase difference between the two sources is 180 deg.

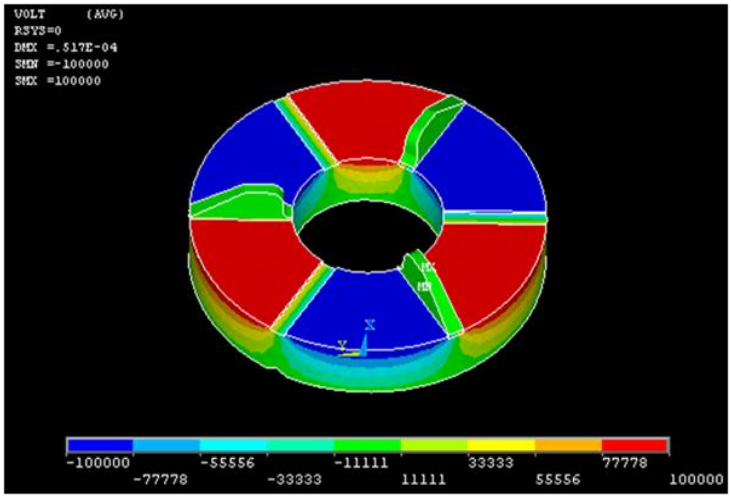

Figure 4.7: Voltage application as excitation source for harmonic analysis

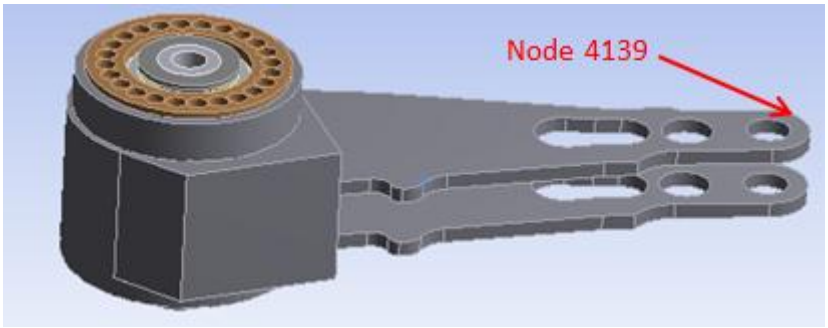

Figure 4.8: Interested displacement response point located at tip of actuator arm

Figure 4.8 above shows the output data point for studying the induced displacements. For HDD purposes, the vibrations experienced at the arm tip is most crucial as that is where the slider is located and in order to ensure superior read write performance, the vibrations at that location must be minimised.

4.3.1 Stator modal analysis results

Figure 4.9 to Figure 4.12 below shows the stator modal analysis results. There are many eigenfrequencies and modes generated from the simulation. However, only a few selected modes will be shown below. For the TRUM study which was undertaken, that would be the first analysis before proceeding to the full analysis involving the whole actuator arm assembly. This step is needed to clarify operational modes and basic functionality first before the full analysis is performed later. The results shown on the left of each mode have been experimentally collected using the set up as shown in Figure 4.13 below. The set up employs a Polytec Scanning Laser Doppler Vibrometer to scan and mapped out the respective modes shapes of the vibrating stator. The electronic circuitry and amplifier which drives up the stator are not shown in the picture.

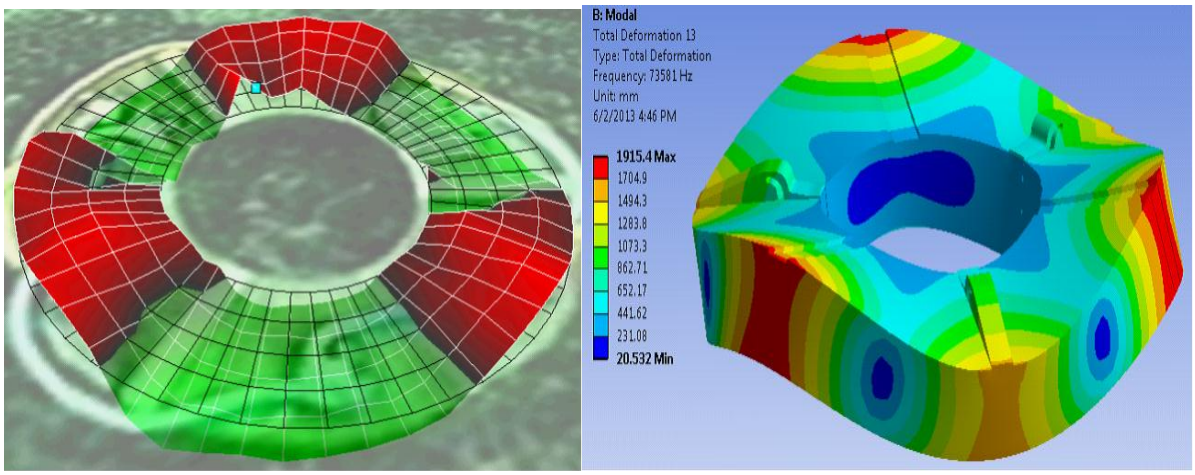

Figure 4.9: Mode Shape (0,3) mode – Experiment – 81kHz , Simulation – 74kHz

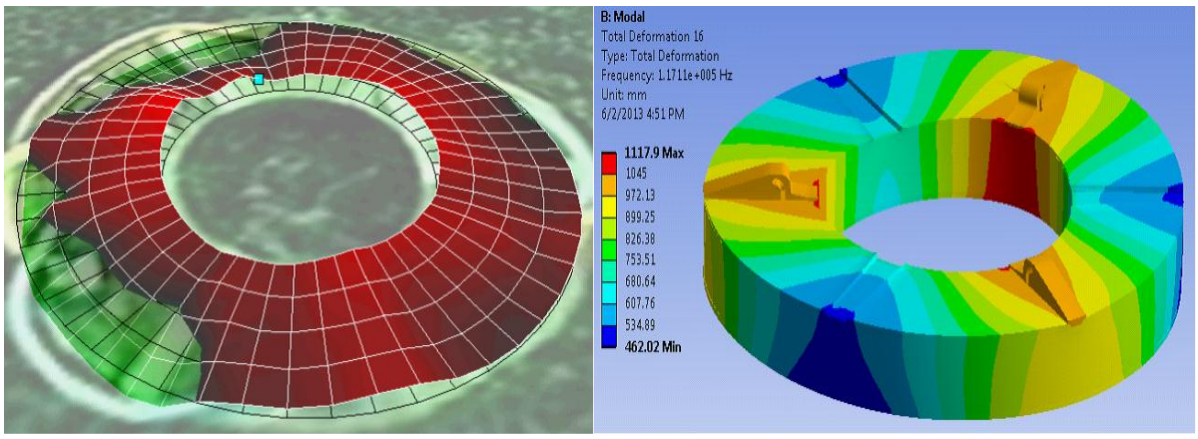

Figure 4.10: Mode Shape (0,0) mode – Experiment – 128kHz , Simulation – 117kHz

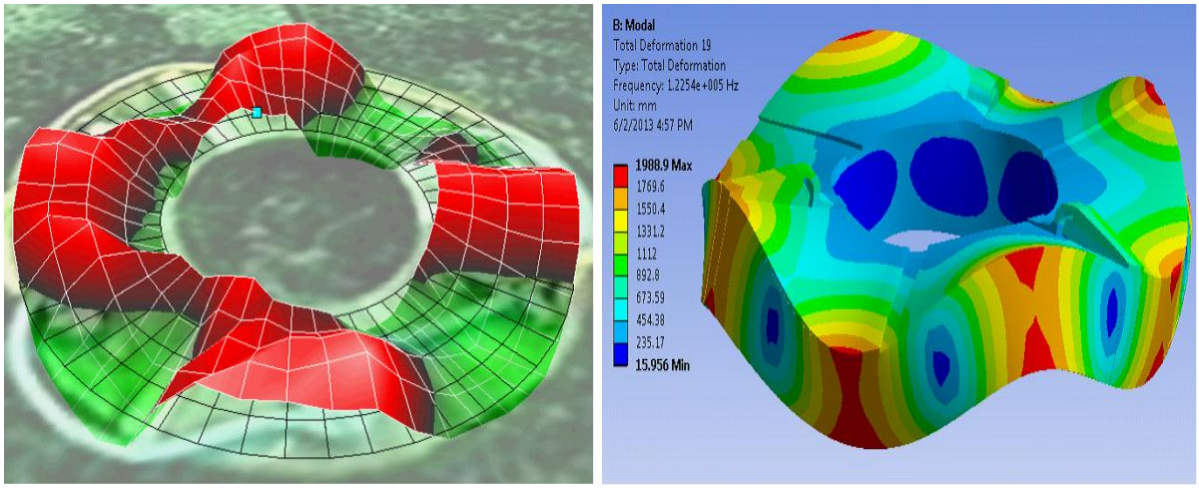

Figure 4.11: Mode Shape (0,4) mode – Experiment – 133kHz , Simulation – 122.5kHz

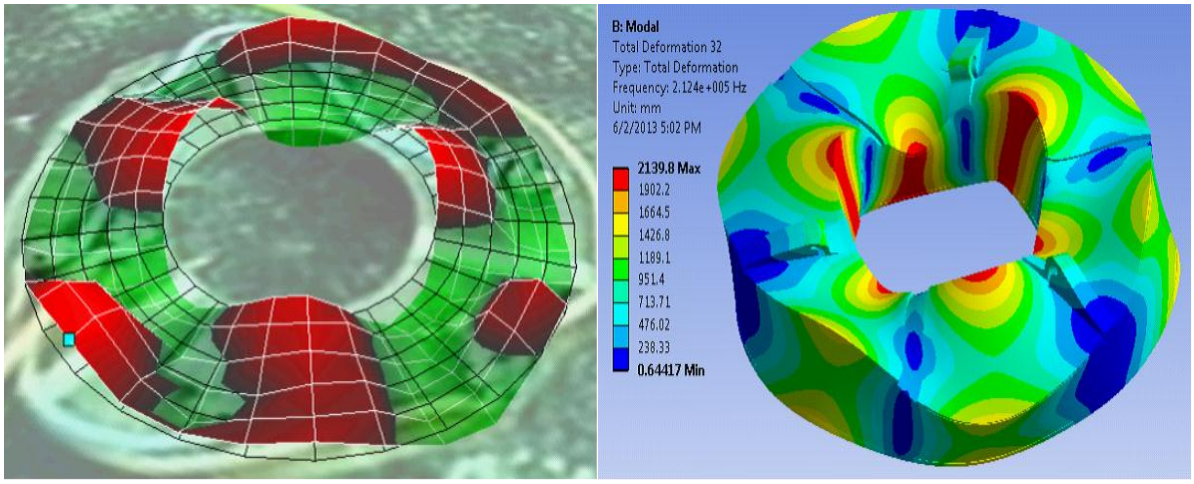

Figure 4.12: Mode Shape (1,3) mode – Experiment – 242kHz , Simulation – 212.5kHz

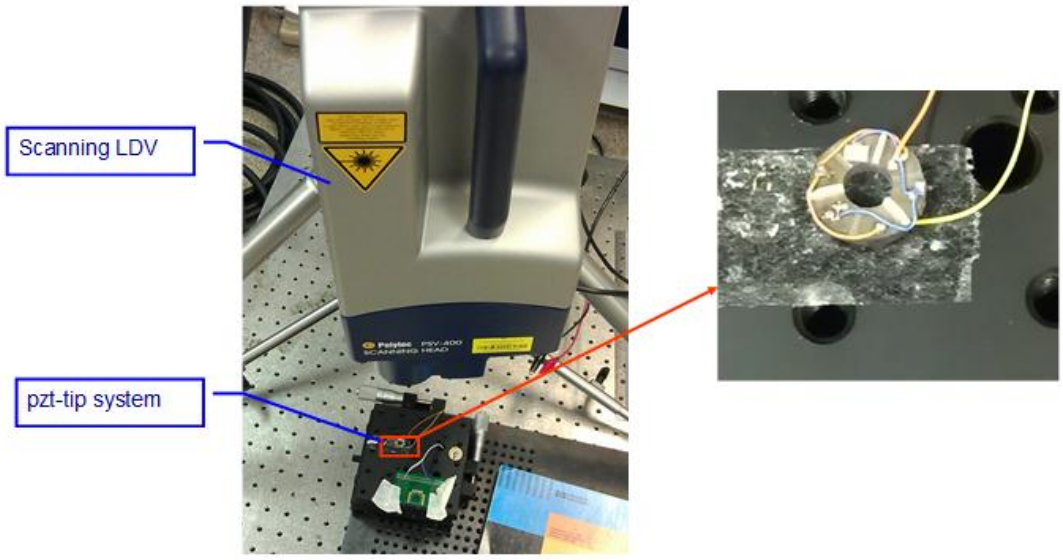

Figure 4.13: Experimental set up to measure mode shapes and modal frequencies of stator

Comparing the results between the simulation and experiments which is summarized in Table 4.3 below, we can conclude that the accuracy of the modal analysis is quite good with about a 10% discrepancy which is acceptable. This can be attributed to differences in the boundary conditions or even material data mismatch between simulation and actual prototype.

Table 4.3: Stator resonance modes comparison.

Mode Shapes	(0,3)	(0,0)	(0,4)	(1,3)
Experimental (kHz)	81	128	133	242
FEM (kHz)	74	117	122.5	212.5
Discrepancy (%)	8.64	8.59	7.89	12.2

4.3.2 Assembly level harmonic analysis results

We will look at the harmonic analysis results next. To simplify analysis here, only results that highlight the issue of low frequency rippling and ultrasonic parasitic vibrations will be presented. Of greater emphasis is the study of how different springs design can affect these vibrations. For the low frequency rippling, it was found that it can only be captured in the simulation whenever one or more of the contact bonds between the rotor and stator has been removed. It is found to be a mode that moves translational and seems to be rocking about the stator with the spring serving as the restoring element for the system. Figure 4.14 below shows a typical motion of such a rippling mode.

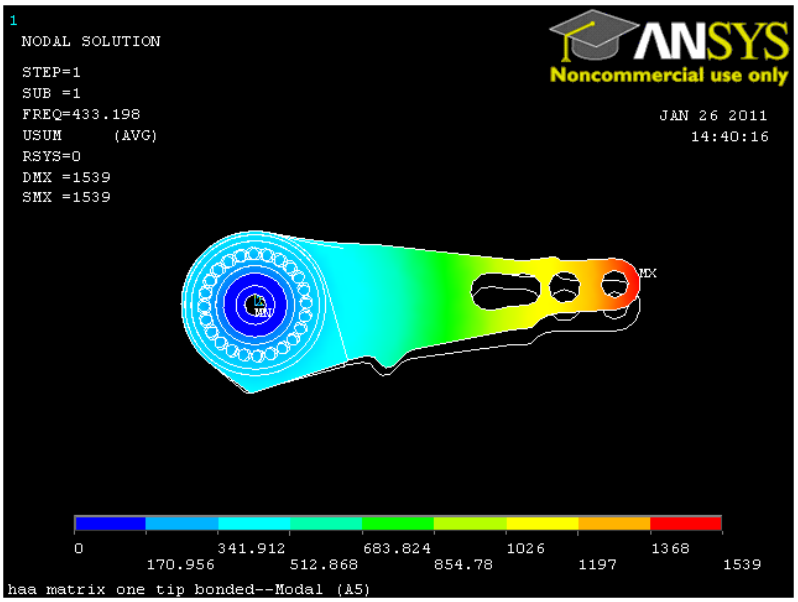

Figure 4.14: Typical ripple mode – translational motion about pivot bearing

The motion is characterised by a large in plane motion compared to the out of plane motion, Figure 4.15 below shows the frequency response plot of from the harmonic analysis results. From the data, the frequency lies at around 420 Hz. Comparing the axial and radial components, it also indicates that the radial component is much larger than the axial component.

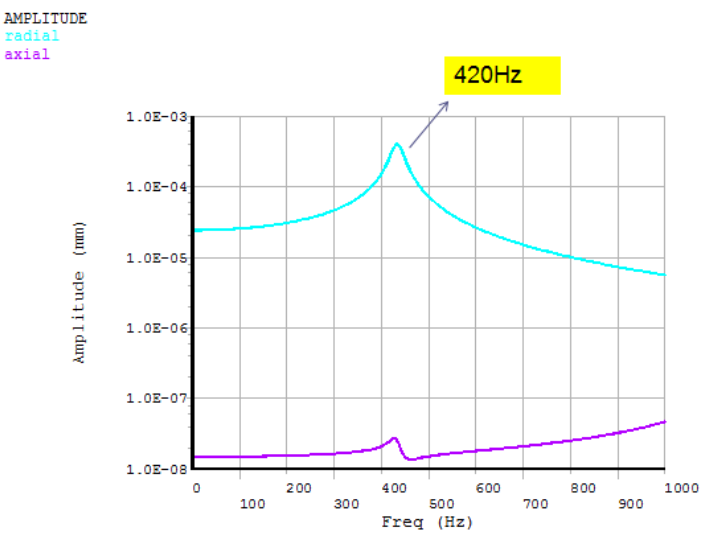

Figure 4.15: Rippling mode manifested in frequency response function

Figures 4.16 and Figure 4.17 below show experimental data that supports the simulation observation. The measured radial vibration is of the order of magnitude 20 times greater than the axial vibrations at the rippling mode. Figure 4.18 shows a typical experimental set up used to measure the frequency response of the HDD actuator using a Laser Doppler Vibrometer. The components are normally mounted onto an isolation table to suppress environmental vibrations. A D-Space controller system and a VCM Driver are often used in conjunction with such a set up to study control strategies.

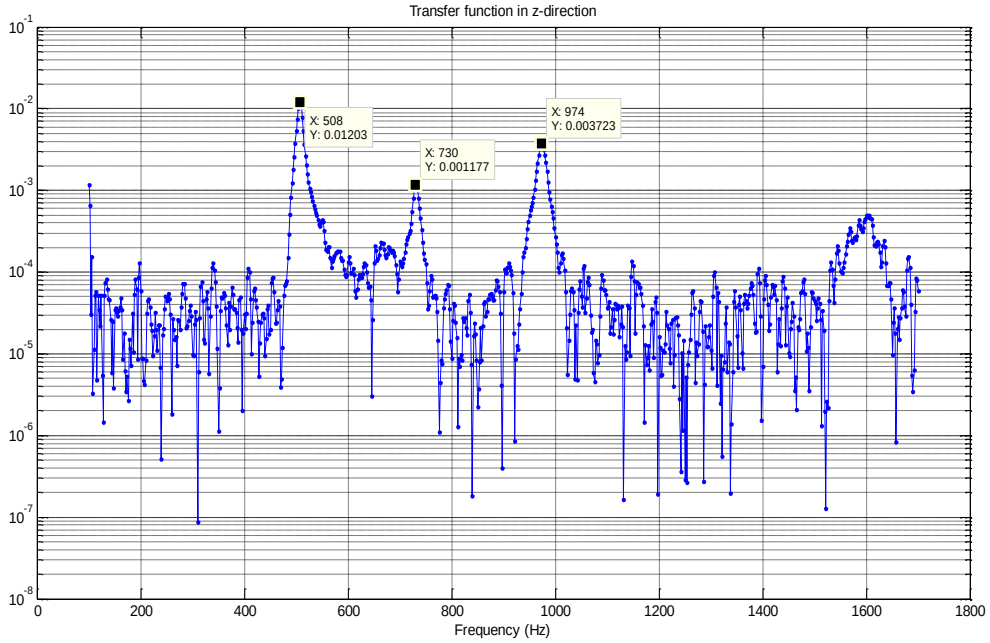

Figure 4.16: Axial vibration gain at 508Hz – 0.01203

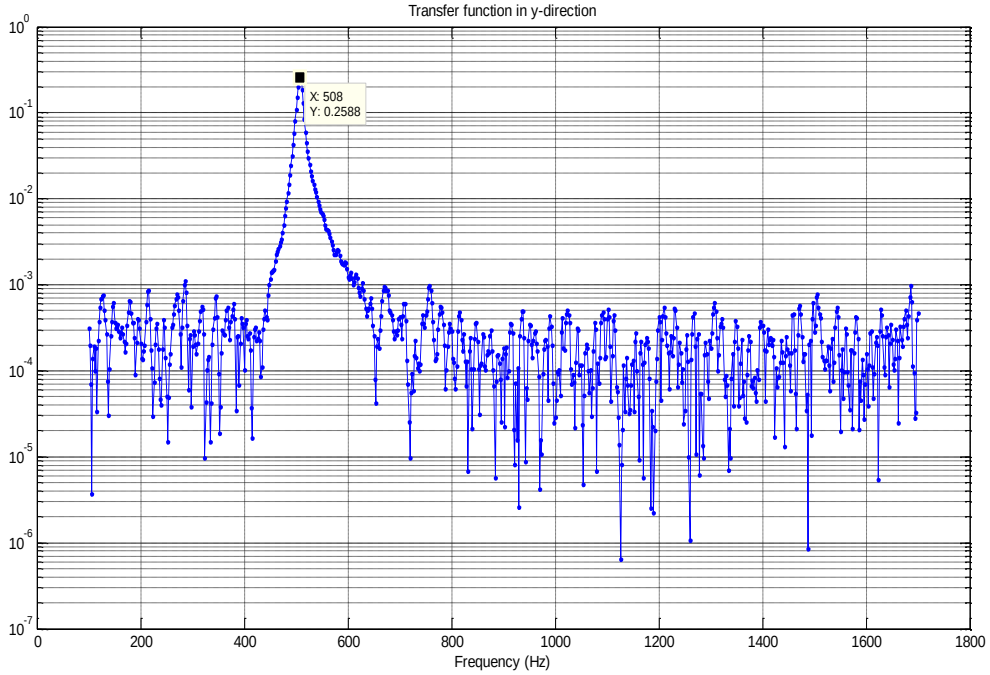

Figure 4.17: Radial vibration gain at 508Hz – 0.2588

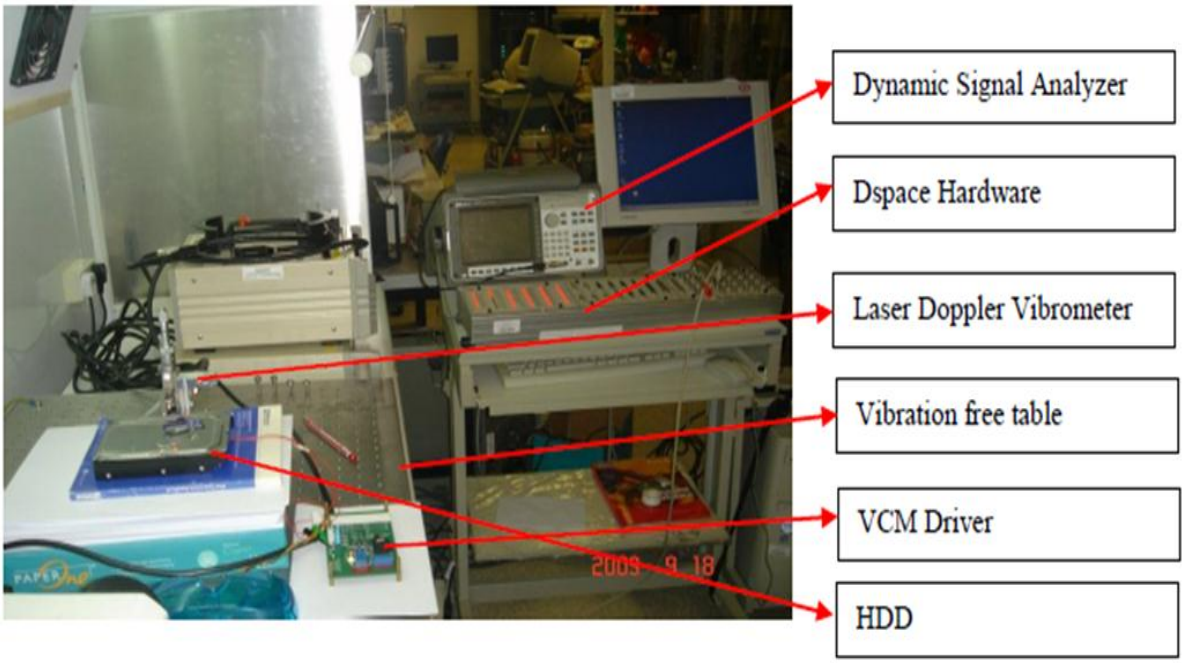

Figure 4.18: Set up to measure HDD frequency response function

Figure 4.19 below shows a part of the plot from the harmonic simulation. It shows the presence of high frequency ultrasonic vibrations being transmitted to the actuator tip at around 120 kHz.

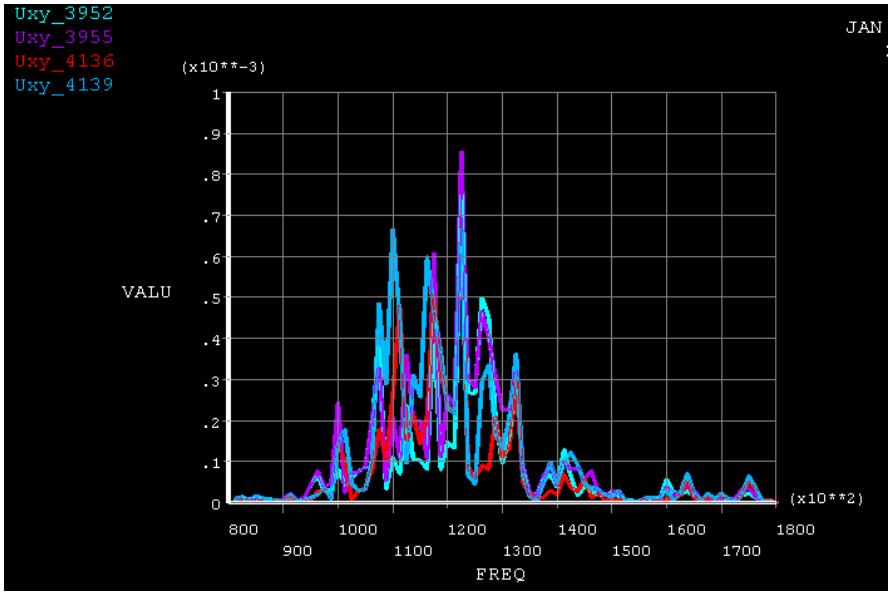

Figure 4.19: Ultrasonic vibration at actuator tip at around 120 kHz

4.4 Pre-Loading Springs Design

One of the main design considerations during the collaboration was the changes made to the pre-loading spring. It was thought that a softer spring could serve as a good interface to mitigate and filter away the higher frequency vibrations as well as also, very importantly, allow for better assembly tolerances and reduces misalignments and unnecessary clearances. The spring should have high rotational stiffness to be able to transmit the torque produced, while at the same time have low axial and radial stiffness to filter away vibrations and made assembly alignment easier. Experimental and FEM harmonic analysis results seem to support such a proposition. Furthermore, the analytical results which will be present later in chapter 6 also points in the same direction. Figure 4.20 to Figure 4.23 below show us the cross section view of the TRUM HDD actuator implemented using several different types of spring design. There are a total of four designs, but we will restrict the study to only two designs. The cylindrical spring design and the new version of flat pull spring design. The reason behind such a choice is that the new and flat pull spring design are similar in construction except for some internal cutting grooves, while the wave spring construction is not suitable for the analytical model developed earlier as the pre-loading component in on the stator instead of the rotor. Thus only the new version of the pull spring and the cylinder spring was considered.

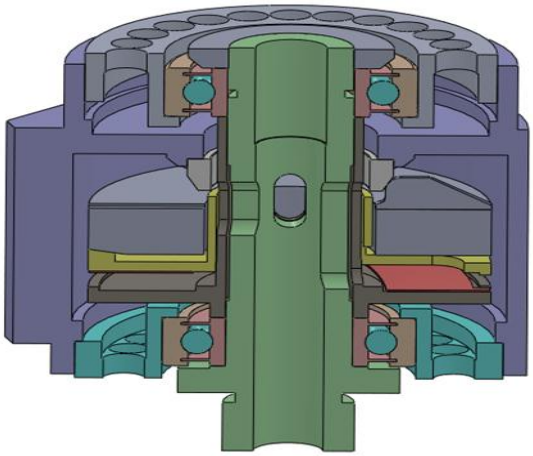

Figure 4.20: Wave spring design TRUM HDD actuator

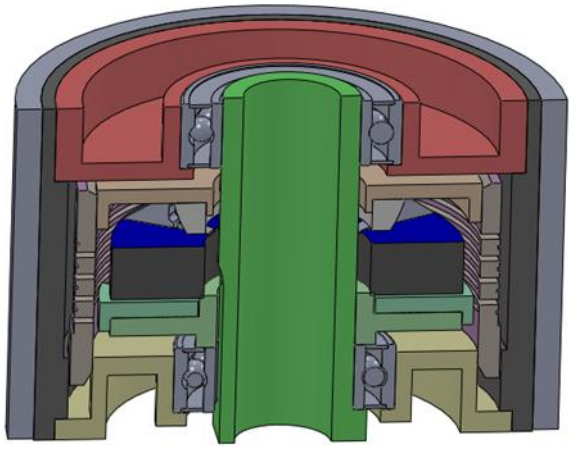

Figure 4.21: Cylinder spring design TRUM HDD actuator

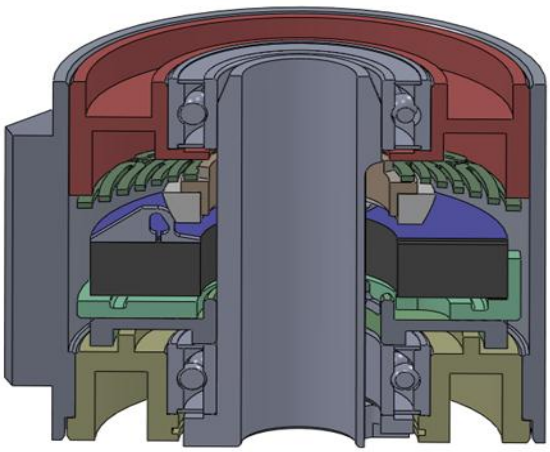

Figure 4.22: Flat Pull spring design TRUM HDD actuator

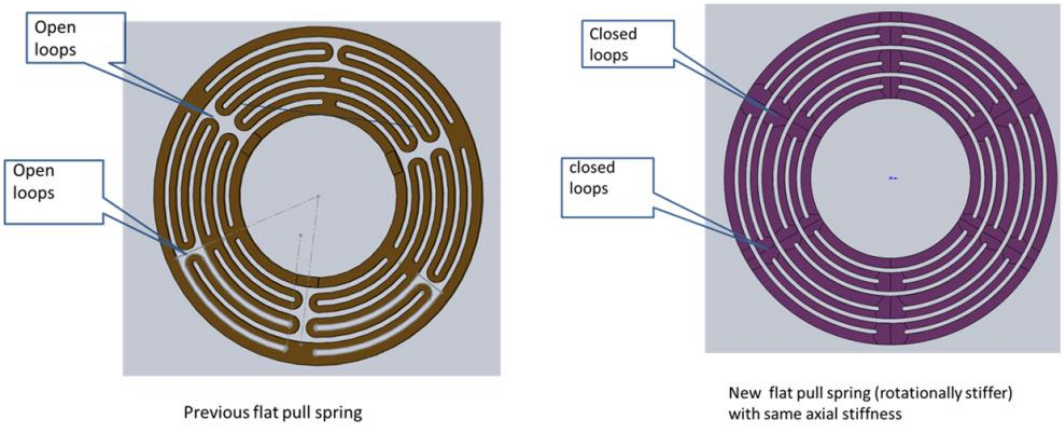

Figure 4.23: Flat Pull spring design – new and old design

Figures 4.24 and 4.25 below show two typical results obtained from harmonic analysis. While Figures 4.26 and 4.27 shows two typical results obtained from experimental frequency response data respectively. It shows the rippling frequency at between 400Hz to 1000Hz, the actual amount of rippling cannot be quantified in a very repeatable manner due to tolerances and assembly factors. It is to note though, that the repeatability in the frequency experience and their relative high amplitude in the frequency response spectrum.

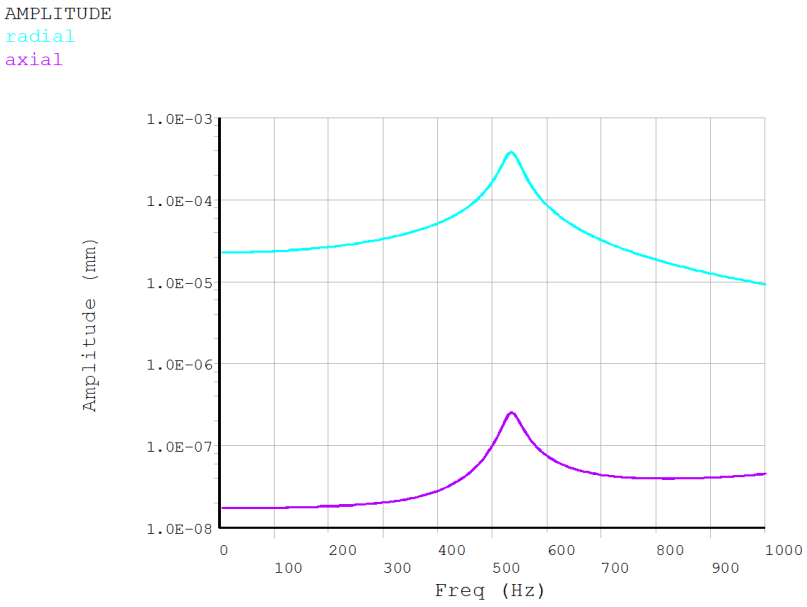

Figure 4.24: Rippling mode at 520Hz for old flat pull spring

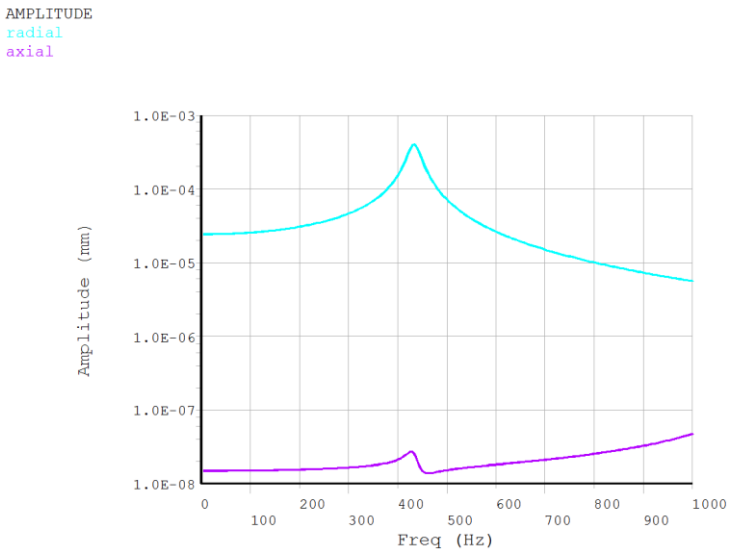

Figure 4.25: Rippling mode at 420Hz for cylinder spring

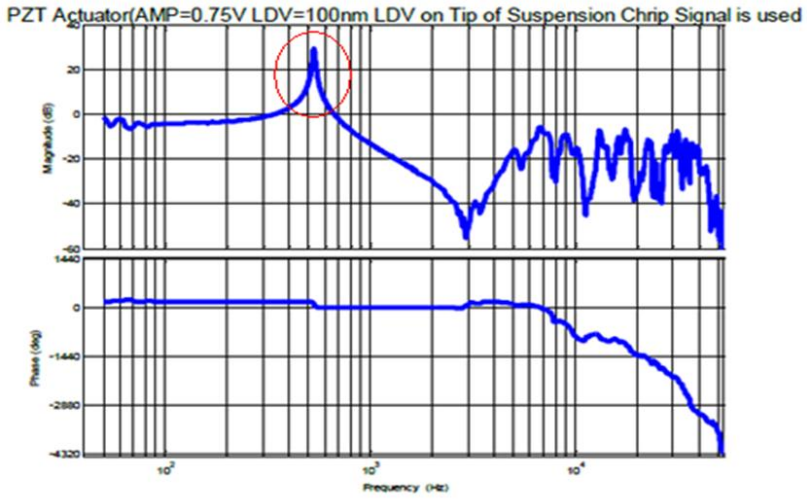

Figure 4.26: Rippling mode at 520Hz for old flat pull spring

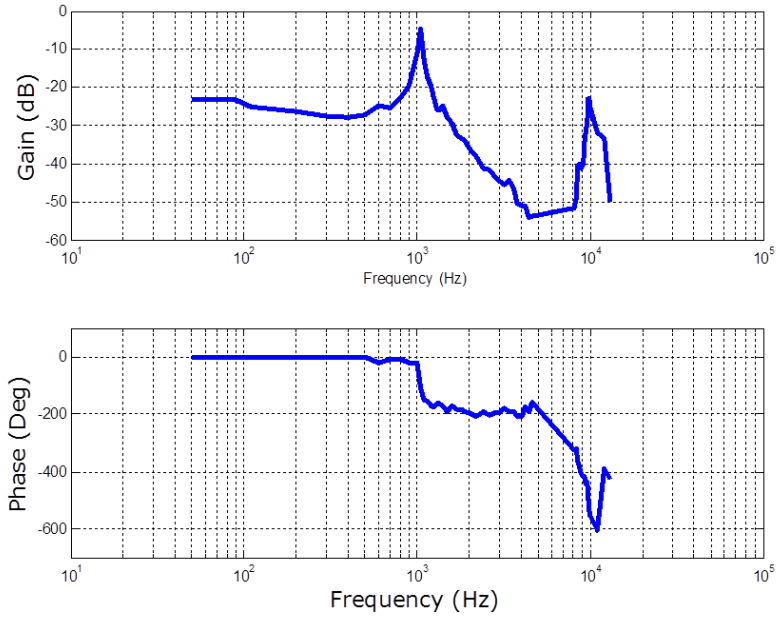

Figure 4.27: Rippling mode at 1050Hz for new flat pull spring

The section below summarises the data collected from harmonic analysis on the high frequency vibrations experienced on the actuator arm tip for the few cases. Table 4.4 below summarises the simulation results together with collected experimental data supplied by Pinanotech in parenthesis. The respective frequency response plots for the following cases are shown from Figure 4.28 to Figure 4.31.

	Wave-spring	Cylinder-spring	Flat-spring	Improved flat-spring
Radial displacement (expt)	16nm (N.A)	0.5nm (2.5)	3.75nm (12.4nm)	2.7nm (3.2nm)
Axial displacement (expt)	37nm (N.A)	0.56nm (1nm)	10nm (22nm)	3.05nm (3.35)

Table 4.4: Summary of results for high frequency ultrasonic vibrations level

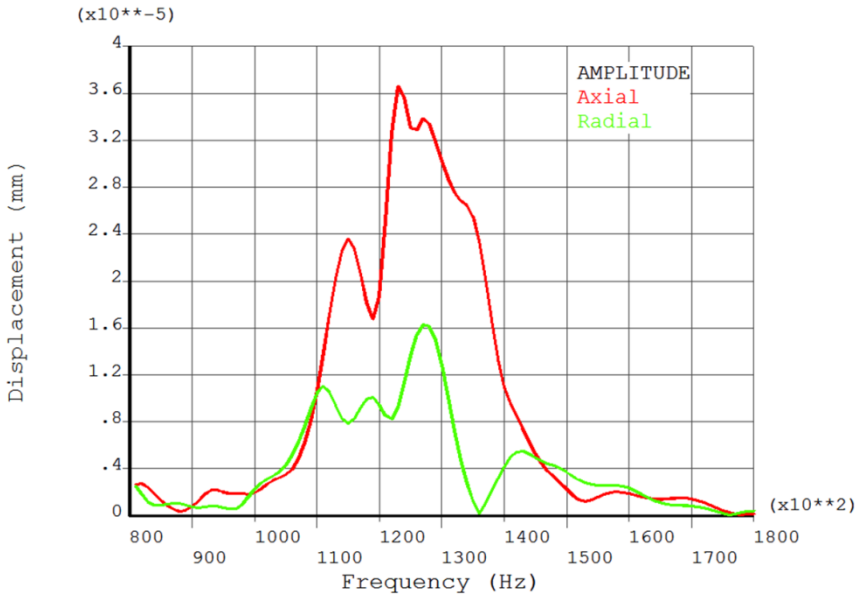

Figure 4.28: Wave spring

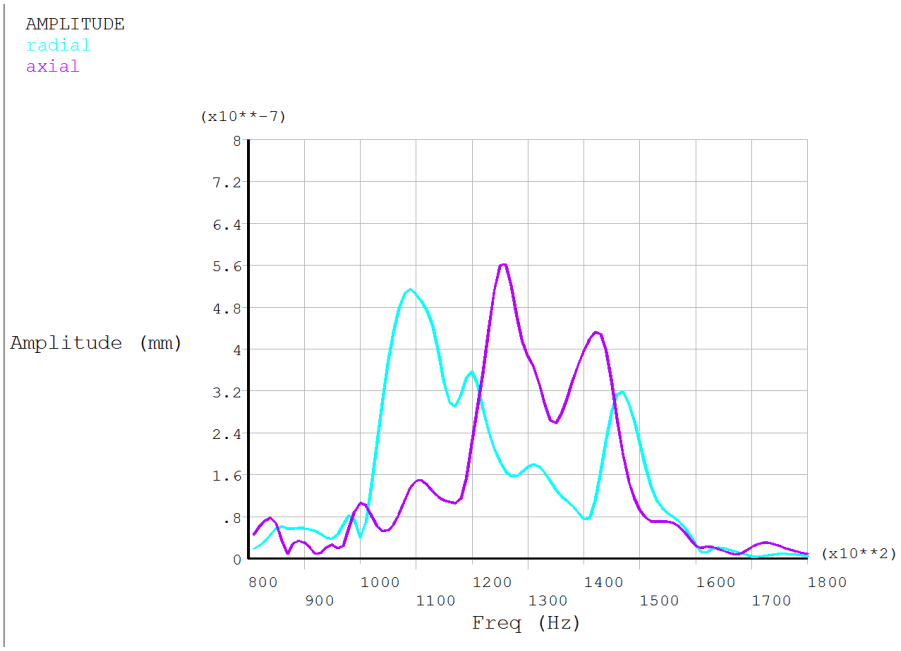

Figure 4.29: Cylinder spring

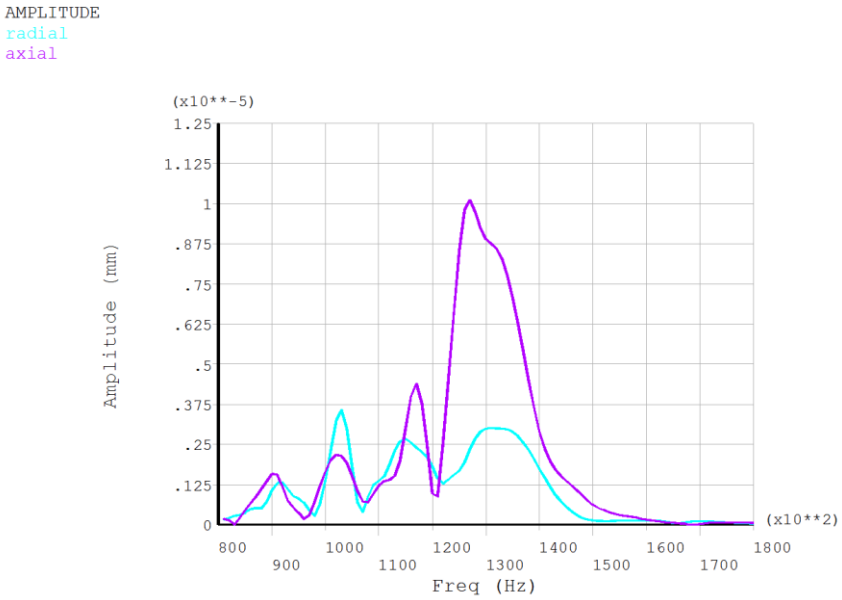

Figure 4.30: Old version Flat Pull spring

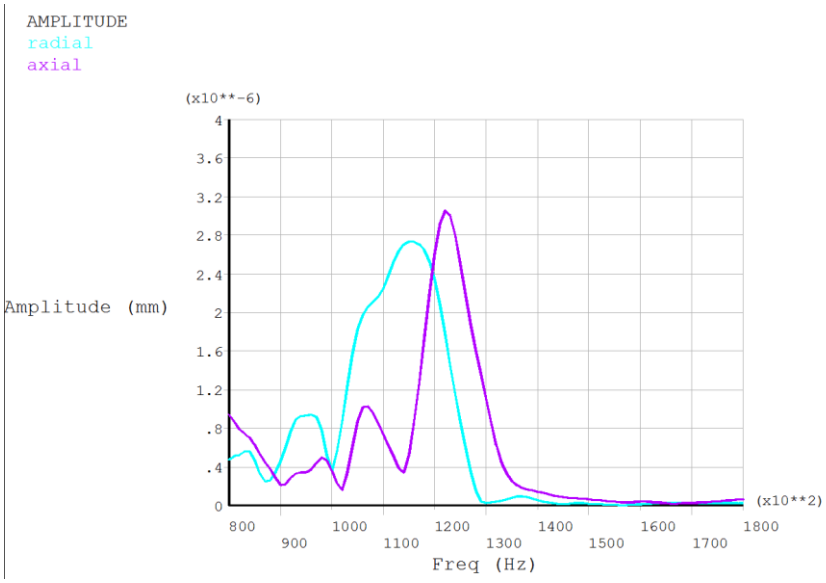

Figure 4.31: New Flat Pull spring

From the above results it can be seen that the cylinder spring performs the best, followed by the new flat pull spring and then the old flat pull spring design. The wave spring performs the worst.

The rippling results are not that easily quantified because of the fact that assembly tolerances and stack up clearance is a very important factor influencing this mode. These imperfections due to engineering imperfections and assembly misalignment are difficult to control and quantified in the prototype. During measurements of frequency response though, a clear frequency peak at the low of 400-1050Hz can be observed for all the springs. It can be inferred that changing spring designs shifts the low frequency resonance around. Instead of only the stiffness factor, the actual quantity of parasitic vibrations experienced can be considered to be due to the combination of several effects. Three processes are important. First, lower spring stiffness represents greater vibration transmissibility attenuation. But, second, it also implies that stator induced forces can cause more motion as weak spring are more easily displaced. Third, the assembly stack up heavily influence the onset and amount of rippling and hence other parasitic vibrations components. The reason is that such tolerances misalignment translates to force and moment imbalances which generate those modes as well as provide clearances for such vibrations to takes place instead of rigidly constraining them.

Static analysis of the springs has been conducted to investigate their relative stiffness in the radial, axial and angular directions. Only two types of springs were chosen for the below study, the cylinder spring and the new flat pull spring. Figure 4.32 to Figure 4.34 show the analysis results for the cylindrical spring while Figure 4.35 to Figure 4.37 shows the analysis results for the new flat spring.

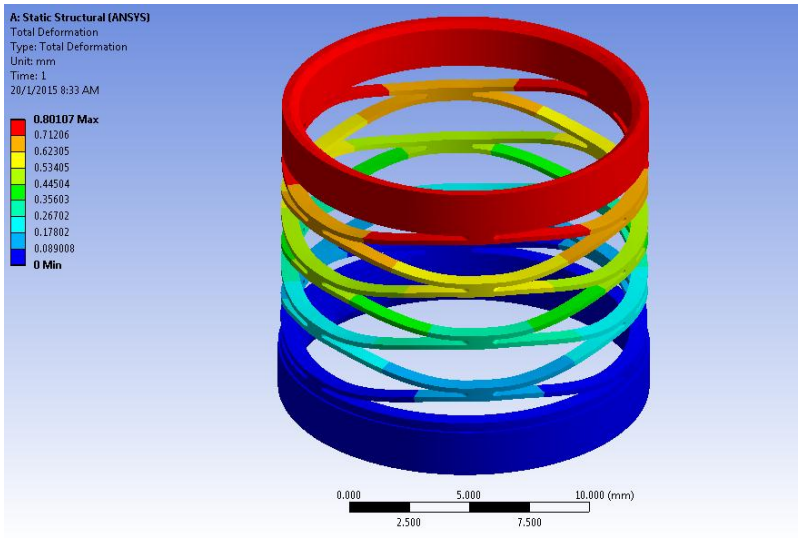

Figure 4.32: Cylinder spring under axial load

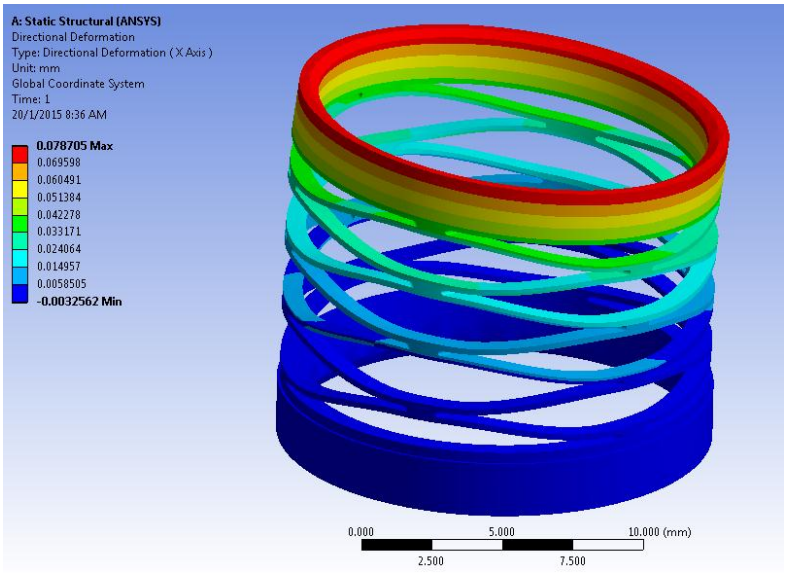

Figure 4.33: Cylinder spring under radial load

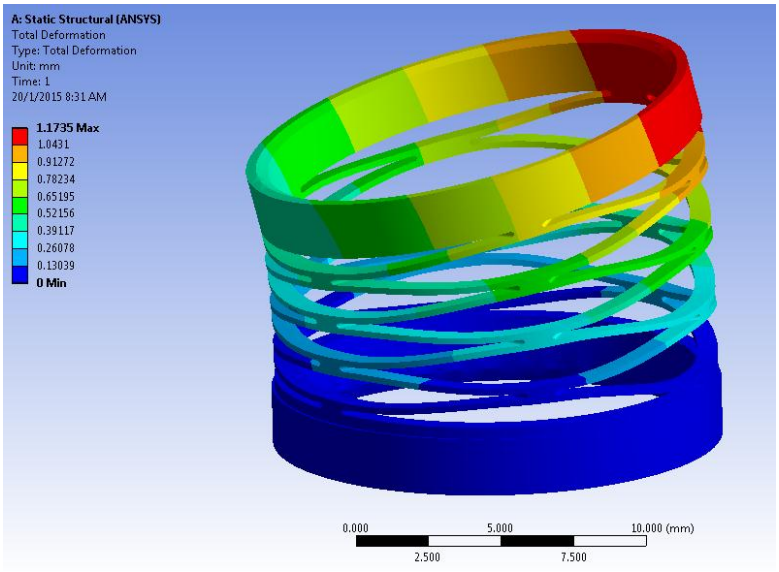

Figure 4.34: Cylinder spring under angular load

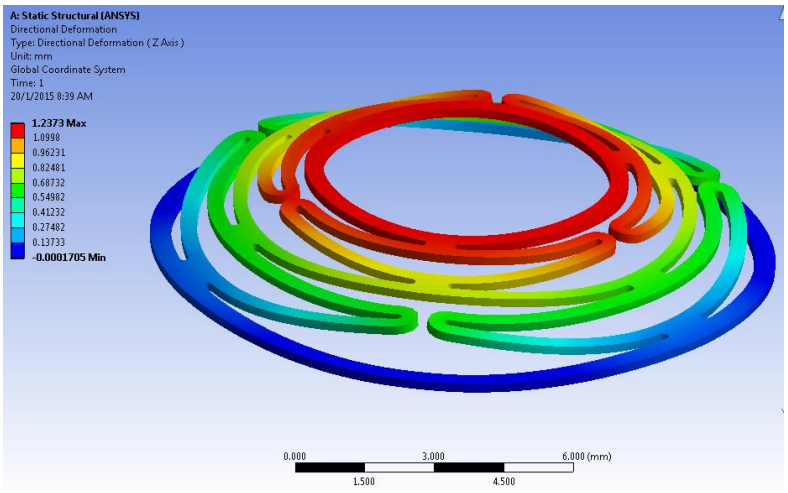

Figure 4.35: New Flat pull spring under axial load

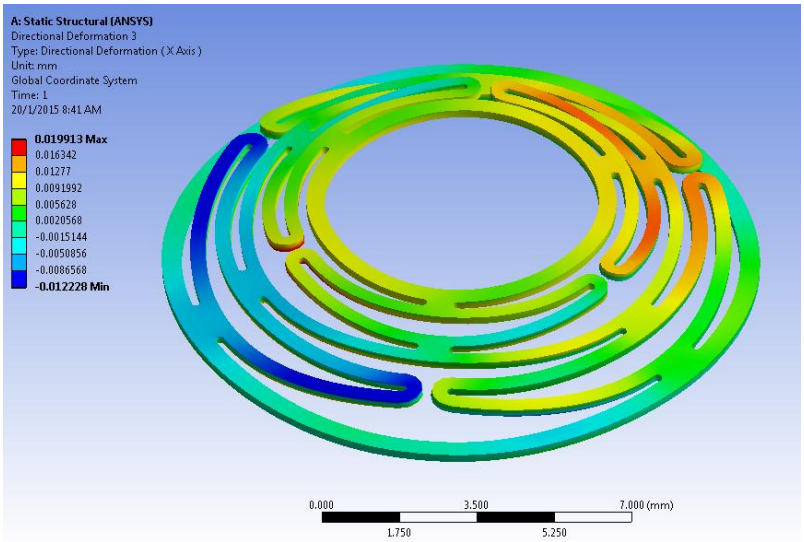

Figure 4.36: New Flat pull spring under radial load

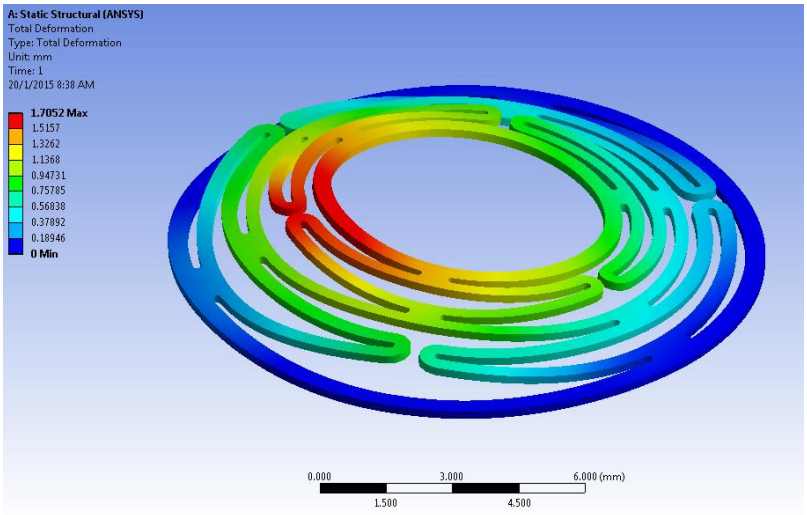

Figure 4.37: New Flat pull spring under angular load

Table 4.5 below gives a summary of the angular stiffness of the two springs.

	Axial Stiffness (N/mm)	Radial Stiffness (N/mm)	Angular Stiffness (Nm/rad)
Cylinder Spring	6.241	12.71	0.17739
New Flat Pull Spring	4.1	126	0.02725

Table 4.5: Spring stiffness of cylinder and new flat pull springs.

For the HDD actuator with mass of 3g and moment of inertia of around $600 gmm^2$. The computed resonance frequencies are shown in Table 4.6 below.

	Axial Resonance (hz)	Radial Resonance (hz)	Angular Stiffness (hz)
Cylinder Spring	162	330	87
New Flat Pull Spring	33	1031	34

Table 4.6: Axial, radial and angular resonance modes

Of particular importance to note is the radial resonance mode as this will be what we would be studying and trying to re-produce in the analytical modelling later to mimic the effects of off plane translations motions. Table 4.7 below shows the springs transmissibility factor

Transmissibility factor (for 120kHz)	Axial	Radial	Angular
Cylinder Spring	3.25777e-6	9.35263e-6	1.54272e-6
New Flat Pull Spring	5.55231e-7	7.57983e-5	5.72393e-7

Table 4.7: Transmissibility Factor

The spring transmissibility factor (X/Y) influences the amount of vibration transmitted from a moving base structure to the mass located at the spring tip as shown in the below Figure 4.38.

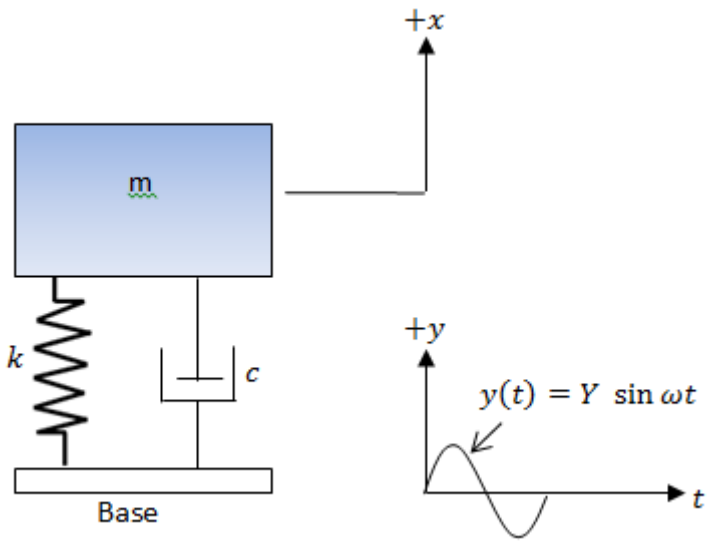

Figure 4.38: Vibration transmitted from a vibrating base to the mass m.

4.5 Conclusion

This chapter presented a comprehensive coverage of the FEM study undertaken to study the dynamical behaviour of the TRUM HDD actuator. Only basic modal and harmonic analysis

has been conducted as the contact interface contact modelling would be too computationally intensive. The modal and harmonic analysis results indicate the issues of low frequency rippling and high frequency ultrasonic vibration transmission. The analysis was performed using several spring designs with different stiffness characteristics and transmissibility factor. It was found that spring design does influence the behaviour but the results were not conclusive. This is because a less stiff spring allows better assembly tolerances and lowers the transmissibility factor, but it also allows greater amount of vibration to be effected onto it with the same force. This observation will be compared with the analytical results in chapter 6 which suggest the same conclusion. Frequency response experimental data was also presented and the issue of rippling was also manifested in the experiment.

CHAPTER 5 -- MATHEMATICAL MODEL OF TRUMS

5.1 Introduction

In chapter 3, the basic operational mechanism underlying TRUMs was explained. In this chapter, the objective is to derive the Equation of Motion (EOM) governing the dynamic behavior of the TRUM. The problem involved here is an electro-mechanical system that is piezoelectrically coupled, with simultaneous contact interactions between a set of stator and rotor. Energy method is the most appropriate in the formulation of EOM for such systems. The Rayleigh-Ritz assumed modes energy method is employed in the modeling formulation. The electrical virtual work performed by the electrodes as well as the external mechanical work done by the interface forces has also been included into the formulation. Frictional effects and the contact kinematics arising from the relative sliding velocities which sets up different stick and slip states are also accounted for in the model.

Unique in this present modeling framework is the inclusion of additional degrees of freedom describing the rotor dynamics. As far as the author knows, previous work in the literature assumes the rotor to have angular motions only in the rotating working configuration and a translational component along the rotating axis. The present study however, removes such constraints and models the rotor having all three rotational and translational degrees of freedom. This is to allow the model to effectively capture the rigid body dynamics of tilting vibrations experienced by an actual rotor and to also study how such interactions impacts on the overall motor behavior. However, such an extension is not trivial as relaxing the constraints introduces the problem of the need to describe the changing domain boundaries of both rotor and stator and also the need to search and capture the evolving state of contact between the two bodies.

5.2 General Modeling Framework of TRUM

The general system is depicted in Figure 5.1 below. It consist of an elastic stator bonded with a thin layer of piezoelectric ceramic and held into place by appropriately placed constraints which serves as fixed boundaries. The rotor is aligned above the stator with an applied pre-load from a spring which presses it onto the stator, ensuring physical contact between the two components. The rotor is modeled as a rigid body having six degrees of freedom (three translational and three rotational). The bottom rotor surface is interposed with a thin layer of compliant viscoelastic material to enhance frictional grip as well as to reduce rotor vibration squeal in actual practice. In the model, the pre-loading spring is modeled in terms of three equivalent stiffness components in the radial, axial and angular directions.

For the electroelastic continuum in consideration, an energy approach utilizing the Rayleigh-Ritz formulation is most appropriate. Assumed displacement field shapes describing the elastic body and electric potential field shapes will be used in the derivation. We first begin from the generalized form of Hamilton's Principle for coupled electromechanical system [Crandell*],

$$\delta \int_{t_1}^{t_2} (\mathcal{L} + W_E + W_M) \, dt + \int_{t_1}^{t_2} \delta (W_T^{ext} + W_N^{ext}) dt = 0 \qquad (5.1)$$

$$\mathcal{L} = E_k - E_U \qquad (5.2)$$

$\mathcal{L}$ is the Lagrangian of the system while δW_E is the variational electrical work done by the application of electrical voltages and δW_M, the variational magnetic work term. δW_T^{ext} and δW_N^{ext} refers to the variational tangential work and variational normal work done, respectively, by the interfacial forces arising from the physical contact between the stator and

rotor. For piezoceramics, the magnetic work term δW_M are negligible and can be omitted from equation (5.1) above.

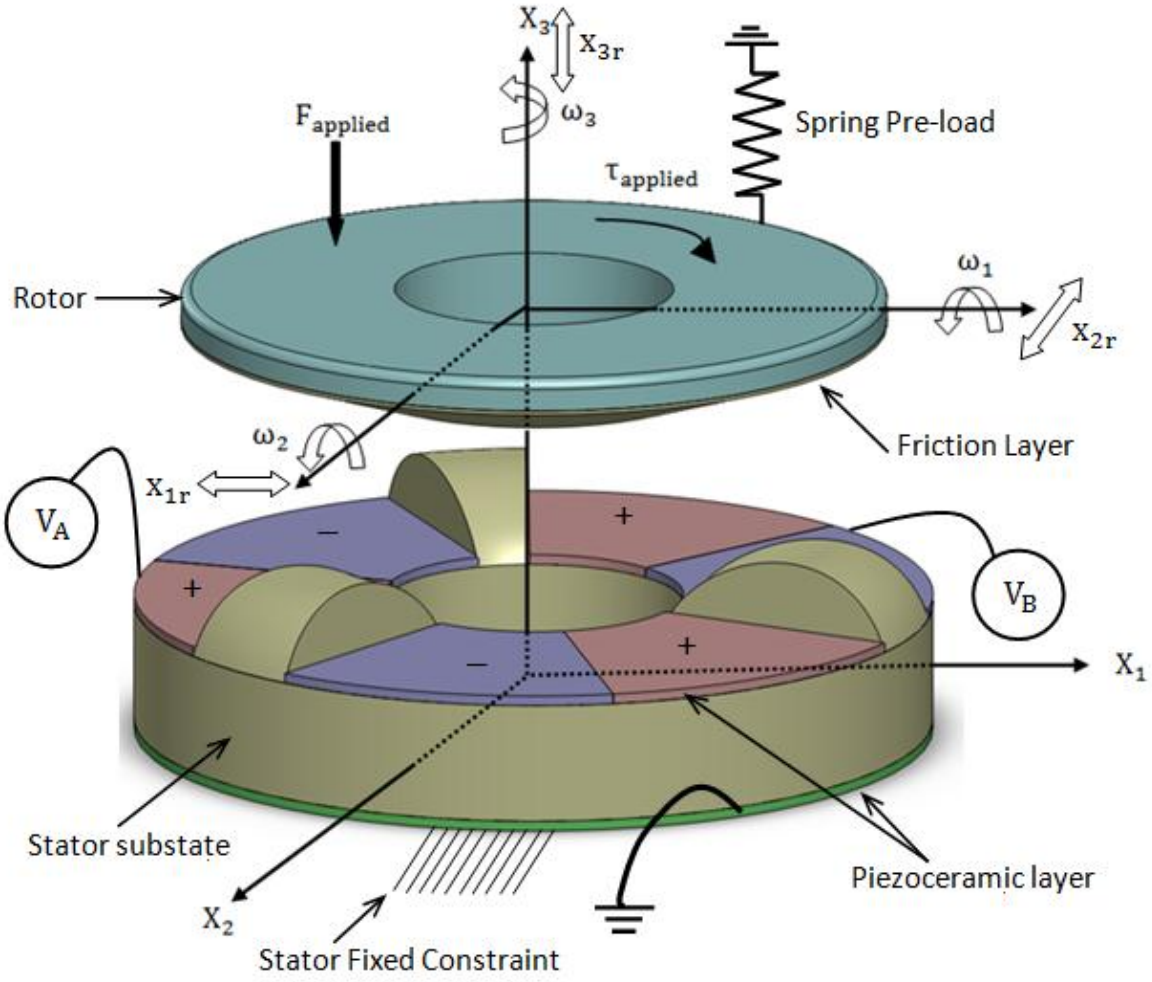

Figure 5.1: General System of TRUM

5.2.1 Formulation of Energy Terms

The kinetic energy of the stator consists of two components, that due to the stator substrate E_{kS} and that due to the piezoceramic layer E_{kP}, and is given by

$$E_k = \frac{1}{2}\int_{V_S} \dot{\mathbf{u}}_\mathbf{o}^\mathbf{T}\,\rho_S\dot{\mathbf{u}}_\mathbf{o}\;dV_S + \frac{1}{2}\int_{V_P} \dot{\mathbf{u}}_\mathbf{o}^\mathbf{T}\,\rho_P\dot{\mathbf{u}}_\mathbf{o}\;dV_P \qquad (5.3)$$

In the above equation, ρ_S and ρ_P refers to the density of the stator substrate and piezoceramic respectively. The vector $\dot{\mathbf{u}}_\mathbf{o}$ represents the centerline velocity of the stator in the radial r, angular θ and axial z direction. Figure 5.2 shows the cross sectional view of a stator under bending deformation and illustrates the velocity vector $\dot{\mathbf{u}}_\mathbf{o}$.

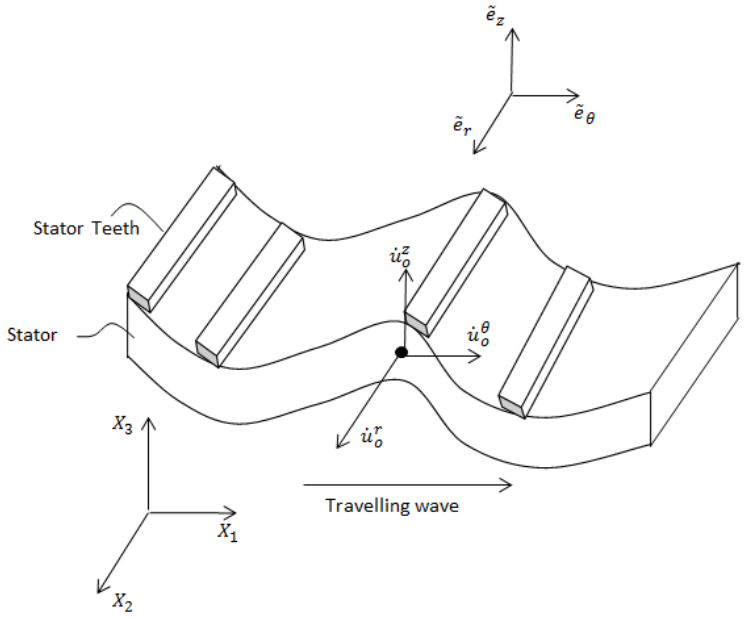

Figure 5.2: Stator velocity along centerline

The electrical energy terms within the piezoelectric volume is given by

$$E_e = \frac{1}{2}\int_{Vp} \boldsymbol{E}^t\, \boldsymbol{D}\, dV \tag{5.4}$$

Whereby $\boldsymbol{D}$ is the electric displacement vector while $\boldsymbol{E}$ is the electric vector, the total mechanical potential energy of the stator due to the internal strains fields induced is expressed as,

$$\mathrm{E_P} = \tfrac{1}{2}\int_{\mathrm{V_S}} \mathbf{S}^{\mathrm{T}}\mathbf{T}\,\mathrm{dV_S} + \tfrac{1}{2}\int_{\mathrm{V_P}} \mathbf{S}^{\mathrm{T}}\mathbf{T}\,\mathrm{dV_P} \tag{5.5}$$

Where **S** is the strain vector and **T** is the stress vector. In terms of cylindrical coordinates as shown in Figure 5.2 above, the components of these vectors are given by the following identities,

$$\mathbf{S} = \begin{Bmatrix} S_1 \\ S_2 \\ S_3 \\ S_4 \\ S_5 \\ S_6 \end{Bmatrix} = \begin{Bmatrix} \varepsilon_r \\ \varepsilon_\theta \\ \varepsilon_z \\ \gamma_{\theta z} \\ \gamma_{rz} \\ \gamma_{r\theta} \end{Bmatrix} \tag{5.6}$$

$$\mathbf{T} = \begin{Bmatrix} T_1 \\ T_2 \\ T_3 \\ T_4 \\ T_5 \\ T_6 \end{Bmatrix} = \begin{Bmatrix} \sigma_r \\ \sigma_\theta \\ \sigma_z \\ \tau_{\theta z} \\ \tau_{rz} \\ \tau_{r\theta} \end{Bmatrix} \tag{5.7}$$

Within the metallic substrate, normal constitutive relation for a linearly elastic material holds,

$$\mathbf{T} = c_S\, \mathbf{S} \tag{5.8}$$

For an isotropic elastic material, the stiffness matrix c_S according to Hooke's law is given by,

$$c_S = c_{ijkl} = \frac{E_S}{1+\upsilon_S}\left(\delta_{ik}\delta_{jl} + \frac{\upsilon_S}{1-2\upsilon_S}\delta_{ij}\delta_{mk}\delta_{ml}\right) \tag{5.9}$$

Where E_S and υ_S are the Young's modulus and Poisson ratio respectively. δ_{ij} is the Kroneker symbol. The constitutive relation for the piezoelectric material not only consists of the mechanical stiffness matrices but also the electromechanical coupling terms, as well as the dielectric terms. Several representations are available depending on the types of applications Ikeda [4], for our purposes, we will be utilizing the below stress-charge representation to formulate the piezoelectric material constitutive model,

$$\mathbf{T} = c_P^E\, \mathbf{S} - e^T \mathbf{E}$$

$$\mathbf{D} = \mathrm{e}\,\mathbf{S} - \epsilon^{S}\,\mathbf{E} \tag{5.10}$$

c_P^E, e and ϵ^S are the piezoelectric stiffness, electromechanical coupling and the dielectric matrices respectively. The superscripts “E” and “S” mean that the properties are taken at conditions of constant electric field and constant strain respectively. Superscript “T” refers to the transpose of the matrices. Given that piezoceramics are transversely isotropic, this means that for a given a rotation about an axis, the elastic property of piezoceramics remains unchanged. The invariance of elastic property towards rotational orientation allows the total number of compliance coefficients to fully describe the stiffness matrices of piezoceramics to drop to 5. As in most TRUM construction, the polarization direction of the piezo layer is also taken to coincide with the axis of transverse isotropy. With the above considerations and assumptions, the constitutive relations for the piezoceramic material when fully expanded is expressed as follows,

$$\begin{Bmatrix} T_1 \\ T_2 \\ T_3 \\ T_4 \\ T_5 \\ T_6 \end{Bmatrix} = \begin{bmatrix} c_{11}^E & c_{12}^E & c_{13}^E & 0 & 0 & 0 \\ c_{12}^E & c_{11}^E & c_{13}^E & 0 & 0 & 0 \\ c_{13}^E & c_{13}^E & c_{33}^E & 0 & 0 & 0 \\ 0 & 0 & 0 & c_{44}^E & 0 & 0 \\ 0 & 0 & 0 & 0 & c_{44}^E & 0 \\ 0 & 0 & 0 & 0 & 0 & \frac{1}{2}(c_{11}^E - c_{12}^E) \end{bmatrix} \begin{Bmatrix} S_1 \\ S_2 \\ S_3 \\ S_4 \\ S_5 \\ S_6 \end{Bmatrix} + \begin{bmatrix} 0 & 0 & e_{31} \\ 0 & 0 & e_{31} \\ 0 & 0 & e_{33} \\ 0 & e_{15} & 0 \\ e_{15} & 0 & 0 \\ 0 & 0 & 0 \end{bmatrix} \begin{Bmatrix} E_1 \\ E_2 \\ E_3 \end{Bmatrix}$$

$$\begin{Bmatrix} D_1 \\ D_2 \\ D_3 \end{Bmatrix} = \begin{bmatrix} 0 & 0 & 0 & 0 & e_{15} & 0 \\ 0 & 0 & 0 & e_{15} & 0 & 0 \\ e_{31} & e_{31} & e_{33} & 0 & 0 & 0 \end{bmatrix} \begin{Bmatrix} S_1 \\ S_2 \\ S_3 \\ S_4 \\ S_5 \\ S_6 \end{Bmatrix} + \begin{bmatrix} \epsilon_{11}^S & 0 & 0 \\ 0 & \epsilon_{11}^S & 0 \\ 0 & 0 & \epsilon_{33}^S \end{bmatrix} \begin{Bmatrix} E_1 \\ E_2 \\ E_3 \end{Bmatrix} \tag{5.11}$$

5.2.2 The Strain-Displacement Relationship

After the constitutive relation which relates the stress to the strain fields have been developed, we will need to express the strains in terms of the displacements field. In terms of cylindrical coordinates, the strains to displacements relationship is given by,

$$\mathbf{S} = [\,\Xi\,]\,\{\mathbf{u}_{\boldsymbol{p}}\}$$

$$= \begin{bmatrix} \frac{\partial}{\partial \mathrm{r}} & -0 & -0 \\ \frac{1}{\mathrm{r}} & \frac{1}{r}\frac{\partial}{\partial \theta} & -0 \\ -0 & -0 & \frac{\partial}{\partial \mathrm{z}} \\ -0 & \frac{\partial}{\partial \mathrm{z}} & \frac{1}{r}\frac{\partial}{\partial \theta} \\ \frac{\partial}{\partial \mathrm{r}} & -0 & \frac{\partial}{\partial \mathrm{r}} \\ \frac{1}{r}\frac{\partial}{\partial \theta} & \frac{\partial}{\partial \mathrm{r}}\frac{1}{r} & -0 \end{bmatrix} \begin{Bmatrix} u \\ v \\ w \end{Bmatrix} \tag{5.12}$$

Whereby $\mathbf{u_p}\,(\mathrm{r}, \theta, \mathrm{t})$ refers to the displacements at any point P of the plate. According to Kirchhoff's Thin Plate Theory, it can be expressed in terms of the centerline gradient, midplane displacements $\mathbf{u_o}\,(\mathrm{r}, \theta, \mathrm{t})$, as well as the offset distance from the centerline Z_s.

$$\mathbf{u_p}\,(\mathrm{r}, \theta, \mathrm{t}) = [\,\Upsilon\,]\{\mathbf{u_o}\}$$

$$= \begin{bmatrix} -1 & -0 & -\mathrm{Z}_s\frac{\partial}{\partial \mathrm{r}} \\ -\frac{\mathrm{R}}{\mathrm{r}}\frac{\partial}{\partial \theta} & -1 & -\frac{Z_s}{r}\frac{\partial}{\partial \theta} \\ -0 & -0 & -1 \end{bmatrix} \begin{Bmatrix} u_0 \\ v_0 \\ w_0 \end{Bmatrix} \tag{5.13}$$

The mid plane deflections can be defined in terms of the superposition of several assumed modes which can be expressed as follows,

$$\{\mathbf{u_0}(r, \theta, t)\} = \Phi_m(r, \theta)\,\boldsymbol{\xi}(t)$$

$$= \begin{bmatrix} \phi_{u1}(r,\theta) & \cdots & \phi_{un}(r,\theta) \\ \phi_{v1}(r,\theta) & \cdots & \phi_{vn}(r,\theta) \\ \phi_{w1}(r,\theta) & \cdots & \phi_{wn}(r,\theta) \end{bmatrix} \begin{Bmatrix} \xi_1(t) \\ \vdots \\ \xi_n(t) \end{Bmatrix} \quad (5.14)$$

Where $\Phi_m(r,\theta)$ represents the assumed mechanical mode shapes while $\xi(t)$ is the mechanical modal amplitudes. The mechanical mode shapes are only dependent on the coordinates r and θ and are independent of time. Inserting equation (5.13) and (5.12) into (5.11) above, the strain–displacements relationship can be re-written as follows,

$$\mathbf{S} = [\,\Xi\,]\,[\,\Upsilon\,]\{\mathbf{u_o}\}$$

$$= [L_m]\{\mathbf{u_0}\} \quad (5.15)$$

Where $[L_m]$ is a mapping operator known as the Lazarus mapping operator which coverts assumed deflection shapes into assumed strain shapes. The partial derivative above is rather lengthy and is computed with the help of Matlab Symbolic toolbox functionality. We can re-write the above for easier manipulation later as,

$$\mathbf{S} = \mathbf{N_M}\,\boldsymbol{\xi}(t) \quad (5.16)$$

Where $\mathbf{N_M}$ is the mechanical strain matrix function,

$$\mathbf{N_M} = [\mathrm{L_m}]\Phi_m(r,\theta) \quad (5.17)$$

5.2.3 The Electric field and Voltage Relationship

Similarly, the electric potential $\varphi(\mathrm{r},\theta,\mathrm{t})$ within the piezoelectric layer can be defined using several assumed shapes as,

$$\varphi(\mathrm{r},\theta,\mathrm{t}) = [\Phi_{\mathrm{E}}(\mathrm{r},\theta)]\,\{\mathbf{V}(\mathrm{t})\}$$

$$= [\ \varphi_1(r,\theta), \dots\dots, \varphi_N(r,\theta)] \begin{Bmatrix} V_1(t) \\ \vdots \\ V_N(t) \end{Bmatrix} \tag{5.18}$$

Whereby $\Phi_E(r,\theta)$ and $V(t)$ refers to the matrix of electrical potential shape functions and externally applied voltage vector respectively. In our study, the stator is driven by two distinct electrode patterns separated spatially by a quarter of a wavelength. Thus, with such a configuration, only two assumed modes for the potential field description is necessary, N = 2. The electric field present within the piezoelectric layer can be expresses as such,

$$\mathbf{E}(r,\theta,t) = -\text{grad}\ \varphi(r,\theta,t) = [\ M\ ]\ \varphi(r,\theta,t) \tag{5.19}$$

The conversion of the assumed shapes of the potential at the electrodes $\varphi(r,\theta,t)$ to the electric field within the piezoelectric layer is performed via the operator matrix [M]. It is assumed that the electric field present within the layer is constant throughout; therefore, [M] can be defined as a function in terms of the thickness $t_P$of the piezoelectric layer.

$$[\ M\ ] = [\frac{1}{t_P}] \tag{5.20}$$

Substituting equation (5.18) into (5.19), we can express the relationship between the applied external voltage $V(t)$ and induced electric field $E(r,\theta,t)$ within as

$$\mathbf{E}(r,\theta,t) = -[\ \mathbf{N}_E\ ]\ \{\mathbf{V}(t)\} \tag{5.21}$$

Whereby $[\mathbf{N}_E]$ is the electrical mapping operator which reads,

$$[\ \mathbf{N}_E(r,\theta)] = [M]\ [\ \Phi_E(r,\theta)] \tag{5.22}$$

5.2.4 Governing Equation of Motion of Stator

With the above formulations, we can now derive the governing equation of motion for the stator. Substituting equation (5.14) into (5.3), the kinetic energy of the stator substrate can be re-written as

$$\frac{1}{2}\int_{V_S} \rho_S \dot{\mathbf{u}}_\mathbf{o}^\mathbf{t} \dot{\mathbf{u}}_\mathbf{o}\, dV = \frac{1}{2}\int_{V_S} \dot{\xi}^t \Phi_M^t \rho_S \Phi_M \dot{\xi}\, dV = \frac{1}{2}\dot{\xi}^t \mathbf{M}_S \dot{\xi} \tag{5.23}$$

With $\mathbf{M}_S$ being the modal mass matrix of the substrate,

$$\mathbf{M}_S = \frac{1}{2}\int_{V_S} \Phi_M^t \rho_S \Phi_M dV \tag{5.24}$$

In a similar manner, the kinetic energy and modal mass matrix of the piezoelectric layer can be expresses as follows,

$$\frac{1}{2}\int_{V_P} \rho_P \dot{\mathbf{u}}_\mathbf{o}^\mathbf{t} \dot{\mathbf{u}}_\mathbf{o}\, dV = \frac{1}{2}\int_{V_P} \dot{\xi}^t \Phi_M^t \rho_P \Phi_M \dot{\xi}\, dV = \frac{1}{2}\dot{\xi}^t \mathbf{M}_P \dot{\xi} \tag{5.25}$$

$$\mathbf{M}_P = \frac{1}{2}\int_{V_S} \Phi_M^t \rho_P \Phi_M dV \tag{5.26}$$

Combining equations (5.24) and (5.26) above, the total modal mass matrix of the stator is given as follows

$$\mathbf{M} \;\; = \mathbf{M}_S + \mathbf{M}_P \tag{5.27}$$

The total kinetic energy of the stator then becomes

$$E_K = \frac{1}{2}\dot{\xi}^t \mathbf{M}_S \dot{\xi} + \frac{1}{2}\dot{\xi}^t \mathbf{M}_P \dot{\xi} = \frac{1}{2}\dot{\xi}^t \mathbf{M} \;\; \dot{\xi} \tag{5.28}$$

Next, we will formulate the strain energy terms of the stator in a similar sense, substituting the constitutive relations developed earlier (5.8) and (5.10) into (5.3), we have the total potential energy of the stator,

$$E_P = \frac{1}{2}\int_{V_S} \mathbf{S}^t c_S \mathbf{S}\ dV + \frac{1}{2}\int_{V_P} \mathbf{S}^t(-e^t\mathbf{E} + c_P^E\mathbf{S})\ dV \tag{5.29}$$

Inserting equations (5.16) and (5.17) into the above, we have the strain energy within the substrate which is given by,

$$\frac{1}{2}\int_{V_S} \mathbf{S}^t c_S \mathbf{S}\ dV = +\frac{1}{2}\int_{V_S} \xi^t\, \mathbf{N}_M^t c_S \mathbf{N}_M\, \xi\ dV = \frac{1}{2}\xi^t\, \mathbf{K}_S\, \xi \tag{5.30}$$

With $\mathbf{K}_S$ being the modal stiffness matrix of the stator substrate which is as follows

$$\mathbf{K}_S = \frac{1}{2}\int_{V_S} \mathbf{N}_M^t c_S \mathbf{N}_M\ dV \tag{5.31}$$

In a parallel manner, the mechanical strain energy with the piezoelectric layer and its corresponding modal stiffness matrix can be expressed as,

$$\frac{1}{2}\int_{V_P} \mathbf{S}^t c_P^E \mathbf{S}\ dV = +\frac{1}{2}\int_{V_P} \xi^t\, \mathbf{N}_M^t c_P^E \mathbf{N}_M\, \xi\ dV = \frac{1}{2}\xi^t\, \mathbf{K}_P\, \xi \tag{5.32}$$

$$\mathbf{K}_P = \frac{1}{2}\int_{V_P} \mathbf{N}_M^t c_P^E \mathbf{N}_M\ dV \tag{5.33}$$

For the piezoelectric layer, an additional potential energy term needs to be defined. This potential energy arises due to the presence of the electromechanical coupling terms which appears in equation (5.29) and can be written as

$$\frac{1}{2}\int_{V_P} \mathbf{S}^t e^t\ \mathbf{E}\ dV = +\frac{1}{2}\int_{V_P} \xi^t\ \mathbf{N}_M^t e^t\ \mathbf{N}_E\ \nu\ dV = \frac{1}{2}\xi^t\ \Upsilon\ \boldsymbol{\nu} + \frac{1}{2}\eta^t \boldsymbol{\nu} \qquad (5.34)$$

With $\boldsymbol{\Upsilon}$ being the electromechanical coupling matrix which is,

$$\Upsilon = \frac{1}{2}\int_{V_P} \mathbf{N}_M^t e^t\ \mathbf{N}_E\ dV \qquad (5.35)$$

The total modal stiffness matrix of the stator is thus given by,

$$\mathbf{K} = \mathbf{K}_S + \mathbf{K}_P \qquad (5.36)$$

Combing equation (5.32), (5.34) and (5.36) above, we have the total potential energy of the stator which is express as,

$$E_P = \frac{1}{2}\xi^t\ \mathbf{K}\quad \xi - \frac{1}{2}\xi^t\ \Upsilon\ \boldsymbol{\nu} \qquad (5.37)$$

Next, the electrical energy terms will be formulated. We begin by inserting equation (5.10) into (5.4) to obtain the total electrical energy,

$$E_e = \frac{1}{2}\int_{V_P} \mathbf{E}^t(\ \varepsilon^S \mathbf{E} + e\mathbf{S})\ dV \qquad (5.38)$$

Again, after substituting equation (5.16), (5.21) and (5.38) into the above, we get electrical energy due to the piezoelectric electromechanical coupling terms,

$$\frac{1}{2}\int_{V_P} \mathbf{E}^t e\mathbf{S}\ dV = \frac{1}{2}\int_{V_P} \nu^t\ \mathbf{N}_E^t\ e\ \ \mathbf{N}_M\ \xi\quad dV = \frac{1}{2}\boldsymbol{\nu}^t\ \Upsilon^{\boldsymbol{t}}\ \xi \qquad (5.39)$$

The electrical energy within the piezoelectric layer due to the electrical permittivity of the material is given by,

$$\frac{1}{2}\int_{V_P} \mathbf{E}^t \varepsilon^S \mathbf{E}\ dV = \frac{1}{2}\int_{V_P} \nu^t\ \mathbf{N}_E^t\ \varepsilon^S\ \mathbf{N}_E\ \nu \quad dV = \frac{1}{2}\boldsymbol{\nu}^t\ C_P\ \boldsymbol{\nu} \tag{5.40}$$

Whereby C_P is the piezoelectric capacitance matrix which reads,

$$C_P = \frac{1}{2}\int_{V_P} \mathbf{N}_E^t\ \varepsilon^S\ \mathbf{N}_E\ dV \tag{5.41}$$

Therefore, combining equations (5.39) and (5.40) into (5.38), the total electrical energy is,

$$E_e = \frac{1}{2}\boldsymbol{\nu}^t\ C_P\ \boldsymbol{\nu} - \frac{1}{2}\nu^t\ \boldsymbol{\Upsilon}\ \xi \tag{5.42}$$

With all the energy terms defined, we are ready to substitute them into the Lagrangian equation (5.2) which gives us,

$$\mathcal{L} = \frac{1}{2}\dot{\xi}^t\ \mathbf{M}\ \ \dot{\xi} - \frac{1}{2}\xi^t\ \mathbf{K}\ \ \xi + \frac{1}{2}\xi^t\ \boldsymbol{\Upsilon}\ \nu + \frac{1}{2}\boldsymbol{\nu}^t\ C_P\ \boldsymbol{\nu} - \frac{1}{2}\nu^t\ \boldsymbol{\Upsilon}\ \xi \tag{5.43}$$

By performing a small variation on the Lagrangian and after some manipulation, we obtain the following,

$$\delta\mathcal{L} = \dot{\xi}^t\ \mathbf{M}\ \ \delta\dot{\xi} - \delta\xi^t\ \mathbf{K}\ \ \xi + \delta\xi^t\ \boldsymbol{\Upsilon}\ \boldsymbol{\nu} + \xi^t\ \boldsymbol{\Upsilon}\ \delta\boldsymbol{\nu} + \boldsymbol{\nu}^t\ C_P\delta\ \boldsymbol{\nu} \tag{5.44}$$

After performing integration by parts on the kinetic energy terms and some manipulation of the terms in variation of the Lagrangian, we have,

$$\delta\mathcal{L} = \frac{d}{dt}\left(\delta\xi^t\mathbf{M}\ \ \dot{\xi}\right) - \delta\xi^t\left(\mathbf{M}\ddot{\xi} + \mathbf{K}\,\xi - \boldsymbol{\Upsilon}\,\nu\right) + (\xi^t\,\boldsymbol{\Upsilon} + \boldsymbol{\nu}^t\,C_P)\delta\,\boldsymbol{\nu} \tag{4.45}$$

The final equation of motion governing the stator can be obtained by substituting equation (5.45) into (5.1) which after some manipulation reads,

$$\int_{t_1}^{t_2} \left[\frac{d}{dt}\left(\delta\xi^t \mathbf{M} \dot{\xi}\right) - \delta\xi^t \left(\mathbf{M}\ddot{\xi} + \mathbf{K}\xi - \Upsilon \boldsymbol{\nu}\right) + \left(\xi^t \Upsilon + \boldsymbol{\nu}^t C_P - q^t\right)\delta\boldsymbol{\nu} \right] dt = 0 \quad (5.46)$$

$\delta\xi$ and $\delta\boldsymbol{\nu}$ are arbitrary variations that are independent of each other. Two matrix equations of motions are obtained by allowing arbitrary variations of ξ andν; the actuator equation and the sensor equation. At the present moment, the forcing vectors due to the variational work terms caused by the interfacial forces are not included into the equation of motion. They will be derived separately in another section when we examine more closely the topological characteristics of both the stator and rotor surface domain boundaries. The sensor equation is not needed in the computation of the mechanical response of the system; however, they can provide us with information with regards the electrical dynamics of the stator subsystem.

Actuator equation

$$\mathbf{M}\ddot{\xi} + \mathbf{K}\xi - \Upsilon \boldsymbol{\nu} = 0 \quad (5.47)$$

Sensor equation

$$\Upsilon^t \xi + C_P \boldsymbol{\nu} = q \quad (5.48)$$

5.3 Kinematics of Stator and Rotor

5.3.1 Kinematics of Stator

In the previous section, the basic equation of motion of the stator subsystem has been derived. In this part of the thesis, we will introduce the external interfacial force terms into the equation of motion. These terms arise from the interactions between the stator and rotor surfaces upon physical contact. An energy approach will be adopted here whereby the variational work done by these forces are defined, followed by the derivation of the modal

forcing vectors after performing the variation. In order to determine the variational displacements and forces generated due to rotor-stator interpenetration, we need to first define the domains of the stator $\mathcal{B}_S$ and rotor $\mathcal{B}_R$ and their corresponding boundaries $\partial\mathcal{B}_S$ and $\partial\mathcal{B}_S$. By defining the topologies of both rotor and stator in mathematical terms we are able to determine the locations as well as the extend of intersection between both boundaries $\partial\mathcal{B}_S$ and $\partial\mathcal{B}_S$. The zones of contacting and non-contacting regions can be revealed and also, if contact does occur; the depth of penetration can be quantified. Figure 5.3 below shows a general schematic of the interactions between the stator and rotor.

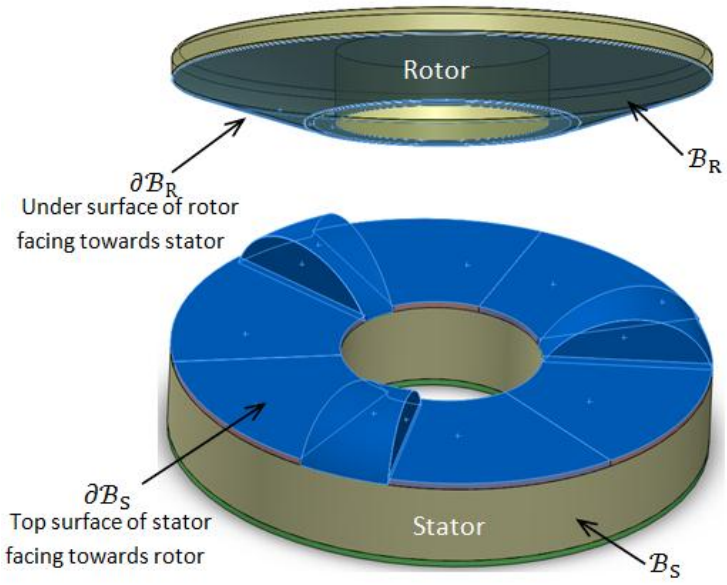

Figure 5.3: Domains and Boundaries of Stator and Rotor

The kinematics of the stator is such that it is assumed to be constrained from all gross rigid body motions. That is its center of mass does not possess any gross translations and rotational motions. The stator is allowed though to vibrate about an equilibrium configuration. This simplification is reasonably acceptable because the design of most stator construction involves the stator being held in place by fasteners onto another main frame that is relatively

stationary. As discussed in previously, the displacements of any point P on the stator $u_o^P(r,\theta,t)e$ is given by,

$$\mathbf{u_p}\,(r,\theta,t) = [\,\Upsilon\,]\{\mathbf{u_o}\}$$

$$= \begin{bmatrix} -1 & -0 & -z_s\dfrac{\partial}{\partial r} \\ -\dfrac{s}{r}\dfrac{\partial}{\partial\theta} & -1 & -\dfrac{z_s}{r}\dfrac{\partial}{\partial\theta} \\ -0 & -0 & -1 \end{bmatrix} \begin{Bmatrix} u_0 \\ v_0 \\ w_0 \end{Bmatrix} \qquad (5.49)$$

Where z_s is the offset distance of the point from the neutral midplane. The stator of most USMs generally will have structures attached onto its surfaces. The role of such structures is to amplify the vibrational stroke length as well as to remove away the wear particles from the contacting surfaces. In USM community, such structures are commonly referred to as stator teeth and their presence will greatly change the topology of the stator domain $\mathcal{B}_S$ and its boundaries $\partial\mathcal{B}_S$. For our purposes, we shall let the placement of the teeth on the stator be such that the surfaces S_{stator} of the teeth are describe by a surface function given by

$$Z_S(r,\theta) = \begin{cases} \mathcal{H}(r,\theta) & \text{for } n\theta_1 \le \theta < n\theta_2 \\ 0 & \text{otherwise} \end{cases} \qquad (5.50)$$

Whereby $Z_S(r,\theta)$ refers to the locus of z coordinates of the stator teeth surface S_{stator}. The condition $n\theta_1 \le \theta < n\theta_2$ is to distinguished teeth locations. In order to simplify the analysis here, the stator teeth are assumed to be rigid, massless and possess axis symmetricity in its placement along the circumferential direction of the stator. Such an assumption is reasonable because the rotor surface is usually being interposed with another layer of viscoelastic material for better grip and frictional characteristics. The stiffness of the stator material is significantly higher than that of the relatively compliant rotor layer. Figure 5.4 below illustrates such a configuration.

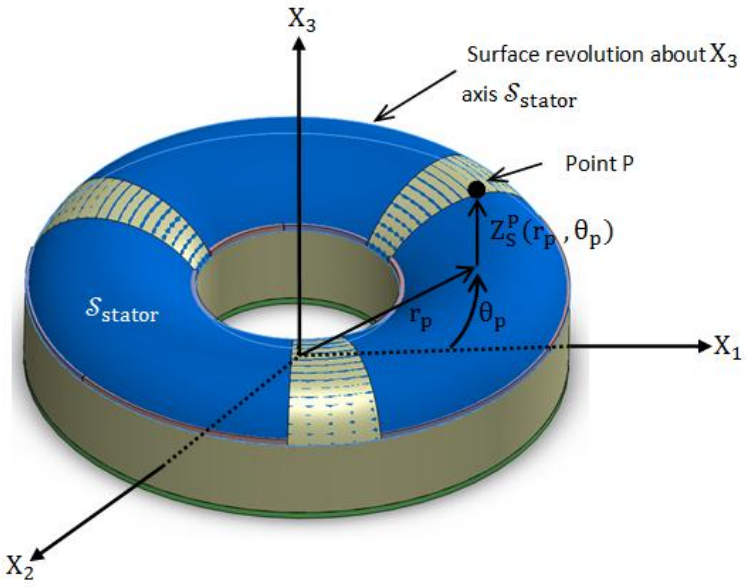

Figure 5.4: Stator surface description with teeth attached

From figure 5.4 above, it can be observed that the displacements kinematics of the stator is changed with the inclusion of the teeth structures. The varying teeth height supplies different moment arm amplification factor at different locations on the stator, it also modifies the final topological structure of the stator domain boundaries. Therefore, the displacements domain of any point P, lying on the stator teeth, is given by the inclusion of the of the fixed z height displacements brought into by the teeth itself as well as the change in the moment arm. After some manipulation, the expression reads,

$$\mathrm{U}^{\mathrm{P}}_{\text{stator domain}}(\mathrm{r},\theta,\mathrm{t}) = \mathrm{U}^{\mathrm{P}}_{\mathrm{SD}}(\mathrm{r},\theta,\mathrm{t}) = \{\,\mathbf{u}^{\mathrm{P}}_{\mathrm{o}*}(\mathrm{r},\theta,\mathrm{t})\} + \begin{Bmatrix} 0 \\ 0 \\ \mathrm{Z_S}(\mathrm{r},\theta) \end{Bmatrix}$$

$$= \begin{bmatrix} -1 & -0 & -\mathrm{Z_S}(\mathrm{r},\theta)\dfrac{\partial}{\partial \mathrm{r}} \\ -\dfrac{\mathrm{s}}{\mathrm{r}}\dfrac{\partial}{\partial\theta} & -1 & -\dfrac{\mathrm{Z_S}(\mathrm{r},\theta)}{r}\dfrac{\partial}{\partial\theta} \\ -0 & -0 & -1 \end{bmatrix} \begin{Bmatrix} u_0 \\ v_0 \\ w_0 \end{Bmatrix} + \begin{Bmatrix} 0 \\ 0 \\ \mathrm{Z_S}(\mathrm{r},\theta) \end{Bmatrix} \quad (5.51)$$

Correspondingly, the velocity components can also be expressed as follows,

$$\dot{U}_{SD}^{P}(r,\theta,t) = \{\, \dot{\mathbf{u}}_{o*}^{P}(r,\theta,t)\}$$

$$= \begin{bmatrix} -1 & -0 & -Z_S(r,\theta)\dfrac{\partial}{\partial r} \\ -\dfrac{s}{r}\dfrac{\partial}{\partial\theta} & -1 & -\dfrac{Z_S(r,\theta)}{r}\dfrac{\partial}{\partial\theta} \\ -0 & -0 & -1 \end{bmatrix} \begin{Bmatrix} \dot{u}_0 \\ \dot{v}_0 \\ \dot{w}_0 \end{Bmatrix} \quad (5.52)$$

From the above expressions, it can be seen that the offset distance z has been replaced with $Z_S(r,\theta)$ to indicate the greater moment arm due to teeth placement. It becomes a function of the r and θ, depending on the design constructs the stator teeth takes and is no longer a constant value.

5.3.2 Kinematics of Rotor

The displacement boundaries of the rotor will be considered next. Unlike the stator which remains at a fixed location, the mathematical descriptions for the rotor will be more involved due to the presence of rigid body motions. Translations and rotations of the rotor means that the domain boundaries $\partial\mathcal{B}_R$ is a function of these parameters and needs to be updated on each time step as these variables changes, this is similar to the shifting and rotations of a curve on a plane. Figure 5.5 below shows the general degrees of freedom of the rotor, the coordinate system and the definition of the rotor domain boundaries.

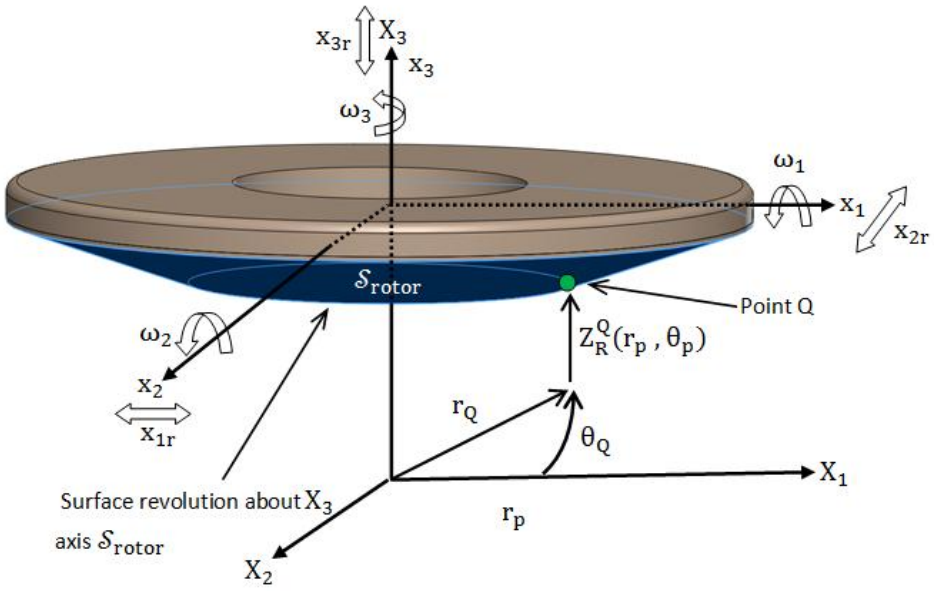

Figure 5.5: Rotor surface description and degrees of freedom

Similar to the approach adopted for the stator, the three dimensional surface of the rotor can be describe by a surface function given by

$$Z_R(r, \theta) = \mathcal{F}(r, \theta) \tag{5.53}$$

Whereby Z_R refers to the z coordinates of the locus of points of the rotor surface S_{Rotor}. To simplify analysis, the rotor surface is assumed to be axis-symmetric. A translational motion $\delta\mathbf{d}_{rotor}$ of the rotor center mass Cm_R equates to a shifting of the entire surface function in the three dimensional space. Since three dimensional motion is allowed and can be resolved into,

$$\delta\mathbf{d}_{rotor} = \delta x_{rotor}\mathbf{i} + \delta y_{rotor}\mathbf{j} + \delta z_{rotor}\mathbf{k} \tag{5.54}$$

Where δx_{rotor}, δy_{rotor} and δz_{rotor} refers to the displacements in the X_1, X_2 and X_3 axis respectively and **i**, **j** and **k** are units vectors in the respective directions. And radial displacements $\delta\mathbf{r}_{rotor}$ are related to Cartesian displacements by,

$$\|\delta r_{rotor}\|^2 = \|\delta x_{rotor} i\|^2 + \|\delta y_{rotor} j\|^2 \tag{5.55}$$

While axial displacements remains the same in both cylindrical and Cartesian coordinate systems, the new rotor surface S_{Rotor} subjected to a given translation displacement $\delta\mathbf{d}_{rotor}$ can be re-written and expressed as follows

$$Z_R(r,\theta) - \delta z_{rotor} = \mathcal{F}(r - \delta r_{rotor}, \theta - \delta\theta_{rotor})$$

$$= \mathcal{F}(r - \delta r_{rotor}, \theta - \delta\theta_{rotor}) + \delta z_{rotor)} \quad (5.56)$$

In the above equation, the rotor z height coordinates will be updated on each and every time step after the rotor translations are computed. Due to axis-symmetric conditions imposed earlier, $\delta\theta_{rotor}$ will not have any effects on the geometrical description and can be safely omitted. Figure 5.6 below illustrates the translation of the rotor surface in three dimensional space.

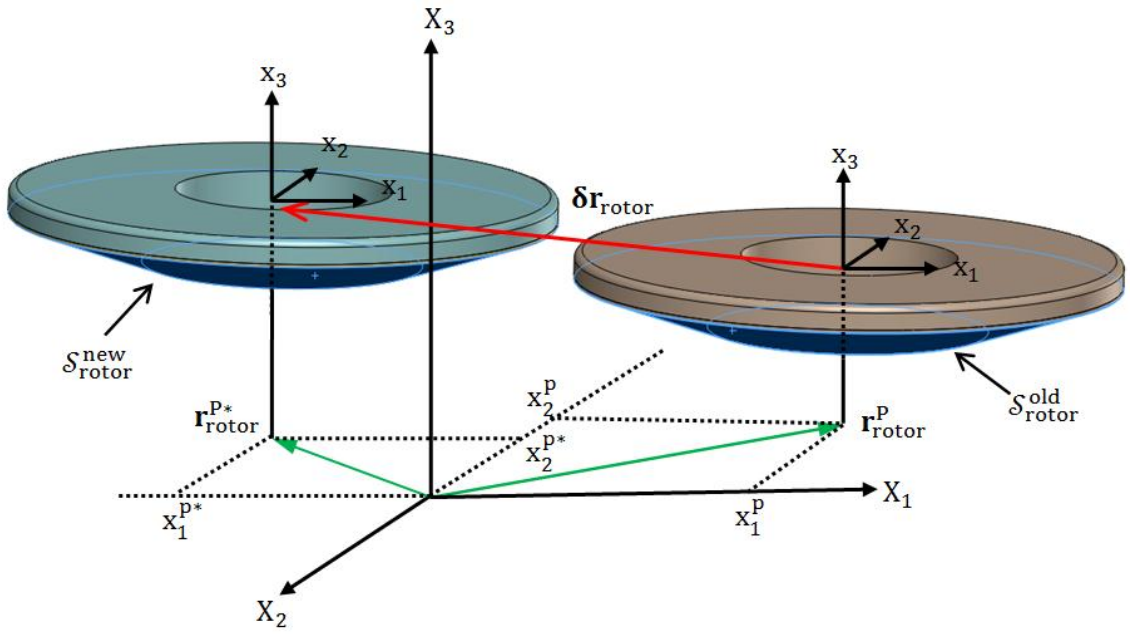

Figure 5.6: Translation of Rotor in 3 dimension space

The changes in the rotor surface boundaries caused by a rotational motion about the rotor center of mass Cm_R is a little more tricky in the sense that a straightforward representation

using a modified mathematical expression is not available. For our purposes, we will approach the problem by looking at the rotor surface S_{Rotor} as consisting of a locus of points Pr_i with coordinates given by $(r_{Pr}, \theta_{Pr}, Z_R(r_{Pr}, \theta_{Pr}))_i$. For a given position vector $\{\mathbf{r_1}\}$ at point P1 with coordinates (r_1, θ_1, z_1) , by application of a rotation matrix $\Re(\delta\psi, \delta\phi, \delta\kappa)$ to it, we will get another vector $\{\mathbf{r_2}\}$ at point P2 with coordinates (r_2, θ_2, z_2).This is equivalent to applying rotations of angles ψ, ϕ and κ about the X_1, X_2 and X_3 axis, respectively in that order, to the vector $\{\mathbf{r_1}\}$. This is illustrated in Figure 5.7 below.

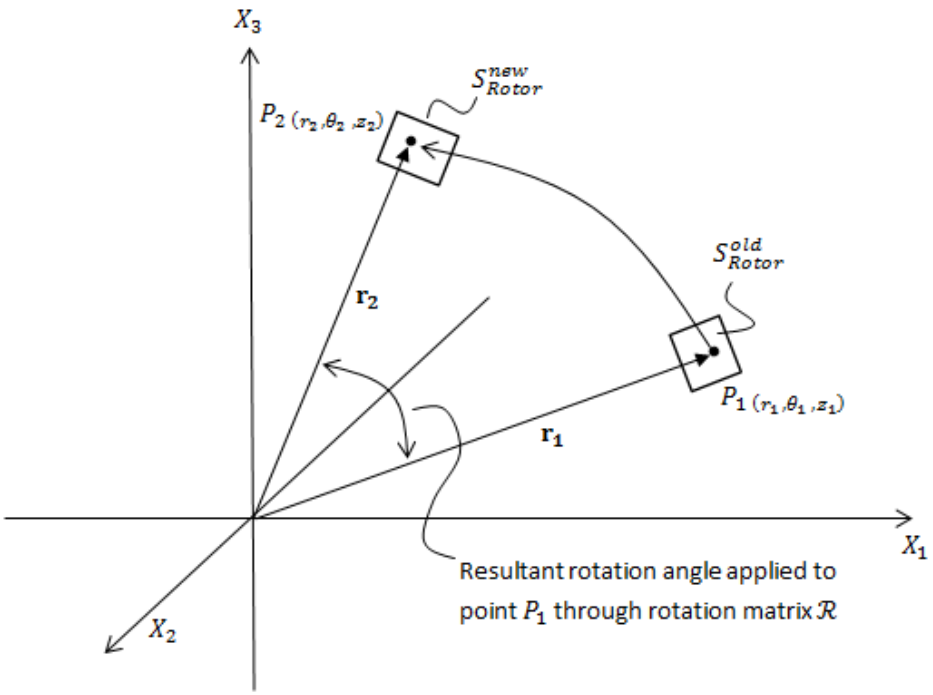

Figure 5.7: Arbitrary rotation of a given surface element of rotor surface from P1 to P2

Mathematically, the operation of rotating a given vector is given by,

$$\{\mathbf{r_1}\,(r_1, \theta_1, z_1)\} = \Re(\delta\psi, \delta\kappa, \delta\phi)\,\{\mathbf{r_2}\,(r_2, \theta_2, z_2)\} \qquad (5.57)$$

Whereby ψ, ϕ and κ refers to the three Euler angles about the X_1, X_2 and X_3 axis respectively. Finite rotations of a rigid body $(\Delta\psi, \Delta\kappa, \Delta\phi)$ are not commutative and the order

with which the rotations apply gives different final configuration. However, infinitesimal rotations can be treated to behave like vectors and hence is commutative. In our present study, we are invoking the vector like properties of infinitesimal rotations of the rotor and have formulated the rotation matrix as a single matrix. This assumption is valid since, firstly, the rotations $\delta\psi, \delta\kappa$ about the X_1, X_2 axis of a TRUM are usually of the order of milliradians or lower and secondly, rotations about the X_3 axis $\delta\kappa$ do not change the geometric configuration of an axis-symmetry structure. The full rotation matrix $\Re(\delta\psi, \delta\phi, \delta\kappa)$ can be expresses as

$$\Re(\delta\psi, \delta\kappa, \delta\phi) = \begin{bmatrix} \cos(\delta\phi)\cos(\delta\kappa) & -\cos(\delta\psi)\sin(\delta\kappa) + \sin(\delta\psi)\sin(\delta\phi)\cos(\delta\kappa) & \sin(\delta\psi)\sin(\delta\kappa) + \cos(\delta\psi)\sin(\delta\phi)\cos(\delta\kappa) \\ \cos(\delta\phi)\sin(\delta\kappa) & \cos(\delta\psi)\cos(\delta\kappa) - \sin(\delta\psi)\sin(\delta\phi)\sin(\delta\kappa) & -\sin(\delta\psi)\cos(\delta\kappa) + \cos(\delta\psi)\sin(\delta\phi)\sin(\delta\kappa) \\ -\sin(\delta\phi) & \sin(\delta\psi)\cos(\delta\phi) & \cos(\delta\psi)\cos(\delta\phi) \end{bmatrix} \tag{5.58}$$

Therefore, for a given point P_R located on the rotor surface S_{Rotor} having coordinates $(x_{Pr}, y_{Pr}, Z_R(r_{Pr}, \theta_{Pr}))$ with the corresponding position vector to that point being represented by the vector $\mathbf{r_P}$ $(x_{Pr}, y_{Pr}, Z_R(r_{Pr}, \theta_{Pr}))$. For a given infinitesimal rotation of the rotor represented by the rotation matrix $\Re(\delta\psi, \delta\kappa, \delta\phi)$, the final position of point P_R, denoted by $P_R{}^*$ having coordinates $(x_{Pr*}, y_{Pr*}, Z_{R*}(r_{Pr*}, \theta_{Pr*}))$ with the corresponding position vector $\mathbf{r_P^*}$ $(x_{Pr*}, y_{Pr*}, Z_{R*}(r_{Pr*}, \theta_{Pr*}))$ is given by the following,

$$\{\mathbf{r_P^*}\ (x_{Pr*}, y_{Pr*}, Z_{R*}(r_{Pr*}, \theta_{Pr*}))\} = [\Re(\delta\psi, \delta\kappa, \delta\phi)]\{\mathbf{r_P}\ (x_{Pr}, y_{Pr}, Z_R(r_{Pr}, \theta_{Pr}))\} \tag{5.59}$$

$$\begin{Bmatrix} x_{Pr*} \\ y_{Pr*} \\ Z_{R*}(r_{Pr*}, \theta_{Pr*}) \end{Bmatrix} = [\Re(\delta\psi, \delta\kappa, \delta\phi)] \begin{Bmatrix} x_{Pr} \\ y_{Pr} \\ Z_R(r_{Pr}, \theta_{Pr}) \end{Bmatrix} \tag{5.60}$$

Since the angular rotations about the X_1, X_2 axis are very small, $\delta\psi = \delta\phi \cong 0$, cosine and sine terms that corresponds to them becomes $\cos(\delta\psi) = \cos(\delta\phi) \cong 1$ and $\sin(\delta\psi) \cong \delta\psi$ and $\sin(\delta\phi) \cong \delta\phi$ respectively,

$$\begin{Bmatrix} x_{Pr*} \\ y_{Pr*} \\ Z_{R*}(r_{Pr*}, \theta_{Pr*}) \end{Bmatrix} = [\Re(\delta\psi, \delta\kappa, \delta\phi)] \begin{Bmatrix} x_{Pr} \\ y_{Pr} \\ Z_{R}(r_{Pr}, \theta_{Pr}) \end{Bmatrix} \quad (4.61)$$

The equation above gives us the final coordinates of rotor surface points after a rotation has been applied. Combining both translations and rotational effects onto the final configuration of the rotor can be achieved by substituting equation (5.56) into (5.61). This is analogous to rotating another surface function, albeit a shifted one, which is expressed below as follows,

$$\begin{Bmatrix} x_{Pr*} \\ y_{Pr*} \\ Z_{R*}(r_{Pr*}, \theta_{Pr*}) \end{Bmatrix}$$

$$= \left[[\Re(\delta\psi, \delta\kappa, \delta\phi)]\right] \begin{Bmatrix} x_{Pr} \\ y_{Pr} \\ \mathcal{F}(r - \delta r_{rotor}, \theta - \delta\theta_{rotor}) + \delta z_{rotor} \end{Bmatrix} \quad (5.62)$$

5.4 Work Performed By External Forces

5.4.1 Pressure Generated During Overlap

The boundaries of the stator and rotor domains were defined in the previous section. In this section, we will examine the interface between the stator and rotor when both domain boundaries meet. In the process of doing so, we can formulate the variational work terms performed during such interactions and hence arrived at the resultant modal force vectors that will appear in the equation of motion of the stator subsystem derived earlier. When the rotor and stator come into physical contact with each other, two types of interface forces will be produced. There will be a normal force acting along the perpendicular line normal to the plane of contact opposing the compression motion, and a tangential frictional force acting along the plane of interaction will be generated. Figure 5.8 below shows a schematic of such an interaction.

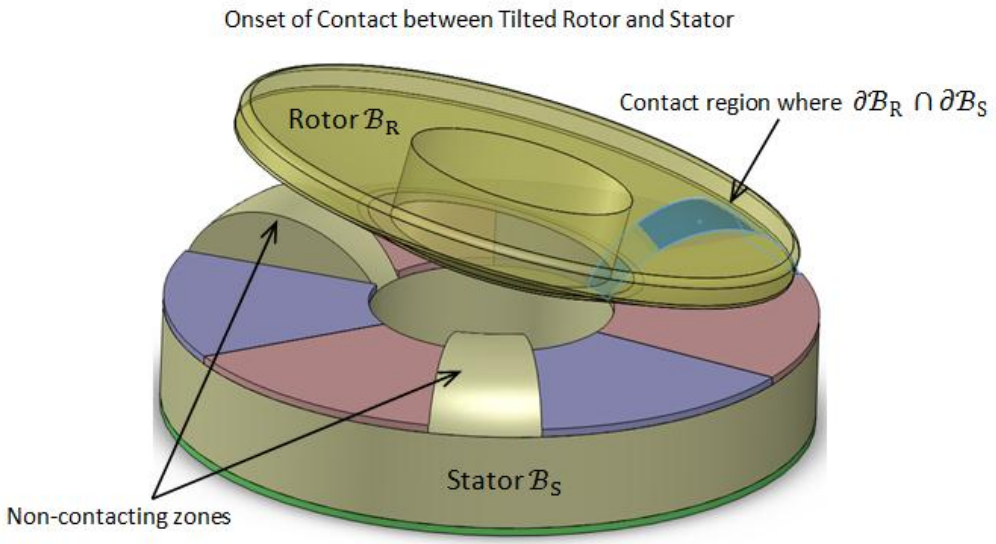

Figure 5.8: Rotor and Stator boundaries overlap

Physical contact and hence reaction forces are present only when the boundary domains of both the stator $\partial\mathcal{B}_S$ and rotor $\partial\mathcal{B}_R$ overlaps, otherwise, no contact occurs. Along the overlap regions, the stator is assumed to be rigid while the rotor is interposed with a thin layer of linear viscoelastic friction material. The degree of overlap between the rotor and stator and their relative velocities will determine the amount of reaction forces generated. Thus, the pressure $P(r, \theta, t)$ that is generated on the surfaces during such interactions can be expressed as follows,

$$P(r,\theta,t) = \begin{cases} k_R g_N + \mu_V \dot{g}_N \text{ when } \partial\mathcal{B}_S \cap \partial\mathcal{B}_R \\ 0 \qquad \text{otherwise} \end{cases} \tag{5.63}$$

$$g_N(\hat{X}_R^*, \hat{X}_S^*, t) = \left|\mathbf{r_R}(\hat{X}_R^*, t) - \mathbf{r_s}(\hat{X}_S^*, t)\right| \cdot \tilde{\mathbf{n}}^* \quad \text{for regions where } \partial\mathcal{B}_S \cap \partial\mathcal{B}_R$$

Where k_R and μ_V is the Young's modulus and viscosity coefficient of the material of the friction layer respectively. To simplify the analysis, the velocity dependent characteristics of the friction layer will not be considered here and that the friction layer shall be treated as a series of linear elastic springs. $g_N(\hat{X}_R^*, \hat{X}_S^*, t)$ is the gap function which gives us the degree of

interpenetration between surface points of the stator and rotor. Its value depends on the vector magnitude formed by the difference of the position vectors of the rotor $\mathbf{r_R}(\hat{X}_R^*, t)$ and stator $\mathbf{r_s}(\hat{X}_S^*, t)$ at overlapping the pair of nodal locations point P and Q. The gap function and its computation will be delved at in more details in a separate section when we look at the contact formulation. The pressure generated on the surfaces is a non-linear function which depends on the presence or absence of contact among different regions. It varies in a temporal manner due to the travelling wave on the stator and the dynamical interactions with the rotor.

5.4.2 Sign Function

Before defining the tangential and normal work terms, we need to further introduce another non-linear function which is the sign function $\text{Sign}^P(r, \theta, t)$. This function arises because of the directional dependence of frictional forces on relative velocities between rotor and stator surface points. In order to analyze the complex three dimensional velocities meaningfully, we will have to distinguish and resolve the velocity vector into components that relate to the physical configuration of the rotor-stator interface. One such choice of resolving the velocity is to use the interface tangential plane as a reference. This is because by using such a plane as the basis of our coordinate system, it allows us to differentiate the velocity components into those that contribute directly to driving up the rotor and those that serve to dissipate the energy from the system. Referring to Figure 5.9 and Figure 5.10 below, it can be seen that the circumferential velocity component V_{T2} serves to drives up or slows down the rotor, while the tangential velocity components V_{T1} and normal V_N are energy dissipating.

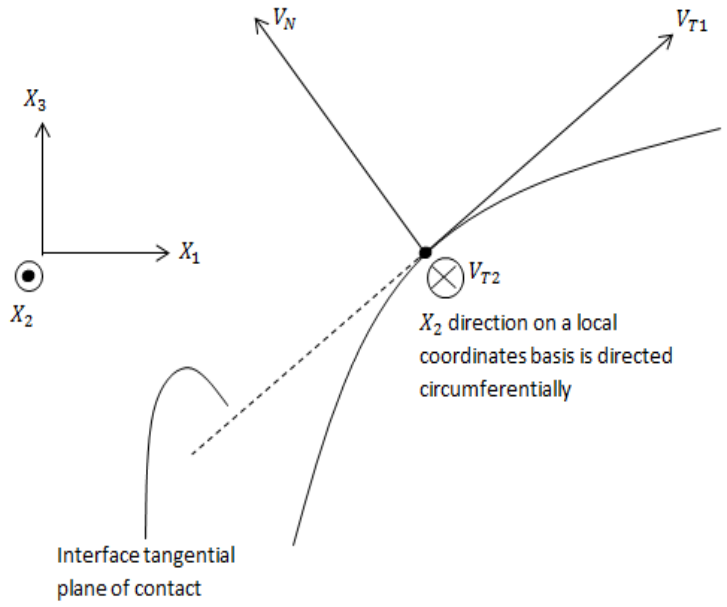

Figure 5.9: Resolving velocity components along tangent interface plane

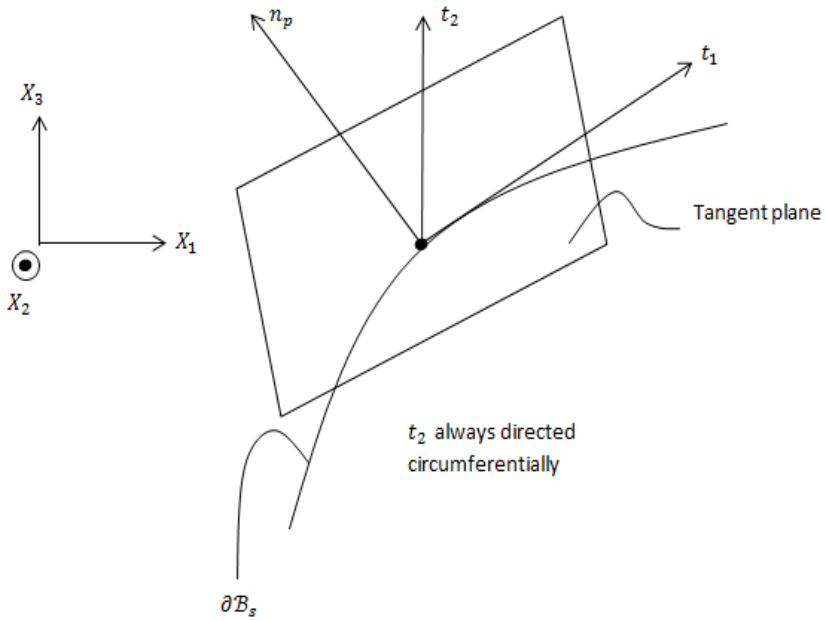

Figure 5.10: Tangent velocity component V_{T2} directed circumferentially.

The velocity at any point P on the rotor V^P is given by the sum of the velocity at its center of mass v_{CM} and the cross product of its angular velocity ω_R with the position vector to point P r_P.

$$\mathbf{V}^{\mathrm{P}}(r,\theta,t) = \mathbf{v}_{\mathrm{CM}}(r,\theta,t) + \boldsymbol{\omega}_{\mathrm{R}} \times \mathbf{r}_{\mathrm{P}} \tag{5.64}$$

To resolve $\mathbf{V}^P$ about the directions along the reference plane normal $\mathbf{n_p}$ and tangential directions $\mathbf{t_1}$ and $\mathbf{t_2}$ respectively, we take the dot products of the vectors respectively as follows,

$$V_N^P(r,\theta,t) = \{\mathbf{v}_{\mathrm{CM}}(r,\theta,t) + \boldsymbol{\omega}_{\mathrm{R}} \times \mathbf{r}_{\mathrm{P}}\} \cdot \mathbf{n_p} \tag{5.65}$$

$$V_{T1}^P(r,\theta,t) = \{\mathbf{v}_{\mathrm{CM}}(r,\theta,t) + \boldsymbol{\omega}_{\mathrm{R}} \times \mathbf{r}_{\mathrm{P}}\} \cdot \mathbf{t_1} \tag{5.66}$$

$$V_{T2}^P(r,\theta,t) = \{\mathbf{v}_{\mathrm{CM}}(r,\theta,t) + \boldsymbol{\omega}_{\mathrm{R}} \times \mathbf{r}_{\mathrm{P}}\} \cdot \mathbf{t_2} \tag{5.67}$$

For corresponding points P on the stator, the velocity can also be obtained accordingly using equation (5.52) and taking their derivative. In a similar sense, we can resolve the velocity vectors into the directions along the reference plane normal n_p and tangential directions t_1 and t_2 , we take the dot products of the vectors respectively as follows,

$$V_N^S = \dot{\mathbf{U}}_{\mathrm{SD}}^{\mathrm{P}}(r,\theta,t) \cdot \mathbf{n_p} \tag{5.68}$$

$$V_{T1}^S = \dot{\mathbf{U}}_{\mathrm{SD}}^{\mathrm{P}}(r,\theta,t) \cdot \mathbf{t_1} \tag{5.69}$$

$$V_{T2}^S = \dot{\mathbf{U}}_{\mathrm{SD}}^{\mathrm{P}}(r,\theta,t) \cdot \mathbf{t_2} \tag{5.70}$$

The normal $\mathbf{n_p}$ and tangential unit vectors $\mathbf{t_1}$ and $\mathbf{t_2}$ along the reference planes will be discussed in more details in another section when we are looking at the contact detection nd between the rotor and stator.

After the respective velocity components have been defined, we are now able to formulate the behavior of the sign function $\mathrm{Sign}^{\mathrm{P}}(\mathrm{r},\theta,\mathrm{t})$ which depends on the relative velocities of both stator and rotor surface points. Since there are three sets of velocity components in the normal $\mathbf{n}_{\mathrm{p}}$ and tangential directions $\mathbf{t_1}$ and $\mathbf{t_2}$, we have three distinct sign functions corresponding to them respectively as $\mathrm{Sign}_{\mathrm{N}}^{\mathrm{P}}(\mathrm{r},\theta,\mathrm{t})$, $\mathrm{Sign}_{\mathrm{T1}}^{\mathrm{P}}(\mathrm{r},\theta,\mathrm{t})$ and $\mathrm{Sign}_{\mathrm{T2}}^{\mathrm{P}}(\mathrm{r},\theta,\mathrm{t})$. The behavior of the sign functions are given as follows,

$$\mathrm{Sign}_{\mathrm{N}}^{\mathrm{P}}(\mathrm{r},\theta,\mathrm{t}) = \begin{cases} \text{when } \mathrm{V}^{\mathrm{P}} > 0 \\ -1 \text{ if } \ \mathrm{V}_{\mathrm{N}}^{\mathrm{P}}(\mathrm{r},\theta,\mathrm{t}) > \mathrm{V}_{\mathrm{N}}^{\mathrm{S}}(\mathrm{r},\theta,\mathrm{t}) \\ +1 \text{ if } \ \mathrm{V}_{\mathrm{N}}^{\mathrm{P}}(\mathrm{r},\theta,\mathrm{t}) < \mathrm{V}_{\mathrm{N}}^{\mathrm{S}}(\mathrm{r},\theta,\mathrm{t}) \\ 0 \text{ if } \ \mathrm{V}_{\mathrm{N}}^{\mathrm{P}}(\mathrm{r},\theta,\mathrm{t}) = \mathrm{V}_{\mathrm{N}}^{\mathrm{S}}(\mathrm{r},\theta,\mathrm{t}) \\ \\ \text{when } \mathrm{V}^{\mathrm{P}} < 0 \\ -1 \text{ if } \ \mathrm{V}_{\mathrm{N}}^{\mathrm{P}}(\mathrm{r},\theta,\mathrm{t}) > \mathrm{V}_{\mathrm{N}}^{\mathrm{S}}(\mathrm{r},\theta,\mathrm{t}) \\ +1 \text{ if } \ \mathrm{V}_{\mathrm{N}}^{\mathrm{P}}(\mathrm{r},\theta,\mathrm{t}) < \mathrm{V}_{\mathrm{N}}^{\mathrm{S}}(\mathrm{r},\theta,\mathrm{t}) \\ 0 \text{ if } \ \mathrm{V}_{\mathrm{N}}^{\mathrm{P}}(\mathrm{r},\theta,\mathrm{t}) = \mathrm{V}_{\mathrm{N}}^{\mathrm{S}}(\mathrm{r},\theta,\mathrm{t}) \\ \\ \text{when } \mathrm{V}^{\mathrm{P}} = 0 \\ +1 \text{ if } \ \mathrm{V}_{\mathrm{N}}^{\mathrm{S}}(\mathrm{r},\theta,\mathrm{t}) > 0 \\ -1 \text{ if } \ \mathrm{V}_{\mathrm{N}}^{\mathrm{S}}(\mathrm{r},\theta,\mathrm{t}) < 0 \\ 0 \text{ if } \ \mathrm{V}_{\mathrm{N}}^{\mathrm{P}}(\mathrm{r},\theta,\mathrm{t}) = \mathrm{V}_{\mathrm{N}}^{\mathrm{S}}(\mathrm{r},\theta,\mathrm{t}) \end{cases} \tag{5.71}$$

$$\mathrm{Sign}_{\mathrm{T1}}^{\mathrm{P}}(\mathrm{r},\theta,\mathrm{t}) = \begin{cases} \text{when } \mathrm{V}^{\mathrm{P}} > 0 \\ -1 \text{ if } \ \mathrm{V}_{\mathrm{T1}}^{\mathrm{P}}(\mathrm{r},\theta,\mathrm{t}) > \mathrm{V}_{\mathrm{T1}}^{\mathrm{S}}(\mathrm{r},\theta,\mathrm{t}) \\ +1 \text{ if } \ \mathrm{V}_{\mathrm{T1}}^{\mathrm{P}}(\mathrm{r},\theta,\mathrm{t}) < \mathrm{V}_{\mathrm{T1}}^{\mathrm{S}}(\mathrm{r},\theta,\mathrm{t}) \\ 0 \text{ if } \ \mathrm{V}_{\mathrm{T1}}^{\mathrm{P}}(\mathrm{r},\theta,\mathrm{t}) = \mathrm{V}_{\mathrm{T1}}^{\mathrm{S}}(\mathrm{r},\theta,\mathrm{t}) \\ \\ \text{when } \mathrm{V}^{\mathrm{P}} < 0 \\ -1 \text{ if } \ \mathrm{V}_{\mathrm{T1}}^{\mathrm{P}}(\mathrm{r},\theta,\mathrm{t}) > \mathrm{V}_{\mathrm{T1}}^{\mathrm{S}}(\mathrm{r},\theta,\mathrm{t}) \\ +1 \text{ if } \ \mathrm{V}_{\mathrm{T1}}^{\mathrm{P}}(\mathrm{r},\theta,\mathrm{t}) < \mathrm{V}_{\mathrm{T1}}^{\mathrm{S}}(\mathrm{r},\theta,\mathrm{t}) \\ 0 \text{ if } \ \mathrm{V}_{\mathrm{T1}}^{\mathrm{P}}(\mathrm{r},\theta,\mathrm{t}) = \mathrm{V}_{\mathrm{T1}}^{\mathrm{S}}(\mathrm{r},\theta,\mathrm{t}) \\ \\ \text{when } \mathrm{V}^{\mathrm{P}} = 0 \\ +1 \text{ if } \ \mathrm{V}_{\mathrm{T1}}^{\mathrm{S}}(\mathrm{r},\theta,\mathrm{t}) > 0 \\ -1 \text{ if } \ \mathrm{V}_{\mathrm{T1}}^{\mathrm{P}}(\mathrm{r},\theta,\mathrm{t}) < 0 \\ 0 \text{ if } \ \mathrm{V}_{\mathrm{T1}}^{\mathrm{P}}(\mathrm{r},\theta,\mathrm{t}) = \mathrm{V}_{\mathrm{T1}}^{\mathrm{S}}(\mathrm{r},\theta,\mathrm{t}) \end{cases} \tag{5.72}$$

$$\mathrm{Sign}_{T2}^{P}(r,\theta,t)=\begin{cases}\text{when } V^{P}>0\\ -1 \text{ if } \ V_{T2}^{P}(r,\theta,t)>V_{T2}^{S}(r,\theta,t)\\ +1 \text{ if } \ V_{T2}^{P}(r,\theta,t)<V_{T2}^{S}(r,\theta,t)\\ 0 \text{ if } \ V_{T2}^{P}(r,\theta,t)=V_{T2}^{S}(r,\theta,t)\\ \\ \text{when } V^{P}<0\\ -1 \text{ if } \ V_{T2}^{P}(r,\theta,t)>V_{T2}^{S}(r,\theta,t)\\ +1 \text{ if } \ V_{T2}^{P}(r,\theta,t)<V_{T2}^{S}(r,\theta,t)\\ 0 \text{ if } \ V_{T2}^{P}(r,\theta,t)=V_{T2}^{S}(r,\theta,t)\\ \\ \text{when } V^{P}=0\\ +1 \text{ if } \ V_{T2}^{S}(r,\theta,t)>0\\ -1 \text{ if } \ V_{T2}^{S}(r,\theta,t)<0\\ 0 \text{ if } V_{T2}^{P}(r,\theta,t)=V_{T2}^{S}(r,\theta,t)\end{cases} \tag{5.73}$$

The physical description of the above three sets of equations are straightforward. It means whenever the stator speed is relatively faster than the rotor speed, it will pull it in its direction and conversely, if the stator speed is lower relatively, it will have a dragging effect.

5.4.3 Variational Work Performed

After the pressure function $P(r,\theta,t)$ and sign functions $\mathrm{Sign}^{P}(r,\theta,t)$ have been defined, the variational work terms can be formulated. Again, as in the previous part, there are three variational work terms in the normal $\mathbf{n_p}$ and tangential directions $\mathbf{t_1}$ and $\mathbf{t_2}$ respectively. Figure 5.11 below shows a schematic of the displacements on a stator surface point P, depending of the location of the contacting region configuration; reference planes with different angular orientations θ_p are formed.

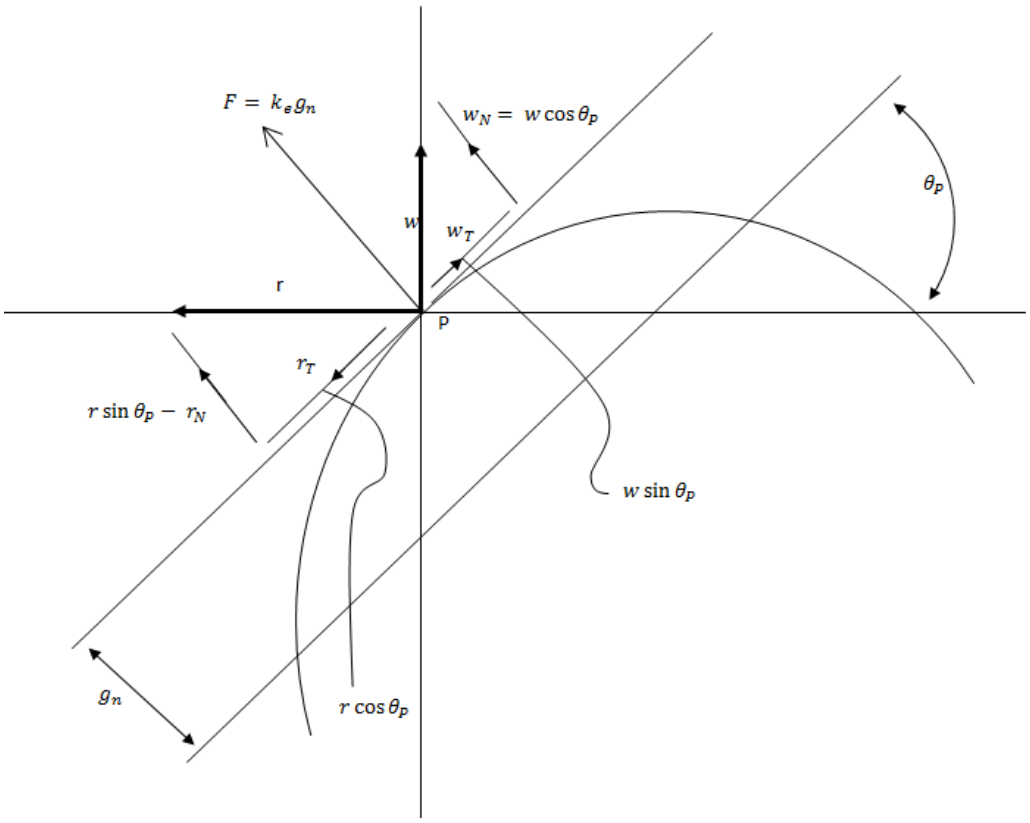

Figure 5.11: Axial (w) and radial (r) displacements resolved along tangential plane

Resolving the displacements components into the respective directions, we have for the variational normal work term δW_n which is defined as the product of the variational normal displacements δn_p with the interface pressure $P(r,\theta,t)$ integrated over the area of contact $\mathcal{A}_c$ and can be expressed as follows,

$$\delta W_n = -\delta\boldsymbol{\xi}^t \iint_{\mathcal{A}_c} r\, P(r,\theta,t)\left\{\cos(\theta_P)\boldsymbol{\Phi}_w^t - \sin(\theta_P)\left[\boldsymbol{\Phi}_v^t + Z_S^P(r,\theta,)\frac{\partial\boldsymbol{\Phi}_w^t}{\partial\theta}\right]\right\} drd\theta \quad (5.74)$$

Similarly, the variational tangential work terms are defined as the product of the interface pressure, coefficient of friction, the Sign function and the variational tangential deflection and a friction angle factor integrated over the area of contact. The friction angle factor was pointed out by Zhao [67] who notes that the frictional forces that arises on the tangential

plane does not necessarily lies along the driving circumferential direction and consists of 2 components. This is illustrated in Figure 5.12 below.

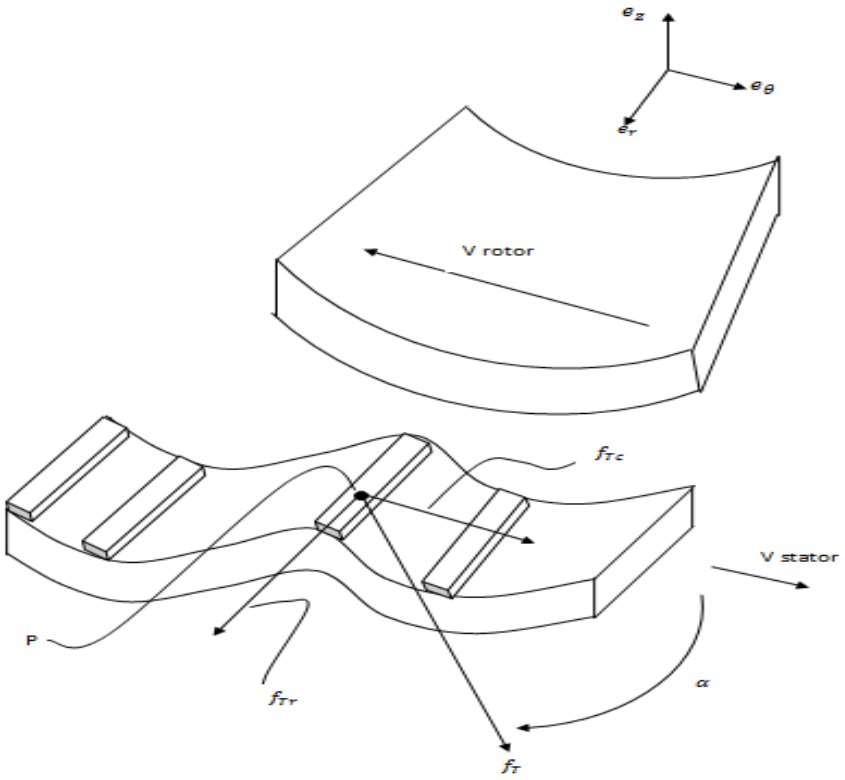

Figure 5.12: Friction angle formed between radial and circumferential directions

The frictional forces in the radial and circumferential direction can thus be resolve into two components which are given by

$$f_{TC} = |\mathbf{f_T} \cos\alpha| \tag{5.75}$$

$$f_{Tr} = |\mathbf{f_T} \sin\alpha| \tag{5.76}$$

Whereby the friction angle is given by the ratio of the speed differences magnitude in both directions relative to the circumferential rotor velocity,

$$|\tan\alpha| = \frac{\left|V_{T1}^{S} - \mathrm{V}_{\mathrm{T1}}^{\mathrm{P}}\right|}{\left|V_{T2}^{S} - \mathrm{V}_{\mathrm{T2}}^{\mathrm{P}}\right|} \tag{5.77}$$

The variational tangential work thus can be expressed as,

$$\delta W_{t1} = \delta \boldsymbol{\xi}^{\mathbf{t}} \mu \iint_{\mathcal{A}_c} r \sin\alpha \, P(r,\theta,t) \; Sign_{t1}^{P}(r,\theta,t) \left\{ \boldsymbol{\Phi}_{\mathbf{v}}^{\mathbf{t}} - \frac{Z_S^P(r,\theta,)}{r} \frac{\partial \boldsymbol{\Phi}_{\mathbf{w}}^{\mathbf{t}}}{\partial \theta} - \frac{R_S^P(r,\theta,)}{r} \frac{\partial \boldsymbol{\Phi}_{\mathbf{u}}^{\mathbf{t}}}{\partial \theta} \right\} dr d\theta \quad (5.78)$$

$$\delta W_{t2} = \delta \boldsymbol{\xi}^{\mathbf{t}} \mu \iint_{\mathcal{A}_c} r \cos\alpha \, P(r,\theta,t) \; Sign_{t2}^{P}(r,\theta,t) \left\{ \sin(\theta_P) \boldsymbol{\Phi}_{\mathbf{w}}^{\mathbf{t}} + \cos(\theta_P) \boldsymbol{\Phi}_{\mathbf{v}}^{\mathbf{t}} - Z_S^P(r,\theta,) \frac{\partial \boldsymbol{\Phi}_{\mathbf{w}}^{\mathbf{t}}}{\partial \theta} \cos(\theta_P) \right\} dr d\theta \quad (5.79)$$

After the calculus of variation is performed on the above equations, we obtained the resultant forcing vectors given below as,

$$\mathbf{F_n} = - \iint_{\mathcal{A}_c} r \, P(r,\theta,t) \left\{ \cos(\theta_P) \boldsymbol{\Phi}_{\mathbf{w}}^{\mathbf{t}} - \sin(\theta_P) \left[\boldsymbol{\Phi}_{\mathbf{v}}^{\mathbf{t}} + Z_S^P(r,\theta,) \frac{\partial \boldsymbol{\Phi}_{\mathbf{w}}^{\mathbf{t}}}{\partial \theta} \right] \right\} dr d\theta \quad (5.80)$$

$$\mathbf{F_{t1}} = \mu \iint_{\mathcal{A}_c} r \sin\alpha \, P(r,\theta,t) \; Sign_{t1}^{P}(r,\theta,t) \left\{ \boldsymbol{\Phi}_{\mathbf{v}}^{\mathbf{t}} - \frac{Z_S^P(r,\theta,)}{r} \frac{\partial \boldsymbol{\Phi}_{\mathbf{w}}^{\mathbf{t}}}{\partial \theta} - \frac{R_S^P(r,\theta,)}{r} \frac{\partial \boldsymbol{\Phi}_{\mathbf{u}}^{\mathbf{t}}}{\partial \theta} \right\} dr d\theta \quad (5.81)$$

$$\mathbf{F_{t2}} = \mu \iint_{\mathcal{A}_c} r \cos\alpha \, P(r,\theta,t) \; Sign_{t2}^{P}(r,\theta,t) \left\{ \sin(\theta_P) \boldsymbol{\Phi}_{\mathbf{w}}^{\mathbf{t}} + \cos(\theta_P) \boldsymbol{\Phi}_{\mathbf{v}}^{\mathbf{t}} - Z_S^P(r,\theta,) \frac{\partial \boldsymbol{\Phi}_{\mathbf{w}}^{\mathbf{t}}}{\partial \theta} \cos(\theta_P) \right\} dr d\theta \quad (5.82)$$

Combining the stator governing equation of motion derived earlier with (5.80), (5.81) and (5.82) above, the overall equation of motion for the stator subsystem is therefore given by,

$$\mathbf{M}\ddot{\xi} + \mathbf{C}\dot{\xi} + \mathbf{K}\xi = \gamma\mathbf{v} + \mathbf{F_n}(\xi, g_N) + \mathbf{F_{t1}}(\xi, \dot{\xi}, g_N) + \mathbf{F_{t2}}(\xi, \dot{\xi}, g_N) \qquad (5.83)$$

5.5 Contact Formulation

5.5.1 Contact Approach

In the previous sections, the topologies describing the domains of the stator and rotor have been defined. The objective of this section is to extend the previous formulation further by taking into account of the situation when both domains overlap and contact occurs. Therefore, contact kinematic quantities such as the gap function between two surface points is needed to describe it. Also, a numerical search algorithm will be required to keep track of contact states which switch from contact to non-contact in a time evolutionary sense.

There are numerous contact models available in the literature and depending on the modelling objective different models and formulations applies. According to Sattel [8], a continuum based approach for the formulation is most appropriate for the TRUM which we are studying since we are more interested in the study of the motor dynamics phenomenon. The approach places more emphasis on the geometrical deformation effects experienced by the stator and the contact layer instead of an involved description of the underlying stress-strain fields' distribution Wrigglers [68]. Moreover, the method does allow for conformal contact and is generic enough for extensions into study of motors or various designs.

For the contact model, a simple non-penetration condition serves as the constraint conditions during normal contact while COULOMB's law with stick-slip transitions is employed to describe the tangential contact. The actual contact phenomena present in USMs are

necessarily more complicated and sophisticated contact models are available to study them. For example, in the cases involving high pressure and large deformation contact there are non-linear penetration laws to describe it Oden and Martins [69]. However, we will not be employing such theories here simply because USMs contact pressure are usually small relatively when compared to what is considered above. There are also other possible frictional mechanisms at work in the contact interface as reported by Maeno and Bogy [70] which will not be considered in this thesis. Maeno [18] reported the possibility of hydrodynamic bearing effects present due to the high frequency motion of surface particles and small air gap between stator and rotor surfaces, while Rehbein and Wallaschek [17] proposed that micro impacts with surface asperities modifies the coefficient of friction. Geometrically, the surface roughness also factor into motor performance very strongly as reported in the experiments by Flynn [56] and Endo and Sasaki [16]. The peak height of the surface roughness should not be higher than the stator vibration amplitude lest it "buries" it which results in the physical contact between the valleys of the wave. Motor performance can deteriorated seriously in such instances as the wave valleys moves in the opposite direction to the wave crests. Recalling the previous section, it can be seen that this aspect of the contact behaviour also cannot be captured in the analytical model as smooth and continuous surface curves are use in the surface description.

5.5.2 Gap Function

For the discussion that follows, all variables that apply to surface points on the stator and rotor will be denoted by a hat symbol ($\hat{\cdot}$) while those surface points that are in contact are additionally denoted with an asterisk sign $(\hat{\cdot})^*$. Figure 5.13 below illustrate a typical configuration of contacting state between a portion of the surface of the rotor and stator.

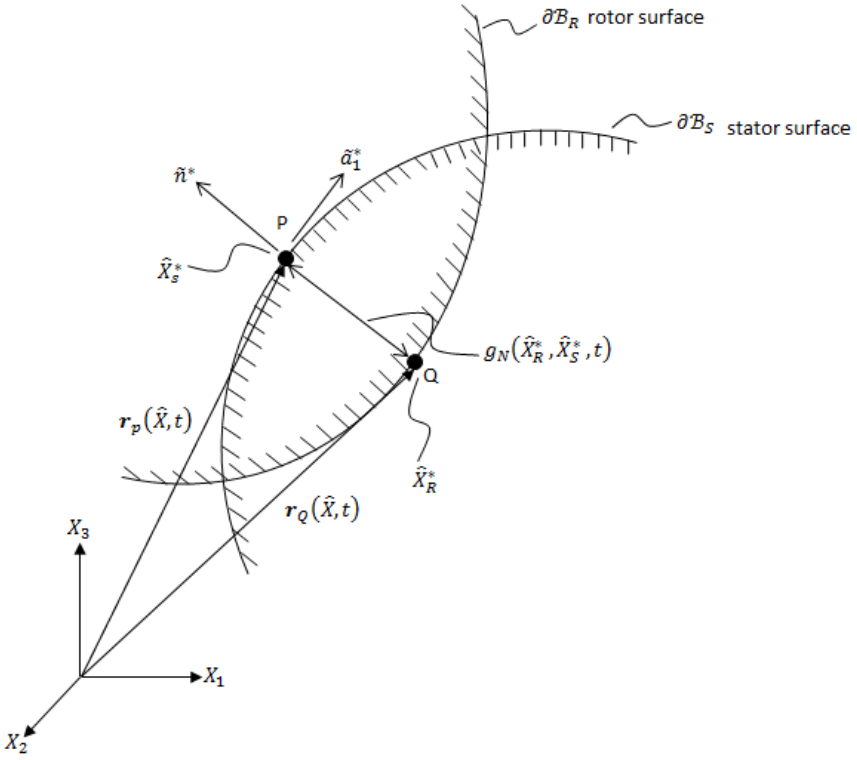

Figure 5.13: General Schematic of contact and gap function

Points P and Q constitute a set of contact pair on the stator and rotor respectively. During contact, for each material point P on the stator $\widehat{\mathrm{X}}_{\mathrm{S}}^{*}$ there corresponds another surface point Q on the rotor $\widehat{\mathrm{X}}_{\mathrm{R}}^{*}$ which can be determined by minimising the distance function $d(\widehat{\mathrm{X}}_{\mathrm{S}}^{*}, \widehat{\mathrm{X}}_{\mathrm{S}}^{*}, \mathrm{t})$, between surface points given below by

$$d\left(\widehat{\mathrm{X}}_{\mathrm{S}}^{*}, \widehat{\mathrm{X}}_{\mathrm{R}}^{*}, \mathrm{t}\right) = \min_{\widehat{\mathrm{X}}_{\mathrm{S}}^{*} \in \partial\mathcal{B}_{\mathrm{S}}} \left\| \mathbf{r}_{\mathrm{r}}\left(\widehat{\mathrm{X}}_{\mathrm{R}}^{*}, \mathrm{t}\right) - \mathbf{r}_{\mathbf{s}}\left(\widehat{\mathrm{X}}_{\mathrm{S}}^{*}, \mathrm{t}\right) \right\| \tag{5.84}$$

The contact pair $\left(\widehat{\mathrm{X}}_{\mathrm{S}}^{*}, \widehat{\mathrm{X}}_{\mathrm{R}}^{*}\right)$ can be found by solving the necessary condition for a minimum for distance between surface points,

$$\frac{\partial}{\partial \widehat{\mathrm{X}}_{\mathrm{S}}} d\left(\widehat{\mathrm{X}}_{\mathrm{S}}^{*}, \widehat{\mathrm{X}}_{\mathrm{R}}^{*}, \mathrm{t}\right)\Big|_{\widehat{\mathrm{X}}_{\mathrm{S}} = \widehat{\mathrm{X}}_{\mathrm{S}}^{*}} = 0 \tag{5.85}$$

We define a local coordinate system located on the stator surface $\widehat{\mathrm{X}}_{\mathrm{S}}^{*}$ point. The orientation of the coordinate system is such that it lies along the tangent plane formed by the contact pairs.

4.13 above illustrates the direction of the unit tangential vectors $\tilde{\mathbf{a}}_1^*$, $\tilde{\mathbf{a}}_2^*$ and unit outside normal vector $\tilde{\mathbf{n}}^*$. The gap function can therefore be defined as

$$g_N(\hat{X}_R^*, \hat{X}_S^*, t) = \left|\mathbf{r_R}(\hat{X}_R^*, t) - \mathbf{r_s}(\hat{X}_S^*, t)\right| \cdot \tilde{\mathbf{n}}^* \tag{5.86}$$

Whereby from this definition of the gap function, we can define the state of contact and non-contact between the surfaces which can be express as,

$$separation: g_N(\hat{X}_R^*, \hat{X}_S^*, t) > 0\,, \qquad penetration: \; g_N(\hat{X}_R^*, \hat{X}_S^*, t) < 0 \tag{5.87}$$

To better evaluate the geometric entities concerning the surface unit normal $\tilde{\mathbf{n}}^*$and tangential vectors $\tilde{\mathbf{a}}_1^*$, $\tilde{\mathbf{a}}_2^*$, we will be required to invoke some basic differential geometry concepts. In differential geometry, a three dimension surface $\mathcal{S}$ can be expressed as follows in parametric form in terms of cylindrical polar coordinates,

$$\vec{\mathbf{x}}(r, \theta) = x_1(r, \theta)\,\vec{\mathbf{r}} + x_2(r, \theta)\,\vec{\boldsymbol{\theta}} + x_3(r, \theta)\,\vec{\mathbf{k}} \tag{5.88}$$

Where r and θ are parameters of the surface. Upon differentiating the above equation () with respect to t gives us,

$$\dot{\vec{\mathbf{x}}}(r, \theta) = \frac{d}{dt}\vec{\mathbf{x}}(r, \theta) = \frac{\partial}{\partial r}\vec{\mathbf{x}}(r, \theta)\,\frac{dr}{dt} + \frac{\partial}{\partial \theta}\vec{\mathbf{x}}(r, \theta)\,\frac{d\theta}{dt} = \overrightarrow{\mathbf{x_r}}(r, \theta)\,\dot{r} + \overrightarrow{\mathbf{x_\theta}}(r, \theta)\,\dot{\theta} \tag{5.89}$$

Here, $\dot{\vec{\mathbf{x}}}$ refers to the tangent vector of $\vec{\mathbf{x}}$ and $\overrightarrow{\mathbf{x_r}}$ and $\overrightarrow{\mathbf{x_\theta}}$ are tangent vectors to the tangent plane of the isoparametric surface $\vec{\mathbf{x}}(r, \theta)$. The unit tangent vectors corresponds to the unit tangent vectors of the local coordinates system discussed earlier

$$\overrightarrow{\mathbf{x_r}}(\hat{X}_S^*) = \tilde{\mathbf{a}}_1^* \tag{5.90}$$

$$\overrightarrow{\mathbf{x_\theta}}(\hat{X}_S^*) = \tilde{\mathbf{a}}_2^* \tag{5.91}$$

The cross product of the tangent vectors ($\overrightarrow{\mathbf{x}_r} \times \overrightarrow{\mathbf{x}_\theta}$) which produces an orthogonal vector perpendicular to the isoparametric surface essentially gives us the surface unit normal vector $\tilde{n}^*$ which can be written as,

$$\tilde{n}^* = \frac{\overrightarrow{\mathbf{x}_r}(\hat{X}_S^*) \times \overrightarrow{\mathbf{x}_\theta}(\hat{X}_S^*)}{\left\|\overrightarrow{\mathbf{x}_r}(\hat{X}_S^*) \times \overrightarrow{\mathbf{x}_\theta}(\hat{X}_S^*)\right\|} \tag{5.92}$$

As highlighted earlier, this vector is very useful in helping us interrogate the surfaces of the stator and rotor as well as in the computation of the gap function $g_N(\hat{X}_R^*, \hat{X}_S^*, t)$. The three vectors together forms the tangent plane and the local coordinate system, this is illustrated in Figure 5.14 below.

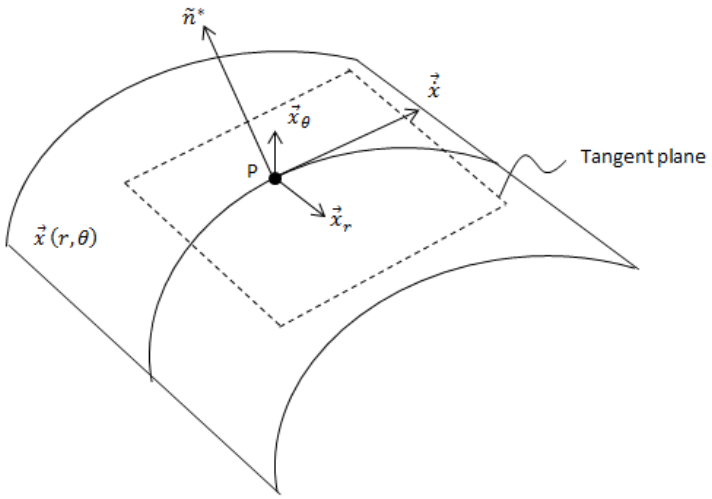

Figure 5.14: Tangent and normal vectors of tangent plane at point P

5.5.3 Contact Detection and Search Algorithm

After the formulation of the gap function in the previous section, we will discuss the development of the contact search algorithm next. In many contact problems, contact occurs at non-predictable places and is generally not known a priori. This is especially true for problems involving processes such as large deformation of objects, self-contact as well as

fragmentation and breakage. Hence, contact search occurrence between solids can be considered to be one of the biggest problems in computational contact mechanics according to Wriggers [68]. Since for O(N) surfaces of a discretized domain, the total number of operations required necessary to check is $O(N^2)$. If such a search has to be performed at each and every iteration step, the computational resources will be completely dominated by this process. Therefore, many methods and algorithm have been developed over the years to reduce the frequency of search and its subsequent complexity.

The general procedures in a contact search procedure consist of three phases. Phase 1 consist of a global contact search whereby it involves a spatial search for potential contact pairs between objects or elements. Phase 2 involves the determination of contact detection that actually occurs. The last phase of the search algorithm performs the computation and quantification of penetration depth and resultant stresses and strains. Fortunately in our situation, according to Wriggers [68], an elaborate contact search algorithm is not necessary if the deformation involved during contact is small as no large slip can occur on the contact surface. A discretization scheme in which nodes on the surfaces matches each other is sufficient for the problem description. Therefore, a linear description of the contact kinematics can be employed and we can further assume that the topology of the system is relatively fixed. We observed that the TRUM system which we are studying can utilise these simplifying analysis methods. First, the deformation experienced by the stator and rotor interface layer is of the order of microns, this compares with the scale of the actual physical system which is usually in the orders of tens of millimetres. Second, the stator can be considered to be relatively fixed spatially which implies that contact zones are relatively predictable. Although the rotor is allowed motion, and slip does occur, the domain of its trajectory is relatively small and can be "predicted" a priori. And lastly, potential contact regions can be limited to and reduced substantially to those regions of the system that consist

of the stator teeth only as that would be the only potential contact points due its significantly raised height.

Given the axis-symmetry of the stator and rotor and the assumption that the stator teeth is a rigid body while the rotor under face is interposed with a deformable viscoelastic layer, our system falls into the class of problems which involves contact between a rigid and deformable body similar to a classical Signorini problem. The rigid axis-symmetric stator teeth thus enforce such symmetry to the problem. The discretization scheme employed separates the stator domains into a series of axis-symmetric nodes clusters in cylindrical coordinates as shown in Figure 5.15 below.

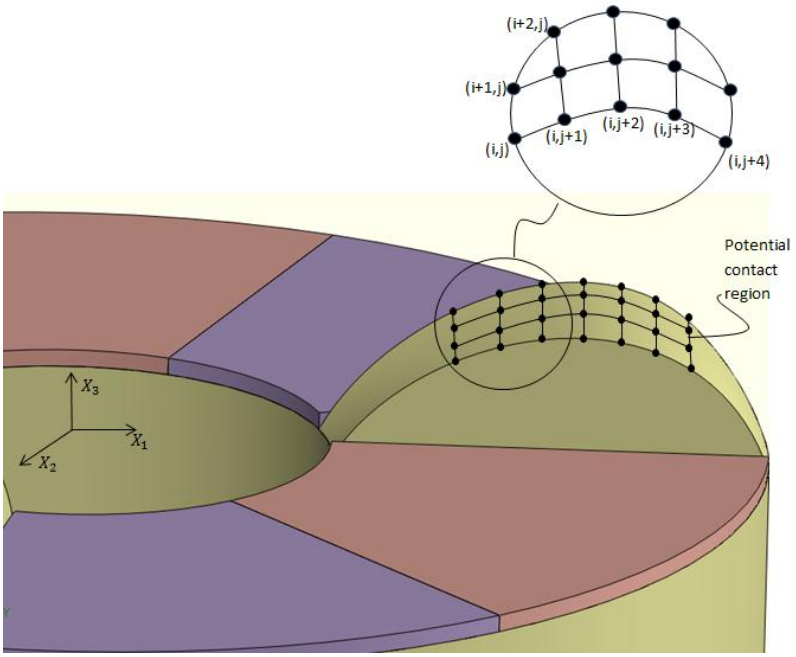

Figure 5.15: Discretization of stator teeth surface into a series of nodes

In the simulation, a total of 40,000 nodes points are used to evaluate the state of the contact between the rotor and stator. The numerical solver will run through all the nodes for each iteration step in the computation of the net forces and moments induced due to contact. In the

program, the locations of the nodes can be changed and the number of nodes can be varied depending on the conditions under study.

The onset of physical contact between nodes points will be indicated by a modified gap function either taking a positive or negative value for a given node pair; Figure 5.16 below illustrates the modified gap function. The function takes the vertical penetration depth between points on the stator and the corresponding vertical line intersection point on the rotor surface.

$$g_N^M(Z_R^P, \mathbf{U}_S^P, t) = |\mathbf{r_R} - \mathbf{r_s}| \tag{5.93}$$

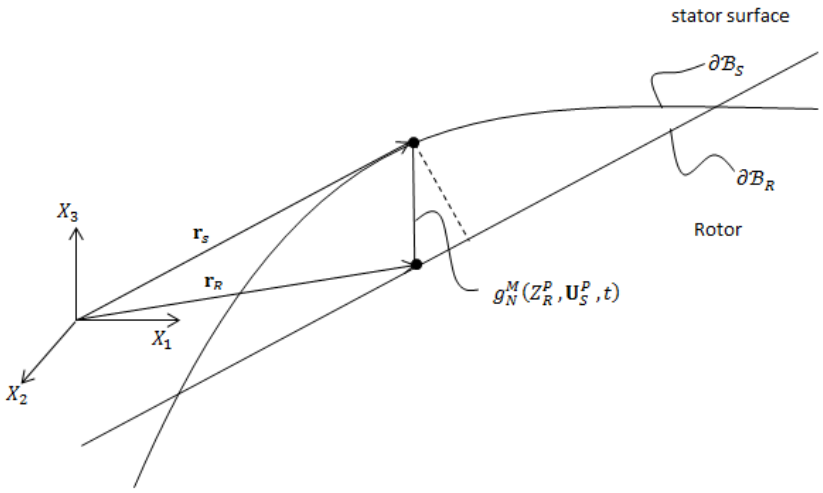

Figure 5.16: Definition of Modified Gap Function as the vertical distance

The motivation underlying this approach is due to the fact that geometrical configuration allowed in the program can take on any surface revolution shapes. Take for example, an inclined stator surface coming into physical contact with a slanting rotor as show in Figure 5.17 below, the rotor surface is assumed to be conical and flat to simplify the presentation here,

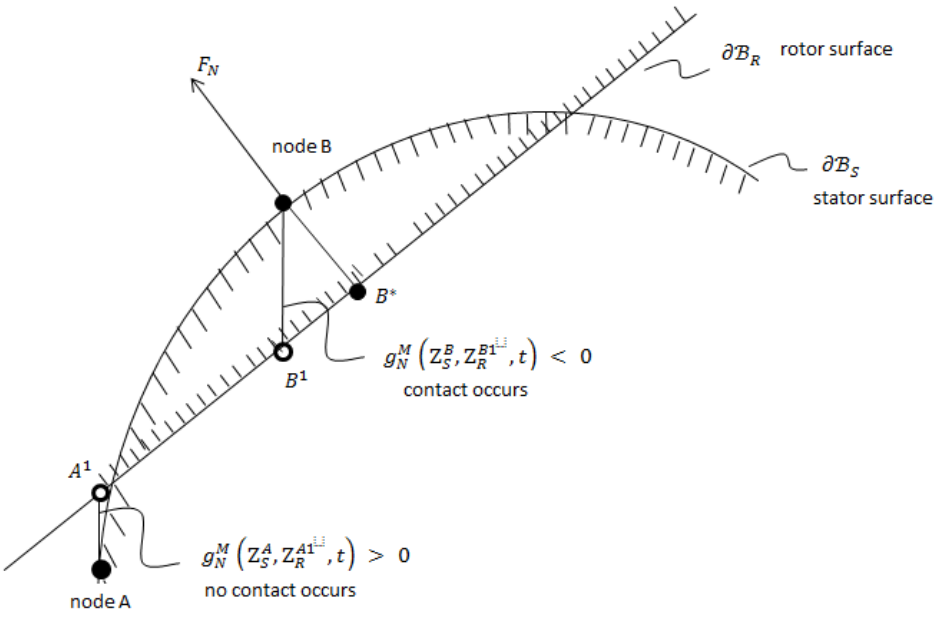

Figure 5.17: Simpler detection of initial contact using modified gap function

From the figure above, points A and B are the discretized nodes located on the stator teeth surface, while points A^1 and $B^1$are points located on the rotor surface which are formed from the intersection between the vertical lines branching out from point A and B to the rotor surface line. Since the z height can be easily computed from equations (5.52) and (5.62) developed in respectively, by calculating their difference, it offers us an easy and straightforward way to determine whether there is a case of preliminary contact.

Inspecting Figure 5.17 again, it can be seen that the challenge here is to determine the point of maximum normal penetration B^*. Whereby, upon discovery of that point, the gap function can be applied to calculate the depth of penetration. That point located on the rotor surface cannot be known a priory and have to be determined in a numerical iterative procedure. We begin first by noting that point B^* is the point of intersection formed by a line $\vec{\boldsymbol{\ell}}\left(\hat{X}_S^*, \hat{n}^*\right)$ and the rotor surface S_{Rotor}. Line $\vec{\boldsymbol{\ell}}\left(\hat{X}_S^*, \hat{n}^*\right)$ passes through point P located on the stator

surface and is parallel to the unit surface normal vector at P, $\hat{\mathbf{n}}^*$. The vector representation of the line can be given as

$$\vec{\boldsymbol{\ell}}\left(\hat{X}_S^*, \hat{n}^*\right) = \overrightarrow{\mathbf{r_p}}\left(\hat{X}_S^*\right) + s_\ell\, \hat{\mathbf{n}}^* = < x_1^p, x_2^p, x_3^p > + s < \hat{n}_{x1}^*, \hat{n}_{x2}^*, \hat{n}_{x3}^* > \qquad (5.94)$$

Whereby $< x_1^p, x_2^p, x_3^p >$ and $< \hat{n}_{x1}^*, \hat{n}_{x2}^*, \hat{n}_{x3}^* >$ refers to the coordinates of point P and the unit vector components of the normal vector $\hat{\mathbf{n}}^*$ respectively. The variable s_ℓ determines the end point and hence the length of the vector line $\overrightarrow{\boldsymbol{\ell}}\left(\hat{X}_S^*, \hat{n}^*\right)$. The approach we have adopted here to discover the intersection point Q located on the rotor surface is to first, increase the vector line length by incrementing s_ℓ and second, check the modified gap function for the distance between point ℓ_P and B_2'. Third, if the distance is within a convergence limit, the gap function is invoked to compute the penetration depth; else the variable s_ℓ will be incremented again. This is illustrated in Figure 5.18 below,

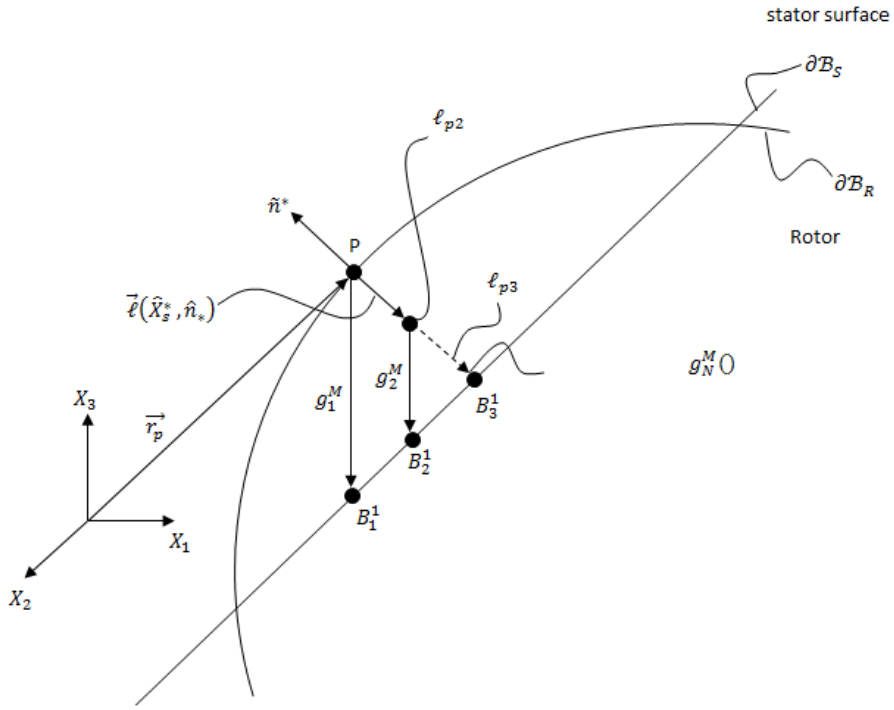

Figure 5.18: Incrementing vector line length to approach rotor surface.

The procedures involve in the search for the contact point and the computation for the convergence is summarised in the below steps.

STEP 1: Compute unit surface normal vector $\tilde{\mathbf{n}}^*$ and form vector line $\overrightarrow{\boldsymbol{\ell}}(\hat{X}_S^*, \hat{n}^*)$

$$\tilde{\mathbf{n}}^* = \frac{\overrightarrow{\mathbf{x_r}}(\hat{\mathrm{X}}_\mathrm{S}^*) \times \overrightarrow{\mathbf{x_\theta}}(\hat{\mathrm{X}}_\mathrm{S}^*)}{\left\|\overrightarrow{\mathbf{x_r}}(\hat{\mathrm{X}}_\mathrm{S}^*) \times \overrightarrow{\mathbf{x_\theta}}(\hat{\mathrm{X}}_\mathrm{S}^*)\right\|} \tag{5.95}$$

$$\overrightarrow{\boldsymbol{\ell}}(\hat{X}_S^*, \hat{n}^*) = \overrightarrow{\mathbf{r_p}}(\hat{X}_S^*) + s_\ell \hat{\mathbf{n}}^* = < x_1^p, x_2^p, x_3^p > + s_\ell < \hat{n}_{x1}^*, \hat{n}_{x2}^*, \hat{n}_{x3}^* > \tag{5.96}$$

STEP 2: Compute modified gap function to determine distance between point Lp and B prime 1

$$\mathrm{g}_N^M(\mathrm{Z}_R^P, \mathbf{U}_S^P, \mathrm{t}) = |\mathbf{r_R} - \mathbf{r_s}| \tag{5.97}$$

STEP 3: Check if distance is within defined limit C_{limit} , if within limit, proceed to step 4. If not, proceed to step 5.

$$\text{check if} \quad \mathrm{g}_N^M(\mathrm{Z}_R^P, \mathbf{U}_S^P, \mathrm{t}) < C_{limit} \tag{5.98}$$

STEP 4: Compute gap function and determine the depth of penetration.

$$\mathrm{g_N}(\hat{\mathrm{X}}_\mathrm{R}^*, \hat{\mathrm{X}}_\mathrm{S}^*, \mathrm{t}) = |\mathbf{r_R}(\hat{\mathrm{X}}_\mathrm{R}^*, \mathrm{t}) - \mathbf{r_s}(\hat{\mathrm{X}}_\mathrm{S}^*, \mathrm{t})| \cdot \tilde{\mathbf{n}}^* \tag{5.99}$$

STEP 5: Increase variable s_ℓ by delta Δs for longer vector line $\overrightarrow{\boldsymbol{\ell}}(\hat{X}_S^*, \hat{n}^*)$, return to step 2 again.

$$s_{\ell_2} = s_{\ell_1} + \Delta s_\ell \tag{5.100}$$

5.5.4 Friction Model

For the friction model used in this study, we shall restrict ourselves to more simple formulations like the classical law of COULOMB. COULUMB's Law is the most frequently used constitutive equation for frictional contact for dry friction. Other more sophisticated frictional laws which models for the interface local and micro mechanical phenomena are also available. For the sake of simplifying the analysis, we will not be considering them in this study. Along a contact interface, the processes in the tangential direction can be classified into 2 different responses. Under the action of a lateral force, there can either be an absence or presence of tangential relative displacements along the contact zones. These behaviours are term stick and slip or sliding respectively.

For COULUMB's Law, contacting surfaces move relative to each other whenever the tangential forces are above a certain limit, below which they will stick with each other. This is graphically represented by Figure 5.19 and denoted by equation (5.101) below.

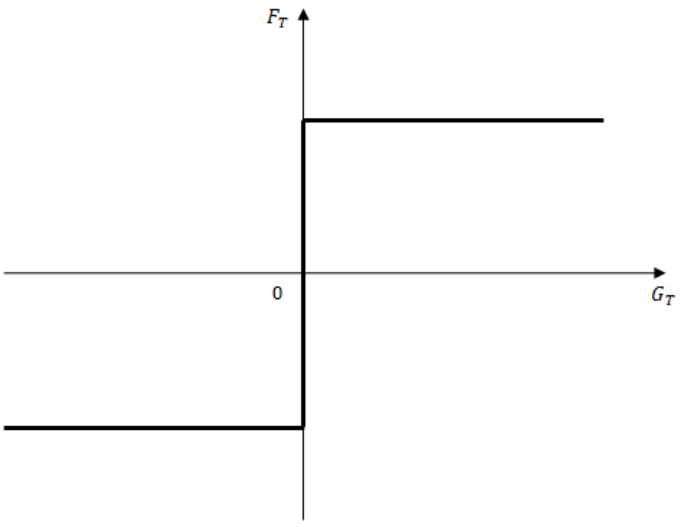

Figure 5.19: Classical COULUMB's Friction Law

$$F_T = \mu\,|F_n|\,\frac{\dot{g}_T}{\|\dot{g}_T\|} \quad if \ \|F_T\| > \mu[F_n] \tag{5.101}$$

Whereby μ denotes the sliding friction coefficient which takes a constant value in the classical COULUMB's law. It is worthwhile to note that in general, the friction coefficient depends on many other factors such as the surface roughness, relative sliding velocities $\dot{g}_T$, temperature θ and normal pressure F_n. Regularization of the stick –slip behaviour to avoid non-differentiability of COULUMB's law is also another method to formulate the tangential constitutive relations. Incorporating such effects gives us a better picture of the processes at work in the contact zones. Thus a variant of the COULUMB's law with a variable frictional coefficient can be useful for further study,

$$\mu = \mu(\dot{g}_T, F_n, \theta) \tag{5.102}$$

5.6 Rigid Body Dynamics of Rotor

5.6.1 Translational Motion EOM

In this section, the dynamics of the rotor will be developed and the governing equations of motion of the rotor subsystem derived. The rotor and stator subsystems are both coupled together through the interface forces terms whenever there are physical interactions between the two components. The rotor is assumed to be a rigid body permitted to move about in three dimensions. Therefore, an additional twelve states are added to the numerical solution process; 3 translational degrees of freedom and their derivatives and 3 rotational degree of freedom and their derivatives. Figure 5.20 below illustrates the general configuration and degree of freedom possess by the rotor subsystem.

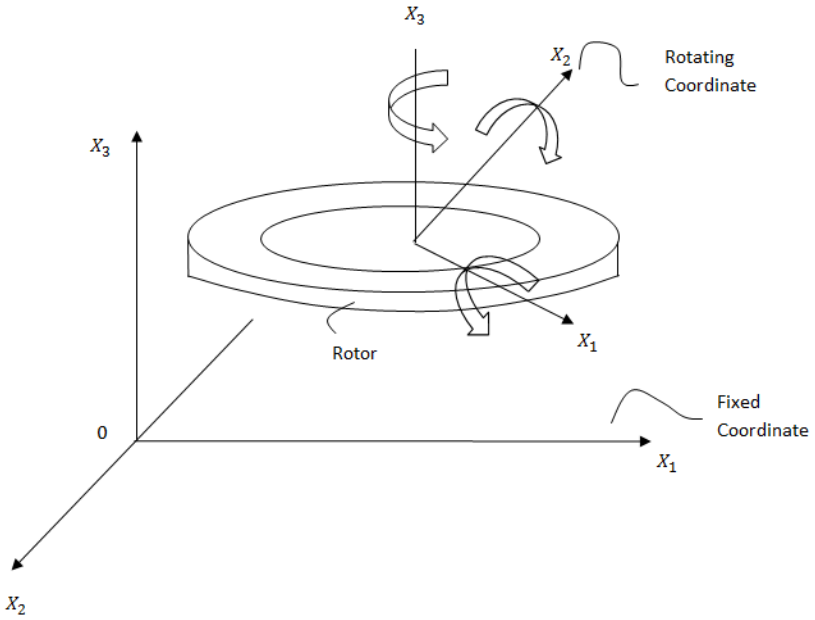

Figure 5.20: Coordinate systems and Degree of Freedom of Rotor

The governing linear equation of motion is relatively straightforward and is given by

$$\sum \boldsymbol{\mathcal{F}}_{\mathbf{R}} = \mathrm{M_R}\, \boldsymbol{a}_{\mathrm{Rc}} = \mathrm{M_R}\, \ddot{\mathbf{X}}_{\mathrm{Rc}} \tag{5.103}$$

Which upon expansion and resolving into components along the three Cartesian axis can be expressed as,

$$\sum \mathcal{F}_{\mathrm{x}} = \mathrm{M_R}\, \ddot{\mathrm{x}}_{\mathrm{Rc}} \tag{5.104}$$

$$\sum \mathcal{F}_{\mathrm{y}} = \mathrm{M_R}\, \ddot{\mathrm{y}}_{\mathrm{Rc}} \tag{5.105}$$

$$\sum \mathcal{F}_{\mathrm{z}} = \mathrm{M_R}\, \ddot{\mathrm{z}}_{\mathrm{Rc}} \tag{4.106}$$

Whereby $\mathrm{M_R}$ refers to the mass of the rotor while $\ddot{\mathrm{x}}_{\mathrm{Rc}}$, $\ddot{\mathrm{y}}_{\mathrm{Rc}}$ and $\ddot{\mathrm{z}}_{\mathrm{Rc}}$ are the accelerations of the mass center of the rotor in the $\mathrm{X}_1, \mathrm{X}_2$ and X_3 directions respectively.

5.6.2 Rotational Motion EOM

The equations of motion governing the rotational behavior of the rotor is more involved in the sense that the momentum and velocity vectors do not necessarily coincides and that finite rotation do not commune in general. We begin first with the most general relations for rotational motion of a rigid body which states that the rate of change in angular momentum $\dot{\mathbf{H}}_{\mathrm{Rc}}$ about the mass center is proportional to the net moments acting on it $\boldsymbol{\mathcal{M}}_{\mathbf{Rc}}$.

$$\sum \boldsymbol{\mathcal{M}}_{\mathbf{Rc}} = \dot{\mathbf{H}}_{\mathrm{Rc}} \tag{5.107}$$

This equation is valid for most general cases of rigid body motion. $\mathbf{H}_{\mathrm{Rc}}$ represents the angular momentum of the rotor in terms of the global fixed axis $\mathrm{X}_1, \mathrm{X}_2$ and X_3. The equation relating the angular momentum of the body to its angular velocity is given by,

$$\mathbf{H}_{\mathrm{Rc}} = [\mathcal{I}]\, \boldsymbol{\omega}_{\mathrm{R}} \tag{5.108}$$

Where $[\mathcal{I}]$ refers to the inertia tensor of the rotor at its mass center and $\boldsymbol{\omega}_{\mathrm{R}}$ is the angular velocity of the rotor. To compute the rate of change of the angular momentum with respect to the fixed axes $\dot{\mathbf{H}}_{\mathrm{Rc}}$ would require us to track the time evolving nature of the inertia tensor $[\mathcal{I}]$ as the body rotates. Thus, in order to avoid such complications, we shall attach to the rotating rotor a body fixed axes such that the inertia tensor remains unchanged during the rotor motion. The relation that expresses the rate of change of a vector with respect to a fixed orientation can be found by adding the rate of change of the vector with respect to the rotating frame $(\dot{\mathbf{H}}_{\mathrm{Rc}})_{\mathrm{xyz}}$ to the cross product, $(\boldsymbol{\Omega} \times \mathbf{H}_{\mathrm{Rc}})$ whereby $\boldsymbol{\Omega}$ is the angular velocity of the rotating frame. Therefore, the rate of change of angular momentum can also be written as,

$$\mathbf{H}_{\mathrm{Rc}} = (\dot{\mathbf{H}}_{\mathrm{Rc}})_{\mathrm{xyz}} + \boldsymbol{\Omega} \times \mathbf{H}_{\mathrm{Rc}} \tag{5.109}$$

$$(\dot{\mathbf{H}}_{\mathrm{Rc}})_{\mathrm{xyz}} = \mathrm{H_x}\tilde{\mathbf{x}}_{\mathbf{1}} + \mathrm{H_y}\tilde{\mathbf{x}}_{\mathbf{2}} + \mathrm{H_z}\tilde{\mathbf{x}}_{\mathbf{3}} \tag{5.110}$$

Where $\mathbf{H}_{\mathrm{Rc}}$ refers to the angular momentum of the rotor with respect to the frame of reference with fixed orientation $OX_1X_2X_3$ and $(\dot{\mathbf{H}}_{\mathrm{Rc}})_{xyz}$ is the rate of change of $\mathbf{H}_{\mathrm{Rc}}$ with respect to the rotating frame Oxyz, while $\tilde{\mathbf{x}}_1$, $\tilde{\mathbf{x}}_2$ and $\tilde{\mathbf{x}}_3$ are unit vectors directed along the rotating axes. $\boldsymbol{\Omega}$ is the angular velocity of the rotating frame Oxyz. Inserting equation (5.110) into (5.107), we have,

$$\sum \boldsymbol{\mathcal{M}}_{\mathbf{Rc}} = (\dot{\mathbf{H}}_{\mathrm{Rc}})_{xyz} + \boldsymbol{\Omega} \times \mathbf{H}_{\mathrm{Rc}} \tag{5.111}$$

Furthermore, if the axes chosen is the principle axes of inertia and if the rotating axes Oxyz is also chosen to coincides with the principle axes of inertia of the body, the inertia tensor can be greatly simplified with the centroidal mass products of inertia of the body taking a zero value and leaving only non-zero values for the centroidal mass moment of inertia of the body. The inertia tensor $[\mathcal{I}]$ reduces to,

$$[\mathcal{I}] = \begin{bmatrix} \bar{I}_{xx} & & \\ & \bar{I}_{yy} & \\ & & \bar{I}_{zz} \end{bmatrix} \tag{5.112}$$

Whereby $\bar{I}_{xx}$, $\bar{I}_{yy}$ and $\bar{I}_{zz}$ denotes the principle centroidal moments of inertia of the body. The simplified equation now reads,

$$\dot{\mathbf{H}}_{\mathrm{Rc}} = \bar{I}_{xx}\,\omega_x\,\tilde{\mathbf{x}}_1 + \bar{I}_{yy}\,\omega_y\,\tilde{\mathbf{x}}_2 + \bar{I}_{zz}\,\omega_z\,\tilde{\mathbf{x}}_3 \tag{5.113}$$

If the rotating frame is attached to the body, its angular velocity would be equal to the angular velocity of the body, and we have $\boldsymbol{\Omega} = \boldsymbol{\omega}$. Inserting equation (5.113) into (5.111), and after some manipulation, we can obtain three scalar equations of motion given below,

$$\sum \mathcal{M}_x = \bar{I}_{xx}\,\dot{\omega}_x - \left(\bar{I}_{yy} - \bar{I}_{zz}\right)\omega_y\omega_z \tag{5.114}$$

$$\sum \mathcal{M}_y = \bar{I}_{yy}\,\dot{\omega}_y - (\bar{I}_{zz} - \bar{I}_{xx})\,\omega_z\omega_x \tag{5.115}$$

$$\sum \mathcal{M}_z = \bar{I}_{zz}\,\dot{\omega}_z - (\bar{I}_{xx} - \bar{I}_{yy})\,\omega_x\omega_y \tag{5.116}$$

The above equations are known as Euler's Equations. To obtain the general solution for the motion of a three dimensional rigid body described by these equations is not trival. First, the equations contain non-linear products of the unknown angular velocities. Hence, a numerical approach is required to solve it. Second, the axis system is attached to the body and thus represents a fundamental challenge which involves the need to track and follow the body configuration as it rotates. A method to follow the time evolving behavior of the body axis as it moves must be developed for these set of equations to be useful to us.

It should be noted that we have simplify the analysis for this study by assuming that the rotor is axisymmetric and hence the products of inertia terms ignored. Else, the full Euler's equation to be solve would be as follows,

$$\sum M_x = I_{xx}\ddot{\theta}_x - (I_{yy} - I_{zz})\,\omega_y\omega_z - I_{xy}(\ddot{\theta}_y - \omega_z\omega_x) - I_{yz}(\omega_y^2 - \omega_z^2) - I_{zx}(\ddot{\theta}_z + \omega_x\omega_y) \tag{5.117}$$

$$\sum M_y = I_{yy}\ddot{\theta}_y - (I_{zz} - I_{xx})\,\omega_z\omega_x - I_{yz}(\ddot{\theta}_z - \omega_x\omega_y) - I_{zx}(\omega_z^2 - \omega_x^2) - I_{xy}(\ddot{\theta}_x + \omega_y\omega_z) \tag{5.118}$$

$$\sum M_z = I_{zz}\ddot{\theta}_z - (I_{xx} - I_{yy})\,\omega_x\omega_y - I_{zx}(\ddot{\theta}_x - \omega_y\omega_z) - I_{xy}(\omega_x^2 - \omega_y^2) - I_{yz}(\ddot{\theta}_y + \omega_z\omega_x) \tag{5.119}$$

The justification for such approximations is that the mass of an HDD actuator arm is mostly concentrated at the pivot central region with the bearings components, top cap, spring and other components located centrally. Thus, such configuration lends it the symmetry for this

simplification. However, it must be pointed out that this is just an approximation and that it will result in some loss of the dynamics richness under study. This can be the topic of future work when an alternative numerical strategy is developed to solve the above full equations.

5.6.3 Rotor Interfacial Forces and Moments

The onset of contact between rotor and stator surfaces generated reaction forces and moments onto the rotor. Figure 5.21 below shows a schematic of the interactions.

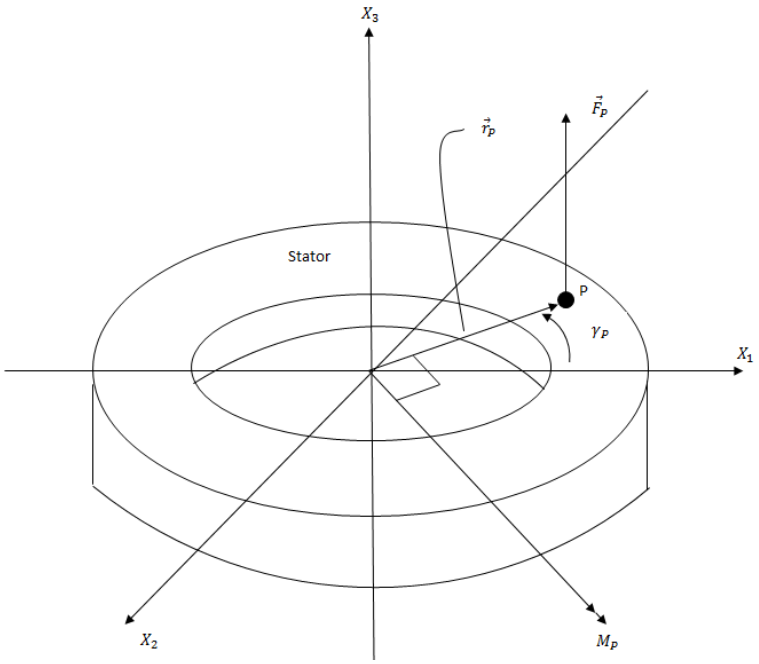

Figure 5.21: Reaction force and Moment resultant at point P

In the figure above, for the sake of clarity, only the stator is shown as it refers to the object whereby reactions forces and moments are generated onto the rotor. But it should be noted that the forces are transmitted to the rotor. For a given point P which is in contact generating a normal reaction force $\vec{F}_p$, there will also produces a moment on the rotor $\overrightarrow{M}_p$. For each and every time step, integration over the entire stator surface domain will produce a resultant

force and moment on the rotor. It should be noted that the moments calculated are based on the global fixed axis $OX_1X_2X_3$.

Referring to Figure 5.22 below, it illustrates a more general configuration of contact between the rotor and stator which includes an inclined surface. Thus, when computing the moment and forces generated we need to take an additional step to resolve the forces accordingly.

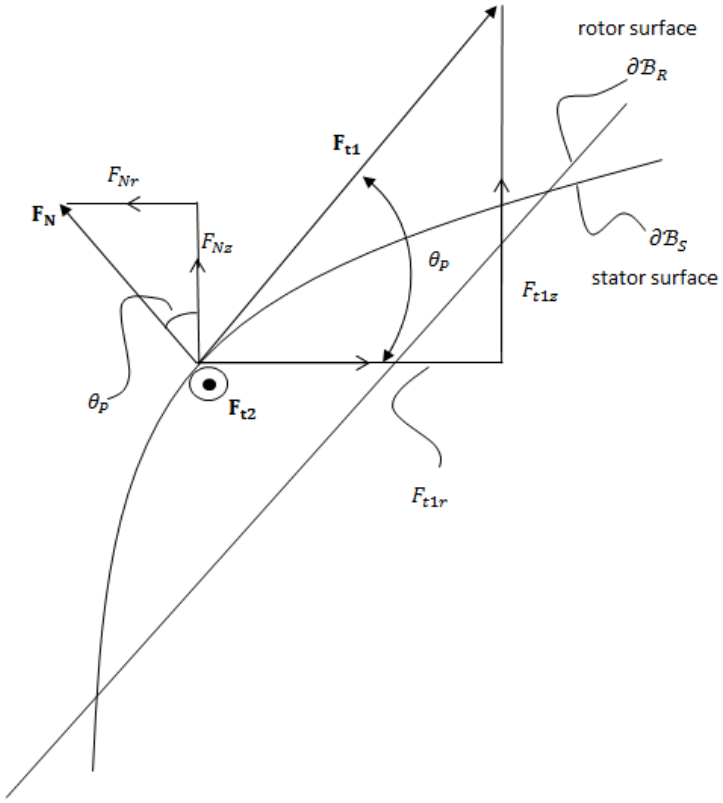

Figure 5.22: Normal and friction forces resolving at contact interface

After some manipulation of the reactions normal force and frictional forces and performing angular resolving, we can obtain the resultant forces and moment generated by performing the below integration over the contact domains, which can be expressed as follows

$$F_{z,interface} = \iint_{A_{contact}} P(r,\theta,t)\{\cos\theta_p + \sin\alpha \sin\theta_p\}\, r\, drd\theta \tag{5.120}$$

$$F_{x,interface} = \iint_{A_{contact}} P(r,\theta,t)\{-\sin\theta_p + \mu\cos\theta_p \sin\alpha\}\, r\cos\gamma_p\, Sign_{t2}^{P}(r,\theta,t)drd\theta \qquad (5.121)$$

$$F_{y,interface} = \iint_{A_{contact}} P(r,\theta,t)\{-\sin\theta_p + \mu\cos\theta_p \sin\alpha\}\, r\sin\gamma_p\, Sign_{t2}^{P}(r,\theta,t)drd\theta \qquad (5.122)$$

$$M_{z,interface} = \iint_{A_{contact}} \mu r^2\, P(r,\theta,t)\cos\alpha\, Sign_{t1}^{P}(r,\theta,t)drd\theta \qquad (5.123)$$

$$M_{x,interface} = \iint_{A_{contact}} P(r,\theta,t)\{\cos\theta_p + \sin\alpha\sin\theta_p\}\, r^2\cos\gamma_p\ drd\theta \qquad (5.124)$$

$$M_{y,interface} = \iint_{A_{contact}} P(r,\theta,t)\{\cos\theta_p + \sin\alpha\sin\theta_p\}\, r^2\sin\gamma_p\ drd\theta \qquad (5.125)$$

In the above equations, γ_p is the angle formed between integration point P and the positive X_1 axis as shown in Figure 5.21 above, this factor is to resolve the resultant moment vector into 2 components along the X_1 and X_2 directions. α is the friction angle discussed previously, it resolves the tangential frictional forces into two components, along the circumferential and radial direction respectively. Lastly, θ_p is the slope of the stator teeth at the location of contact P, it resolves the normal and tangential forces into the X_3 and X_1 radial direction respectively.

5.6.4 Coordinate Transformation

After the resultant moments have been formulated in the previous section in the fixed frame of reference, we will need to transform it into the local coordinate axis moving together with the rotor in order to employ Euler's equations. For the TRUM which we are studying, we first

observe that rotation along the X_3 axis is much greater than the rotations about the other two axes, X_1 and X_2. The rotor is designed to rotate along the X_3 axis for basic functionality requirement while the tilting rotations about the X_1 and X_2 are parasitic angular motions and are restricted from large movements from the way the motor is being constructed. From this premises, we can employ one simplifying assumption in our analysis which is that rotations about the X_1 and X_2 axis (θ_1 and θ_2) are relatively small and hence it is sufficient that we track only θ_3 to fully describe the rotating body fixed axes. The subsequent reaction forces and moment computation arising from the interaction between the stator and rotor will be resolved into components with respect to this rotating frame of reference. Figure 5.23 below illustrates the rotating frame of the body fixed axes of the rotor.

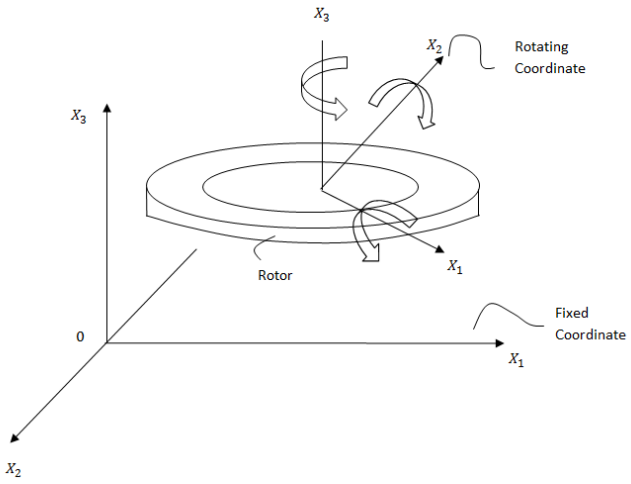

Figure 5.23: Rotating frame of reference attached to rotor.

There is a need to distinguish and resolve the reaction forces and moments into components that relate to the rotating frame of reference of the rotor because the stator is rigidly located in a fixed frame of reference $OX_1X_2X_3$. Whenever reactions forces and hence moments that are produced due to contact, they always does so in the fixed frame as we perform a search throughout the stationary stator domain. However, in order to apply the Euler's equations derived earlier to describe the rotor dynamics, the reaction moments with respect to the

rotating frame is needed. Figure 5.24 below illustrates a two dimension coordinate transformations,

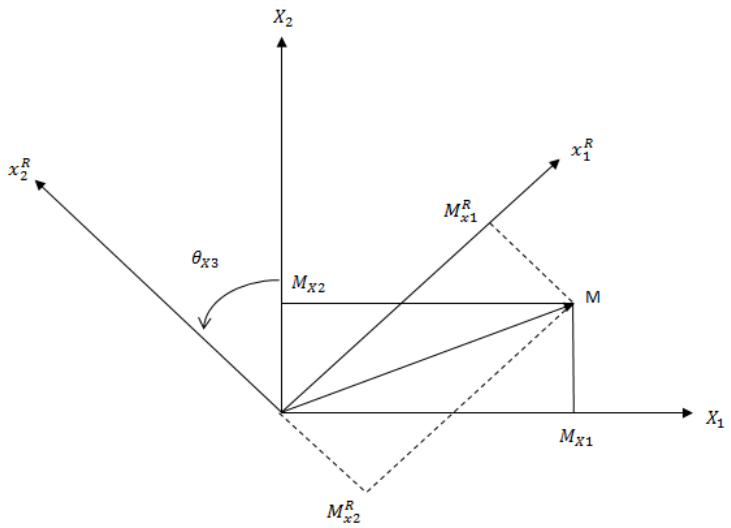

Figure 5.24: 2-Dimensional coordinate transformation

For a given vector M, its components is related by the below transformation matrix,

$$[T] = \begin{pmatrix} \cos\theta_{x3} & \sin\theta_{x3} \\ -\sin\theta_{x3} & \cos\theta_{x3} \end{pmatrix} \tag{5.126}$$

Thus the components of the moments can be transformed as such,

$$\begin{Bmatrix} M_{x1} \\ M_{x2} \end{Bmatrix} = \begin{pmatrix} \cos\theta_{x3} & \sin\theta_{x3} \\ -\sin\theta_{x3} & \cos\theta_{x3} \end{pmatrix} \begin{Bmatrix} M_{X1} \\ M_{X2} \end{Bmatrix} \tag{5.127}$$

It is worthwhile to note that when we are calculating the angular state of the rotor when computing the penetration, we will need to transform back the rotor states to conform with the fixed global axis by using the transpose of the transformation matrix above.

The overall equation of motion of the rotor can thus be expressed as follows with the interfacial forces terms, externally applied forces and torque and spring stiffness and damping terms included.

$$\ddot{\theta}_z = \frac{C_z}{I_{zz}}\dot{\theta}_z + \frac{1}{I_{zz}}\tau_{z,interface} + \frac{(I_{yy} - I_{xx})}{I_{zz}}\,\dot{\theta}_x\dot{\theta}_y - \frac{\tau_{z,applied}}{I_{zz}} \tag{5.128}$$

$$\ddot{\theta}_x = \frac{C_x}{I_{xx}}\dot{\theta}_x + \frac{1}{I_{xx}}\tau_{x,interface} + \frac{(I_{yy} - I_{zz})}{I_{xx}}\,\dot{\theta}_y\dot{\theta}_z - \frac{\tau_{x,applied}}{I_{xx}} \tag{5.129}$$

$$\ddot{\theta}_y = \frac{C_y}{I_{yy}}\dot{\theta}_y + \frac{1}{I}\tau_{y,interface} + \frac{(I_{zz} - I_{xx})}{I_{yy}}\,\dot{\theta}_x\dot{\theta}_z - \frac{\tau_{y,applied}}{I_{yy}} \tag{5.130}$$

$$\ddot{z} = -\frac{k_z}{M}z - \frac{C_z}{M}\dot{z} + \frac{1}{M}F_{z,interface} - \frac{F_{z,applied}}{M} \tag{5.131}$$

$$\ddot{x} = -\frac{k_x}{M}x - \frac{C_x}{M}\dot{x} + \frac{1}{M}F_{x,interface} - \frac{F_{x,applied}}{M} \tag{5.132}$$

$$\ddot{y} = -\frac{k_y}{M}y - \frac{C_y}{M}\dot{y} + \frac{1}{M}F_{y,interface} - \frac{F_{y,applied}}{M} \tag{5.133}$$

5.7 Overall Governing Equation of Motions for TRUM System

After the developments of the governing equations of motions of the stator and rotor subsystem are ready and the contact interactions model between them formulated, the combined state equations of the entire TRUM in in linear form for the stator subsystem and non-linear form for the rotor subsystem can be written as follows,

$$\{\dot{\boldsymbol{x}}_{\boldsymbol{s}}\} = [\mathbf{A}_s \quad 0_{2nx12}]\{x_s\} + [\mathbf{B}_3 \quad 0_{2nx6}]\{\mathbf{f_s}\} \tag{5.134}$$

$$\{\mathbf{x_s}\} = \begin{Bmatrix}\xi \\ \dot{\xi}\end{Bmatrix} \tag{5.135}$$

$$\{\dot{\mathbf{x}}_\mathbf{r}\} = f(\mathbf{x_n}, \mathbf{f_r}) \tag{5.136}$$

$$\{\mathbf{f_s}\} = \left\{\Upsilon\mathbf{v} + \mathbf{F_n}(\xi, \mathcal{g}_0) + \mathbf{F_{t1}}(\xi, \dot{\xi}, \mathcal{g}_0) + \mathbf{F_{t2}}(\xi, \dot{\xi}, \mathcal{g}_0)\right\} \tag{5.137}$$

$$A_s = \begin{bmatrix} 0_{n\times n} & I_{n\times n} \\ -\mathbf{M}^{-1}\mathbf{K} & -\mathbf{M}^{-1}\mathbf{C} \end{bmatrix} \tag{5.138}$$

$$B_3 = \begin{bmatrix} 0_{n\times n} \\ \mathbf{M}^{-1} \end{bmatrix} \tag{5.139}$$

$$x_r = \begin{Bmatrix} \theta_z \\ \dot{\theta}_z \\ w_f \\ \dot{w}_f \end{Bmatrix} \tag{5.140}$$

$$\ddot{\theta}_z = \frac{C_z}{I_{zz}}\dot{\theta}_z + \frac{1}{I_{zz}}\tau_{z,interface} + \frac{(I_{yy} - I_{xx})}{I_{zz}}\dot{\theta}_x\dot{\theta}_y - \frac{\tau_{z,applied}}{I_{zz}} \tag{5.141}$$

$$\ddot{\theta}_x = \frac{C_x}{I_{xx}}\dot{\theta}_x + \frac{1}{I_{xx}}\tau_{x,interface} + \frac{(I_{yy} - I_{zz})}{I_{xx}}\dot{\theta}_y\dot{\theta}_z - \frac{\tau_{x,applied}}{I_{xx}} \tag{5.142}$$

$$\ddot{\theta}_y = \frac{C_y}{I_{yy}}\dot{\theta}_y + \frac{1}{I}\tau_{y,interface} + \frac{(I_{zz} - I_{xx})}{I_{yy}}\dot{\theta}_x\dot{\theta}_z - \frac{\tau_{y,applied}}{I_{yy}} \tag{5.143}$$

$$\ddot{z} = -\frac{k_z}{M}z - \frac{C_z}{M}\dot{z} + \frac{1}{M}F_{z,interface} - \frac{F_{z,applied}}{M} \tag{5.144}$$

$$\ddot{x} = -\frac{k_x}{M}x - \frac{C_x}{M}\dot{x} + \frac{1}{M}F_{x,interface} - \frac{F_{x,applied}}{M} \tag{5.145}$$

$$\ddot{y} = -\frac{k_y}{M}y - \frac{C_y}{M}\dot{y} + \frac{1}{M}F_{y,interface} - \frac{F_{y,applied}}{M} \tag{5.146}$$

In the above, the rotor equation of motions is needed to be written separately due to the non-linear terms involving the products of two angular velocities in a single expression. The resulting problem possesses several non-linear terms which will therefore need a numerical solution procedure. The Runge-Kutta or Adams-Bashforth methods are not suited for this class of problem and will require very small time steps in the solution process. As the processes we are studying consist of a high frequency oscillations as well as low frequency components, an implicit stiff solver type is required to evaluate these expressions with

reasonable speed. To further enhance the computational speed, a Jacobian pattern was also supplied to the solver to reduce the initial formulation of the sparse matrix.

To compute the power characteristics from the output states, the following calculations are performed. First, the average power output from the system can be calculated from the applied torque and the steady state speed of the system as given below by,

$$< P_{out} > = < \tau_{applied\,\omega_{rotor}} > where\ \omega_{rotor} = \ \ddot{\theta}_2(t) \tag{5.147}$$

The input power can be obtained through the sensor equation developed earlier. The current of the system is obtained by first taking the time derivative of the sensor equation,

$$\dot{q} = \ \gamma^r \dot{\xi} + \ C_p \dot{V} \tag{5.148}$$

Whereby γ^r is the electromechanical coupling matrix and C_p is the piezoelectric capacitance matrix. From the equations, it can be seen that the power is a function of both the modal amplitudes and the input voltages. Thus, by taking the the product of the current and applied voltages, we can determine the input power,

$$P_{in}(t) = V \cdot \dot{q} = \ V_A(t)\ \dot{q}_A(t) + \ V_B(t)\ \dot{q}_b(t) \tag{5.149}$$

The summation term on the right hand side of the equation arises due to the fact there are only two electrodes pattern (A and B). The efficiency can be calculated by taking the ratio of the output to input power as follows,

$$\eta = \frac{< P_{out} >}{< P_{in} >} \tag{5.150}$$

5.8 Formulations Specific to Present Study

In this chapter, the governing equations of motion for the TRUM system have been derived. It is worthwhile to note the salient differences between the current formulations with existing

literature to bring into focus the specific configuration under study and to help further clarify the additional features and physical effects which the model is trying to capture.

1) The derivation under section 5.2 which shows the formulation of the governing equations of motion for the stator subsystem is common and can be found in existing literature.
2) When formulating the external variational work terms, existing literature which assumes the rotor to have only axial and rotational degree of freedom, handles the term in a straightforward manner.
3) Axisymmetric rotor configuration implies that contact penetration is uniform throughout the domain and predictable. In the current study, asymmetric condition of the rotor configuration breaks the above regularity in geometry.
4) Due to this, the simplicity in the formulation of the work and contact terms from existing literature becomes invalid and becomes more involved as a result.
5) The kinematics of rotor for existing literature is described by only its axial height and rotational angle. To develop the contact penetration law, only a simple subtraction of height differences between rotor height and stator vibrational height is required.
6) The variational work and friction terms from existing literature applies only to simple flat surfaces which needs only resolving in the normal and tangential plane which lies perpendicular to the stator plane.
7) For the current study, point (6) and (7) becomes more complicated because the rotor surface becomes slanted and the rotor/stator contact plane can take any angle.
8) More elaborate kinematics of the stator and rotor surface needs to be defined to address different geometry of surface contact. A contact search and depth computation methods is required to track the changing spatial contact states. And Euler's Equations is needed to describe the dynamics of the rotor.

9) Although the basic rationale for the computations remains the same between formulations from existing literature and the current study. The remaining formulations presented in sections 5.3 to 5.7 have been developed to handle this added complication as brought about by the additional degrees of freedom from the rotor.

5.9 Conclusions

This chapter has introduced the analytical modelling framework for a TRUM system. There are seven developments presented which will be briefly summarized below. First, the basic governing equation of motion for the stator subsystem was derived by using a Rayleigh-Ritz assumed modes energy approach. Basic constitutive relations governing the mechanical and electrical behaviors of the materials were employed and the final equation of motions was without the external forcing terms.

Next, the kinematics of the rotor and stator are formulated by taking into account of first, the effects of stator teeth and second the fact that the rotor is capable of moving in all 6 degree of freedoms. In the derivation, the stator and rotor are both assumed to possess axis-symmetry in their geometry construction. The stator is a non-moving component in terms of rigid body motions but is allowed to oscillate and vibrate about an equilibrium position. The main purpose of this section is to formulate equations that describe the rotor domains as it gets updated after each computation time step. That the rotor states will be reflected in the rotor domain as it moves about. This is to facilitate the computation of contact and penetration in subsequent sections.

After the above, the variational done by external interface forces are formulated. Two non-linear functions are introduced for the derivation; the pressure function which depends on the

presence or absence of gap and the Sign function which depends on the relative velocities between surface points. The Sign function is needed to evaluate and distinguished the sign of the frictional force induce along the interface.

The next section is concerned with the formulation of contact kinematical quantities such as the gap function and the development of an effective strategy to detect the onset of contact and compute contact penetration depth. Basic differential geometry concepts were introduced to compute the normal vector and tangential vector of the tangential plane. A modified gap function to enable preliminary contact detection was also formulated. It is based on the vertical distance between the rotor and stator surfaces. Since the rotor surface cannot be described by a single analytical function, steps for the search for contact points was presented. The approach taken was an incremental iterative process which uses a vector line to gradually approach the rotor surface.

The rigid body dynamic of the rotor was derived last. The translational motion was describe by simple linear Newton's Law of Motion. For the rotation motion description, Euler's equation was employed. Using the Euler's equation, complex gyroscopic forces which couple the rotational motions together can be accounted. However, the coordinates system needs to be a body fixed rotating coordinate system. A strategy to transform moments computed in the fixed global coordinate system to the local rotating frame of reference was presented.

After the above developments, the overall governing equations of motion for the entire TRUM are shown. Numerical methods to solve the system of equations were briefly discussed and the chapter concludes by showing how power characteristics can be calculated from the system parameters.

Chapter 6 -- Analytical Computation of the Parasitic Rippling and Ultrasonic Frequencies

6.1 Background of Rippling and Ultrasonic High Frequency Issues

In the previous chapter it was observed from both harmonic FEM study and frequency response experiment that there exist significant parasitic vibrations which range from the case of a very low frequency at around a couple of hundreds of hertz to thousand hertz to the very high ultrasonic excitation frequencies. Low frequency vibrations can be mitigated by appropriate servo control strategies but they can become a real problem if the amplitude becomes too large and affects the overall bandwidth and performance of the HDD. High frequency vibrations which transmit to the slider, on the other hand, directly impact on the read write capability by inducing resonance of the slider and creating uncontrollable high frequency motions.

The results from the previous chapter suggest to us that the low frequency rippling phenomena arises due to the rigid body motions of the rotor-spring-stator system. Whenever one of the contacting teeth-rotor zones are removed from the model, the rotor will display a swaying motion that involves the body oscillating about the “fixed” stator teeth zones with the pre-loading spring providing the necessary restoring force for the vibrating system. Together with collected experimental data, it points to the fact that offsetting translational vibrational motion of the rotor does indeed get excited and is manifested in actual TRUM actuator operations. Furthermore, though it is not surprising, it is found that changing the spring preloading design can influence not only the rippling vibration, but also the level of high frequency parasitic vibrations transmitted in the sense that it is by acting like a filter.

6.2 Non-Uniformity in Micro impacts of forces and moments distributions as source of parasitic vibrations

The problem then, with the current state of the art analytical model available in the literature is that none of them have studied how the overall rigid body rotor dynamics of TRUM rotor interacts with the vibrating stator and thus no models are available which incorporate the capability to simulate or capture these effects. As mentioned previously, only rigid body motion along the rotational axis and axial directions are commonly included, the other 4 degrees of freedom have not been dealt with. The filtering effect of the pre-loading spring stiffness and damping has also not been included into their modelling framework. Thus, the motivation of the present work is to address this gap and hopes that with such an introduction into the modelling framework, we will be able to better capture the remaining dynamics of the rotor and gain a better understanding of the overall stator induced vibrational characteristics of the rotor. Many authors have suggested the importance and studied rotor flexibility in influencing the TRUM behaviour. However, such studies have also restricted the analysis within the domain of penetration quantification among vibrating bodies and how such interactions affects motor overall speed performance. They also do not consider and concern themselves specifically with the other rotor rigid body motions induced as such if there is any. Such an inclusion, though, could be a useful enhancement for future study in this work.

In an ideal symmetric analytical model whereby the rotor is only allowed axial and rotational motion, the results from the model developed in this thesis does not indicate the existence of such rippling phenomena or high ultrasonic vibrations transmission. Such a condition was achieved simply by setting the initial conditions for angular tilt orientations to be zero. By virtue of the symmetry of the problem, there will not be an uneven distribution of forces. This

is illustrated in Figure 6.1 below whereby forces and moments balanced out due to equal depth of penetration.

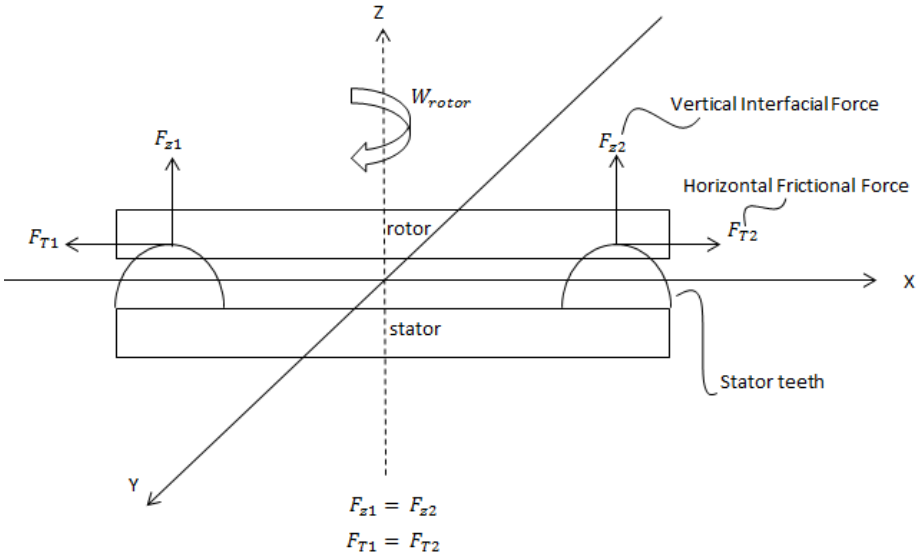

Figure 6.1: Uniform force and moment as there is no uneven penetration in the model

To simulate and excite the tilting and translation modes, an initial perturbation in the form of a slight tilt angle of around 0.00001 rad was introduced. This is to break the symmetry and introduce a form of disturbance such that different penetration depth results and the force and moment distribution changes. This is illustrated in Figure 6.2 below,

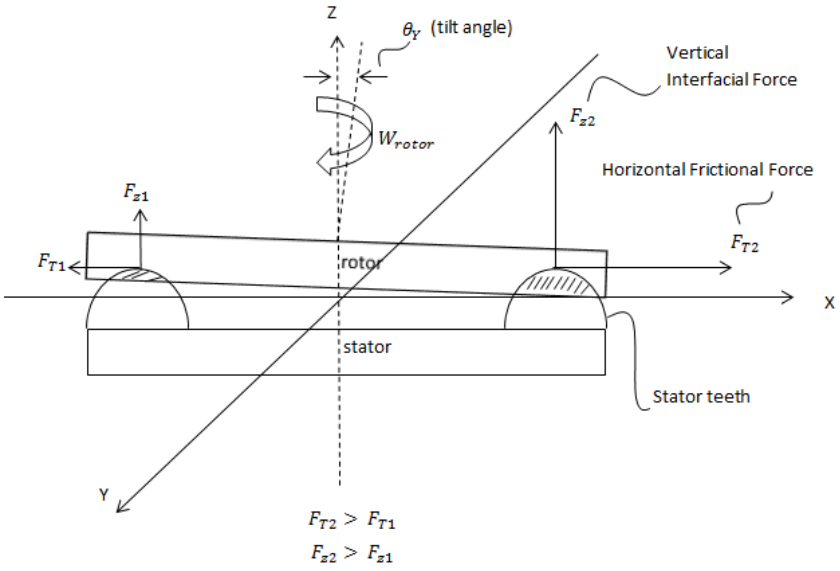

Figure 6.2: Initial tilting disturbance conditions results in uneven penetration depth

What we are interested here in this study is the resultant in plane motions that would be induced due to the uneven dragging forces. This would become the in-plane horizontal vibration of the actuator arm. The tilting vibrations itself then translate physically as the axial vibrations experienced by the actuator arm tip. It is worth mentioning that such "breakage" in symmetry of loading conditions in a TRUM actuator is not uncommon. This is because of limited engineering precision during the fabrication processes and the need to allow for clearances during the entire stack up and assembly process. All these engineering allowances only mean that geometrically, between the many components there would exist small gaps and clearances, misalignments, eccentricity of shafts and differences in fits tolerances to name a few for example.

For the TRUM HDD actuator which we are studying, such imperfections could come from misalignment of stator teeth, different teeth height, non-parallelism of rotor and stator surface, uneven assembly of springs which could result in the form of a bias torque applied, insufficient surface flatness and roughness control of the rotor, bearing eccentricity

misalignment and even the tightening of torque screw caps can deform the structure and introduces micro distortions into the stack up. All these may seem to be of little importance as long as the motor runs and works normally. However, if the objective is to employ such an actuator device for high speed precision positioning device for HDD applications, they become very important considerations. As the results to be presented later shows, small bias torque and tilted conditions can and do produce very small motions in the read write plane. They could be small for normal motor standards, but for HDD purpose, 50nm is a lot due to the high track density requirements.

To narrow down the scope of our study in this thesis, two perturbation factors will be studied as the factors that mimic the geometrical imperfections discussed earlier. First, a simple slight tilt is introduced to stimulate the conditions whereby the rotor is not perfectly parallel to the stator and possess a slight clearance. The second condition is when we applied a bias torque constantly to the system, this is to emulate the conditions whereby the spring is misaligned and thus is in a slightly deformed configuration throughout the operations. For each condition, two cases will be studied with the two springs discussed earlier, the new version of the flat pull spring and the cylinder spring. Table 1 below summarises the 4 cases.

	CYLINDER SPRING	PULL SPRING
Initial Tilt	Case 2	Case 1
Initial Tilt + Bias Torque	Case 4	Case 3

Table 6.1: 4 case studies

6.3 Simulation Results

It is interesting to note that the simulation results show up many unknown high frequency peaks generated in the spectrum apart from the ultrasonic vibration and spring rippling

frequency. Their origin is not clear at this moment but the regularity and constancy in which they show up in the different cases suggest that they are not simple noise but could be due to the complex-non-linear interaction between the rotor and stator model. To quantify the spring performance, we will look at the axial and radial vibrations generated in the rippling and ultrasonic frequencies only. To compute the axial vibrations due to tilt, a nominal 20mm of moment arm is times with the angular displacements.

The dynamic responses of the rotor in the rotational Z-axis for the 4 cases under study are shown in Figure 6.3 to Figure 6.10 respectively. It can be observed that the rotational speed of the four cases did not show much difference and are nearly identical in both the time and frequency domains. This is because there aren't much major changes in the operational conditions between the four cases. A slight bias tilting of the rotor of the order of micro radians cannot be considered to affect the pre-load or major vibrational amplitude. Both the time and frequency domain also did not exhibit significant ultrasonic vibrations components. It can therefore be inferred that slight angular distortions does not affect the rotor rotational motion significantly. Tables 6.2 to 6.5 below summarize the results.

	Pull Spring – Case 1 (nm)				
Frequency	**1165.5 Hz**	**30.930 kHz**	**88.4Hz**	**119 kHz**	**128kHz**
θ_z					
θ_x	-	0.3183	-	-	0.001399
θ_y	-	157	-	-	0.21886
z	-	-	-	6.7	-
x	54.72	-	0.3566	Not detected	-
y	9.51	-	0.000754	Not detected	-

Table 6.2: Pull Spring – Case 1

	Cylinder Spring – Case 2 (nm)				
Frequency	**383.85 Hz**	**30.930 kHz**	**88.4Hz**	**119 kHz**	**128kHz**
θ_z					
θ_x	-	0.6876	-	-	0.001015
θ_y	-	119.6	-	-	0.1695
z	-	-	-	6.79	-
x	220	-	0.256	Not detected	-
y	37.45	-	0.00478	Not detected	-

Table 6.3: Cylinder Spring – Case 2

	Pull Spring – Case 3 (nm)				
Frequency	**1165.5 Hz**	**30.930 kHz**	**88.4Hz**	**119 kHz**	**128kHz**
θ_z					
θ_x	-	3.34	-	-	0.2299
θ_y	-	488.73	-	-	0.683
z	-	-	-	6.8	-
x	79.7	-	-	1.79	-
y	16.78	-	0.02352	0.0264	-

Table 6.4: Pull Spring – Case 3

	Cylinder Spring – Case 4 (nm)				
Frequency	**383.85 Hz**	**30.930 kHz**	**88.4Hz**	**119 kHz**	**128kHz**
θ_z					
θ_x	-	2.2194	-	-	0.003295
θ_y	-	356.1	-	-	0.5393
z	-	-	-	6.58	-
x	341.49	-	0.8235	1.184	-
y	67	-	0.01837	0.02713	-

Table 6.5: Cylinder Spring – Case 4

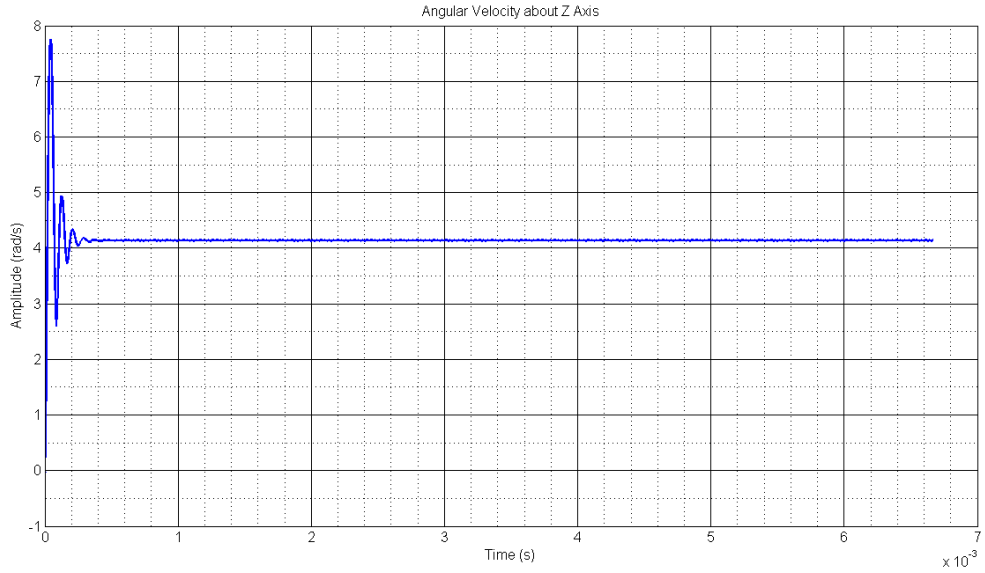

Figure 6.3: Case 1 – Pull Spring Angular Velocity about Z Axis (time)

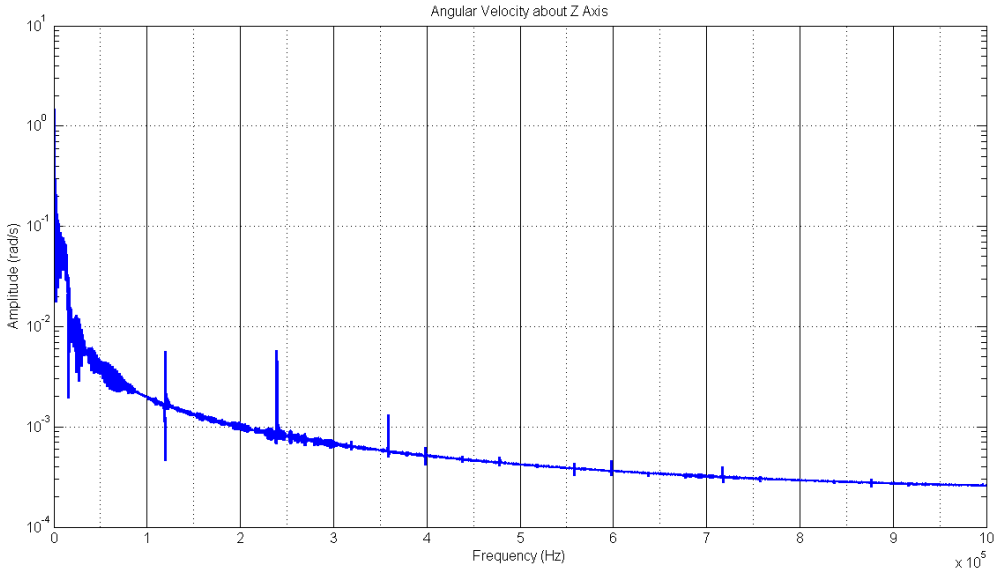

Figure 6.4: Case 1 – Pull Spring Angular Velocity about Z Axis (frequency)

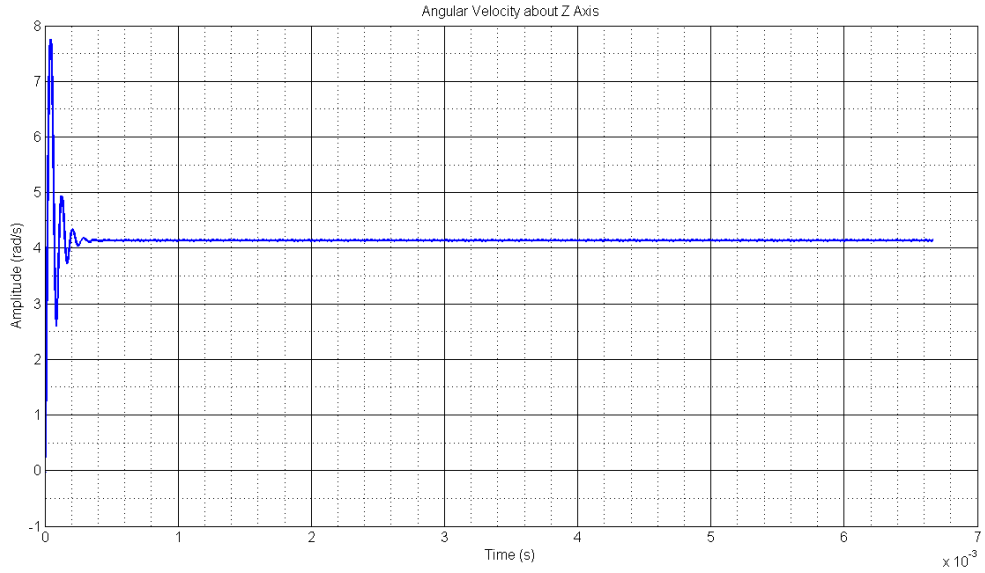

Figure 6.5: Case 2 – Cylinder Spring Angular Velocity about Z Axis (time)

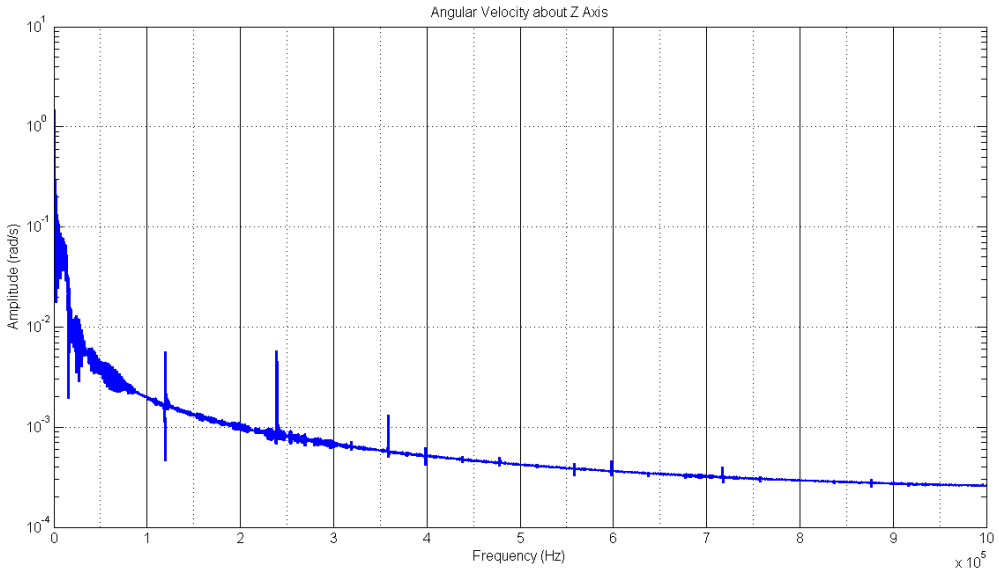

Figure 6.6: Case 2 – Cylinder Spring Angular Velocity about Z Axis (frequency)

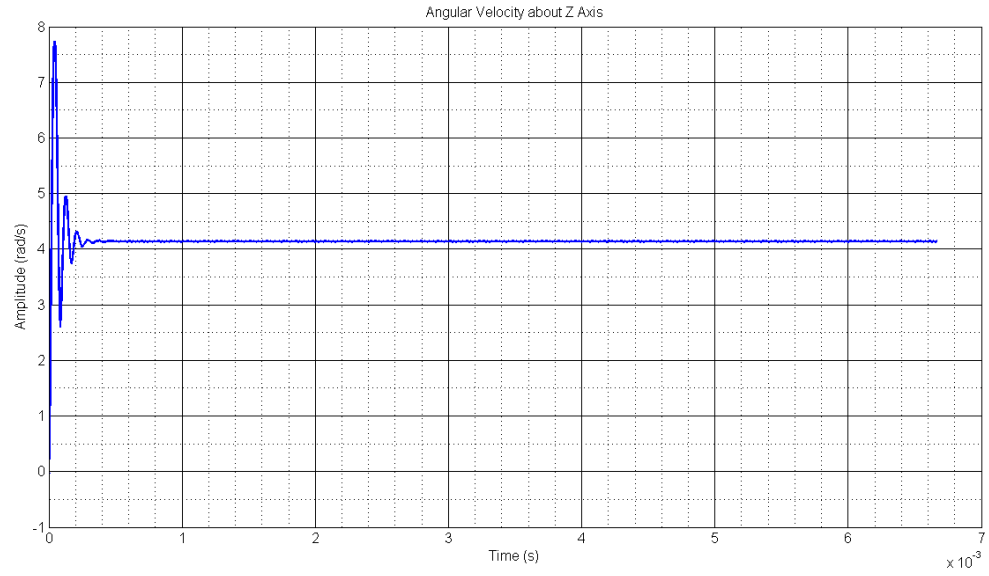

Figure 6.7: Case 3 – Pull Spring Angular Velocity about Z Axis (time)

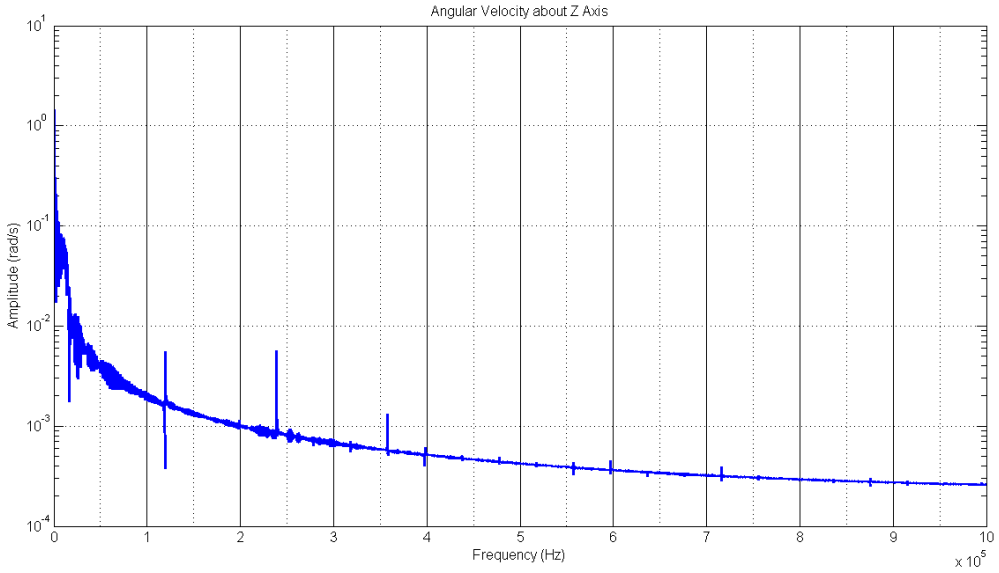

Figure 6.8: Case 3 – Pull Spring Angular Velocity about Z Axis (frequency)

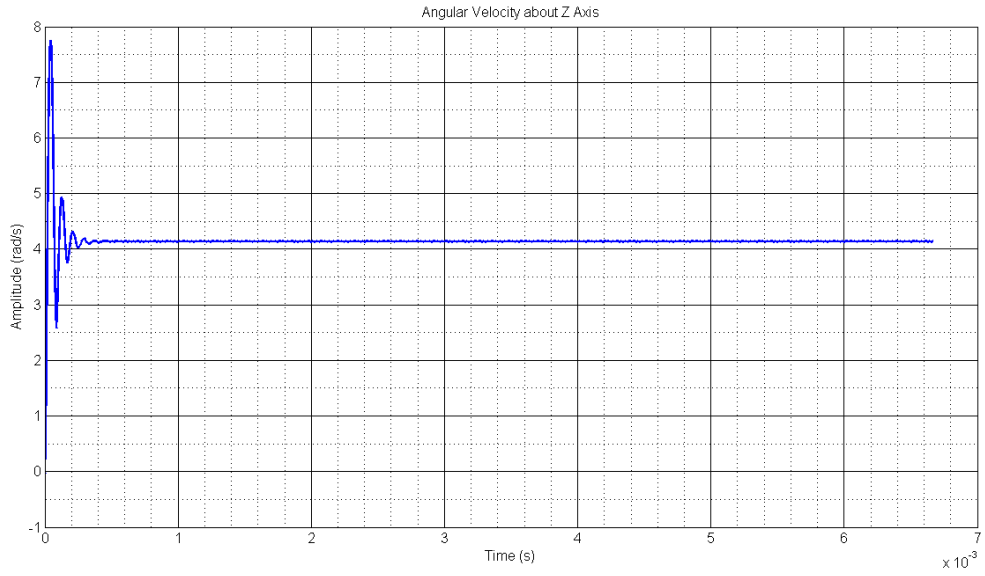

Figure 6.9: Case 4 – Cylinder Spring Angular Velocity about Z Axis (time)

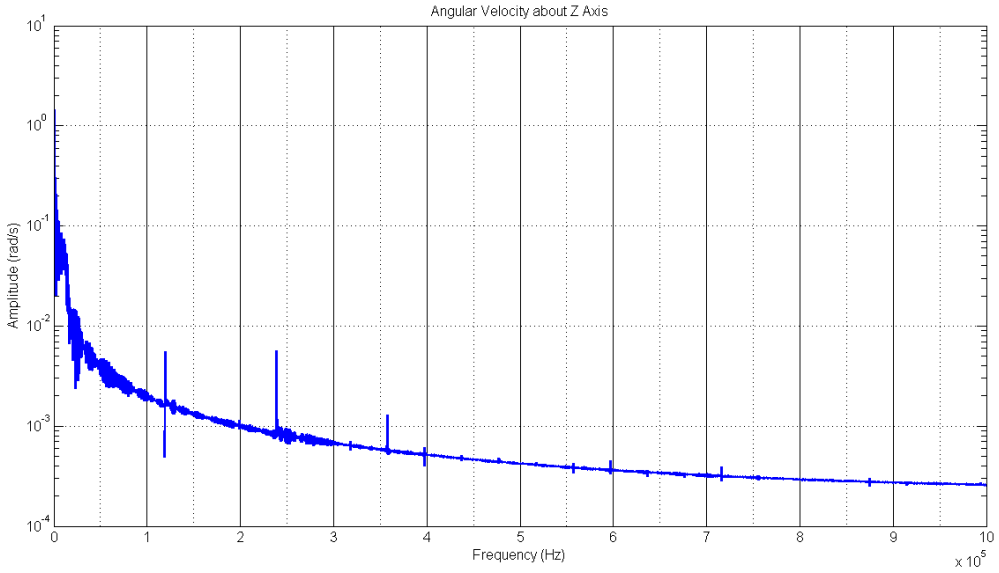

Figure 6.10: Case 4 – Cylinder Spring Angular Velocity about Z Axis (frequency)

Figure 11 to Figure 18 below show the dynamic responses of the rotor in the rotational X-axis for the 4 cases under study, respectively. First, it can observe that the tilting vibrations experienced by both the cylinder and flat spring model increases with increasing bias tilt torque. At ultrasonic frequency, for the cylinder spring, the vibrations increase from 0.001015 nm to 0.003295 nm while for the flat spring model, the vibrations increase from 0.001399 nm to 0.2299 nm. Second, the cylinder spring model shows an overall reduced level of vibrations in both conditions of applied bias torque. This is directly the result of it having higher angular stiffness and hence is less prone to be distorted by the same forces. It should be mentioned that the bias torque was applied along the angular Y axis and that the tilting vibrations manifested here is simply the result of the gyroscopic coupling present in the model whereby all angular motions are related by the Euler's equation. Thus, compared with the angular vibrations experienced along the Y-axis, the induced vibrations here is much lesser and smaller.

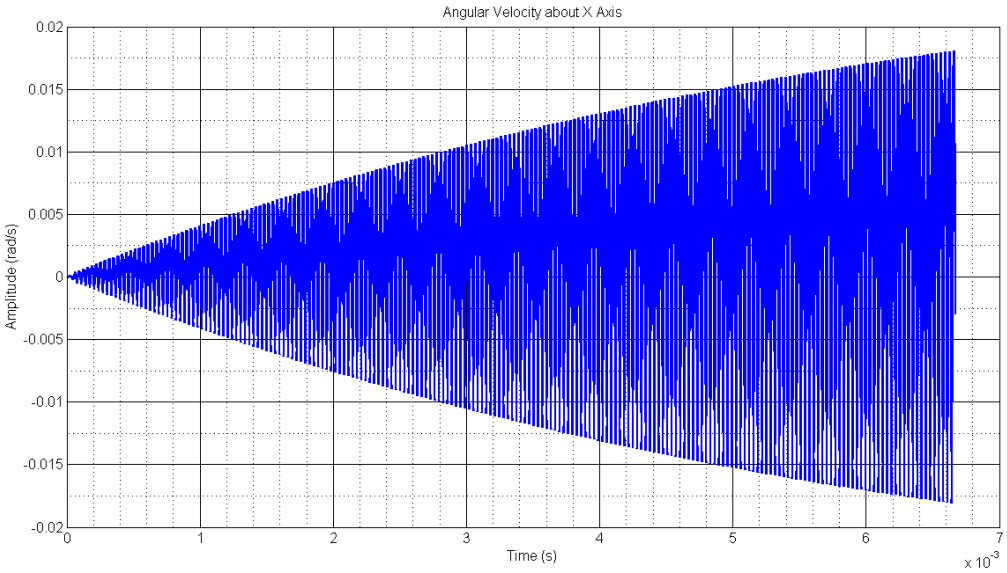

Figure 6.11: Case 1 – Pull Spring Angular Velocity about X Axis (time)

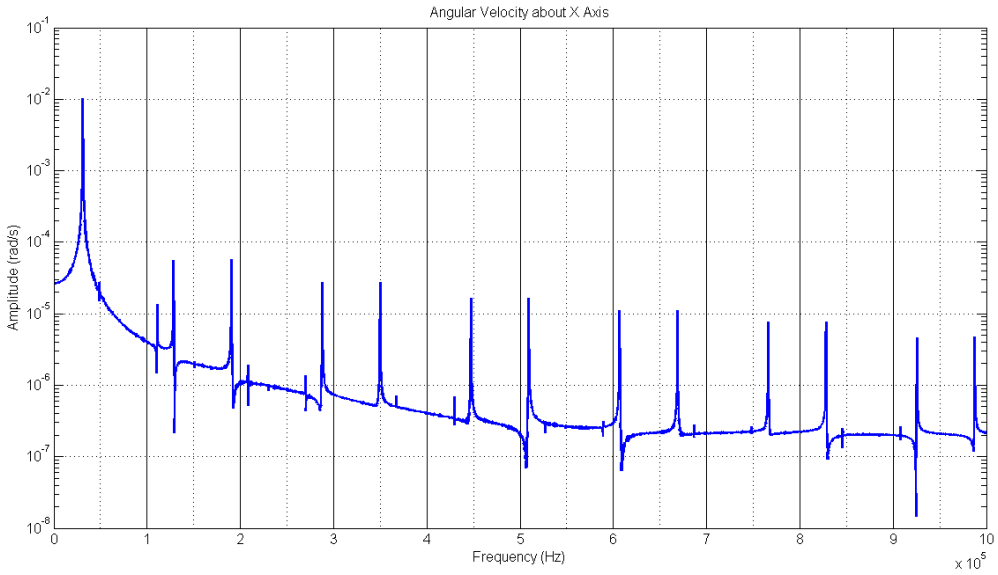

Figure 6.12: Case 1 – Pull Spring Angular Velocity about X Axis (frequency)

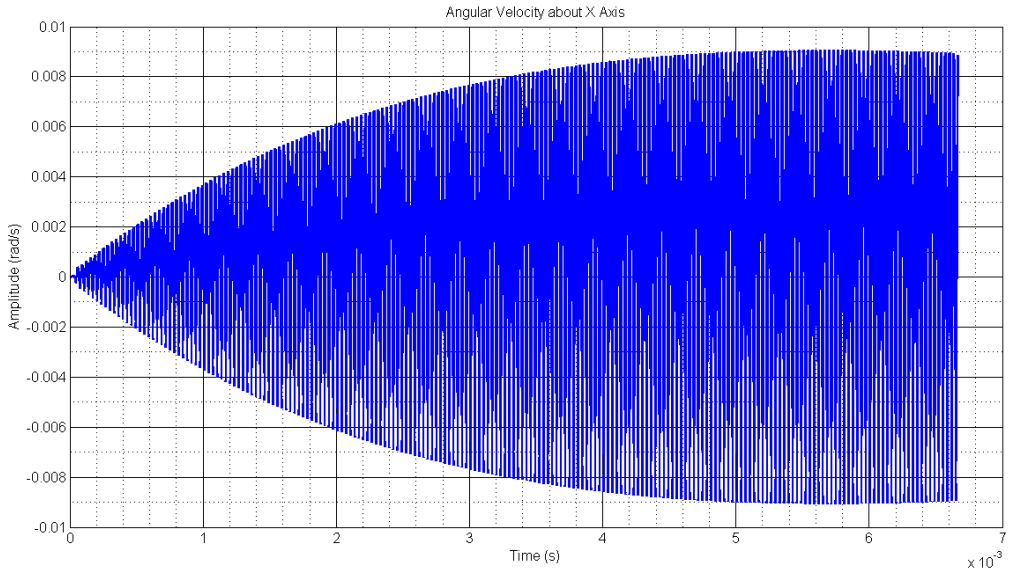

Figure 6.13: Case 2 – Cylinder Spring Angular Velocity about X Axis (time)

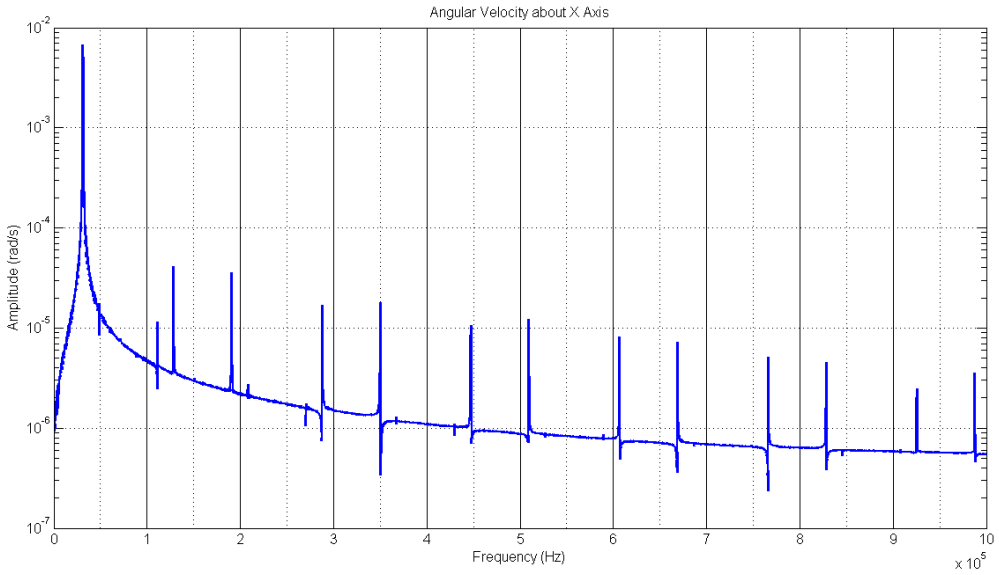

Figure 6.14: Case 2 – Cylinder Spring Angular Velocity about X Axis (frequency)

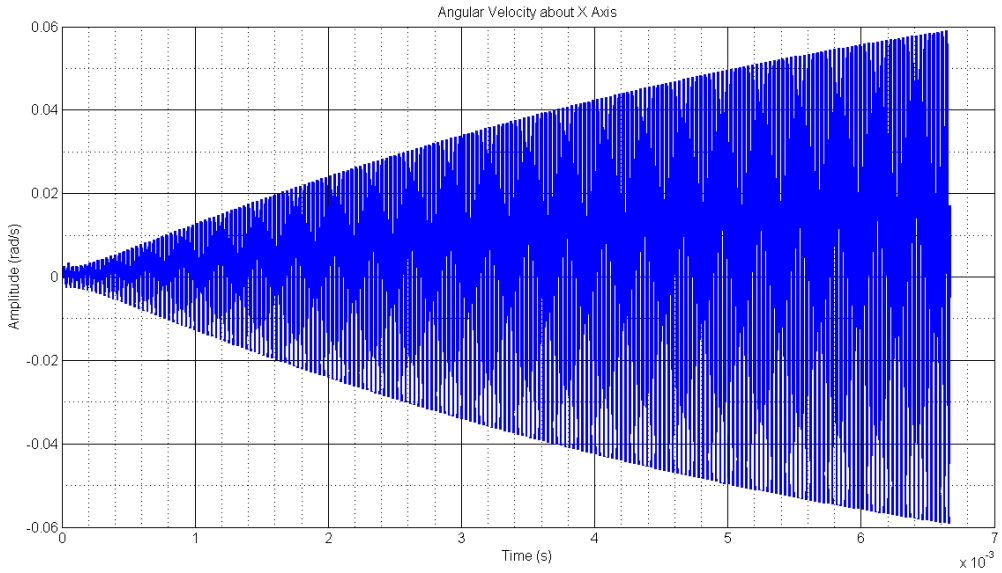

Figure 6.15: Case 3 – Pull Spring Angular Velocity about X Axis (time)

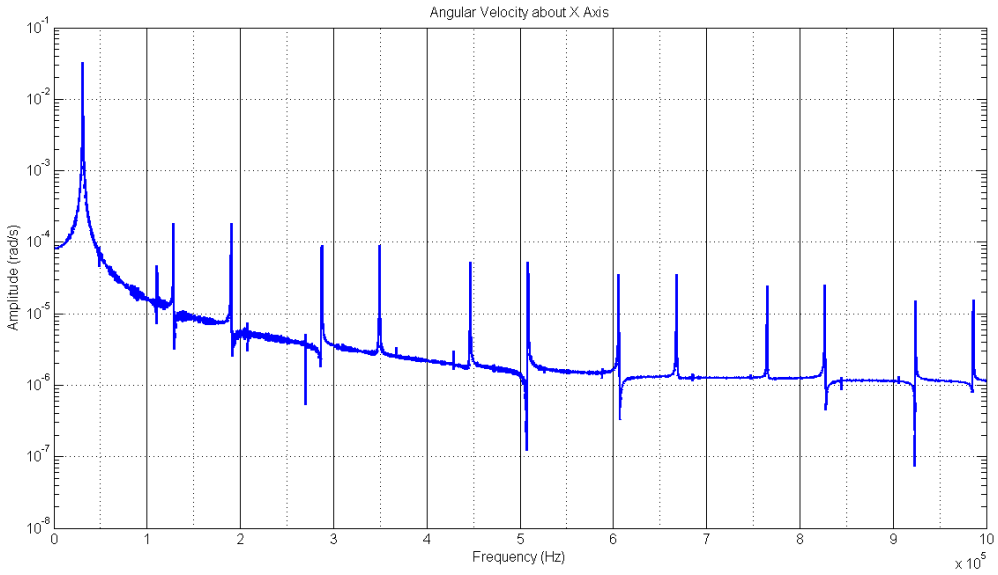

Figure 6.16: Case 3 – Pull Spring Angular Velocity about X Axis (frequency)

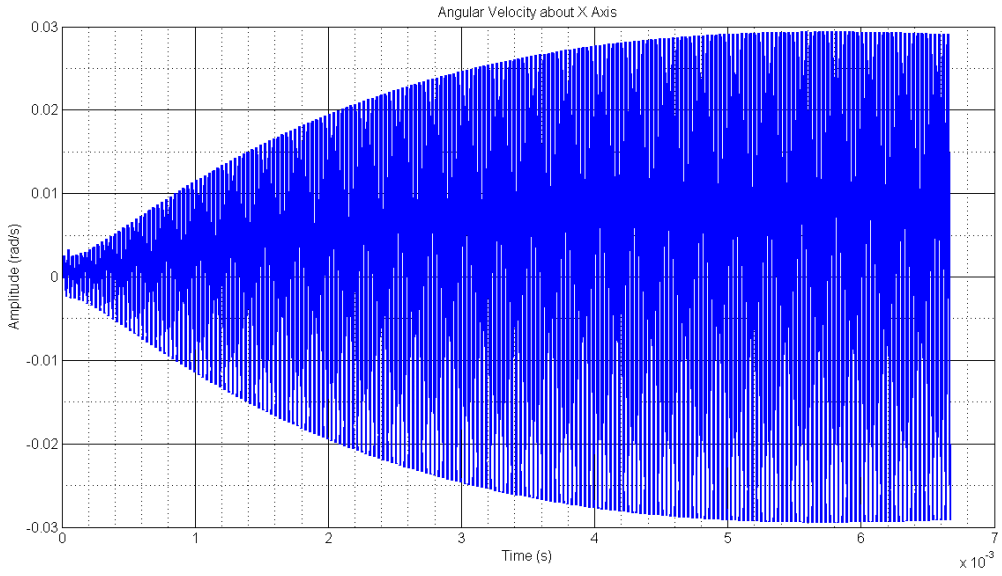

Figure 6.17: Case 4 – Cylinder Spring Angular Velocity about X Axis (time)

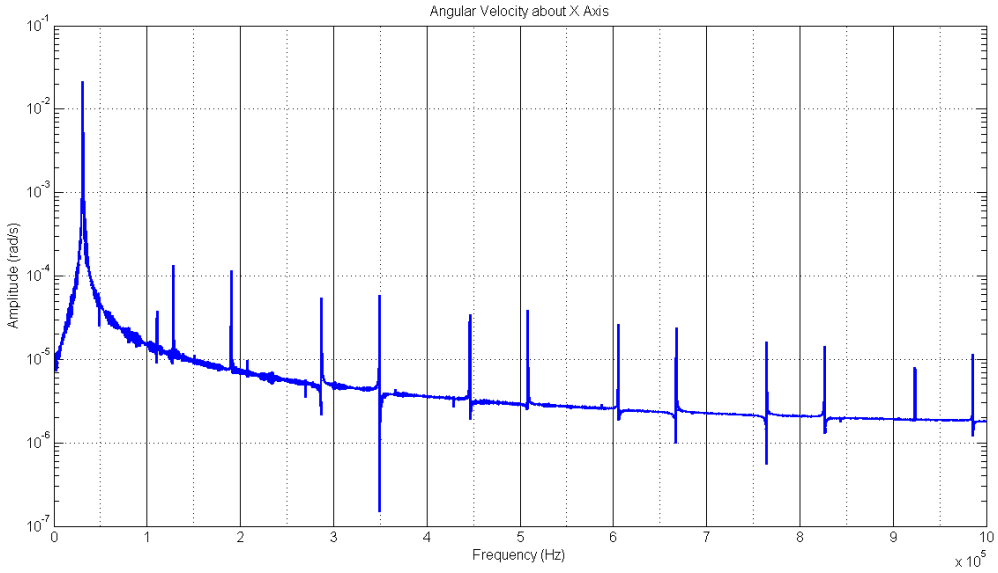

Figure 6.18: Case 4 – Cylinder Spring Angular Velocity about X Axis (frequency)

The dynamic responses of the rotor in the rotational Y axis are shown in Figure 19 to Figure 26 below respectively. It can be inspected that the level of tilting vibrations is much higher than that experience compared to the rotational X axis. The reason is that this is the direction whereby the initial perturbation is being introduced into the model. However, the behaviour of the tilting vibrations with increased spring stiffness and increases applied bias torque remains the same. First, it can observe that the tilting vibrations experienced by both the cylinder and flat spring model increases with increasing bias tilt torque. For the cylinder spring, the vibrations increase from 0.1695 nm to 0.5393nm while for the flat spring model, the vibrations increases from 0.21886nm to 0.683nm. Second, the cylinder spring model shows an overall reduced level of vibrations in both conditions of applied bias torque.

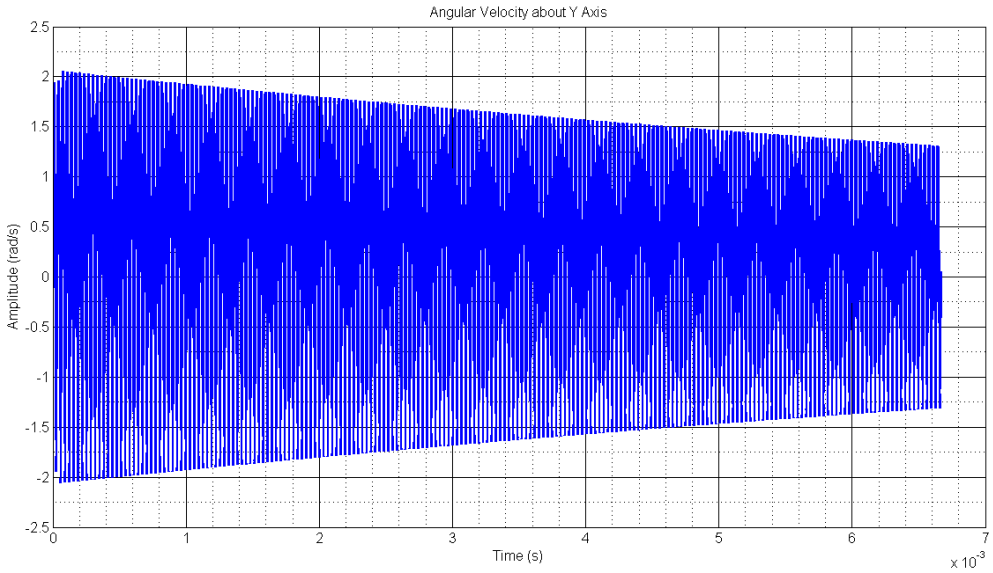

Figure 6.19: Case 1 – Pull Spring Angular Velocity about Y Axis (time)

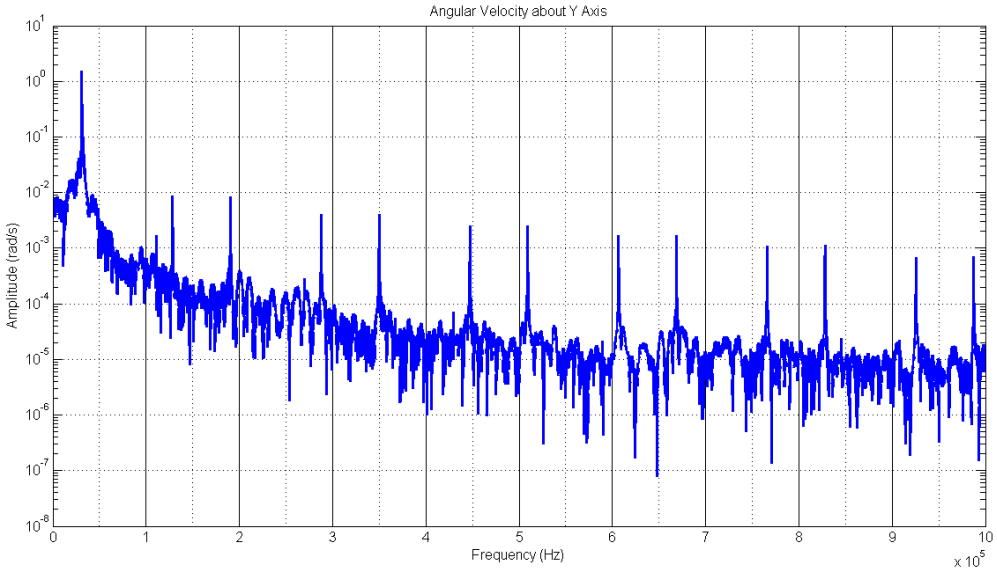

Figure 6.20: Case 1 – Pull Spring Angular Velocity about Y Axis (frequency)

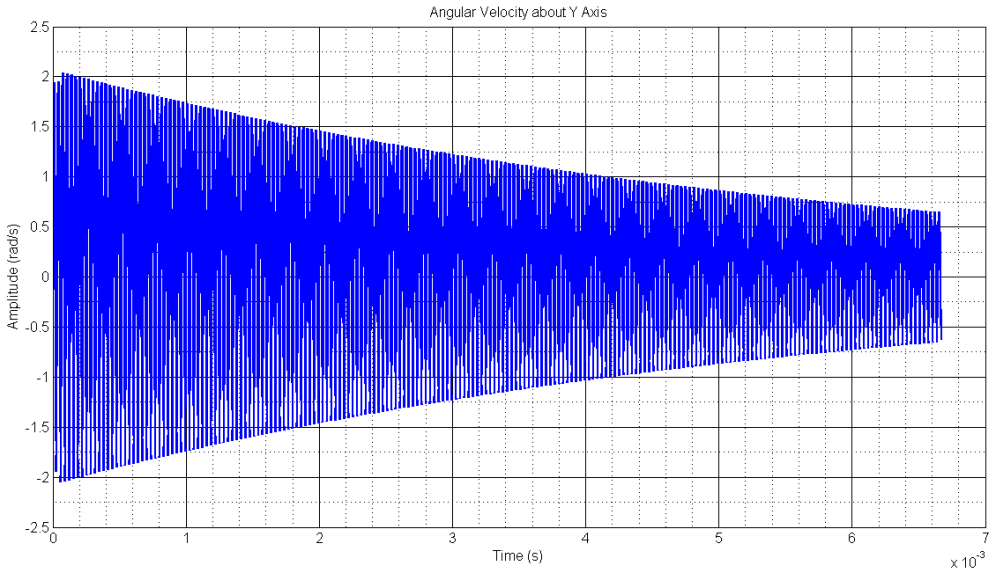

Figure 6.21: Case 2 – Cylinder Spring Angular Velocity about Y Axis (time)

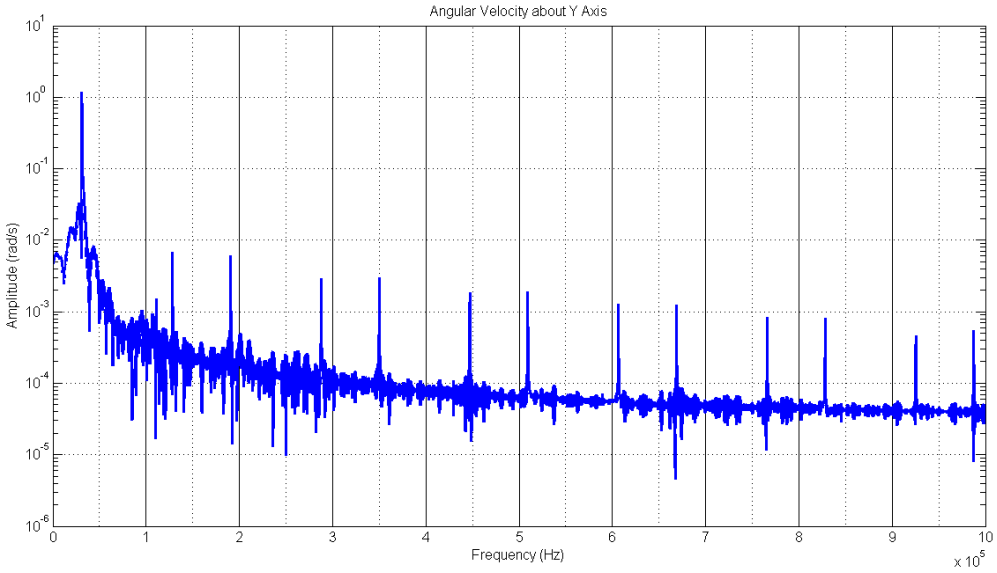

Figure 6.22: Case 2 – Cylinder Spring Angular Velocity about Y Axis (frequency)

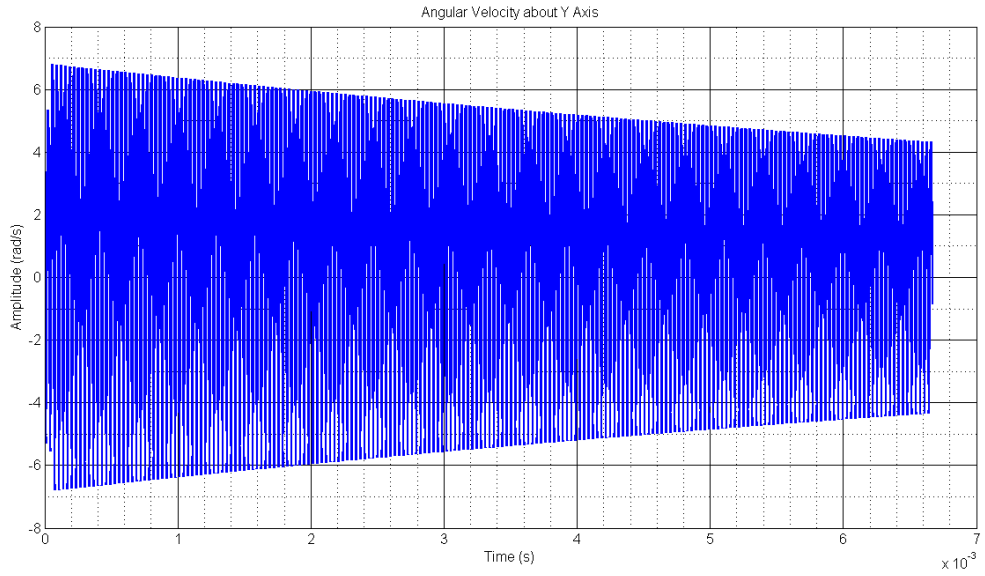

Figure 6.23: Case 3 – Pull Spring Angular Velocity about Y Axis (time)

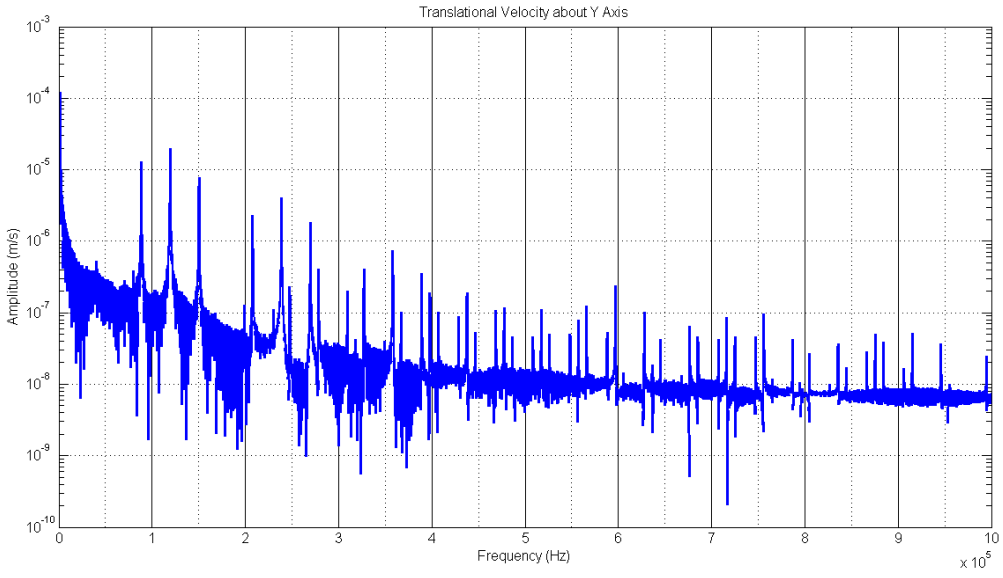

Figure 6.24: Case 3 – Pull Spring Angular Velocity about Y Axis (frequency)

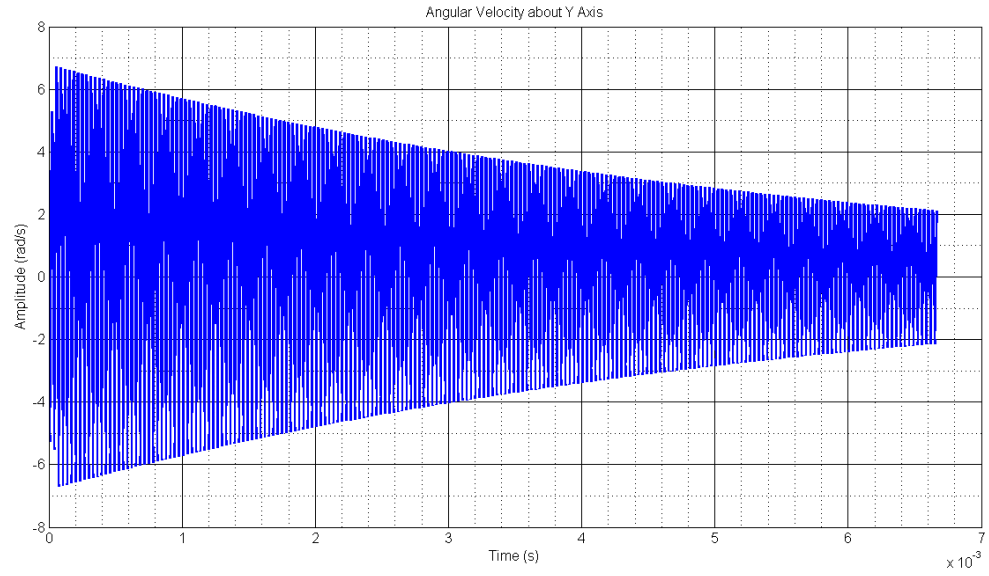

Figure 6.25: Case 4 – Cylinder Spring Angular Velocity about Y Axis (time)

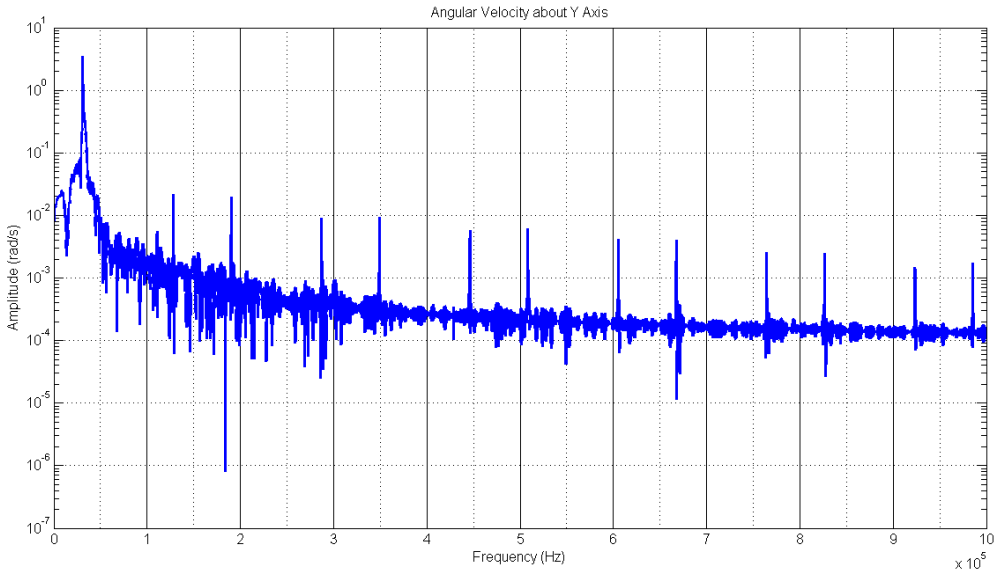

Figure 6.26: Case 4 – Cylinder Spring Angular Velocity about Y Axis (frequency)

Figure 27 to Figure 34 below show the dynamic responses of the rotor translational axial vibrations for the 4 cases under study. First, it can be observed from the time and frequency domains that the levels of ultrasonic vibrations experienced by the rotor are relatively stable. There isn't any clear trend exhibited between the two spring types as well as for different bias torque applications. This could be due to the fact that first, the axial stiffness of the two springs is relatively similar. Second and more importantly, the axial vibrational behaviour is governed pre-dominantly by the level of preloading and damping in this condition. This is similar to the situation whereby we can imagine the rotor is being pressed firmly down onto the stator surface. The level of compression and forces generated is relatively large and usually far outweighs the dissimilarity introduced by the tilting. Lastly, taken as a whole, when we do force integration over the entire stator surface to compute axial interface forces in the simulation, the dissimilarity in axial force distributions actually cancels out and comes back to the same value to equilibrate with the applied axial pre-load.

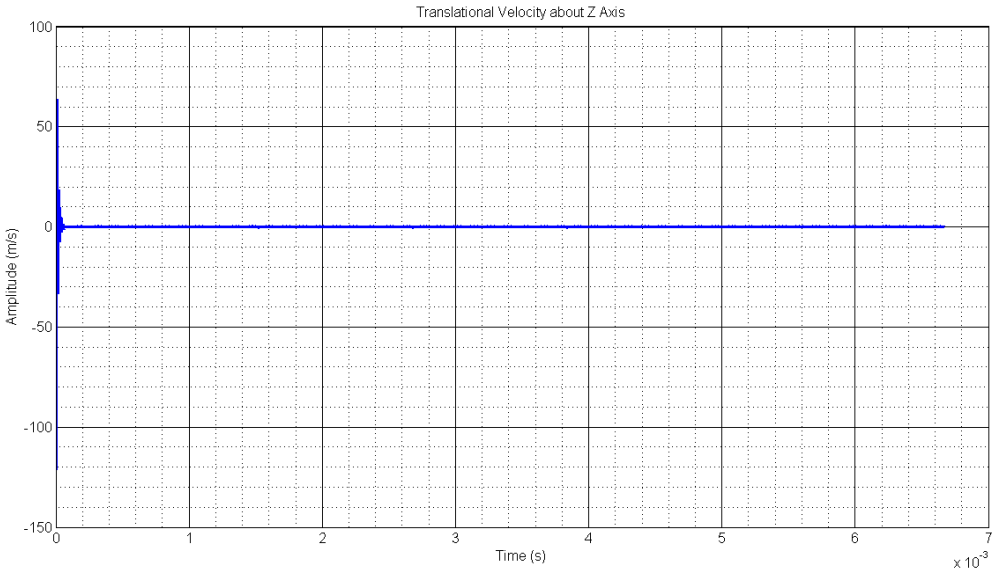

Figure 6.27: Case 1 – Pull Spring Translational Velocity about Z Axis (time)

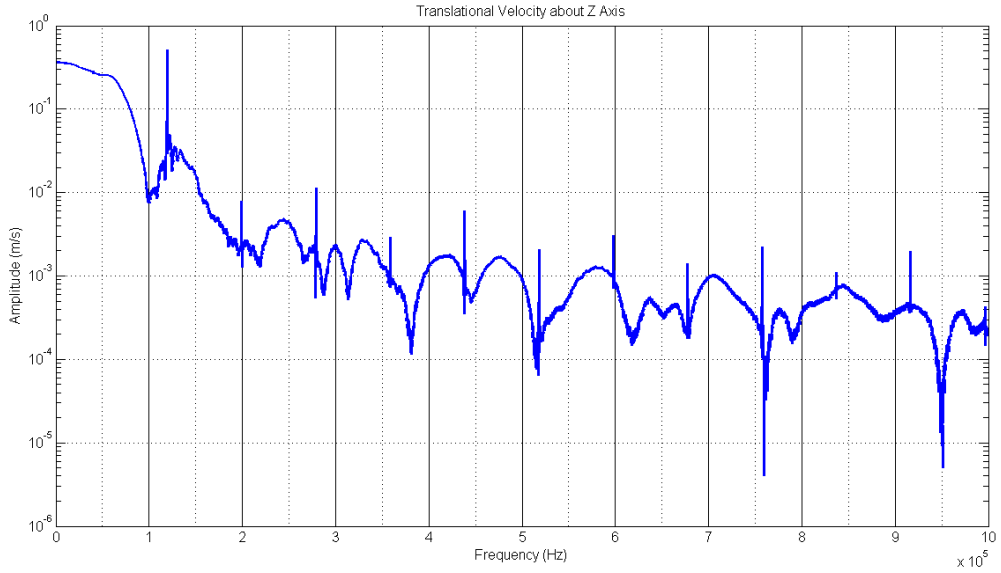

Figure 6.28: Case 1 – Pull Spring Translational Velocity about Z Axis (frequency)

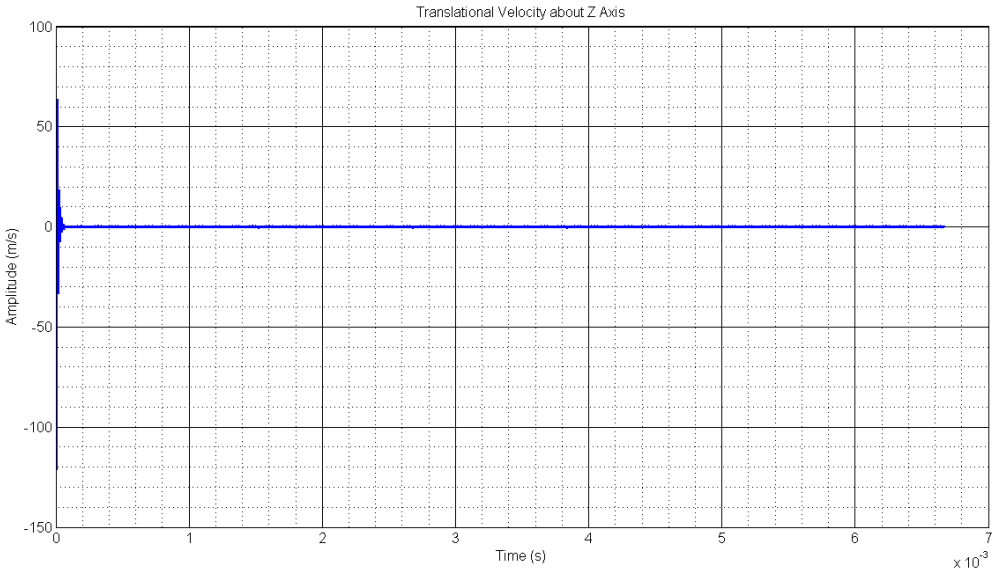

Figure 6.29: Case 2 – Cylinder Spring Translational Velocity about Z Axis (time)

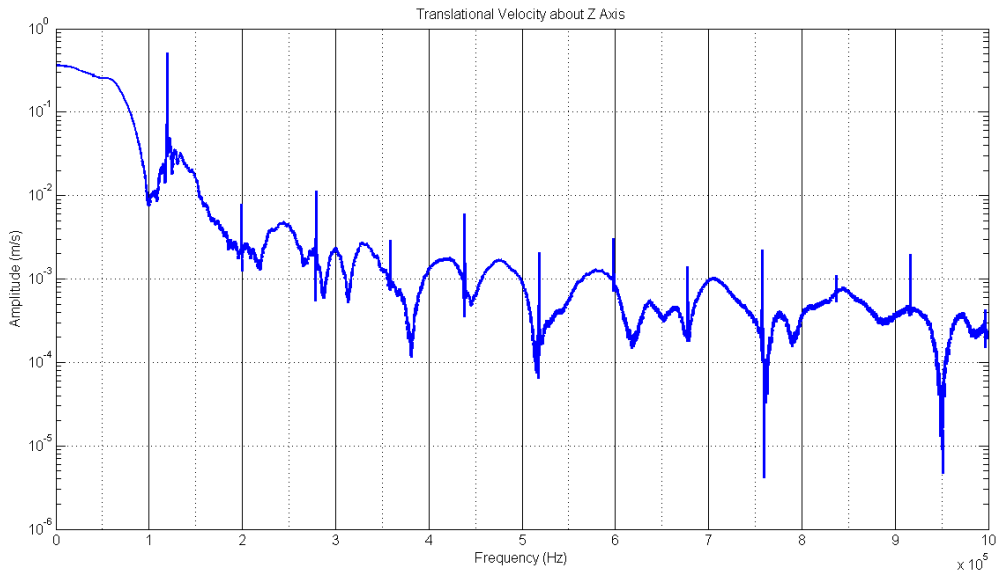

Figure 6.30: Case 2 – Cylinder Spring Translational Velocity about Z Axis (frequency)

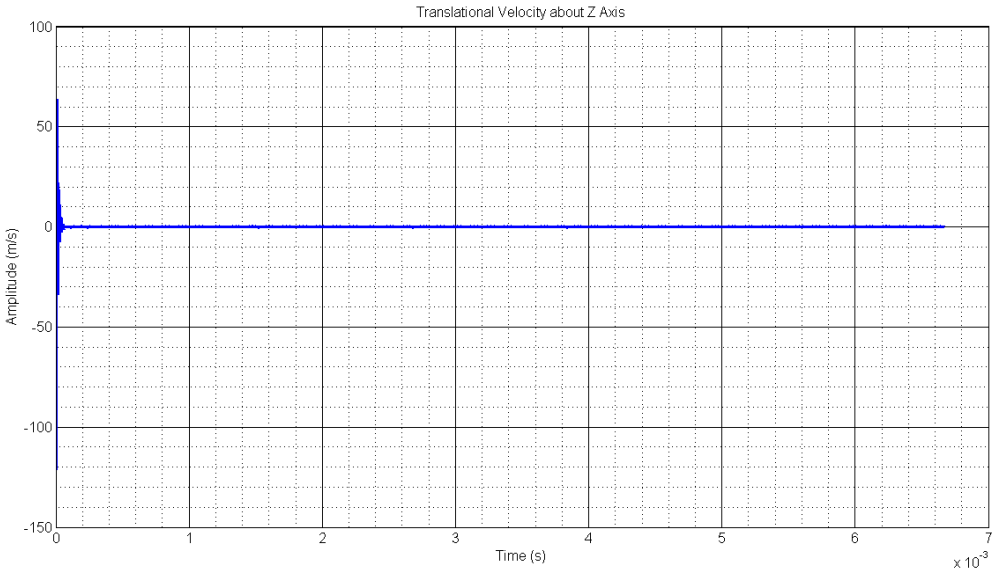

Figure 6.31: Case 3 – Pull Spring Translational Velocity about Z Axis (time)

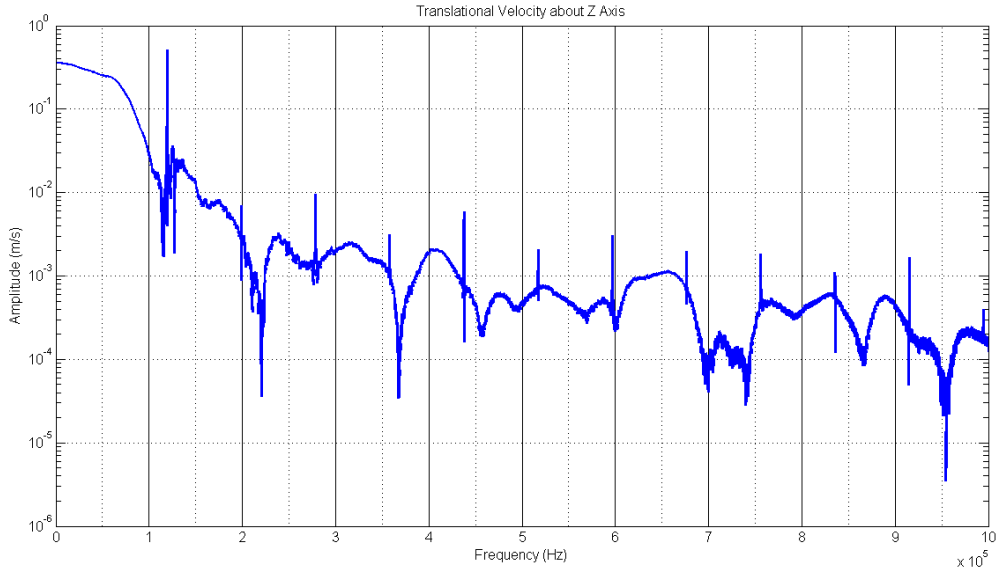

Figure 6.32: Case 3 – Pull Spring Translational Velocity about Z Axis (frequency)

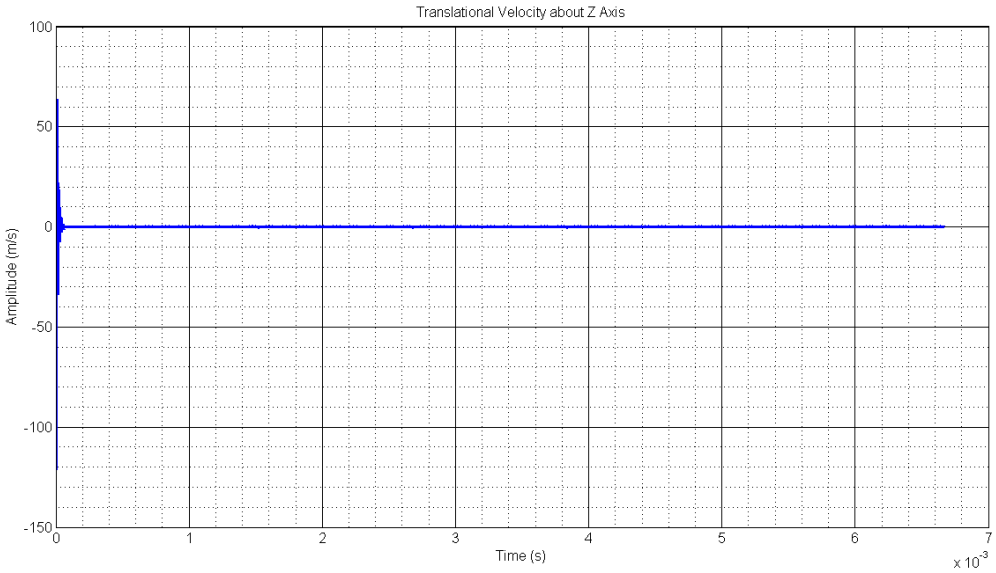

Figure 6.33: Case 4 – Cylinder Spring Translational Velocity about Z Axis (time)

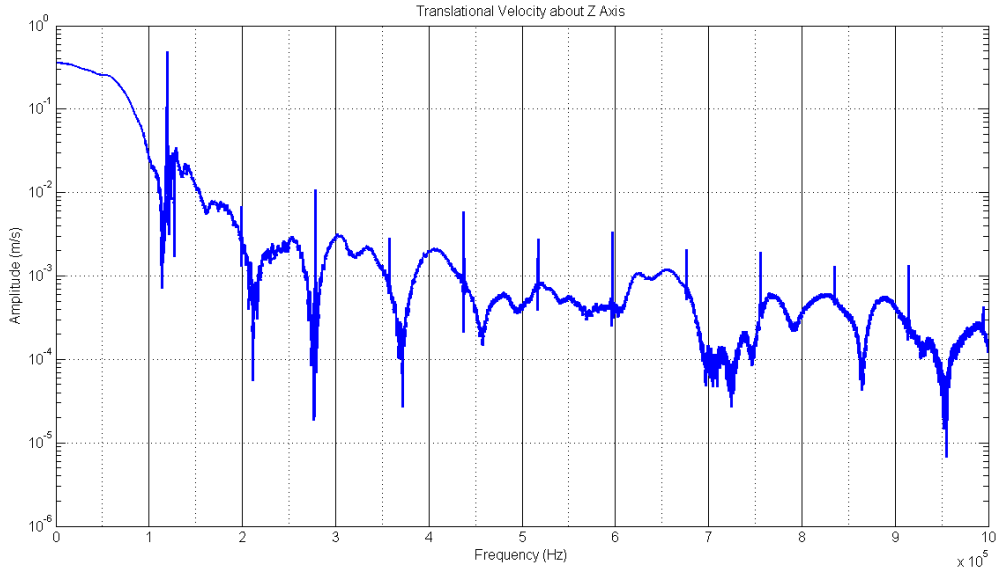

Figure 6.34: Case 4 – Cylinder Spring Translational Velocity about Z Axis (frequency)

The dynamic responses of the rotor in the translational X axis from the 4 case studies are shown from Figure 35 to Figure 42 respectively. From both the time and frequency domain data, it can be seen that the trend exhibited in the behaviour of the motion induced follows very closely with the case involving the tilting motions. First, it can observe that the translational vibrations experienced by both the cylinder and flat spring model increases with increasing bias tilt torque. For the cylinder spring, the vibrations increase from 220 nm to 341.49nm while for the flat spring model, the vibrations increases from 54.72nm to 79.7nm. Second, the flat spring model shows an overall reduced level of vibrations in both conditions of applied bias torque. This is due to the fact that the flat spring is actually stiffer in the radial direction than the cylinder spring. Furthermore, it should be mentioned that the bias torque was applied along the angular Y axis and that the translational motions manifested here along the X axis is simply the result of the breakage in force similarity along the X direction. Thus, compared with the translational vibrations experienced along the Y-axis, the induced vibrations here is much greater.

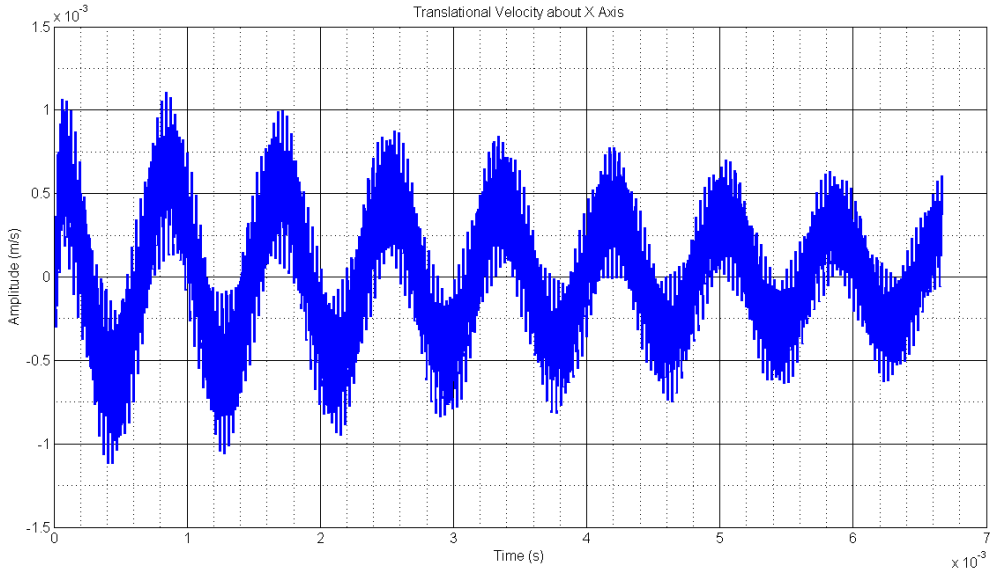

Figure 6.35: Case 1 – Pull Spring Translational Velocity about X Axis (time)

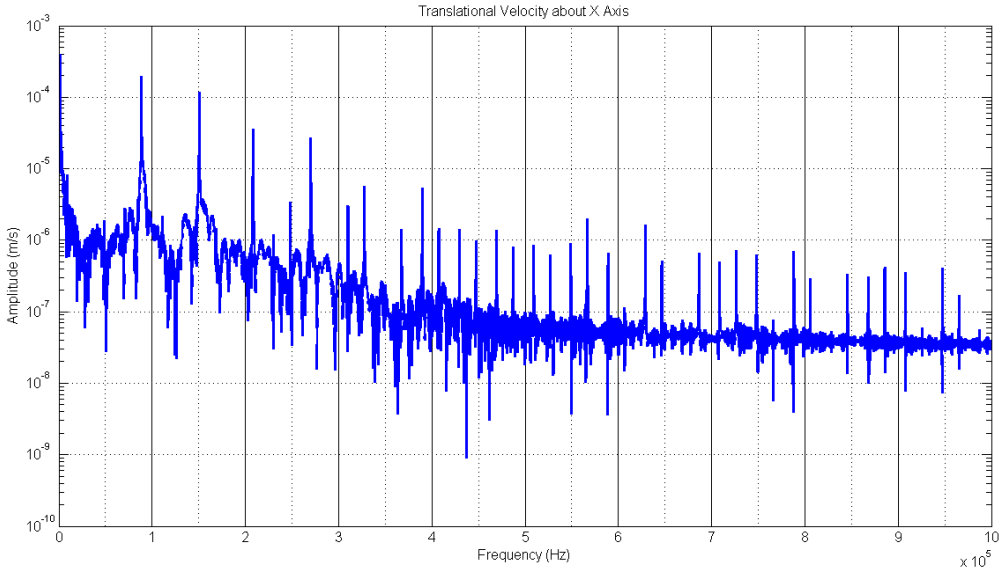

Figure 6.36: Case 1 – Pull Spring Translational Velocity about X Axis (frequency)

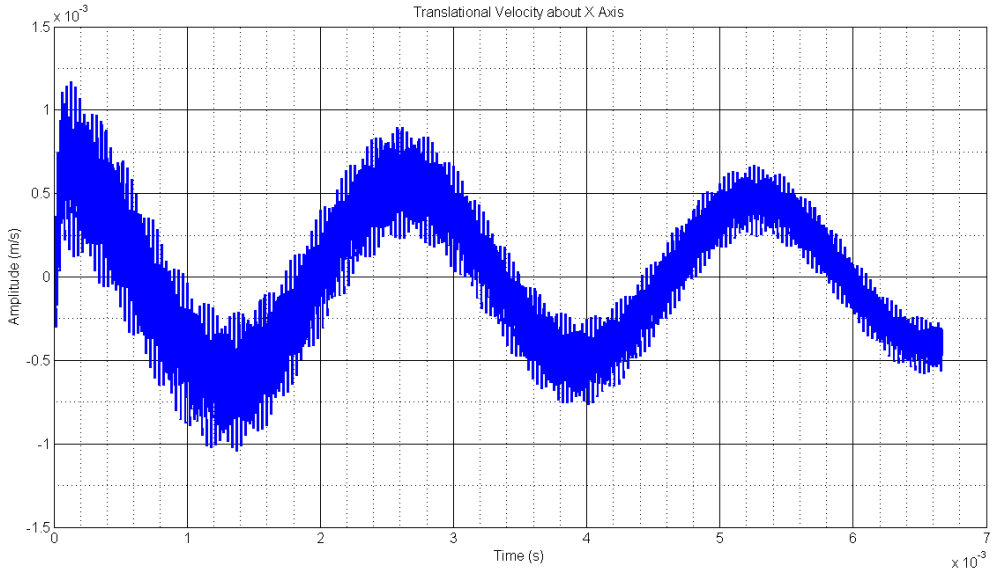

Figure 6.37: Case 2 – Cylinder Spring Translational Velocity about X Axis (time)

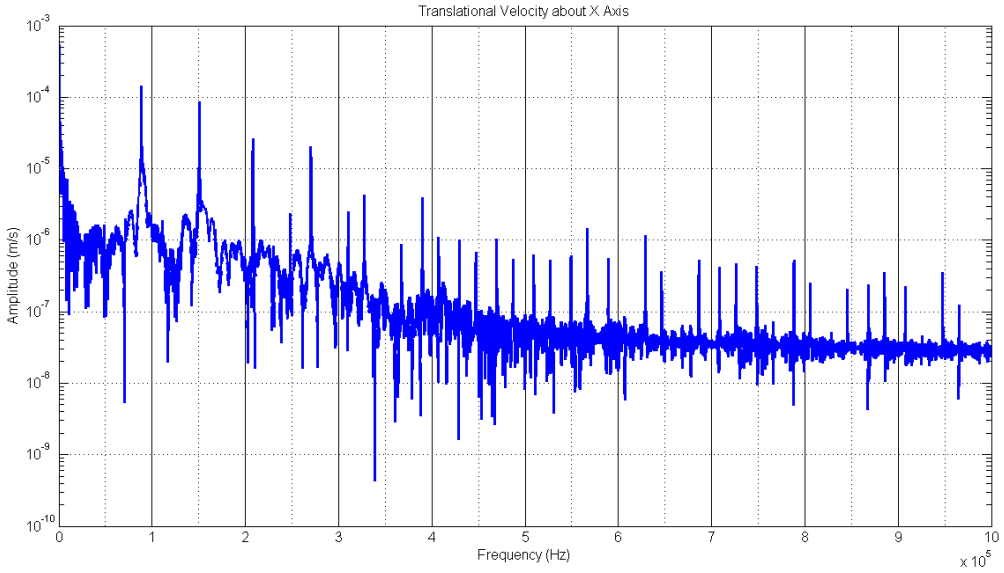

Figure 6.38: Case 2 – Cylinder Spring Translational Velocity about X Axis (frequency)

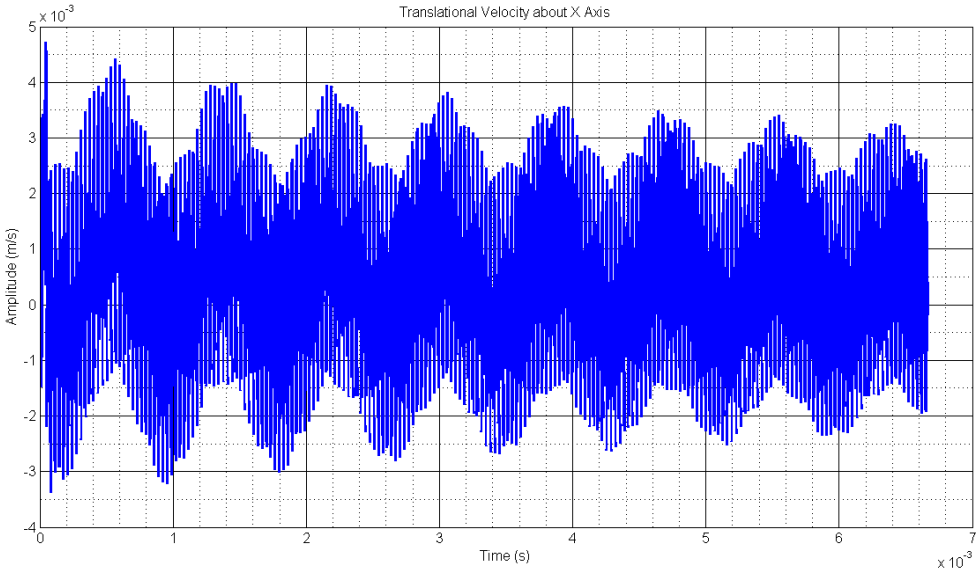

Figure 6.39: Case 3 – Pull Spring Translational Velocity about X Axis (time)

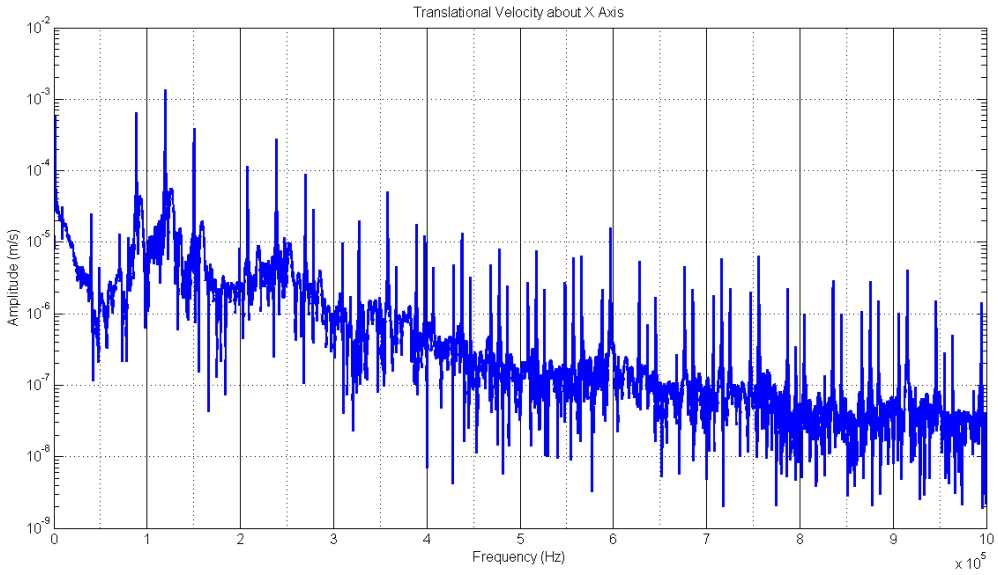

Figure 6.40: Case 3 – Pull Spring Translational Velocity about X Axis (frequency)

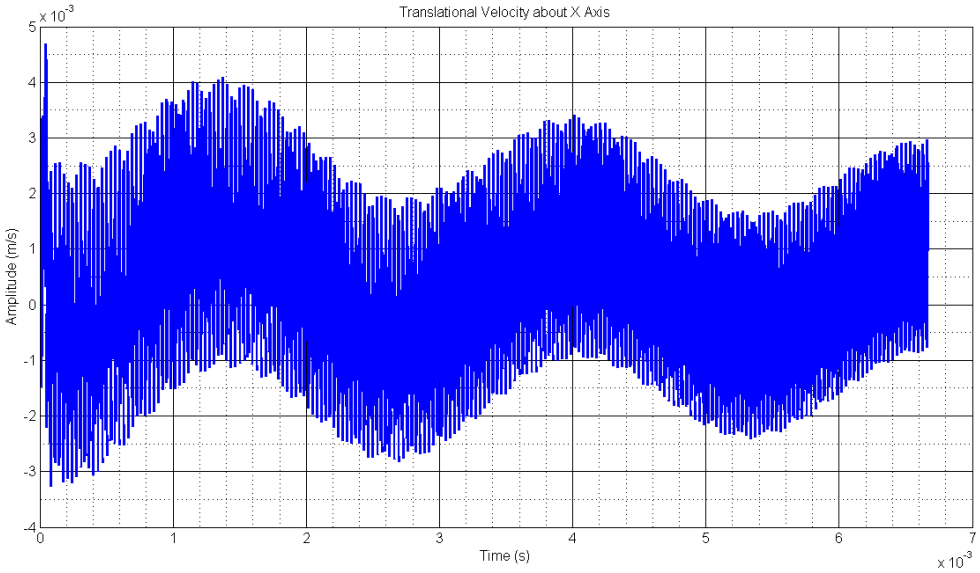

Figure 6.41: Case 4 – Cylinder Spring Translational Velocity about X Axis (time)

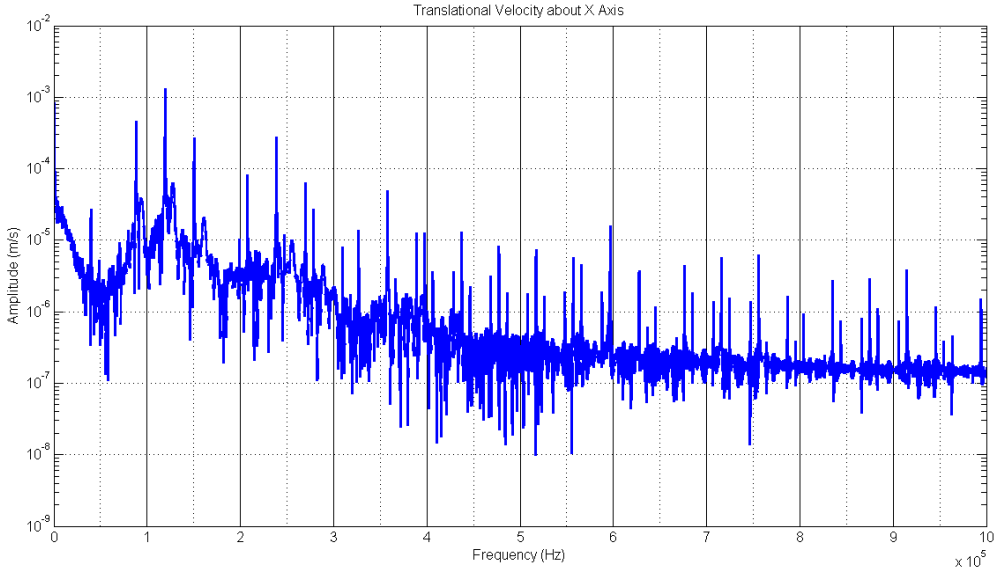

Figure 6.42: Case 4 – Cylinder Spring Translational Velocity about X Axis (frequency)

The dynamic responses of the rotor in the translational Y axis from the 4 case studies are shown from Figure 43 to Figure 50 respectively. From both the time and frequency domain data, it can be seen that the trend exhibited in the behaviour of the motion induced also follows very closely with the case involving the translational X axis motions. First, it can observe that the translational vibrations experienced by both the cylinder and flat spring model increases with increasing bias tilt torque. For the cylinder spring, the vibrations increase from 37.45 nm to 67nm while for the flat spring model, the vibrations increases from 9.51nm to 16.78nm. Second, the flat spring model shows an overall reduced level of vibrations in both conditions of applied bias torque.

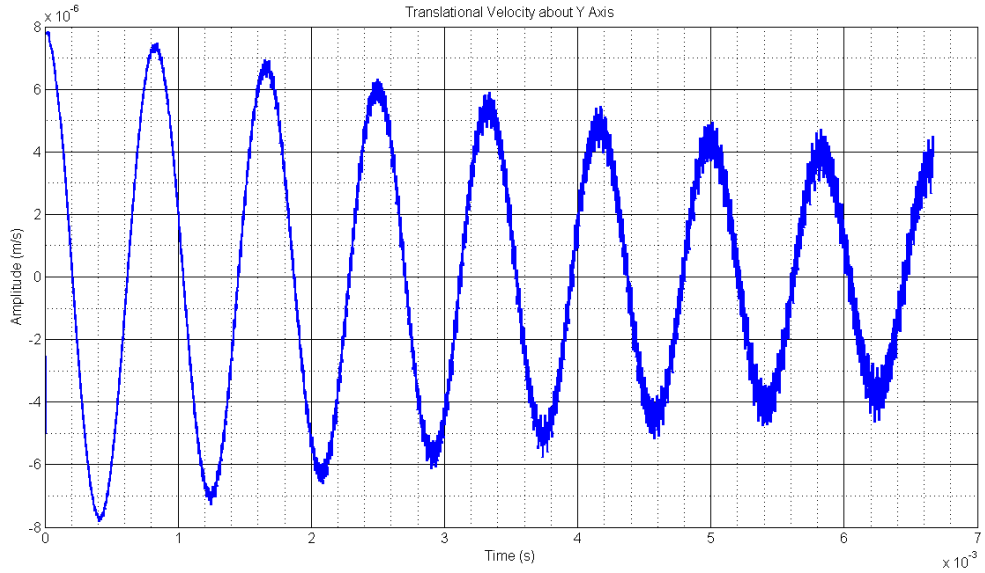

Figure 6.43: Case 1 – Pull Spring Translational Velocity about Y Axis (time)

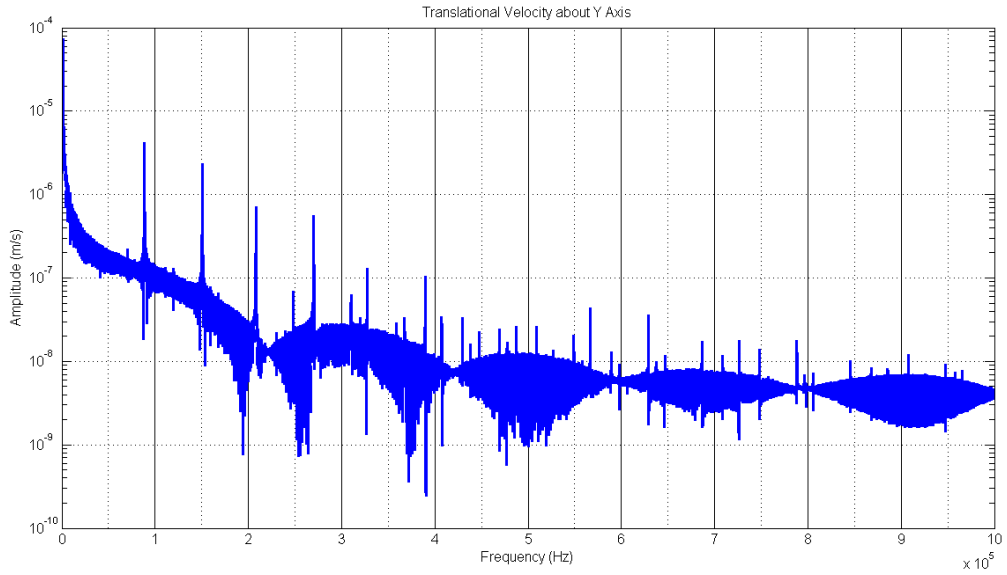

Figure 6.44: Case 1 – Pull Spring Translational Velocity about Y Axis (frequency)

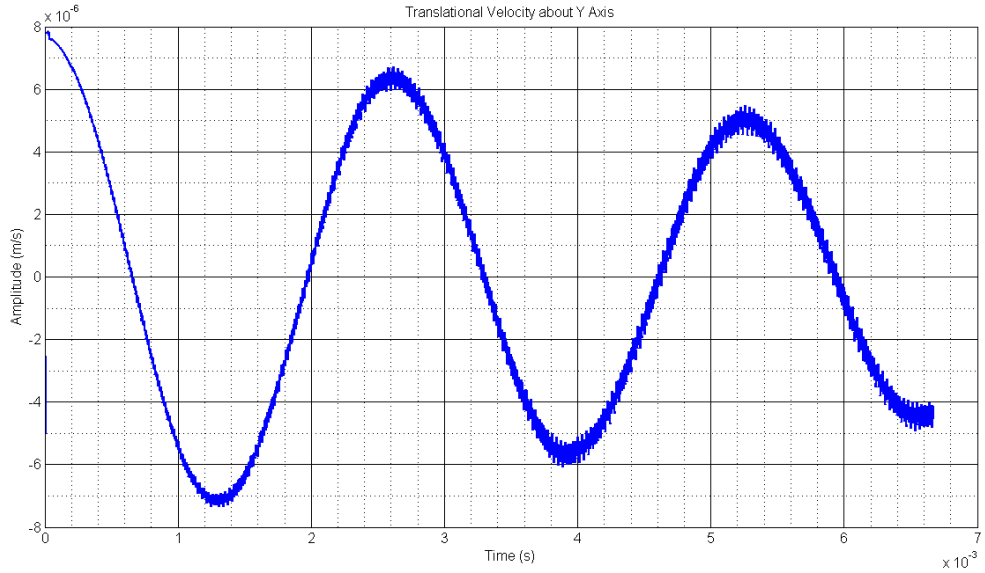

Figure 6.45: Case 2 – Cylinder Spring Translational Velocity about Y Axis (time)

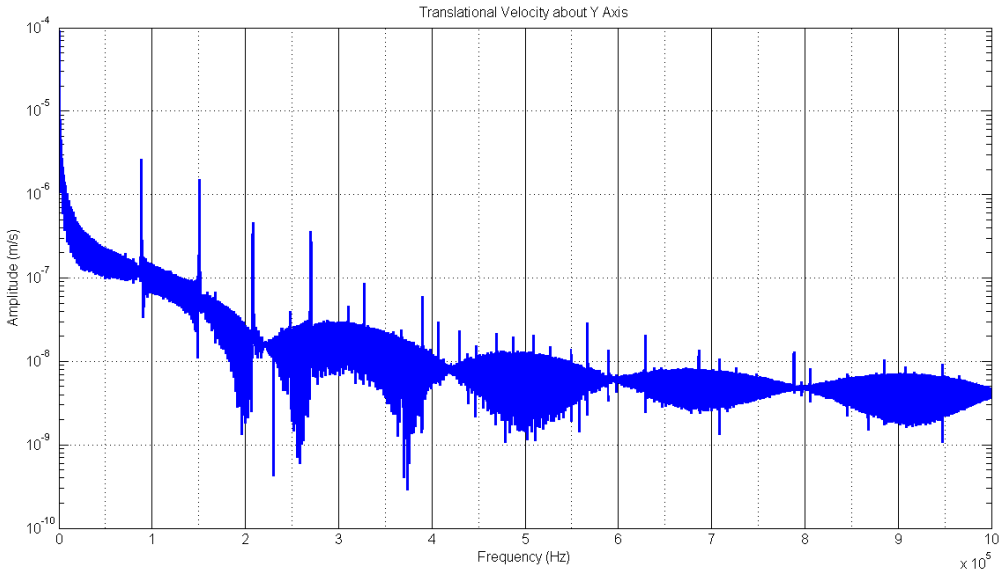

Figure 6.46: Case 2 – Cylinder Spring Translational Velocity about Y Axis (frequency)

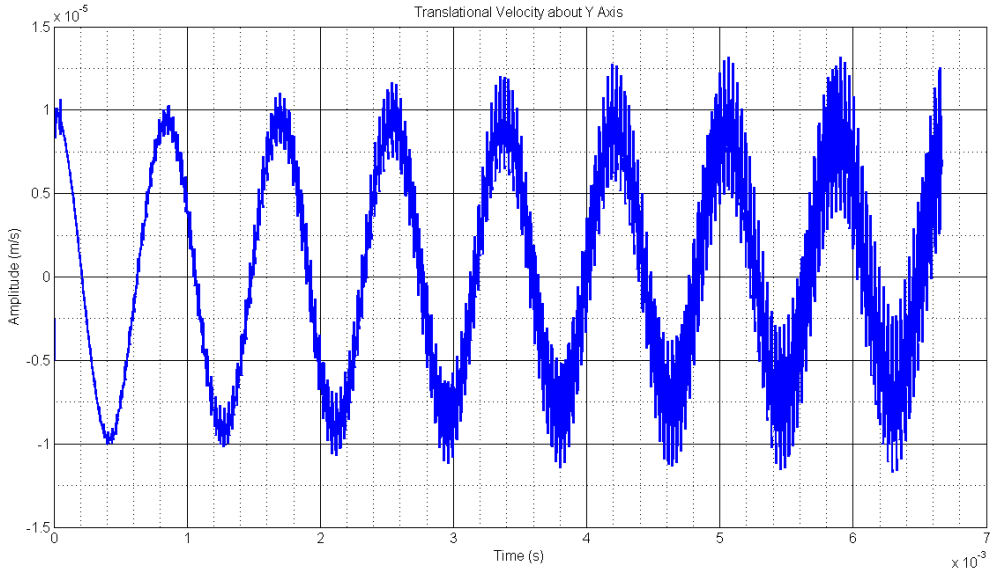

Figure 6.47: Case 3 – Pull Spring Translational Velocity about Y Axis (time)

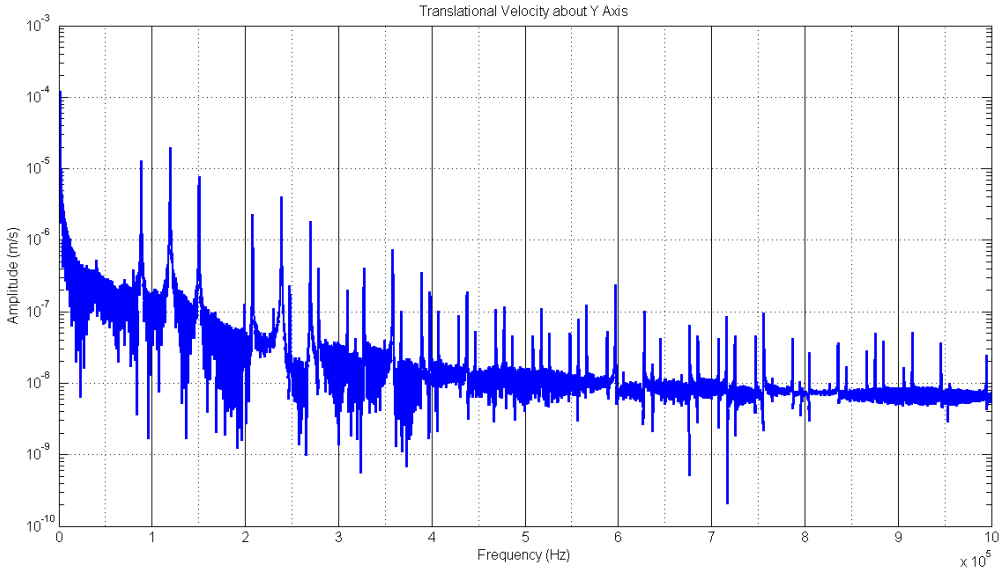

Figure 6.48: Case 3 – Pull Spring Translational Velocity about Y Axis (frequency)

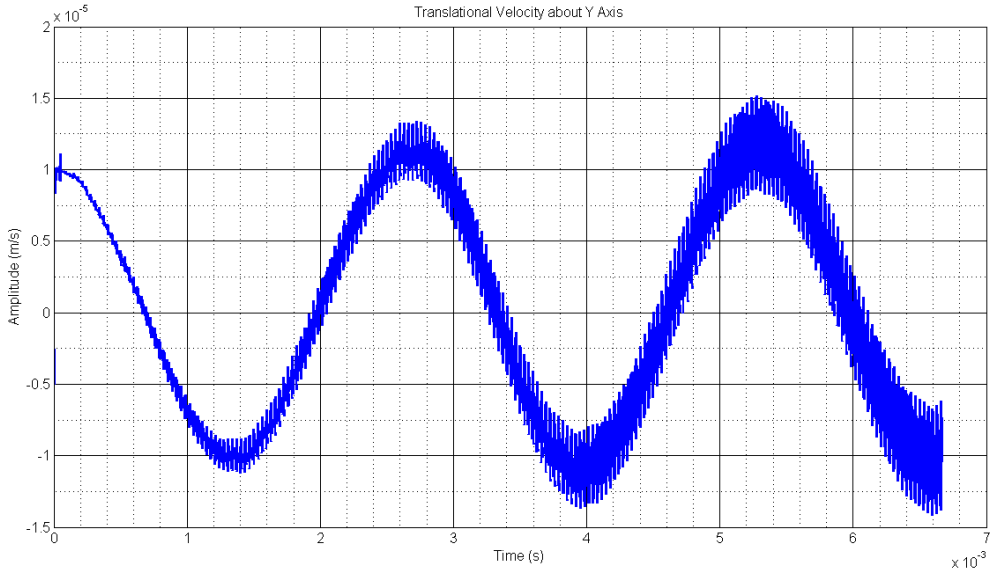

Figure 6.49: Case 4 – Cylinder Spring Translational Velocity about Y Axis (time)

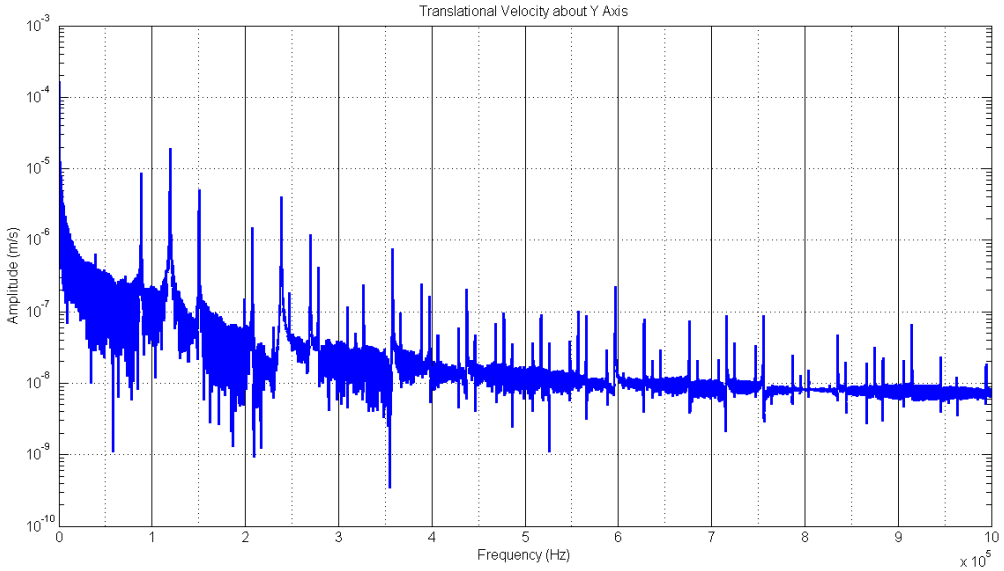

Figure 6.50: Case 4 – Cylinder Spring Translational Velocity about Y Axis (frequency)

To better understand the behaviour of the translational vibrations as well as the tilting rotational vibrations, the trajectories of the displacement profiles and the tilting rotational vector are plotted against each other. Figures 51, 53, 55 and 57 show the displacement trajectories formed by plotting the dynamic response of the rotor in the translational X axis against the response in the translational Y axis. Correspondingly, the angular velocity vector along the X axis is plotted against the angular velocity vector along the Y axis as shown from Figures 52, 54, 56 and 58. The observations of the simulation results drawn earlier can be better visualised by the following trajectories profile diagrams. There are couple of interesting things and phenomena that we can derive from and note for in the diagram though.

1) First, as mentioned earlier, the gyroscopic effect of the angular motions has resulted in a highly skewed but non-zero angular velocity plot. This means that the rotor is actually rotating circularly like a spinning top due to the non-zero induced angular velocity along the x-axis.
2) Second, the resultant angular velocity vectors formed by both $\dot{\theta}_x$ and $\dot{\theta}_y$ rotates along with the rotor. Indicating that the body fixed local axes actually moves together with the rotor changing orientation.
3) Third, analogous to the above, we can also see that for the cases involving the higher bias tilt torque applied, we can observe that the lateral displacement trajectories also rotates along with the rotor body. The physical explanation is that the point of contact between the tilted rotor surfaces is moving circumferentially as the rotor rotates. In the process, the dragging unbalance forces also changes in orientation, which also brings along the changes in the translational motion.
4) The effects seen in the third point above cannot be observed for the cases involving only a simple tilted initial condition like Case 1 and 2. The displacement trajectories remains relatively fixed in orientation as the initial perturbation causes oscillation but

is not sufficient to drag it along as in the case above whereby the rotor is forced to be tilted in one direction. By inspecting the initial trajectories, we can even observe how the direction is being forced to change 90 degree to conform to the applied bias effects.

5) As the rippling vibrations dies down or stabilizes the high frequency vibrations do not seem to be dying down for Case 3 and 4, suggesting that a constant forcing function by the stator vibration will sustain the parasitic ultrasonic vibrations due to the continuous contact and rubbing. It is to be noted that the ultrasonic vibrations of 120kHz was not detected for case 1 and 2 when there wasn't any externally applied bias torque.

6) Lastly, thought it does not seem obvious from the time domain data which exhibits defined sinusoidal oscillations coupled with some high frequencies oscillations interposed onto it. The combined motion exhibited is actually rather haphazard and noisy. The trajectories for the displacement profiles seem unpredictable and random while the angular velocities vectors showed more regularity and predictability. Though, it is to be noted that high frequency oscillations are also present in the angular velocity trajectories.

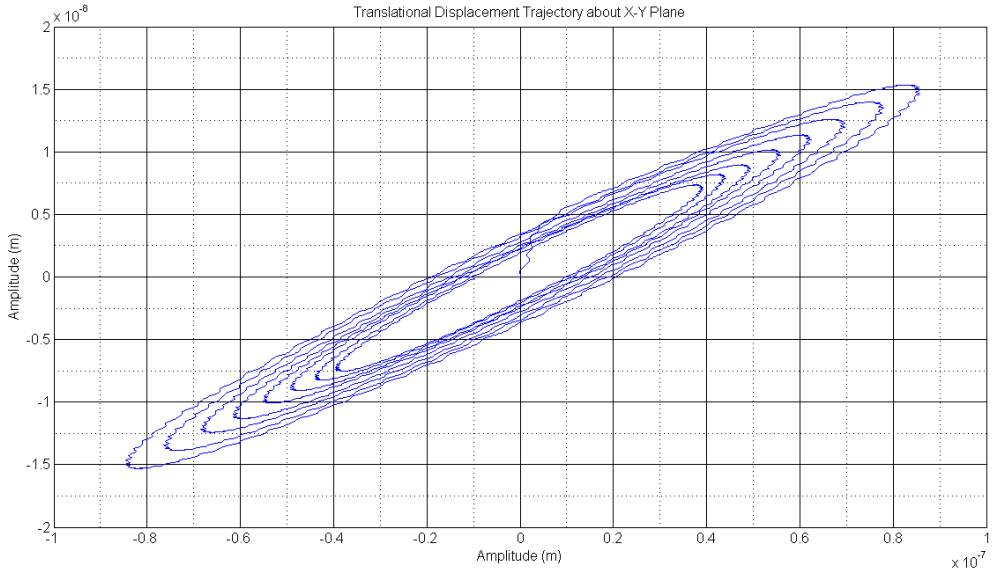

Figure 6.51: Case 1 – Pull Spring Translational Displacement Trajectory about X-Y Plane (amplitude)

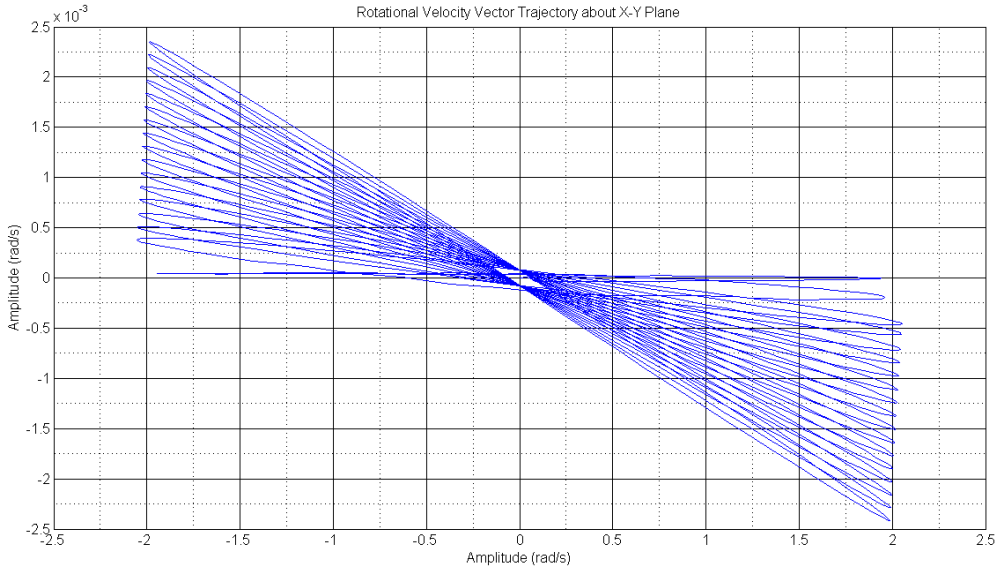

Figure 6.52: Case 1 – Pull Spring Rotational Vector Trajectory about X-Y Plane (amplitude)

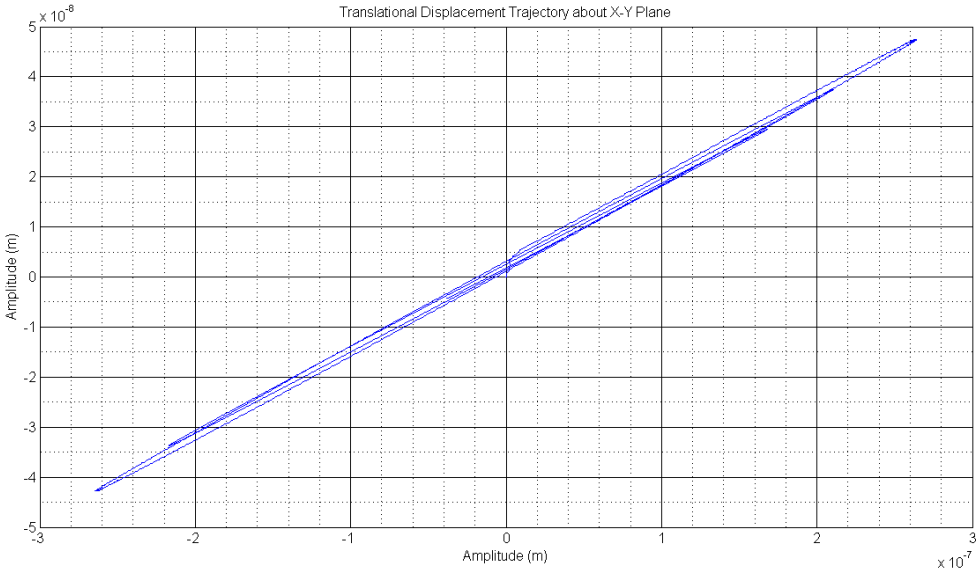

Figure 6.53: Case 2 – Cylinder Spring Translational Displacement Trajectory about X-Y Plane (amplitude)

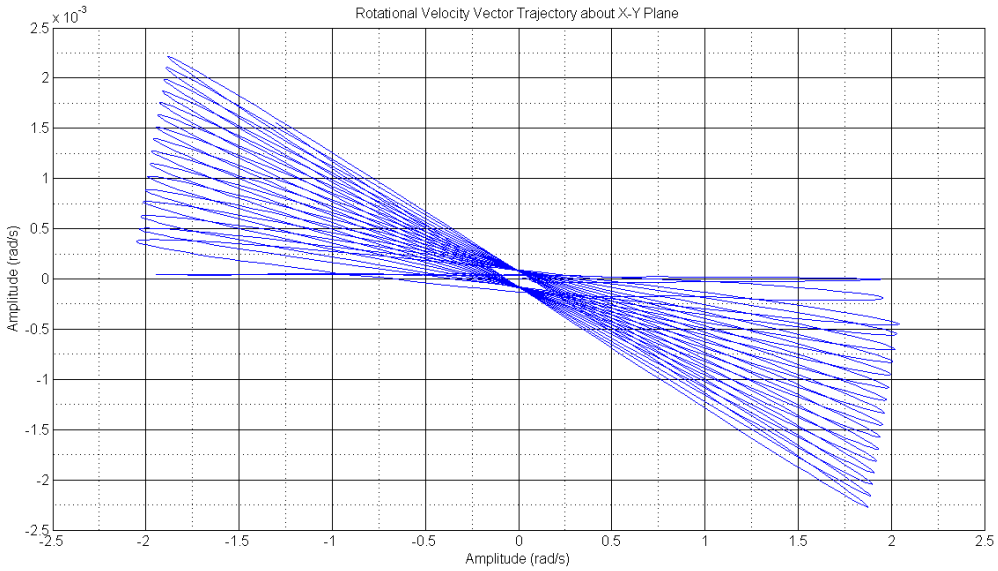

Figure 6.54: Case 2 – Cylinder Spring Rotational Vector Trajectory about X-Y Plane (amplitude)

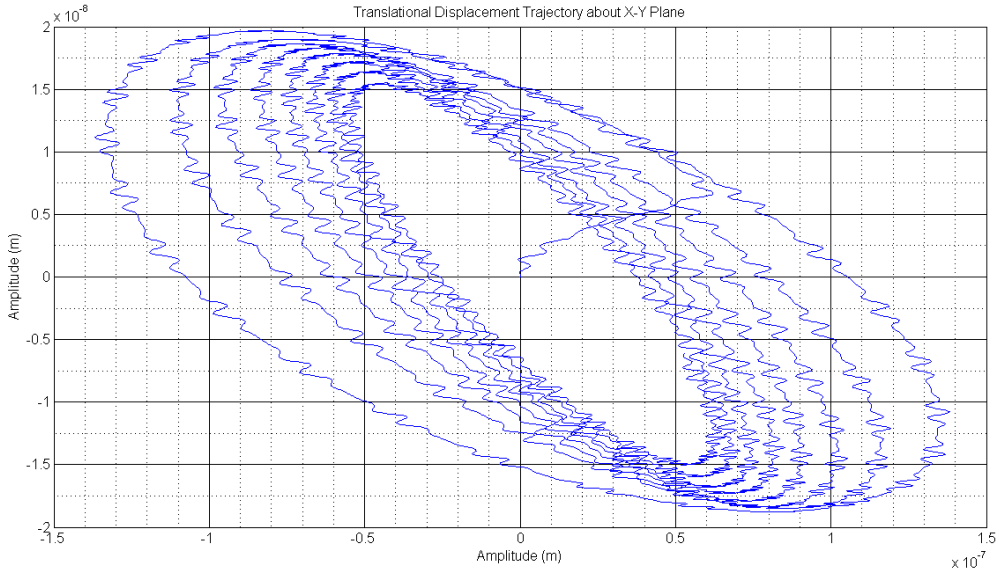

Figure 6.55: Case 3 – Pull Spring Translational Displacement Trajectory about X-Y Plane (amplitude)

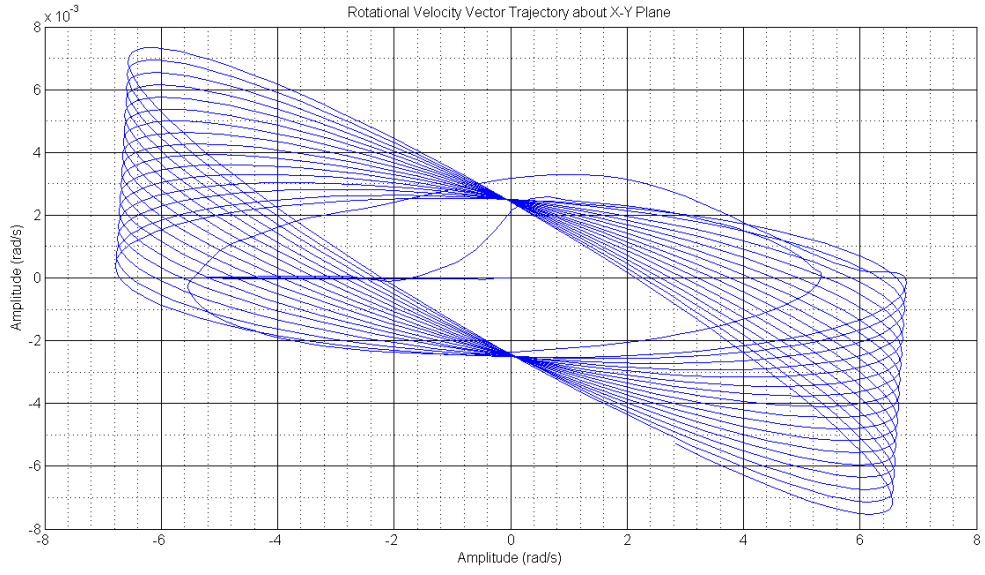

Figure 6.56: Case 3 – Pull Spring Rotational Vector Trajectory about X-Y Plane (amplitude)

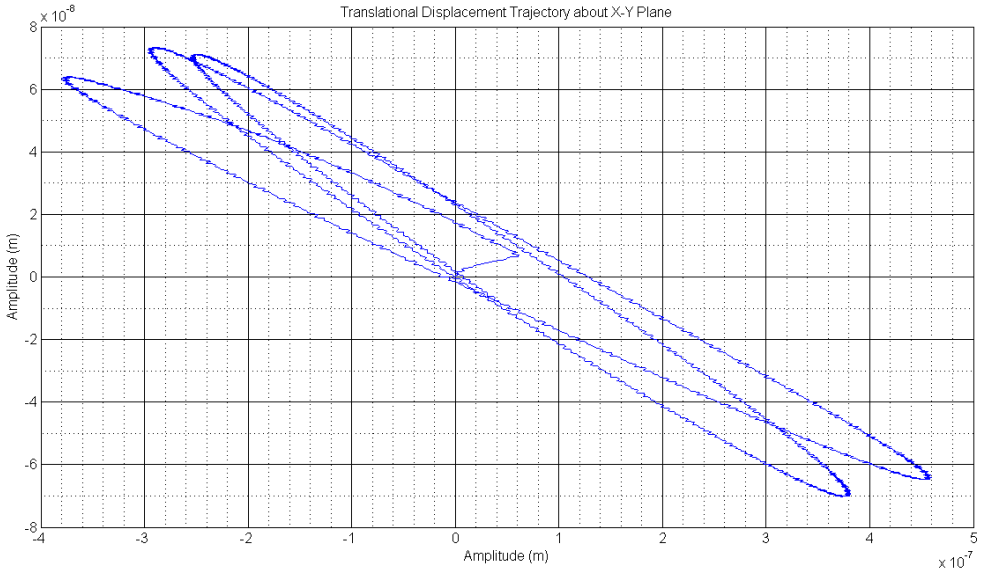

Figure 6.57: Case 4 – Cylinder Spring Translational Displacement Trajectory about X-Y Plane (amplitude)

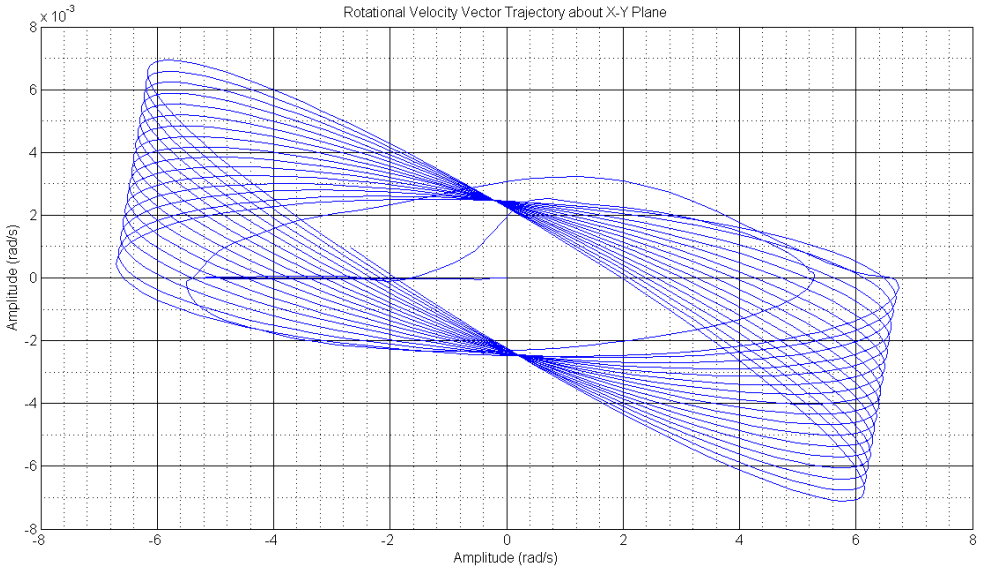

Figure 6.58: Case 4 – Cylinder Spring Rotational Vector Trajectory about X-Y Plane (amplitude)

Table 6.2 and 6.3 below shows a summary of the data collected when compared with results obtained through FEM numerical simulation and experimental results. For the rippling mode, exact experimental results were not forthcoming due to the fact that the levels experience varies greatly. However, they are measured and simulated to be in the ranges of microns.

	CYLINDER SPRING		PULL SPRING	
(nm)	Radial	Axial	Radial	Axial
Simulation	0.5	0.5	2.7	3.05
Experiment	2.5	1	3.2	3.35
Case 1	-	-	-	0.21886
Case 2	-	0.1695	-	-
Case 3	-	-	1.79	0.683
Case 4	1.184	0.5393	-	-

Table 6.6: Ultrasonic Frequency Vibrations Comparisons

	CYLINDER SPRING		PULL SPRING	
(nm)	Radial	Axial	Radial	Axial
Case 1	-	-	54.72	-
Case 2	220	-	-	-
Case 3	-	-	79.7	-
Case 4	341.49	-	-	-

Table 6.7: Low Frequency Rippling

From table 6.6, it can be observe that the simulation results do not match quite well with the experimental data. The measured experimental data is around 1 to 4 times larger than that simulated. However, the overall trend is encouraging in that it does shows that cylinder spring generally has overall less vibrations experienced compared with the pull spring. Furthermore, it can be seen from the data that greater distortion in the stack up as characterized by the applied torque in case 3 and 4 shows an overall increase in vibrations experience. Observing table 6.7, it can be seen that the levels of rippling simulated is of the order of only 1um or less. This is also much lesser than that reported in experiment whereby they are usually in the microns range. The simulation also did not indicate the presence of low frequency axial vibrations. This could be due to the fact that the distortion introduce into

the model did not exhibit axial non-uniformity. To do so, an axially directed clearance could be introduced to allow for the rotor to vibrate instead of being compresses tightly onto the stator. The experimental data also shows that the axial component of rippling is very much less than the translational component (less than 10 times lower).However, with greater distortion, more rippling is observe which is an encouraging phenomenon again indicating that mismatch could very well be due to different levels of distortions applied.. Generally, the cylinder spring shows greater rippling vibrations due to its low stiffness which makes it very soft. The reason was postulated earlier in the chapter that this is due to greater amount of uneven forces and moments generated. Thus, the mismatch in experimental and simulation can also be attributed to the fact that we are not able to know the exact imperfections in the actual prototype. It could be very well that more distortions are needed in the model by applying a higher torque to increase the vibration levels. But the fact that the model is able to capture and correspond a tilted configuration to all these vibrations exhibited by the model has already provided us a tool to study and in a sense measure and quantify the level of parasitic vibrations given such a such level of imperfections in stack up.

To conclude, we can see that to really understand and mitigate parasitic vibrations such as the low frequency rippling phenomena and high frequency ultrasonic vibrations, it is not enough to just look at the stiffness of the spring. There is a combination of three factors.

1) Greater spring stiffness means it is more difficult to drag them into motion.
2) However, stiffer springs means much worst transmissibility factor. These can be observed by looking at the vibrations of the cylinder springs, it is less stiff and experience greater rippling vibrations but it has less high frequency ultrasonic vibrations.
3) Geometrical Stack up of the entire rotor which includes the spring plays a crucial role in the level of distortions experienced and the overall level of vibrations induced.

6.4 Conclusion

The chapter begins with an introduction of the problem of rippling and high ultrasonic vibration transmission as indicated by both FEM and experimental data. It is postulated that this is due to the presence of uneven distribution of micro impact forces and moments impinging onto the rotor. The source of such phenomena is due to imperfections in the geometrical stack up of the TRUM which breaks the symmetry of the forces induced. An inclined surface, for example, results in differences in penetration depth which results in uneven reaction forces and moment. Different engineering factors suggesting how this could arise was presented. Four cases involving the cylinder spring and flat pull spring with an applied bias torque and initial tilt was used in the simulation study. It was found that the cylinder spring performed better in the high ultrasonic range than the pull spring due it lower transmissibility factor. However, in terms of rippling, it experiences more vibration because it is less stiff. It was found that with greater applied bias torque, the level of parasitic vibrations will show an overall increase. This suggests that the mismatch between the experiment and simulated results could be due to uncertainties in the level of imperfections in the actual prototyped model. The results is encouraging in the sense that a simple tilted configurations has results in many vibrations induced and showed that this could be a useful framework to help further our understanding and quantity of how engineering design, assembly and fabrication imperfections can translate into parasitic vibrations.

CHAPTER 7 -- Speed Optimization Parameters study

7.1 Basic operational characteristics

In the previous chapters, the vibrations characteristics of the TRUM actuator in terms of the parasitic rippling and ultrasonic vibrations have been discussed. In this chapter, first we will look at the speed torque experimental data collected by our collaborators in this project Pinanotech. We will look at some of the basic transient behavior of starting up the rotor and stopping it. Next we will generate the speed torque curves for a few cases to study the issue of speed optimization by varying some of the important parameters like the axial pre-load applied the tooth height as well as the span of the teeth. It was found that an optimal value exists for each parameter and that more does not mean better.

This part of the chapter will show the basic operational behavior of the TRUM when it is running. It is to be noted that the motor characteristics employed for the discussion in this section is not the HDD TRUM model. As the dynamic transient is too fast for proper illustrations, the model employed here is a much slower motor so that the transients character can be better discussed. Figure 7.1 below shows the modal amplitudes during start up. There are two curves, each representing one of the two orthogonal modes. They differ in phase by 90 deg. The graph shows that during the initial transient start up stage, there are a few low frequency oscillations before the motor reaches steady state at 5ms. This corresponds closely with the rotor flexural z-height variation during start up, indicating the importance of the pre-loading and hence the interactions between the mechanical modal amplitudes and the rotor speed.

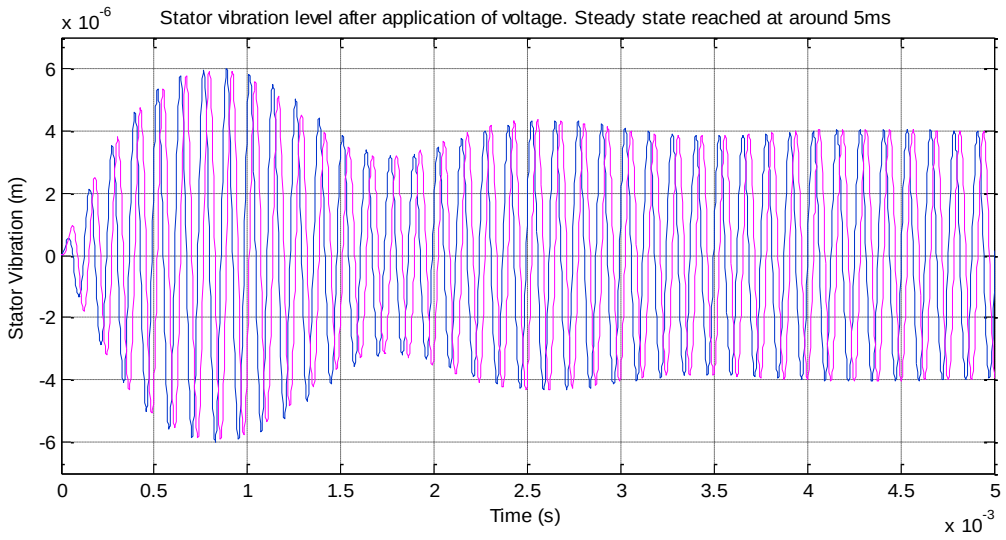

Figure 7.1: Stator vibration after switching on motor. Steady state reaches at around 5ms. Two curves above shows the orthogonal modal coordinates out of phase by 90 deg or a quarter of the operating wavelength.

Figure 7.2 below shows the variation of the rotor flexural height during start up. As there is an externally applied pre-load acting on the rotor, it will need to be deflected downwards to established vertical equilibrium.

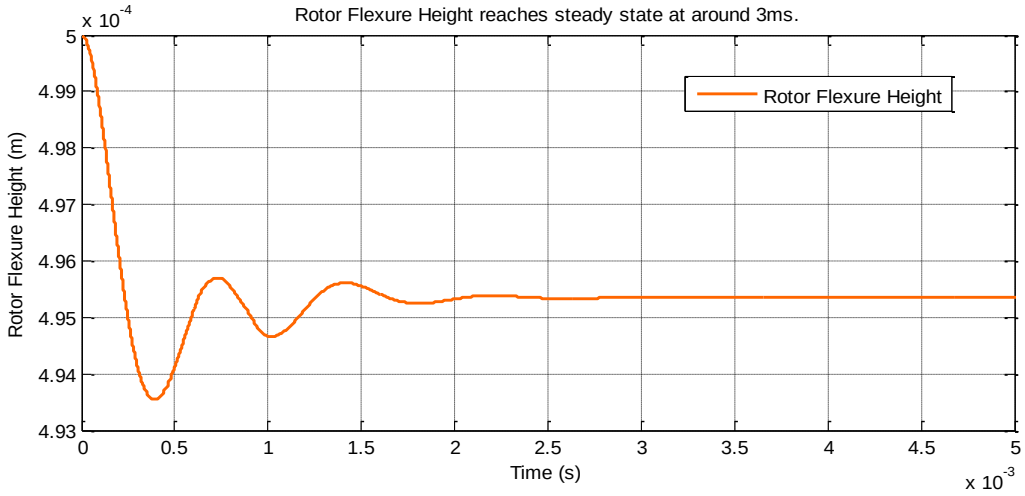

Figure 7.2: Rotor flexure vibration in the z-direction. Settle at around 3ms. Externally applied pre-load causes rotor to be compresses downwards by around 50um before reaching equilibrium in the z-axis.

Figure 7.3 below shows the variation of the rotor angular velocity as the externally applied torque increases. As expected, the angular velocity decreases. A series of such curves can be constructed to illustrate the speed-torque characteristics of the motor; this will indicate to us the stall torque as well as their non-linear behavior.

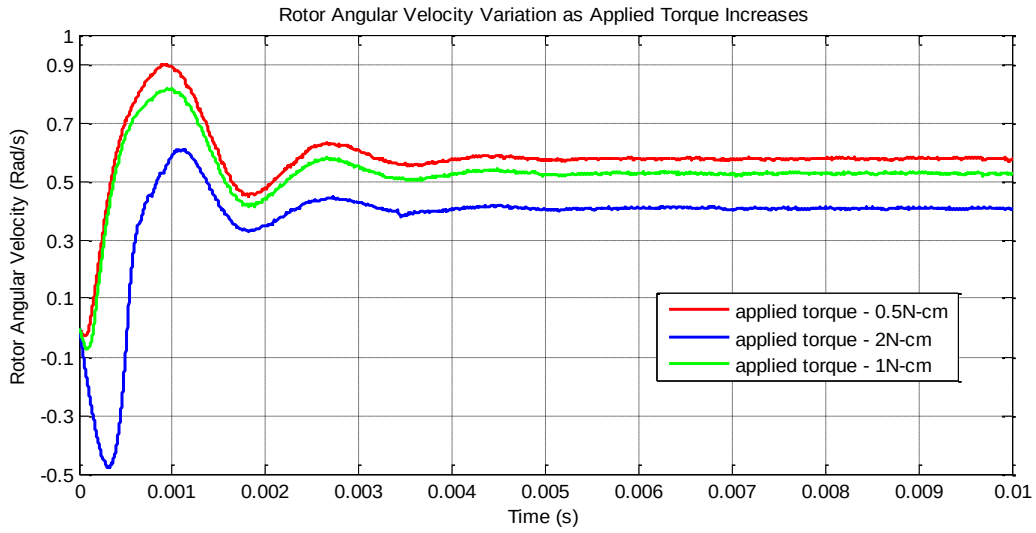

Figure 7.3: Rotor angular velocity decreases as the amount of externally applied torque increases.

Figure 7.4 below shows what happens when the motor is being switch off suddenly by setting the excitation voltage to 0 at 5ms. At 5 ms, in order to prevent back rotation, the external torque applied is also set to zero. From the figure, we can observe that the rotor angular velocity actually increases when the voltage and external torque is set to 0. In the sudden absence of the external torque, the inertia of the rotating rotor drives it faster before the damping effects catches in. After a slight increase in rotor angular velocity, it starts to decrease gradually to zero as the stator vibration dies down and the rotor damping further slows down the rotor.

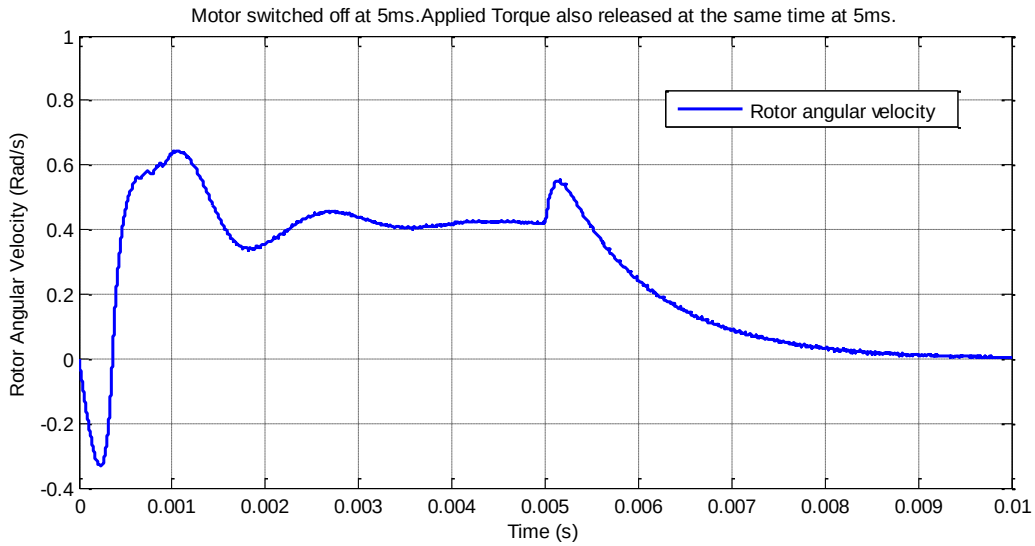

Figure 7.4: Rotor angular velocity during start up and upon cutting off of voltage supply at 5ms.

7.2 Experimental Data of Speed Torque Curve

Figure 7.5 below shows the experimental set up by Pinanotech to measure the speed torque curves. As can be observed, the TRUM housing construction is very different from the case when employed as an HDD actuator. The reason is straightforward because a normal HDD actuator cannot be used for speed torque testing as the stroke length is limited by the surrounding casing. Nevertheless, this set of data provides us with some sense of guideline of the modelling performed.

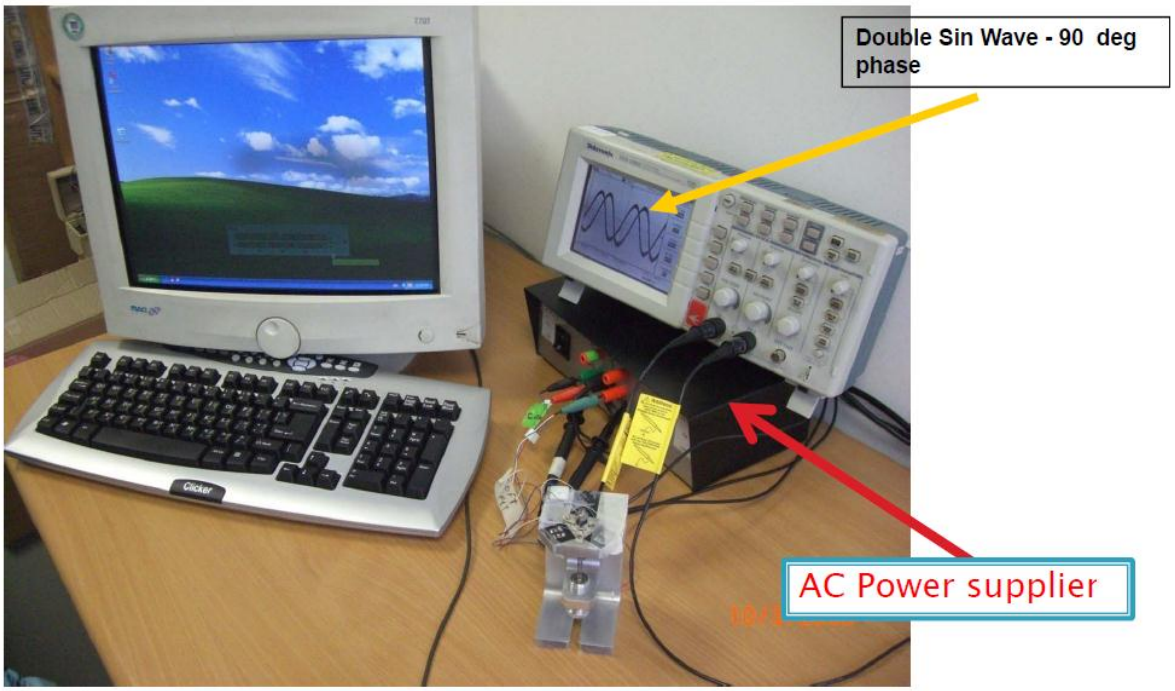

Figure 7.5: Experimental set up to measure speed torque curve.

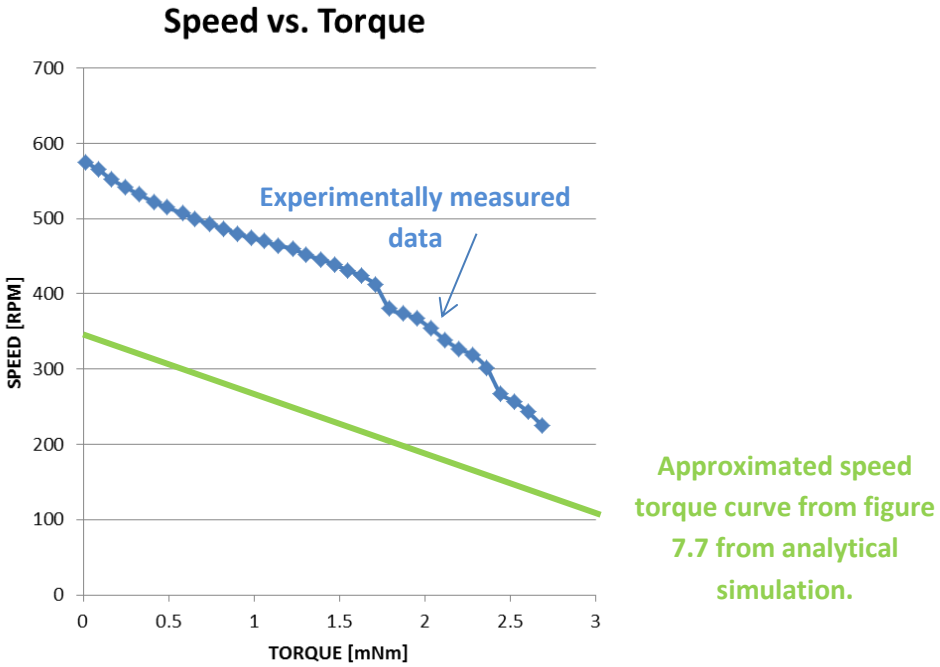

Figure 7.6: Experimental and simulated speed torque curve.

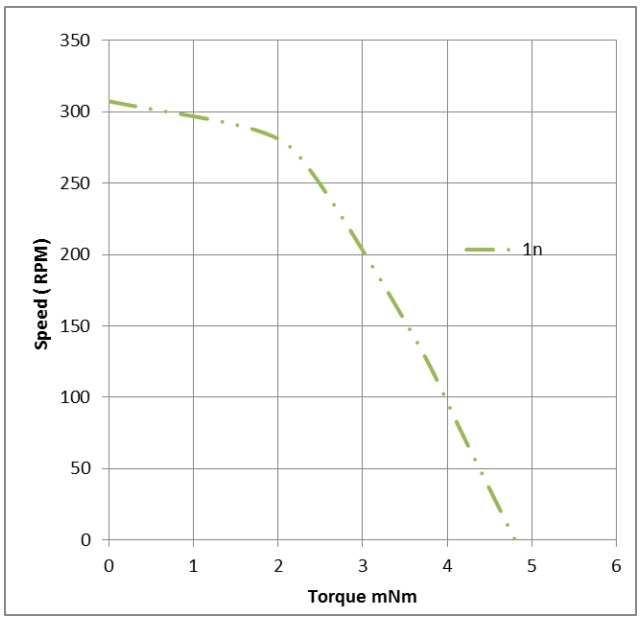

Figure 7.7: Simulated Speed-Torque curve from analytical model

Figure 7.6 and Figure 7.7 above shows measured and simulated speed torque curves at 1N pre-load for the TRUM driven at 100V pk-pk respectively. It can be observed that there is some discrepancy between the measured speed-torque curve and the simulated results. The simulated results shows lower performances in terms of the maximum speed achieve, but the torque produced is somewhat similar. Such dissimilarities are to be expected as there are several factors which need to be tweaked to better fit experimental results. Of which, the friction coefficient is a very important parameter and many reported research actually uses experimental data to back suggest what types of simulation input, especially friction coefficient, is required. This is not surprising since the operation of a TRUM actually involves many physics which are really never fully understood. For example, the friction behaviour between high frequency surfaces, the non-linear resonance behaviour of actual stator under loading and the non-linear material properties of the piezoceramics under prolonged heating are highly complex phenomena .Nevertheless, the general trend was captured and the torque produced was in the ball park value. If necessary, more precise fine tuning of actual input parameters can be further investigated.

We will discuss several important factors that may suggest for the mismatch between the measured data sets before proceeding to discuss the speed optimisation factors in the next section.

1) The friction coefficient used in the model was a generic value of 0.3 which represent metal to metal sliding contact. In the actual prototype, there is actually a thin layer of viscoelastic material added to improve grip and enhance the torque transmitted. This factor is introduced can easily shift the entire speed- torque curve upwards in a directly proportional magnitude. Many studies employ an "equivalent" friction coefficient in their model to fit measured experimental results.
2) It was observed experimentally that as a TRUM rotor run over a period of time and heats up, it performs worst. Reasons suggested for such an observation includes the fact that as the system heats up, they become softer and hence more flexible and pliable inducing a temperature induced shift of the resonance. Also, the piezoceramics material properties could also change due to the higher temperatures. Temperatures effects on material behaviour of resonance behaviour were not studied at all in the model.
3) Next, the boundary conditions between the experimental set up and the modelling assumptions normally do not match perfectly. Idealization employed in the model is necessary as certain physical configurations cannot be adequately described. For example, the mounting of the stator in the real set up is more flimsy and includes a soft layer of glue which attaches the parts together. In the model, the stator is rigidly fixed at certain locations. Next, the geometry of the teeth, loading magnitude could also not be controlled to preciseness. As will be seen later, at lower and lower pre-loads it can be observe that the sensitivity towards speed increment is very high.

4) There are many other sources of uncertainties such as the non-linear behaviour of the piezometerial under different temperatures, cross coupling terms and electrodes applications. Even the electronic circuitry supplying the high voltages to drive up the piezoceramics requires considerations as they interact dynamically with the mechanical system.

7.3 Speed Torque Curves and Parameters Influence

After running over 100 cases of the simulations we have the motor performance curves of the TRUM. We will discuss the effects of pre-load first before proceeding to look at the effects of teeth height and lastly the influence of the teeth span (how much teeth area circumferentially)

7.3.1 Axial Pre-Loading

Figure 7.8 and Figure 7.9 show the effects of increasing pre-loading on the speed-torque behaviour. It can be observed that as the pre-loading increases, there is a gradual shift in the motor behaviour from high no load speeds and low stall torque to exhibiting lower and lower no load speeds and higher stall torque. According to Hagood [7], this phenomenon can be attributed to the normal forcing on the stator which takes energy out of the stator system which causes a decrease in the stator surface velocity and hence directly impacts on the rotor velocity generated. Also, at the pre-load of 3N, there is high power but the efficiency is not the best. Another useful way of looking at this behaviour can be achieved by inspecting the generic stator travelling wave formed during operation. It is a well-known fact that wave crest drives the rotor while wave valleys retards motion by dragging back on the rotor. And that wave crest peaks have the highest positive velocities while wave valleys bottom has the

highest negative velocities. Figure 7.9 below illustrates such a velocity distribution on a wave cycle.

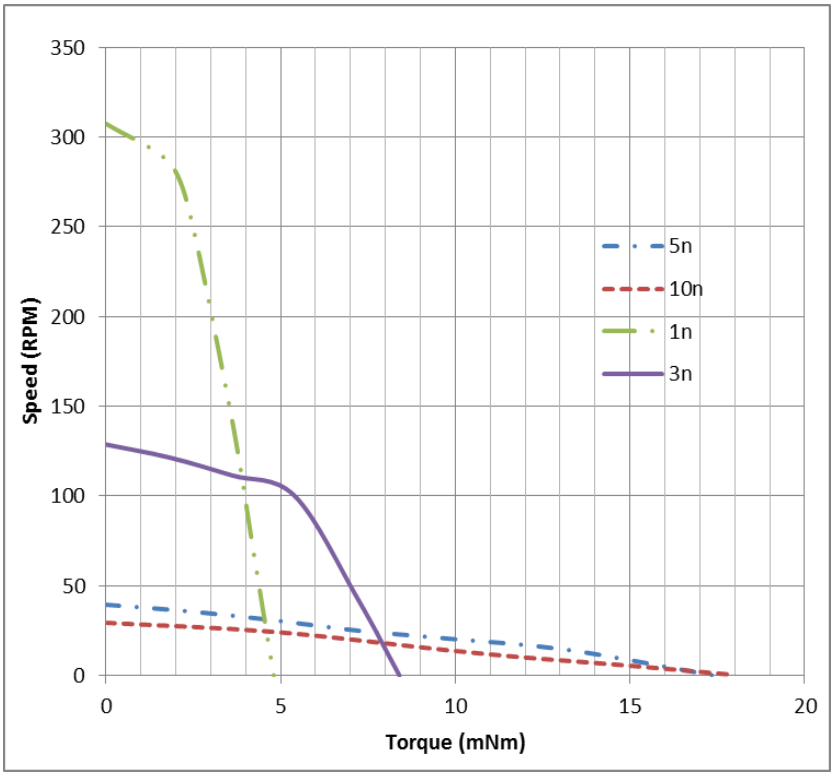

Figure 7.8: Effects of Pre-Loads on Speed – Torque

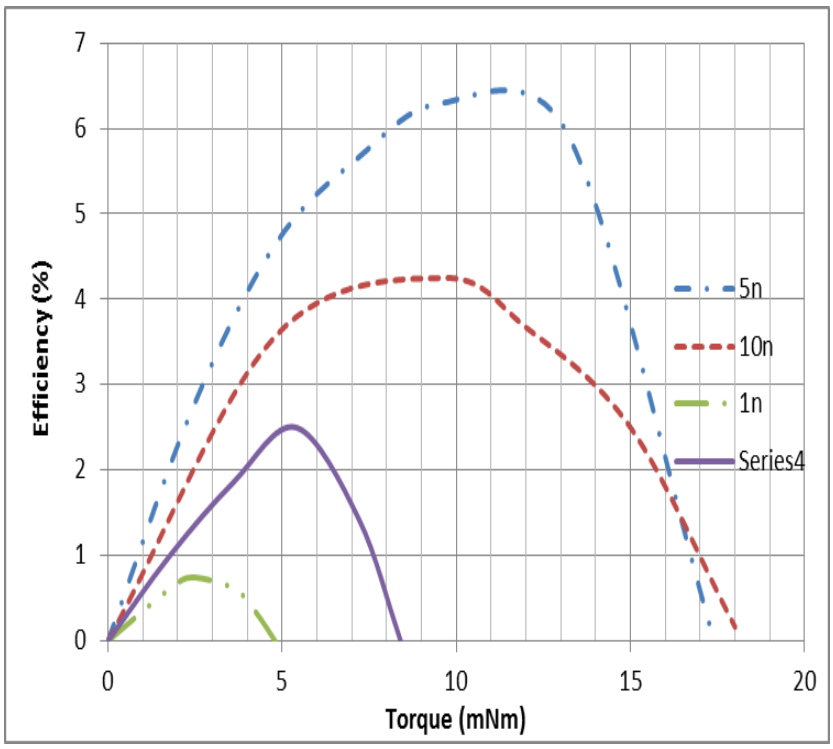

Figure 7.9: Effects of Pre-Loads on Efficiency

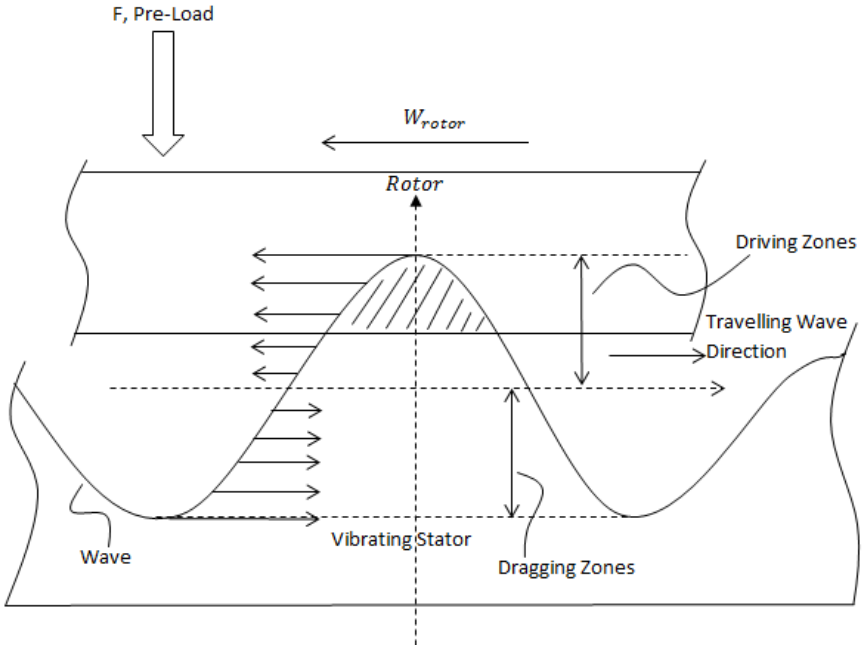

Figure 7.10: Dragging and Driving zones for a given travelling wave

From the figure, it can be seen that with greater and greater pre-load until top half of the travelling wave, the rotor can enjoy more pushing actions from the stator. When the rotor pre-

load is applied higher this drives its immersion into the lower half of the wave crest its starts to experience the dragging effects of the stator. Incorporating such a perspective seems to explain the behaviour of speed torque and efficiency curves to axial loading quite well.

First, at low preloads, the rotor is operating at the top zones of the wave crest. Since the wave crest is moving at high velocities, the rotor also moves at high speeds.

Second, since the submerge zones of the rotor into the wave at low pre-loads is lesser, we can expect that it receives less pushing forces and hence shows lower stall torque as externally applied torque can easily overcome the small force generated at the small submerged zones.

Third, as pre load increases, the rotor gets push down further into the wave. The rotor is exposed to lower speeds at the lower positive zones and hence slows down, but as there are more pushing contact zones the stall torque improves.

Fourth, if the preload is too high and the rotor gets push down into the dragging zones, speed further degrades while stall torque remains relatively the same. But the effect is shown as a net decrease in efficiency as energy is actually wasted dragging back itself. Previously, before this point is reached, pushing it further down increases motor efficiency continuously as more of the driving wave crest is being employed for the driving instead of being wasted away as structural vertical vibrations.

Of course, it should be noted that there could be other mechanism at work. Such as the fact that as pre-load increases, the stator vibration actually decreases as it is not allowed to resonate freely and that at high ore-load more energy is needed to provide the vertical forcing which does not aid in driving up the motor. To conclude, no optimum value of pre-load exists for a given motor configuration. High output power does not correspond with high efficiency.

A choice needs to be made with regards the power requirements, efficiency criteria and the operational speed torque combinations.

7.3.2 Stator teeth height

The positive effects of stator teeth are in universal agreement. They not only provide the needed amplification moment arm for the stator vibrations, it has also been reported that the grooves among teeth actually provides a pathway for wear particles which allows for smoother operations. The stator teeth itself has also been designed to provide better compliance and hence rotor-stator contact which improves rotor performance. In the simulation though, the stator teeth is assumed to be a rigid massless body and its only function is to provide the added amplification factor.

Figure 7.11 and Figure 7.12 below show the speed-torque curves with different teeth height. As can be expected, it can be seen that with greater teeth the rotor no load speeds increases very much while stall torque drops by a little. The efficiency curve also increases until up to a certain point and shows a decline in efficiency even as higher speeds are achieved with greater teeth height. This could be due to the fact that the tangential work term is small initially compared to the normal work terms and hence with greater teeth height, more efficiency use of the energy is possible for greater speed and efficiency. Beyond a certain height, when both energy terms are comparable, greater speed can only come with reduced efficiency as more energy is needed to sustain the normal energy term also.

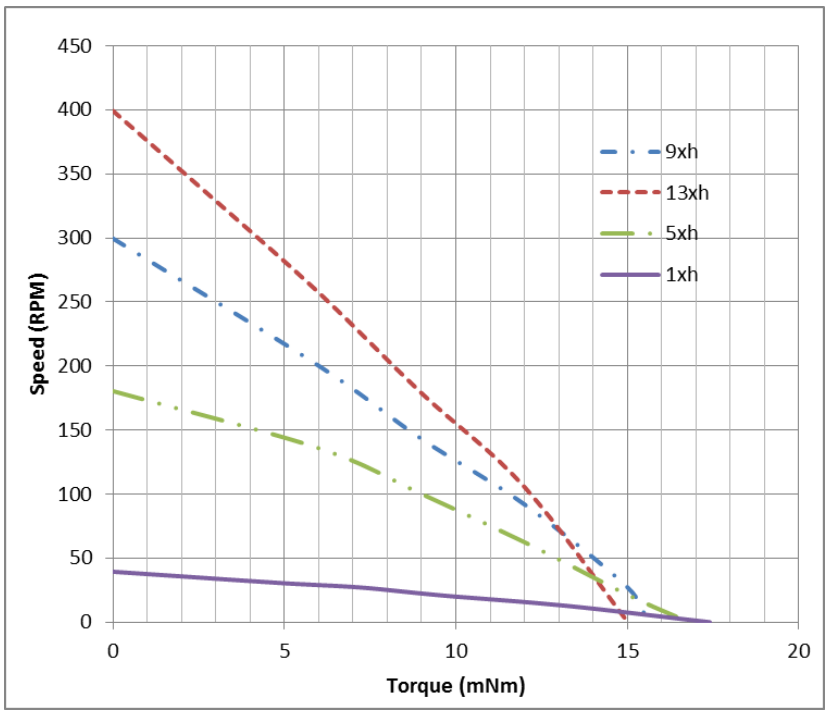

Figure 7.11: Effects of teeth height on Speed – Torque

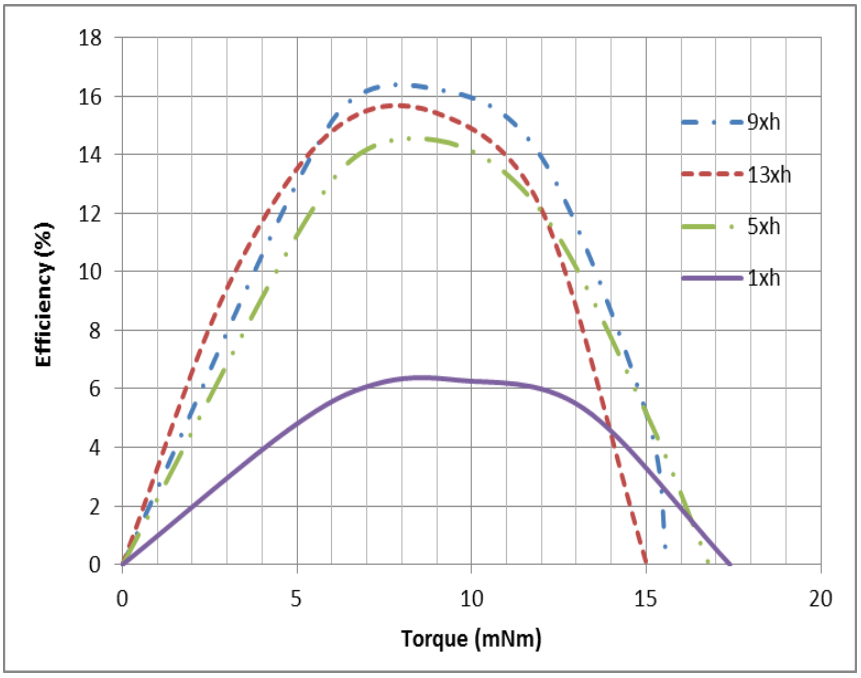

Figure 7.12: Effects of teeth height on efficiency

Physically, we can also interpret the increase in speed and efficiency simply as a result of change in energy allocation. Since mathematically, tooth height increase only gets reflected

in the moment arm amplification factor and the stator vibrations profile remains relatively unchanged. This implies that more energy is being devoted to driving the rotor circumferentially instead of axially and hence greater efficiency.

7.3.3 Teeth Span

Lastly, Figure 7.13 and Figure 7.14 below show the effect of changing the area of the teeth span circumferentially around the rotor. The behaviour exhibited is similar to the effects of pre-load whereby more teeth do not mean better performance in terms of efficiency. The behaviour is also necessarily more complicated since by changing the teeth span another important factor creeps into the picture. That is the driving period devoted to the spinning up of the rotor. With less teeth span, it is expected that the time allocated to driving the rotor is also lesser as some zones remains out of physical contact during the travelling wave phase. Moreover, we can expect the stator vibration to be more varied spatially since areas without teeth can vibrates more freely. So, we have few factors at work here, for a given pre-load, changing teeth span is effectively changing the pressure as the downward axial force is redistributed but still present.

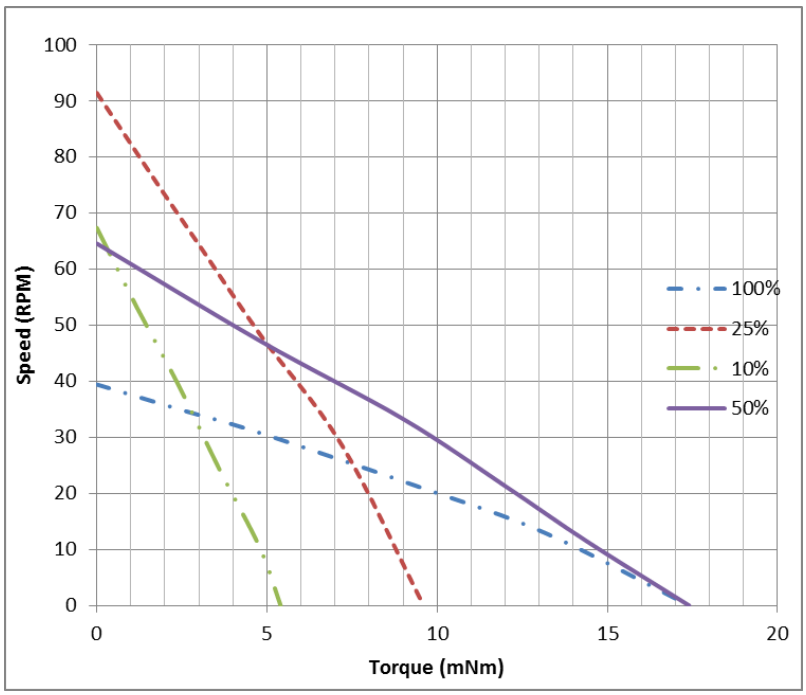

Figure 7.13: Effects of teeth span on Speed – Torque

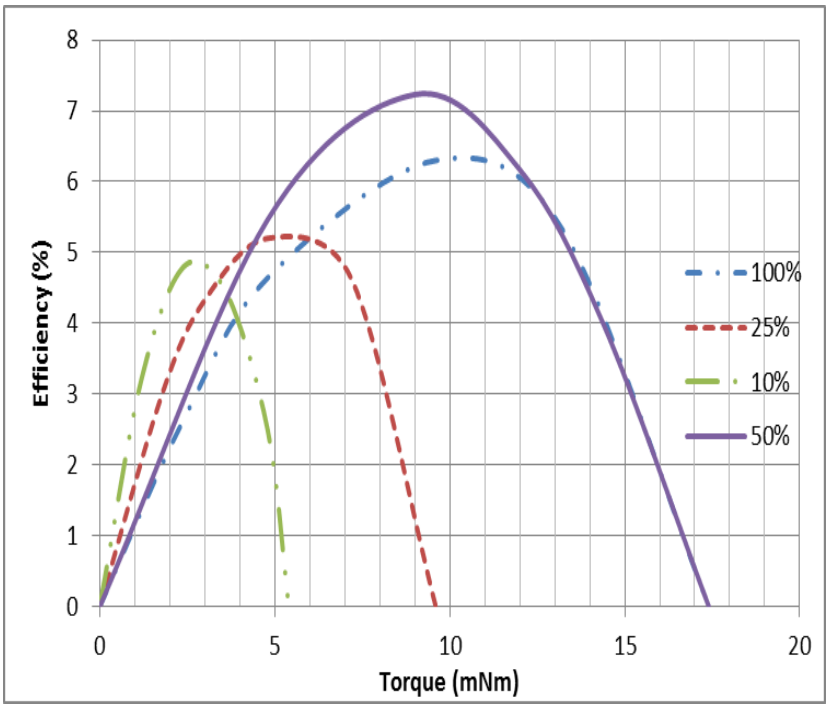

Figure 7.14: Effects of teeth span on efficiency

Looking at the data we, can see that initially by reducing teeth span, the speed actually increases with increase in efficiency. This implies that the benefits brought about by a

increase in pressure on teeth offset the decrease in contact time offered. However, as teeth span further decreases, there reaches a point whereby both speed and efficiency will decrease. This is to be expected as too little teeth only means that the majority of the travelling wave during a given cycle is doing nothing and represents great energy wastage. Thus, to conclude, for a given pre-load, since stator teeth is usually present in all USMs, there is also the potential to optimise the speed torque behaviour by studying how much teeth is needed.

7.4 Conclusion

This chapter first compared the measured speed torque experimental data with simulated results. It was found that there were some discrepancies between the two data sets. Several suggestions were presented to explain the observed differences. This included the effects of friction parameters mismatch as well as the effects of temperatures rise and boundary conditions incompatibility. This is because real TRUM operates based on very complex non–linear physical processes which are never fully understood. Many parameters inputs to the model are mere attempts at guessing or approximating unknown physics into a single equivalent value. Nevertheless, the trend of the curve is about right and the torque produced is also within the experimental range. Next, the effect of axial pre-loading, teeth height and teeth span on the speed torque curves and efficiency are presented and discussed. It was found that greater pre load lowers the no load speed but enhances the stall torque. However, a high power does not coincide with the highest efficient of the motor. This suggests that no optimal conditions really exist as we have to settle for power, torque, speed and efficiency trade-offs. Next, it was found that greater teeth height can and do improve the speed torque behaviour and efficiency. But the benefits will stop for a given height when the tangential and normal work terms are equal in magnitudes. Lastly, for teeth span, it was found that few parameters are at work. Greater teeth span means more forcing time between rotor and stator

contact, but it also means less pre-load effects and more uneven vibrations as the axial force is being spread over a greater and varied area. Both factors interact with each other and the results suggest that for a given preload, there is an optimum teeth span which we can improve the motor performance in terms of speed and efficiency.

CHAPTER 8 -- CONCLUSION

8.1 Conclusions

The objective of this research work undertaken is to provide a greater insight onto the dynamics of a Travelling Wave Ultrasonic Motor (TRUM). Due to its advantages, there is a growing trend of more widespread applications using TRUM. In our study, the goal is to adopt TRUM technology for use as a precision actuator for Hard Disk Drives (HDD). However, it was found that the dynamical performance of such an actuator was lacking in terms of its vibrations characteristics which was plague by several parasitic vibrations, as well as slower speed torque characteristics. Other important issues include the presence of acoustical noise and contamination problem caused by wear particles. The latter two problems are not covered in this dissertation. The present research focuses on the development of an analytical framework capable of capturing and simulating the parasitic vibrations experience by the HDD actuator.

A. Development of Analytical Modelling Frame

In order to study the low frequency rippling phenomena and the transmission of high ultrasonic vibrations to the actuator arm, a new and novel analytical model needs to be built. The model uses a Rayleigh Ritz Energy approach in the formulation of the governing equation of motions. The rotor is allowed to move dynamically in all six degrees of freedom with the inclusion of coupling gyroscopic effects. The main contributions in this part of the research are listed below:

1) An analytical model that models the TRUM rotor motion in all six degrees of freedom was developed. According to the author knowledge, this is the first analytical TRUM

model that has incorporated such rotor dynamics into the overall equation of motions governing TRUM system.

2) The results from this model has allows us to gain greater insight into the operating mechanisms underlying the generation of parasitic rippling vibrations. It was postulated that breakage in the rotor-stator loading symmetry can results in uneven penetration and hence unequal force-moment distribution which causes the onset of such motions.
3) The frequency spectrum from the simulation also shows very rich dynamical rotor behaviour with many higher order harmonics and other specific frequency components due to the stator rotor interactions. Of which, because the pre-loading spring characteristics have been incorporated into the model, the effects of springs design and transmissibility factor can also be studied.
4) Though slight imperfections in the TRUM stack up can be ignored safely for most other motor purposes. The model predicts that such imperfections can actually produce small vibrations in other axis in the orders of tens to hundreds of nanometre. Though small, these kinds of values are not acceptable if it is to be used as a HDD actuator.

The simulation results have been corroborated with experimental data and there exist some discrepancies which are not unexpected. However the trend exhibited by the data is encouraging as it points in the same direction and postulates as what the model would predict. The discrepancies between the experimental data and simulated results could be attributed to the fact that actual geometrical imperfections of the prototype model cannot be predicted accurately.

B. FEM study of TRUM systems

To first understand the TRUM operating characteristics, analysis of the TRUM by a numerical package such as ANSYS is necessary. Harmonic analysis and modal analysis results clarifies the operational mode shapes as well as supply us with an abundance of data with regards the vibrations modes of an entire TRUM assembly system. The main contribution from this research is as follows:

1) By varying the contact conditions between the rotor and stator components, it was discovered that a low frequency rippling exist for a TRUM. It was this results and the experimental data that has provided the motivation to develop the analytical model discussed earlier.
2) Harmonic analysis results of the entire TRUM assembly have allowed us to determine the vibrational transmissibility from the stator all the way to the actuator arm tips. By changing spring types, it was shown that the high frequencies transmitted can be altered. Again, this result and the supporting experimental data has provided the impetus to consider in more depth the inclusion of the spring pre-loading characteristics into the analytical framework.

FEM studies conducted in this research has shed light and discovered on new processes at work and has thus provided us the initial insight and motivation to develop a model to quantify and deepen our understanding on the cause of such behaviour.

C. Speed Torque Characteristics and Optimisation of Speed

The results presented in this section indicates to us that for a TRUM, there are many factors at work influencing the net speed, power efficiency, torque capacity as well as power generated. Higher and higher preload forces the peak speed down and higher tooth height provides amplification factor while less teeth can sometime mean higher speed due to less pressure on stator surfaces but at other time speed can decrease due to less contact time

between the travelling wave and rotor. To establish a clearly defined trend that means optimum operating TRUM condition isn't really possible. There are trade-offs in the selection of operational configurations.

8.2 Future Work

With the ability of the model being able to capture the resultant translational dynamics of the rotor under the influence an applied bias torque. It can be envisioned that the approach can be extended to simulate other types of assembly and tolerances stack up imperfections. Examples could include the effects of radial misalignments, uneven stator teeth height and the presence of clearances between rotor and stator.

In terms of the modelling framework, improvements can be made in the modelling of the rotor dynamics by incorporating the full Euler's Equation of motion so that uneven rotor geometry can also be taken into account. Also, in the modelling of the stator, the effects of stator rotary inertia and shear deformation have been omitted in the previous formulations. Although the effects should be small given the low amount of vibrations experience in the stator, nevertheless, it should be included as the diameter to thickness ratio isn't exactly thin in our case. For the stator under study the ratio of the diameter to thickness around 6.5. To apply the thin plate theory, the ratio should be at least around 10.

Different contact interface constitutive relations can also be studies. For example, by using the viscoelastic relations instead of a purely linear spring mode we can study the time dependence effects of the contact layer to relative velocities of compression. Other more elaborate friction models can also be studied to understand the effects on the overall TRUM characteristics. Explicit FEM studies can be conducted to better understand the complex

friction processes at work along the interface and provides us with more accurate inputs to the model.

The incorporation of frictional heating effects as well as control strategies into the model is also important directions of research if the TRUM is to be used as a precision actuator. As such devices function as a system and the overall performance is not only the result of superior mechanical characteristics or control strategies, it is the net product of both the mechanical “plant” factor interacting with the servo algorithm.

BIBLIOGRAPHY

[1] K. Ragulskis et al. “Vibromotors for Precision Microrobots”. Hemisphere Publishing Corporation. 1998

[2] T. Sashida. “Trial construction and operation of an ultrasonic driven motor”. In Japanese. Oyo Buturi, vol 51, 713-720. 1982.

[3] K. Spanner. “Survey of the various operating principles of ultrasonic piezomotors”. Actuator, 10th International Conference on New Actuators. 2006.

[4] T. Ikeda. “Fundamentals of Piezoelectricity”. Oxford University Press. 1990.

[5] T. Sashida and T. Kenjo. “An Introduction to Ultrasonic Motors”. Oxford Science Publications. 1993

[6] B. Nogarede and E. Piecourt. “Modelisation of a travelling wave piezoelectric motor by equivalent electromechanical circuit”. In proc ICEM. 1994

[7] I.V.N. Hagood and A.J McFarland. “Modelling of a piezoelectric rotary ultrasonic motor”. IEEE Trans. on Ultrasonics, Ferroelectrics and Frequency Control. Vol 42(2),210-224. 1995

[8] T. Sattel. “Dynamics of Ultrasonic Motors”. PhD Thesis MIT. 2002

[9] F. Lu, H.P. Lee, S.P. Lim. “Contact modelling of viscoelastic friction layer of travelling wave ultrasonic motor”. Smart Mater. Struct. Vol 10(2), 314-320. 2001

[10] Le Letty et al. “Combined finite element normal mode expansion methods in electroelasticity and their application to piezoactive motors”. International Journal for Numerical Methods in Engineering. Vol 40, 3385-3403. 1997

[11] J. Wallaschek. “ Contact Mechanics of Piezoelectric Ultrasonic Motors”. Smart Materials and Structure. Vol 7, 369-381. 1998

[12] W.H. Duan et al. Finite element solution for intermitten-contact problem with piezoelectric actuation in ring type USM”. Finite Elements in Analysis and Design. Vol 43, 193-205. 2007.

[13] Z.Y. Yao et al. “Analytical solution on the non-linear vibration of a travelling wave ultrasonic motor”. Journal of Electroceram. Vol 20, 251-258. 2008.

[14] Z. Boumous et al. “Effect of shearing deformation on the transient response of a travelling wave ultrasonic motor”. Science and Actuators A : Physical. Vol 150, 243-250. 2009.

[15] C.S. Zhao. “Ultrasonic Motors – Technologies and Applications”. Science Press Beijing. 2011.

[16] A. Endo and N. Sasaki. “Investigation of frictional material for ultrasonic motor”. In proc 7th Symp on Ultrasonic Electronics, Kyoto. Japanese Journal of Applied Physics. 1986.

[17] P. Rehbein and J. Wallaschek. “Friction and wear behaviour of polymer/steel and alumina/alumina under high frequency fretting conditions”. Wear. Vol 216, 97-105. 1998.

[18] T. Maeno et al. “Finite element analysis of the rotor/stator contact in a ring type ultrasonic motor”. IEEE Trans on Ultrasonics, Ferroelectrics and Frequency Control. Vol 39(6), 668-674. 1992.

[19] T. Kamano et al. “Characteristics and model of ultrasonic motor”. Journal of Applied Physics. Proc 8th Symp on Ultrasonic Electronics, 189-191. 1988.

[20] O. Zharii and A.F. Ulitko. “Smooth contact between the running Rayleigh wave and a rigid strip”. Trans ASME. Vol 62, 362-367. 1995.

[21] P. Le Moal and P. Minotti. “A 2-d analytical approach of the rotor/stator contact problem including rotor bending effects for high torque piezoelectric design”. European Journal of Mechanics, A/Soilds. Vol 16(6), 1067-1103. 1997.

[22] X. Cao and J. Wallaschek. “Estimation of the tangential stresses in the stator/rotor contact of travelling wave ultrasonic motors using visco-elastic foundation models”. Contact Mechanics II. Computational Mechanics Publications, 53-61. 1995.

[23] J. Schmidt, P. Hagedorn and Bingqi M. “A note on the contact problem in an ultrasonic travelling wave motor”. International Journal of Non-Linear Mechanics. Vol 31(6), 915-924. 1996.

[24] T. Sattel, P. Hagedorn, J. Schmidt. “The contact problem in ultrasonic travelling wave motors, part 1 : modelling”. Journal of Applied Mechanics. 2001.

[25] A. M. Flynn. “Piezoelectric Ultrasonic Micromotors”. PhD Thesis MIT. 1997.

[26] S. Ueha, Y. Tomikawa, M. Kurosawa and N. Nakamura. “ Ultrasonic Motors Theory and Applications”. Clarendon Press, Oxford. 1993.

[27] Y. Fan et al. “Properties of potassium titanate whisker reinforced polytetrafluoroethylene based friction materials of ultrasonic motors”. Journal of Applied Polymer Science. Vol 125, 3313-3317. 2012.

[28] P.S. Schenker et al. “A composite manipulator utilizing rotary piezoelectric otors: new robotic technologies for mars in-situ planetary science. In SPIE. Vol 3041. 1997.

[29] M. Schreiner et al. “Robotic wrist actuatorwith high torque piezoelectric travelling wave motor”. Actuator, 7th International Conference on New Actuators. 375-378. 2000.

[30] J. Maas et al. “Model-based control of travelling wave type ultrasonic motors”. Proc of 3rd International Heinz Nixdorf Symposium. 1999.

[31] H. Guo et al. “Mechanism analysis and output characteristics experiments of an ultrasonic motor with circumferential surface drive”. Journal of Electroceram. Vol 28, 118-122. 2012.

[32] D. Avirovik et al. “L-shaped piezoelectric motor – part II : Analytical modelling”. IEEE Transactions on Ultrasonics, Ferroelectrics and Frequency Control. Vol 59(1). 2012.

[33] M.S. Yoon et al. “Compact size ultrasonic linear motorusing a dome shaped piezoelectric actuator”. Journal of Electroceram. Vol 28, 123-131. 2012.

[34] Y.X. Liu et al. “A U-shaped linear ultrasonic motor using longitudinal vibration transducers with double feet”. IEEE Transactions on Ultrasonics, Ferroelectrics and Frequency Control. Vol 59(5). 2012.

[35] Y.X. Liu, W.S. Chen, P.L. Feng, J.K. Liu. “A Square-type rotary ultrasonic motor with four driving feet”. Sensors and Actuators A : Physical. Vol 180, 113-119. 2012.

[36] Y. Ting et al. “Stator design of a new type of spherical piezoelectric motor”. IEEE Transactions on Ultrasonics, Ferroelectrics and Frequency Control. Vol 57(10). 2010.

[37] D.M. Sun et al. “A piezoelectric linear ultrasonic motor with the structure of a circular cylindrical stator and slider”. Smart Materials and Structures. Vol 119. 2010.

[38] S. Kondo et al. “Travelling wave type ultrasonic linear motor using twin bending bars”. Physics Procedia. Vol 3, 1053-1058. 2010.

[39] B.N. Zhai. “Modelling, design and fabrication of ultrasonic linear moor”. Master Thesis National University of Singapore. 1999.

[40] C. H. Yun et al. Multi-degree of freedom ultrasonic micromotor for guidewire and catheter navigation – The NeuroGlide actuator”. Applied Physics Letter. Vol 100. 2012.

[41] D.A. Henderson. “Simple Ceramic Motor. Inspiring Smaller Products”. Actuator, 10th International Conference on New Actuators. 2006.

[42] T . Sattel, P. Hagedorn and J. Schmidt. “The contact problem in ultrasonic travelling wave motor, part II : Numerical Analysis”. Journal of Applied Mechanics. 2001.

[43] S.I. Furuya et al. “Load-adaptive frequency tracking control implementation of two phase resonant inverter for ultrasonic motor”. IEEE Transactions on Power Electronics. Vol 7(3), 542-550. 1992.

[44] B. Herzog. “Entwicklungsgrundlagen fur modulare ultraschallantriebe”. In German. PhD Thesis. Quote from Sattel. 1993.

[45] T. Sattel and P. Hagedorn. " On the contact between rotor and stator in an ultrasonic travelling wave motor". ISROMAC. 2000.

[46] Y. Izuno. "Adaptive control based high performance drive system implementation of travelling wave type ultrasonic motor". Electrical Engineering in Japan. Vol 112(1), 1147-1154. 1992.

[47] T. Sattel and P. Hagedorn. "A note on non-intermittend contact problems of a special class of ultrasonic motors". In Proc DETC, ASME Sesign Engineering Technical Conference. 1999.

[48] S. Ueha and E. Mori. "Effects of surface conditions of components of temperature upon performance of a bolt-clamped Langevin type longitudinal transducer". Journal of Acoustical Society Japan. Vol 35(9), 468-476. 1979.

[49] J.H. Hu et al. "An experimental investigation of the temperature field in small piezoelectric vibrators". Ultrasonics. Vol 41(9), 731-775. 2004.

[50] X.L. Lu et al. "Analysis of the temperature field of travelling wave rotary ultrasonic motors". IEEE Transactions on Ultrasonics, Ferroelectrics and Frequency Control. Vol 58(12). 2011.

[51] F. Lin and L. Kuo. "Driving circuit for ultrasonic motor servo drive with variable-structure adaptive model following control". IEEE Proceedings . 1997.

[52] T. Senjyu et al. "Speed control of ultrasonic motors by adaptive control with a simplified mathematical model". IEEE Proceedings. 1997.

[53] Y. Izuno and M. Nakaoka. " High performance and high precision ultrasonic motor-actuated positioning servo drive system using improved fuzzy-reasoning controller". IEEE PESC. 1994.

[54] J. Maas, T. Schulte, H. Grotstole. "High performance speed control for inverter-fed ultrasonic motors optimised by a neural network". In Proc Actuator, 260-263. 1998.

[55] F. Cheng et al. "A BPNN-PID based long stroke nanopositioning control scheme driven by ultrasonic motor". Precision Engineering. Vol 36, 485-493. 2012.

[56] A.M. Flynn. "Performance of Ultrasonic mini-motors using design of experiment". Smart Materials and Structures. Vol 7(3). 1998.

[57] J.L. Pons et al. "Parametrical Optimisation of Ultrasonic Motors". Sensors and Actuators A : Physical. Vol 107, 169-182. 2003.

[58] P. Bouchilloux and K. Uchino. "Combined finite element analysis- genetic algorithm method for the design of ultrasonic motors". Journal of Intelligent Material System Structures. Vol 14(10), 657-667. 2003.

[59] J.M. Fernandez et al. “Sensitivity analysis and optimisation of a standing wave ultrasonic linear motor”. IEEE Transactions on Ultrasonics, Ferroelectrics and Frequency Control. Vol 53(7). 2006.

[60] S. Li et al. “Particle swarm optimization combined with finite element method for design of ultrasonic motors”. Sensors and Actuators A : Physical. Vol 148(2), 285-289. 2008.

[61] S. Ueha, Y. Hashimoto, Y. Koike. “Non-contact transportation using near field acoustic levitation”. Ultrasonics. Vol 38, 26-32. 2000.

[62] I. Hirom. “Frequency characteristics of non-contact ultrasonic motor with motion error correction”. Precision Engineering. Vol 31(4), 351-357. 2007.

[63] R. Yano. “Positioning of an object in near field acoustic levitation and its application”. Proceedings of Symposium on Ultrasonic Electronics. Vol 31, 531-532. 2010.

[64] J.H. Hu et al. “Characteristics of a noncontact ultrasonic motor using acoustic levitation”. Ultrasonic Symposium. 1996.

[65] F. Claeyssen “Amplified Piezoelectric Actuators : Static and Dynamic Applications”. Ferroelectrics Vol351,3-14, 2007.

[66] Y. Kawai et al. “High power travelling wave type ultrasonic motor”. Japan Journal of Applied Physics. Vol34, 2711-2714. 1995.

[67] Zhao Chun Sheng, “Ultrasonic motor technology and application”, Science Press Hub (2007)

[68] Wriggers. P., “Computational contact mechanics’, Wiley((2002)

[69] J.A.C. Martins, J.T. Oden. “Existence and uniqueness results for dynamic contact problem with non-linear normal and friction law.” Nonlinear Analysis, 11, 407-428, 1987.

[70] T. Maeno, D.B. Bogy. “Effect of the hydrodynamic bearing on rotor/stator contact in a ring type ultrasonic motor.” Ultrasonics Symposium, Vol 2, 933-936, 1991.